In situ Observation of Phase Transformations in Steels

Zur Erlangung des akademischen Grades eines

Doktors der Ingenieurwissenschaften (Dr.-Ing.)

von der KIT-Fakultät für Maschinenbau des
Karlsruher Instituts für Technologie (KIT)

genehmigte

Dissertation

von

M.Sc. Michael Pfund

aus Schwäbisch Gmünd

Kurzfassung

Festkörperumwandlungen spielen eine wichtige Rolle bei der Herstellung und Verarbeitung von Stählen. Sie sind das effektivste Werkzeug, um die mechanischen Eigenschaften von Stählen zu optimieren. Eine Kette dieser Umwandlungen ist oft an den Verarbeitungsschritten von der Schmelze bis zum Endprodukt beteiligt.

Das Ziel dieser Arbeit ist es, eine durchgehende Prozessbeschreibung und Charakterisierung der resultierenden Mikrostrukturen zu realisieren, die eine umfassendere Optimierung dieser Prozesse ermöglichen kann. Um diesem Ziel näher zu kommen, wurden in dieser Arbeit experimentelle und rechnergestützte Werkzeuge erarbeitet. Es wurde ein Experiment zur Hochtemperatur Elektronenrückstreubeugung entwickelt, das es ermöglicht, das Gefüge von Stählen während der Wärmebehandlung durch Rückstreubeugung und einfache Bildgebung abzubilden. Ergänzende Computerprogramme wurden entwickelt, die es ermöglichen, die Rückstreudaten der Mikrostruktur verschiedener Verarbeitungsschritte zu kombinieren, um die mikrostrukturelle Entwicklung quantitativ zu verfolgen. Die Kombination von Rückstreudaten mit Bildgebungssequenzen aus dem Rasterelektronenmikroskop ermöglicht zudem die Charakterisierung hochdynamischer Prozesse, die (noch) nicht durch Elektronenrückstreubeugung charakterisiert werden können.

Diese Werkzeuge wurden auf die Ferrit-Austenit-Ferrit- und die Austenit-Martensit-Umwandlung angewendet. Die neuen Methoden, die in dieser Arbeit entwickelt wurden, ermöglichen eine genauere Charakterisierung der Umwandlung und ihrer Produkte: Die Orientierungen der Austenitphase wurden direkt *in situ* gemessen, anstatt des bisher üblichen Ansatzes bei dem diese mit Rekonstruktionsalgorithmen abgeschätzt werden. Dies ermöglicht erstmals eine quantitative Beschreibung mehrerer Merkmale von Martensit-Mikrostrukturen wie Variantenauswahl, Variantenpaarung und die Martensithabitusebene. Darüber hinaus ermöglicht es die Berechnung von genauen Orientierungsbeziehungen für diese Phasenumwandlungen.

Diese umfassendere Charakterisierung trägt dazu bei, mehrere Merkmale dieser Transformationen zu erklären: Die Rolle der verschiedenen Grenzflächen bei der Nukleation von Martensit sowie deren Entstehung und Entwicklung werden geklärt. Zusätzlich wird der Einfluss der Austenitkorngröße auf die Variantenauswahl untersucht und die Ergebnisse verschiedener Austenitrekonstruktionsalgorythmen mit den realen, gemessenen Mikrostrukturen verglichen. Variantenauswahl und Variantenpaarung in vollmartensitischen und zweiphasigen Mikrostrukturen werden verglichen.

Abstract

Solid-solid phase transformations play an important role in production and processing of steels. They are the most effective tool to tune the mechanical properties of steels. Frequently, a chain of these transformations is involved in the processing steps from the melt to the final products.

The aim of this thesis is to develop a through-process description and characterization of microstructures before, after and during solid-solid phase transformations which can enable a more comprehensive optimization of these processes. Experimental and computational tools were developed to approach this goal. A high temperature electron backscatter diffraction setup was designed which enables to map the microstructure of steels during heat treatments by backscatter diffraction and imaging. Complementary computational tools were developed that allow for the combination of the backscatter data of the microstructure at different processing steps to track the microstructural development in a quantitative way. The combination of backscatter data with scanning electron microscopy imaging sequences further allows for the characterization of highly dynamic processes which cannot be characterized soley by backscattering (yet).

These methods were applied to the ferrite-austenite-ferrite and the austenite-martensite transformations. The new methods which were developed in this thesis enable a more detailed characterization of the transformation and its products: The orientations of the austenite phase were directly measured *in situ* instead of the up to now prevailing approach that uses reconstruction algorithms for an estimation of these orientations. For the first time, this allows for a quantitative description of several features of martensite microstructures such as variant selection, variant pairing, and martensite habit plane. It furthermore allows for the calculation and mapping of orientation relationships for these phase transformations.

This more comprehensive characterization helps to elucidate several characteristics of these transformations: The role of annealing twins in the austenite for the nucleation of martensite as well as their origin and development are clarified. Additionally, the influence of the grain size of the austenite on the selection of martensite variants is evaluated and the results of various prior austenite reconstruction algorithms are compared to the microstructures measured. Variant selection and variant pairing in both, fully martensitic and dual-phase microstructures are compared.

Danksagungen

Contents

Nomenclature

α	Body centered cubic (bcc) phase in steels, ferrite
α'	bcc/bct hard phase in steels, martensite
AHSS	Advanced High Strength Steels
AI	Artificial Intelligence
ANN	Artificial Neural Network
APT	Atom Probe Tomography
bcc	Body Centered Cubic
BC	Band Contrast
BF	Bright Field
bct	Body Centered Tetragonal
B_s	Bainite start temperature
BS	Band Slope
BSE	Back Scattered Electrons
CCD	Charge-coupled device
CP	Complex Phase
CPD	Close Packed Direction
CPP	Close Packed Plane
CSL	Coincidence Site Lattice
δ	Delta iron
DEMO	DEMOnstration Power Plant
DET	Divorced Eutectoid Transformation
DF	Dark Field
DP	Dual Phase
DSC	Differential Scanning Calorimetry
EBSD	Electron Backscatter Diffraction
EBSP	Electron Backscatter Pattern

EDX	Energy Dispersive X-ray
EF	Epitaxial Ferrite
fcc	Face Centered Cubic
FIB	Focused Ion Beam
γ	Face centered cubic (fcc) phase in steels, austenite
GBE	Grain Boundary Engineering
GND	Geometrically Necessary Dislocation
GOS	Granular Orientation Spread
GT	Greninger-Troiano
GT', iGT	Inverse Greininger-Troiano
HSLA	High-Strength Low-Alloy
HT EBSD	High Temperature EBSD
HV	High Vacuum
ICP-OES	Inductively Coupled Plasma Optical Emission Spectrometry
IF	Intercritical Ferrite
IGBD	Intrinsic Grain Boundary Dislocation
IO	Input/Output
IPF	Inverse Pole Figure
IPS	Invariant Plane Strain
ITER	International Thermonuclear Experimental Reactor
KS	Kurdjumov-Sachs
KSN	Kurdjumov-Sachs-Nishiyama
k_{VSS}	Variant Selection Strength factor
LSCM	Laser Scanning Confocal Microscopy
LM	Light Microscopy
MAD	Mean Angular Deviation
MC	Monte Carlo
MDF	Misorientation Density Function

M_0	Equilibrium temperature (T_0)
M_f	Martensite finish temperature
M_s	Martensite start temperature
NW	Nishiyama-Wasserman
ODF	Orientation Density Function
OM	Orientation Mapping
OPS	Oxide Particle Suspension
OR	Orientation Relationship
PAG	Prior Austenite Grain
PAGB	Prior Austenite Grain Boundary
PAR	Prior Austenite Reconstruction
PID	Proportional-Integral-Derivative
PTMC	Phenomenological Theory of Martensitic Crystallography
RAFM	Reduced Activation Martensitic Ferritic Steel
SE	Secondary Electron
SEM	Scanning Electron Microscopy
SFE	Stacking Fault Energy
STEM	Scanning Transmission Electron Microscopy
TEM	Transmission Electron Microcopy
TKD	Transmission Kikuchi Diffraction
TRIP	Transformation Induced Plasticity
TTT	Time-Temperature-Transformation
TWIP	Twinning Induced Plasticity
UHV	Ultra High Vacuum
VSS	Variant Selection Strength
XRD	X-ray Diffraction

1 Introduction

Steel has replaced most other structural materials since the introduction of the Bessemer process in 1856 which marks the start of mass-production of steel. Despite the steady development of new materials, steels remain the world's most important structural material. Today, steel comprises approximately 75% of all major appliances mostly due to high strength in relation to its weight and price. This dominance stems from the diverse range of properties achievable through alloying and various heat treatments. Steels can be hard, strong, ductile, paramagnetic, ferromagnetic, corrosion resistant and weldable. They can be easily recycled and are by far the most recycled material in the world.

The prevalence of steels as structural materials is a result of steady improvement of alloy design and processing. Over half of all the types of steels used in today's cars did not exist 10 years ago and are about 30% stronger than a decade ago. Dual-phase steels (DP) were the first steels of a new generation of high-strength low-alloy (HSLA) steels which were developed in the 1970s and are now widely used in the automotive industry. This class of materials belongs to advanced high strength steels (AHSS) which further comprise the later developed alloys such as transformation induced plasticity (TRIP), twinning-induced plasticity (TWIP) and complex phase (CP) steels. This development highlights the increasing importance of microstructure and phase transformations of steels and their precise control during manufacturing and processing.

Most steels pass a chain of production steps from crude iron to the final product. This chain of production steps is not only intended to shape the material into a product but also to influence its microstructure to achieve specific properties. The production steps usually include heat treatments leading to phase transformations capable of changing the properties of the material. The ongoing success story of steelmaking is partly based on the many phase transformations which can be used to very effectively control the microstructure of steels. The interplay of heat treatment, alloying chemistry and phase transformations allows to tune the properties of steels in relative wide limits (e.g. tensile strengths from 140 MPa to 6 GPa [1], [2]).

The complexity of this interplay renders alloy design a costly and time-consuming task. Modern characterization methods and tools of computational thermodynamics can assist in this process but the basic strategy, which is largely dependent on a trial-and-error approach, did not change considerably since the early days of steelmaking. A departure from this approach based on Cohen's reciprocity [3] was outlined by G. B. Olson [4]. The former consists of three links which concatenate performance, properties, structure and processing. Starting with the first link, the target properties required by the performance in application are identified. The second link consists of the design of a microstructure to obtain the desired properties. The third link represents the identification of processing parameters to obtain the tailored microstructure. This concept is schematically illustrated in Figure 1.1.
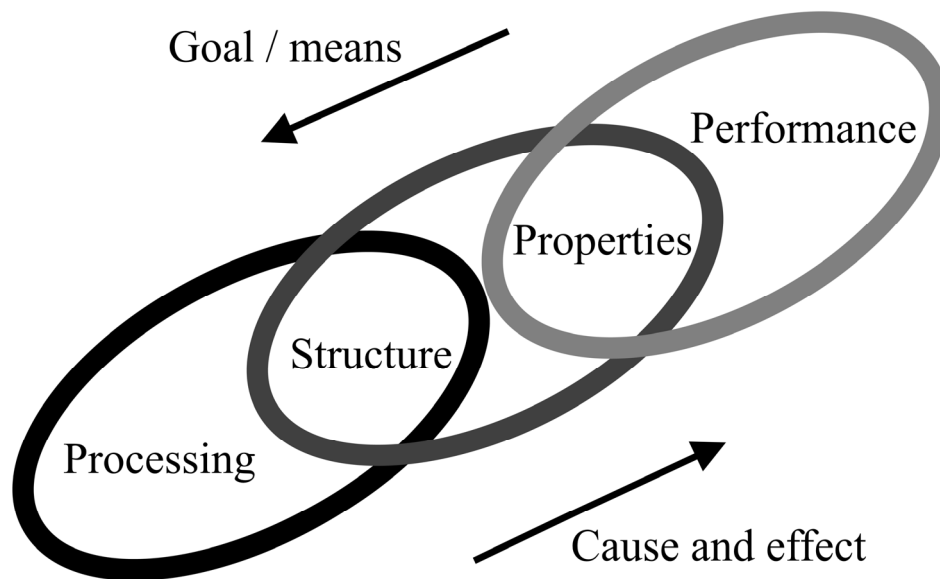
Figure 1.1: Olson's link chain model representation of Cohen's reciprocity. Adapted from [4].

The implication of a straightforward design process from requirements to microstructure and processing is in practice misleading. Complete understanding of microstructure-property relations as well as the influence of processing on microstructure is a prerequisite of this approach. Olson envisioned a hierarchy of computational design models to fulfill this task instead. The quality of its results can however only be as good as the quality of these models and/or *in silico* simulations. Optimization approaches based on machine learning and datamining comprising artificial neural networks (ANN) and artificial intelligence (AI) may help to overcome these shortcomings. This strategy does not require complete understanding of the processes involved and the quality of its results is not bound to any material model. The most important prerequisite for the development of reliable ANN are large amounts of information on the microstructure at every link of the processing chain for the training of the AI. The development of characterization methods with improved resolution, accuracy and reduced measurement time can provide this data.

The aim of this work is to develop an experiment capable of performing microstructural characterization during the steps of a processing chain. This was accomplished by developing a novel high temperature *in situ* EBSD experiment. The large amount of data (crystallographic information from EBSD maps, SEM images) collected during these experiments require for suitable software tools in order to allow for a quantitative analysis of microstructural processes (grain growth, phase transformations) during the steps of the processing chain. This set of software tools is able to combine the information of every link of the chain into a single unified data set. The basic idea behind this concept is to achieve a complete characterization of a material by including its processing history. Although focusing on the crystallography of phase transformations in steels, this experimental approach and the related software tools are not restricted to the characterization during processing of steels but can be applied to various crystalline materials and their processing.

The combination of microstructural information at different processing steps allows for an improved analysis of associated mechanisms. This work is one of the very few *in situ* studies on austenite microstructure evolution of various steels at processing temperatures. It describes the ferrite-austenite phase transformation, intercritical annealing and microstrcucture evolution in the austenite phase. This data and the aforementioned analysis tools allow for an unprecedented characterization of the product microstructure.

A focus was put on microstructure evolution during austenitization and intercritical annealing as well as the martensitic transformation. These topics are not only relevant for the optimization of processing of steels but are also of great interest for the understanding of fundamental processes. Despite the vast amount of literature that contains research on steels, fundamental questions still remain unanswered:

1. Crystallography and preferred sites for martensite nucleation.

2. Martensite transformation sequence. This includes, especially for lath martensite, martensite variant selection mechanisms and martensite variant pairing.

3. Orientation relationships between ferrite and austenite, austenite and martensite. In particular variations of the orientation relationship on a microstructural level.

4. Reliability of parent austenite reconstruction algorithms which are often used for the study of austenite microstructure.

5. Role of austenite twins during annealing, austenite and martensite formation.

6. Crystallography of microstructural evolution during intercritical annealing including the role of special interfaces (twins, phase and grain boundaries)

7. The influence of the presence of ferrite on martensite nucleation and subsequent formation (dual-phase steels).

Some of these issues were already frequently addressed and discussed in literature. New and more comprehensive insights in these open questions are however enabled by more and more sophisticated measurement techniques and associated computational methods. This work uses new experimental and computational approaches to shed new light on these old questions resulting in a new perspective on some aspects of heat treatments of steels. The large body of literature concerning martensite formation led to the decission to limit the scope of this thesis to lath martensite. The scope of this thesis was additionally limited from a metallurgical point of view to two "model" alloys: These are a EUROFER alloy and pure plain low carbon steels.

This thesis is structured as follows: The first part of Chapter 2 gives an introduction into microstructural constituents of steels with a focus on crystallographic aspects. These sections are deliberately kept short due to the vast amount of research which was published on these topics. The second part gives an overview on the state of research concerning the observation of phase transformations in steels. Chapter 3 describes the experimental methods which are used throughout this thesis. The experimental setup developed during this thesis is motivated and described in this chapter. Chapter 4 describes the computational methods which were developed during this thesis for the analysis of the measured crystalographic data. The computational procedure which is used for the spatial and crystallographic alignment and combination of different orientation maps from one area is described in this chapter. Important statistical aspects concerning the interpretation of orientation relationships between two phases are analyzed in Chapter 5. The martensitic transformation starting from a fully austenite microstructure for a EUROFER steel is investigated in Chapter 6 using the methods described before. Intercritical annealing and martensite formation of the same EUROFER steel starting from a dual-phase microstructure is analyzed in Chapter 7. Chapter 8 and 9 are concerned with martensite formation in two pure low carbon steels with different carbon contents. Chapter 8 focuses on austenite-ferrite transformation and annealing. It analyzes and describes the formation of austenite twins. Chapter 9 describes the formation of martensite and pearlite from steel exhibiting higher carbon content. The main results are summarized and discussed in Chapter 10. The appendix can be found in Chapter 11.

The experiments and observations made in this thesis were conducted on different materials. The heat treatments also led to very different product microstructures even for the same materials. The chapters that deal with experiments (Chapter 6 – Chapter 9) are listed in the following table in order to give a first glance at the different product microstructures.
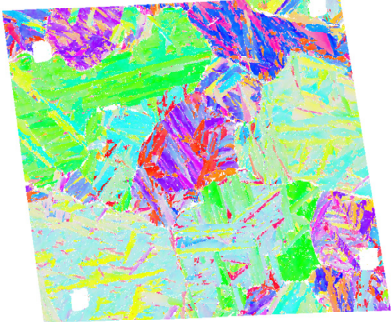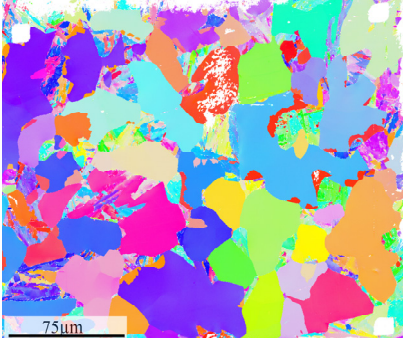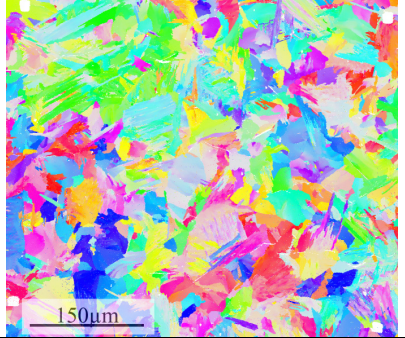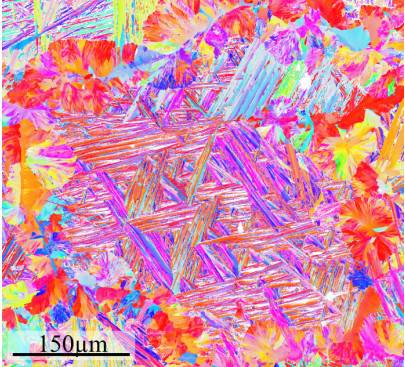
	Material	Transformation	Product Microstructure
Chapter 6: Martensite Formation in EUROFER Steel	EUROFER	Fully austenitic microstructure ↓ Fully martensitic microstructure	
Chapter 7: Intercritical Annealing of EUROFER Steel	EUROFER	Intercritical annealing (austenite and ferrite) ↓ Ferrite and martensite islands	
Chapter 8: Origin of Austenite Annealing Twins	FeC 0.105 wt.% C	Fully austenitic ↓ Mixture of different transformation products (ferrite, martensite, Widmanstätten structures)	
Chapter 9: Martensite Formation in Plain Carbon Steel	FeC 0.240 wt.% C	Fully austenitic ↓ Martensite and pearlite	

Table 1.1: Overview of materials and product microstructures in the Chapters concerning *in situ* experiments.

2 Background

This chapter contains two sections: The first part is an introduction to the microstructural constituents that are commonly observed in steels. The relevant literature associated with their structure and formation is reviewed. All of these constituents in steels are the products of different phase transformations. These transformations have very complex partly conflicting characteristics which are still subject to ongoing disputes. A selection of theories developed for the description and explanation of these phase transformations is reviewed. Within the transformations, emphasis is put onto the martensitic transformation. The most important theories related to this transformation with regard to steels are discussed. Specific phenomena connected to this transformation such as different martensite morphologies, martensite variant selection, prior austenite reconstruction (PAR), orientation relationships and martensite nucleation are highlighted.

The second part reviews the relevant literature about the investigation of these phase transformations. This review is mostly restricted to steels and to observations of their microstructure. Here focus is put on *in situ* studies. This section is intended to give a concise yet comprehensive overview of the technical and experimental state of the art regarding *in situ* high temperature setups for the study of phase transformations.

2.1 Microstructural Constituents of Steels

This paragraph is intended to introduce the microstructural constituents which can be observed in steels. The term "phase" and "microstructural constituent" are often synonymously used. A phase is a region of space (a thermodynamic system), throughout which all physical properties of a material are uniform. In the sense of this definition pearlite is not a phase. The metastable Fe-Fe_3C phase diagram shown in Figure 2.1 reveals that Pearlite consists of two phases namely of cementite (Fe_3C) and ferrite which are arranged in a lamellar structure. Therefore the term "microstructural constituent" is used further on to describe phases or reoccurring distinct mixtures of phases. The common microstructural constituents of steels consist of the most important phases ferrite, austenite and cementite featuring different structures [5], [6]. They often form very far away from thermodynamic equilibrium during rapid cooling. This is illustrated with a schematic TTT (Time-Temperature-Transformation) diagram shown in Figure 2.2 where a qualitative classification of several non-equilibrium constituents is made.
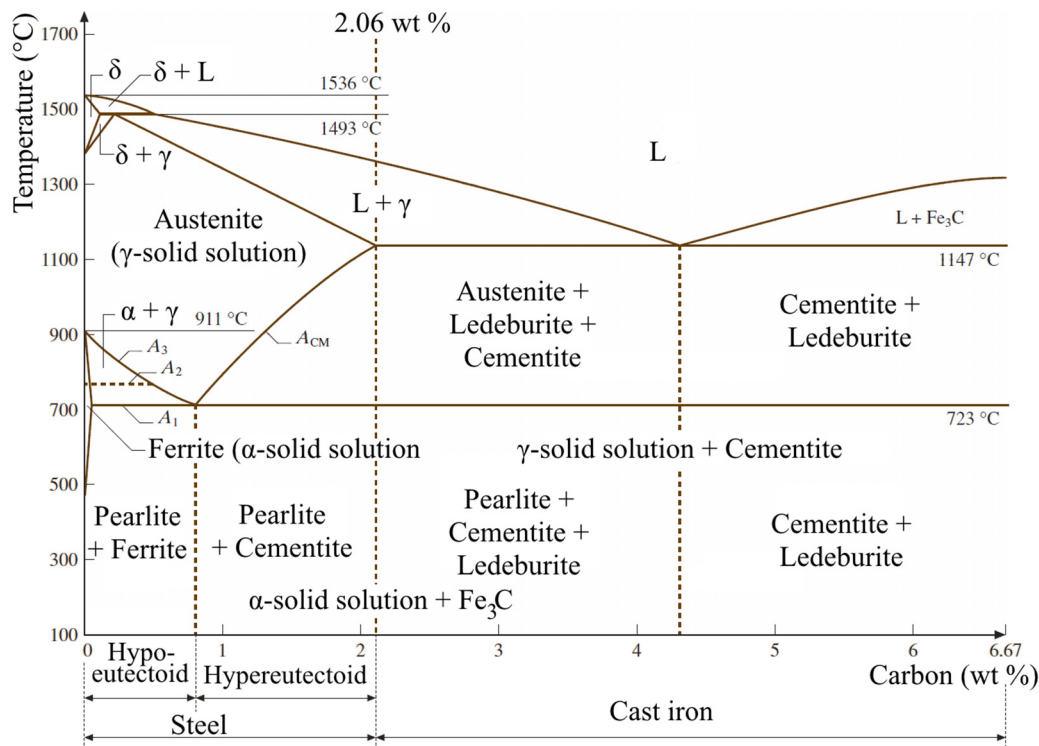
Figure 2.1: Metastable Fe-Fe₃C (6.67 wt% C) phase diagram, adapted from [7].

An overview of steel processing, its structure and properties is given by Krauss [8], [9]. Comprehensive and systematic classifications of the constituents were for example proposed by Aaronson [10], Christian [11] and Bhadeshia [12]. Aaronsons approach of a classification was solely based on the morphology of the constituents applying Dubé's morphological classification system [13] on steel microstructures. But the constituents can also be classified based on their transformation, structure and/or crystallography. A summary of the criteria to classify the transformation products and application to the microstructural constituents of steels on the basis of Bhadeshia is shown in Table 2.1. The following review of the relevant literature shows that some of these classifications are still a matter of ongoing debates.

2.1.1   Austenite

Most heat treatment procedures in the process chain for steel production or processing will include the transformation to austenite. The microstructure of austenite at elevated temperatures is difficult to investigate because of high temperatures and connected difficulties (oxidation, drift). Austenitization and ferrite formation was therefore often investigated using hot stage microscopy or laser scanning confocal (LSCM) hot stage microscopy [14]–[19]. These techniques enable the observation of interfaces due to thermal grooving (cf. Chapter 2.2.2.3). It is however not possible to determine the phase or local orientations. Full crystallographic information can be obtained using *in situ* electron backscatter diffraction (EBSD) experiments. Such experiments were conducted by Fukino et al. [20], [21] and Lischewski et al. [22]–[25] to study the formation of austenite. They observed the nucleation and growth of the austenite phase and confirmed that the OR (orientation relationship) between ferrite and austenite is close to the KS (Kurdjumov-Sachs) OR. The same result was found earlier through XRD measurements on stabilized austenite by Brückner et al. [26], [27]. Microstructural investigations on austenite of different compositions including local orientation measurements at different temperatures are still missing. Instead the austenite microstructure is often reconstructed from EBSD maps of the martensite microstructure using parent austenite grain reconstruction algorithms (cf. Chapter 2.1.8.9 on p. 21).
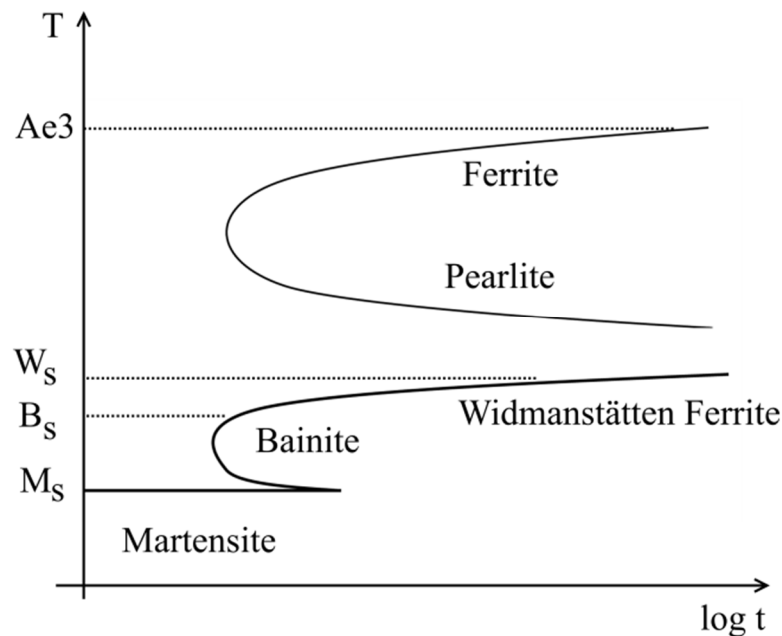
Figure 2.2: A schematic TTT (Time-Temperature-Transformation) diagram. W_S denotes the Widmanstätten start B_S the Bainite start and M_S the martensite start temperature. Ae3 denotes the temperature below which ferrite is formed. Adapted from [28].

In plain carbon steel austenite will be only stable at elevated temperatures above 723 °C. This may change if alloying elements are introduced that stabilize austenite (e.g. Mn, Ni, Co, N) [28]. Retained austenite may be present in steel at room temperature depending on the alloying chemistry and heat treatment. Retained austenite is mechanically stabilized and/or stabilized by alloying elements. It may transform to martensite under mechanical loading and can therefore enhance the mechanical properties [29]–[34] of the steel (transformation induced plasticity (TRIP) [35], [36] effect). It can also be used to determine prior austenite orientations.

2.1.2 Allotriomorphic Ferrite

The term Allotriomorphic Ferrite was first used by Aaronson [10] describing the transformation product formed after the nucleation of ferrite at austenite grain boundaries upon cooling. Allotriomorphic ferrite means that the shape i.e. the dominant growth direction is not connected to any crystallographic direction but to the shape of the austenite grains. This shape is a consequence of the nucleation of ferrite at austenite grain boundaries. The transformation of austenite to allotriomorphic ferrite is inhibited by solute drag effects and the diffusion of carbon [37]–[39]. The fraction of allotriomorphic ferrite, its formation kinetics [40] and crystallographic properties [41], [42] are of great importance for alloy design. Allotriomorphic ferrite is shown in Figure 2.3 in a schematic representation of the ferritic transformation products of austenite marked as (a).

Comment	α'	α_{lb}	α_{ub}	α_a	α_W	α	α_i	P
Nucleation and growth reaction	X	X	X	X	X	X	X	X
Plate morphology	X	X	X	X	X	O	O	O
IPS shape change with shear component	X	X	X	X	X	O	O	O
Diffusionless reaction	X	O	O	O	O	O	O	O
Reconstructive diffusion during nucleation	O	O	O	O	O	X	X	X
Often nucleates intragranularly on defects	X	O	O	X	O	O	X	O
Diffusionless growth	X	X	X	X	O	O	O	O
Reconstructive diffusion during growth	O	O	O	O	O	X	X	X
Atomic correspondence of all atoms during growth	X	X	X	X	O	O	O	O
Atomic correspondence of subst. atoms during growth	X	X	X	X	X	O	O	O
Bulk redistribution of X atoms during growth	O	O	O	O	O	$\otimes$	$\otimes$	$\otimes$
Local equilibrium at interface during growth	O	O	O	O	O	$\otimes$	$\otimes$	$\otimes$
Local paraequilibrium during growth	O	O	O	O	X	$\otimes$	$\otimes$	O
Diffusion of carbon during transformation	O	O	O	O	X	X	X	X
Carbon diffusion controlled growth	O	O	O	O	X	$\otimes$	$\otimes$	$\otimes$
Cooperative growth of ferrite and cementite	O	O	O	O	O	O	O	X
High dislocation density	X	X	X	X	$\otimes$	O	O	O
Incomplete-reaction phenomenon	O	X	X	X	O	O	O	O
Necessarily has a glissile interface	X	X	X	X	X	O	O	O
Always has an orientation within the Bain region	X	X	X	X	X	O	O	O
Growth across austenite grain boundaries	O	O	O	O	O	X	X	X
High interface mobility at low temperatures	X	X	X	X	X	O	O	O
Displacive transformation mechanism	X	X	X	X	X	O	O	O
Reconstructive transformation mechanism	O	O	O	O	O	X	X	X

Table 2.1: Summary of the characteristics of solid-state transformations in steels. The compared transformation products here are martensite (α'), lower bainite (α_{lb}), upper bainite (α_{ub}), acicular ferrite (α_a), Widmanstätten ferrite (α_W), allotriomorphic ferrite (α), idiomorphic ferrite (α_i) and pearlite (P). The symbols in the corresponding columns show if the comment holds true (X) or not (O) or if both cases have been observed ($\otimes$). After Bhadeshia [12] and Christian [11] (p.9).

2.1.3 Idiomorphic Ferrite

In contrast to allotriomorphic ferrite, idiomorphic ferrite nucleates intragranularly. A schematic example of idiomorphic ferrite morphology is depicted in Figure 2.3e. Inclusions were identified as the predominant nucleation site inside austenite grains [43], [44]. It is often facetted because of preferred crystallographic growth directions. Idiomorphic ferrite is reported to improve the toughness of steels [45] and can be used for grain refinement. Therefore its nucleation mechanism, morphology and crystallography are of great interest [46].

2.1.4 Acicular Ferrite

Acicular ferrite can be recognized by its needle-shaped crystallites when viewed in a cross section. These crystallites are lenticular in shape. Acicular ferrite nucleates inside austenite grains on inclusions and can form an interlocking "basket weave" structure [47], [48]. The single ferrite grains of this structure are separated from each other by high angle boundaries. The character of the grain boundaries, the interlocking chaotic structure and low grain size result in a very high resistance to crack propagation [49]. Acicular

ferrite is therefore a microstructural constituent that is of high interest in steel welds [50]–[55]. Because of its morphology it is a fine Widmanstätten constituent which in contrast to Widmanstätten ferrite is not nucleated at austenite grain boundaries or Allotriomorphic ferrite but at inclusions. A clear distinction between acicular ferrite and other transformation products like intragranular bainite and other Widmanstätten constituents is therefore difficult [5], [56]–[59].
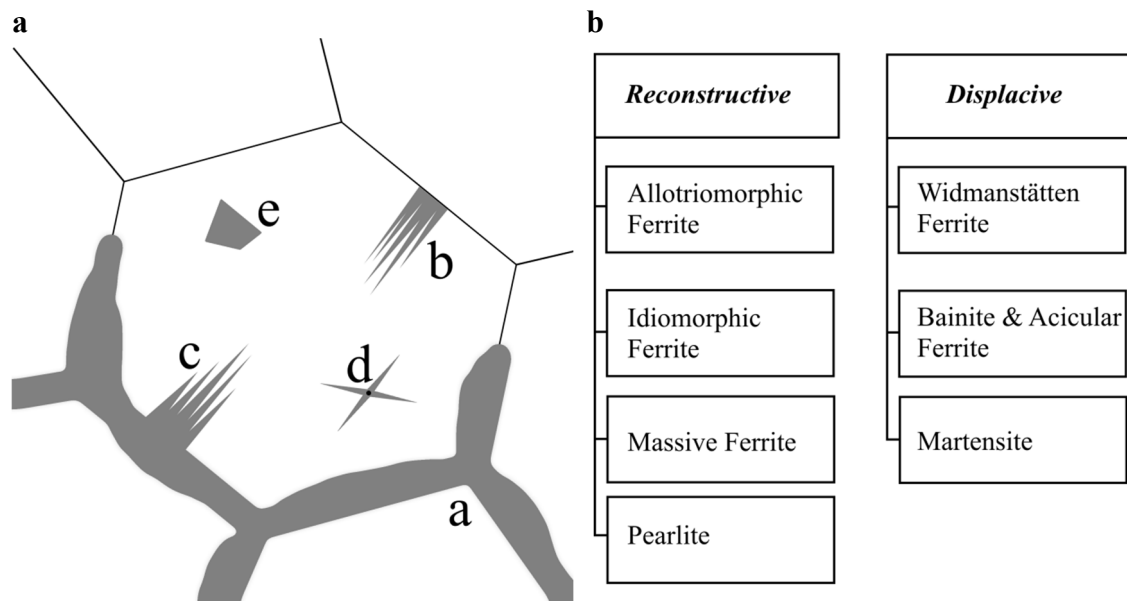
Figure 2.3: a) Schematic illustration of different ferritic microstructural constituents which can be found in steels. Austenite grain boundaries are marked by straight black lines; the shape of the ferrite transformation products is marked in grey. *(a)* illustrates the appearance of allotriomorphic ferrite at austenite grain boundaries. *(b)* shows the formation of primary Widmanstätten ferrite nucleated directly at an austenite grain boundary. *(c)* shows the shape of primary Widmanstätten ferrite which nucleates from allotriomorphic ferrite. *(d)* shows the morphology of acicular ferrite which usually nucleates at an inclusion/particle. *(e)* illustrates the shape of idiomorphic ferrite inside an austenite grain. **b)** Classification of austenite transformation products by the transformation process proposed by Bhadeshia [28].

2.1.5 Widmanstätten Ferrite

Widmanstätten ferrite forms at relative high temperatures close to A_{e3} (cf. Figure 2.1 and Figure 2.2) with very low undercooling. Ferrite crystals nucleate and form needle like structures. Pronounced Widmanstätten structures are usually observed for steels containing less than ca. 0.4% carbon. The needle like shape of Widmanstätten crystallites is supposed to be a consequence of a self-accommodation process due to the displacive nature of the transformation [60], [61]. A schematic representation of primary Widmanstätten ferrite can be seen in Figure 2.3b. Primary Widmanstätten ferrite nucleates at austenite grain boundaries. Needles formed within one Widmanstätten colony mostly share the same crystallographic orientation [62]–[64]. The OR between austenite and Widmanstätten ferrite is close to the KS OR. Secondary Widmanstätten ferrite is also called sideplate ferrite [10] and can be seen in Figure 2.3c. In this case it nucleates at previously formed allotriomorphic ferrite. A clear distinction between Widmanstätten structures and bainite is not always clear due to the displacive transformation mechanism common to both transformation products [65]–[67]. Plate growth occurs under paraequilibrium carbon conditions. The velocity of growth is controlled by the diffusion of carbon whereas substitutional alloying atoms do not diffuse fast enough. The growth proceeds in a cooperative formation of pairs of adjacent self-accommodating plates which form by a displacive mechanism [68], [69].

2.1.6 Epitaxial Ferrite

Epitaxial ferrite forms during quenching from the intercritical regime by epitaxial growth of existing intercritical ferrite into austenite. It is challenging to distinguish epitaxial ferrite from intercritical ferrite due to its epitaxial growth [70], [71]. An improvement of the mechanical properties of dual phase steels by an increased phase fraction of epitaxial ferrite was reported in the literature [72]–[75]. The difference between intercritical and epitaxial ferrite is mostly of chemical nature. The moving ferrite/austenite interface is faster than the diffusion of alloying elements leading to a concentration gradient in the epitaxial ferrite [71], [76]. This concentration gradient ideally reaches from the equilibrium composition of ferrite to the equilibrium composition of austenite [77].

2.1.7 Bainite

Steels containing bainite distinguish themselves by their high strength [78]–[84] accompanied by good ductility [85]–[89] and respectable fracture toughness [90]–[92]. Bainite usually consist of finely dispersed Cementite in a ferrite matrix that exhibits a high dislocation density. There is still an ongoing discussion about the structure of bainite, the nature of the transformation which is responsible for its formation and its distinction from other transformation products (mostly martensite and other ferritic transformation products resulting from a displacive transformation). Bainite formation is accompanied by the formation of a surface relief outlining the dimensions of single bainite laths [93]. It forms by nucleation and coherent growth. The rate of growth is dependent on temperature and the composition of austenite but is always very slow compared with that of martensite. There are two opposing theories for the formation of bainite in literature: The diffusional and the displacive theory [94]–[101]. This leads to cases were a transformation product is called bainite by advocates of one theory only [102], [103]. This ongoing discussion [104]–[106] gets more complicated by the description of very different bainite morphologies in literature. These include granular bainite [107], [108], columnar bainite and inverse bainite [109]. Two major morphologies can however be distinguished: Upper bainite and lower bainite [12], [110], [111]. Upper bainite consists of sheaves of several ferrite laths with carbide precipitated along lath boundaries and at the tips. Lower bainite consist of finer laths with carbides precipitated inside the laths at an orientation of ca. 55° - 60° to the axis of the lath.

Ko and Cottrell [112] observed the formation of bainite in different steels using hot-stage microscopy confirming the low growth rates by direct observation. They concluded that a displacive transformation mechanism must be responsible for the observed surface relief but also diffusive processes must be active due to the low transformation rate. They proposed that the driving force present during the bainitic reaction at temperatures above M_S and M_0 are not sufficient to account for the strain energies associated with the displacive transformation, the increase in surface energy and the resistance of the matrix and/or the friction of the moving transformation interface. As the free-energy difference between austenite and supersaturated ferrite is not large enough at the given temperature no bainite will form. Ko and Cottrell suggested that this driving force may be increased by diffusive processes if carbon diffusion is still feasible at the transformation temperature. The diffusion of carbon from supersaturated ferrite into austenite will reduce the strain energies due to lower volume difference and increase the free-energy difference at once. The mechanism of carbon diffusion i.e. either carbide precipitation or diffusion into surrounding austenite is highly dependent on the rate of carbon diffusion and thereby highly dependent on the transformation temperature resulting in the formation of either upper or lower bainite.

2.1.8 Martensite

If steel is cooled from its high temperature phase (austenite) to room temperature it can transform into ferrite [28], [113]. If the cooling rate is high enough martensite forms. The required cooling rate, the transformation temperatures and the microstructure formed during this transformation depends on the composition and the microstructure of the austenite phase [114]. Alloying elements such as carbon and manganese determine the transformation temperatures as well as the cooling rates required for transformation. A complex interplay of thermodynamics, microstructure and alloying chemistry determines the properties of the transformation product.

2.1.8.1 The Martensitic Transformation

The martensitic transformation in steels usually occurs athermally after sufficient undercooling at M_S and does not require any diffusive processes. It can be described as a cooperative motion of a group of atoms from the face centered cubic (fcc) austenite γ phase to the body centered tetragonal (bct) martensite α' phase. This transformation is due to its cooperative transformation mechanism accompanied by a shape change which is evident from the formation of a surface relief and the generation of lattice imperfections (dislocations and/or twins) to accommodate this shape change [115].

2.1.8.2 Martensite Morphologies

Two main martensite morphologies can be observed in steels depending on their alloying chemistry [114], [116]–[121]. This is shown in Figure 2.4 where martensite morphology is shown in dependence of carbon content and the martensite start temperature. The observed morphologies are a result of different mechanisms facilitating the accommodation of the shape strain:

Plate martensite [122]–[124] is found in high-carbon, high-nickel and high nitrogen binary iron alloys. It consists of plates which are arranged in a way that minimizes the effects of the shape strain. The plates are usually of lenticular shape consisting of fine parallel twins [116].

Lath martensite [125]–[130] is mostly found in low-carbon, maraging, interstitial free and low-alloy steels. It is hierarchically structured into packets which consist of parallel blocks which are further subdivided into laths which exhibit only small misorientations between each other. It contains a very high dislocation density [116], [131].

The characteristics of these morphologies can be directly connected to the dominant mechanisms for the accommodation of transformation misfit: This is slip for lath martensite resulting in a high dislocation density and twinning for plate martensite resulting in a high density of twins. The dominating mechanism is mainly determined by the strength and the stacking fault energy of the alloy which is a direct consequence of its composition. Some other varieties of martensite morphologies like butterfly [132]–[134], lenticular [135], [136] and thin-plate martensite [137]–[139] exist besides lath and plate martensite.

The elongated shape of both martensite morphologies is a result of minimization of strain energy. Christian [140] described the strain energy associated with the growth of martensite based on Eshelbys equation [141], [142] for the strain energy of an oblate sphere as a function of the thickness c and the length r of the martensite plate as:

$$E = \frac{c}{r}\mu\left(s^2 + \delta^2\right)$$

<div align="right">Eq. 2.1</div>

With s the shear strain and δ the volume strain associated with the transformation and μ the shear modulus of the austenite. The strain energy E becomes minimal for given transformation strains if the aspect

ratio c/r of the martensite particle becomes minimal resulting in the elongated, lenticular shape of martensite units.

The strain energy associated with the transformation is the largest energy term opposing the transformation. An overview of typical values of the energy contributions associated with the martensitic transformation is given in Table 2.2.
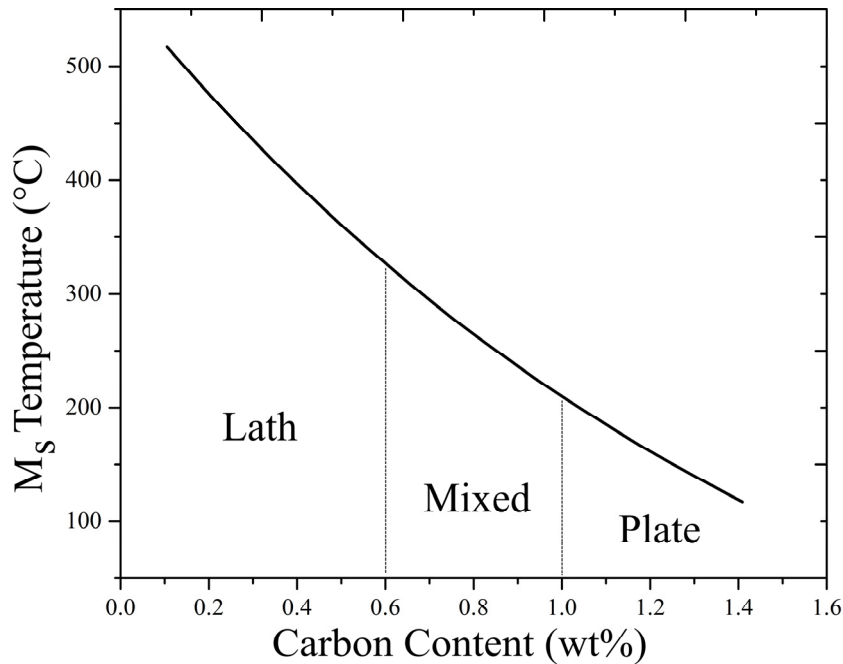
Figure 2.4: Change of martensite morphology from lath structure at low carbon contents to plate structure for high carbon contents and MS temperature as a function of the carbon content. Data from [9].

Martensite morphology is also affected by austenite grain size: The M_S and M_f temperature decrease with decreasing austenite grain size [143]. This reduces the packet size and block length [144]–[147]. The M_S temperature is also affected by the quenching rate: The M_S temperature increases with increasing quench rate. This can also influence martensite morphology for example it can change from lath to plate type with increasing quench rate [148]–[150].

Energy term	(J/mol)
Strain energy	600
Twin interfacial energy	100
γ/α' interface energy	1
Stored energy due to dislocations	20

Table 2.2: Typical values of stored energies associated with martensitic transformation, after [151].

From a technical standpoint, lath martensite has the highest significance of all martensite morphologies as it is formed in most commercial steels [119]. Such steels exhibt excellent properties at low production cost.

2.1.8.3 Martensite Nucleation

The direct observation of the nucleation of martensite from austenite in steel is demanding since it occurs at high speed and requires high spatial resolution. Consequently, only a few reports of this type are present in the literature. Experiments observing the martensitic transformation in FeNi powders suggested that the nucleation occurs heterogeneously [152], [153]. Therefore, the existence of "frozen in" nuclei called "embryos" was assumed. The structure and formation mechanism of these embryos is difficult to assess. A first model for martensite nucleation is based on theoretical considerations: Jaswon suggested that a structure resembling a bcc structure can be achieved by the dissociation of fcc Shockley partial dislocations [154]. A more complete theory was proposed by Kaufman and Cohen [155] and Olson and Cohen [156]–[158] following the same idea based on the "hard sphere model" of Bogers and Burgers [159]. It describes the martensite nucleation by the dissociation of a $a_{fcc}/2\ [1\bar{1}0]$ screw dislocation on a (111) plane forming three $a_{fcc}/18\ [1\bar{2}1]$ and three $a_{fcc}/18\ [2\bar{1}\bar{1}]$ partial dislocations. This configuration then leads to an arrangement of atoms that can be described as semicoherent bcc embryo within the fcc lattice. Defects that are able to provide such dislocation configurations may act as preferred nucleation sites [156], [160], [161]. Easterling and Thölen [162] proposed a similar mechanism which enables martensite nucleation from a single dislocation. This would, however, contradict the observed heterogeneous nature of martensite nucleation. Olson and Cohen [160] instead suggested grain boundary segments [163] and twins containing the required dislocations or partial dislocations as preferred nucleation sites. The nucleation of martensite at grain boundaries was assumed to be restricted to such boundaries containing the dislocations required for the formation of an embryo structure [164]. The incoherent part of a twin containing Shockley partials could be a preferred nucleation site concerning the nucleation of martensite at twins. Overall several microstructural features have been proposed as preferred nucleation sites for martensite. These include grain boundaries [164], [165], twin boundaries, single dislocations [166], free surface [152], inclusion interfaces [167], [168] and interfaces in general [169].

Other concepts on martensite nucleation are based on stress instabilities [170], Phonon mechanisms [171]–[175] or soliton mechanisms [176]–[180]. This shows that approaches towards the problem of martensite nucleation beyond models based on classical nucleation theory have been made. However such models are mostly present outside the material science community.

2.1.8.4 Martensite Growth

Martensite growth includes the motion of a glissile interface and the accommodation of transformation strains. The latter may predominantly be facilitated by different mechanisms like plastic/elastic deformation or variant selection. The structure of the interface can be described as consisting of two types of dislocations [181], [182]: Coherency dislocations enable the transformation from austenite to martensite to maintain coherency of the two crystals. Anti-coherency dislocations are responsible for the accommodation of the misfit strain caused by the transformation. Newer experiments suggest a ledge-like growth mechanism [183], [184].

The interface between austenite and martensite is called the habit plane. This plane is common to the parent and product phase [126], [185], [186]. It is macroscopically undistorted and unrotated during the transformation (cf. chapter 2.1.8.8). Different habit planes were proposed for steels of different chemical composition in the literature. Some approximate martensite habit planes are listed below in Table 2.3.

Composition (wt%)	Approximate habit plane	Ref.
Fe-20.2Ni- 5.65Mn-0.009C	$\{557\}_\gamma$	[126]
Fe–33Ni	$\{259\}_\gamma$	[187]
Fe-33Ni	$\{3\ 10\ 15\}_\gamma$	[188]
Fe-0.35C & some FeNi	$\{111\}_\gamma$	[189]
FeC (C > 0.55)	$\{225\}_\gamma$	[190]

Table 2.3: Some approximate martensite habit planes observed in literature.

A further aspect of martensite growth is the autocatalytic effect [114]. The stress fields of already formed martensite laths can locally lower the energy for transformation causing the growth of further martensite laths [191]. The autocatalytic effect acts in one single austenite grain but may also cause nucleation of laths in neighboring grains [192]. The autocatalytic effect is described as the main mechanism for the growth of martensite by Furuhara et al. [193]. They describe the nucleation of martensite at an austenite grain boundary followed by the growth of this variant until an equilibrium between the driving force of the martensitic transformation and the elastic strain energy of the surrounding austenite is reached. Further variants may then be autocatalytically nucleated resulting in the hierarchical structure observed for lath martensite. This implies that the lath size is directly correlated to the strength of austenite and the driving force of the transformation.

Variations of lath size can be observed in lath martensite. These variations are thought to be caused by the transformation sequence [194]. The first lath formed inside an austenite grain is less constrained than laths which are formed subsequently. This suggests that the largest laths formed first and that the smaller ones formed later during the transformation.

2.1.8.5 Orientation Relationships in Steels

Orientations are usually defined as rotations that convert coordinates with respect to a crystal reference system into coordinates with respect to a specimen reference system [195]. This can be written as

$$s = oc \qquad\qquad \text{Eq. 2.2}$$

With the specimen coordinates $s = (x, y, z)$, the crystal coordinates $c = (a_1, a_2, a_3)$ and the orientation o. A similar conversion is connected to the concept of misorientation [196]: A misorientation m transforms the coordinates with respect to one crystal into another crystals reference frame. If these two crystals have the orientations o_1 and o_2 this can be written as:

$$m = o_2^{-1}o_1 \qquad\qquad \text{Eq. 2.3}$$

Using Eq. 2.2 this can be written as

$$mc_1 = o_2^{-1}o_1c_1 = o_2^{-1}s = c_2 \qquad\qquad \text{Eq. 2.4}$$

With the development of orientation mapping and the automated calculation of misorientations came a need for comprehensible visualization of misorientations [197]. One approach to this problem became practical with computers and dedicated easy to use software packages. The visualization in three-dimensional misorientation spaces [198]–[201] has the advantage that every misorientation appears only once and that symmetrically equivalent misorientations result in a single data point.

Special misorientations are often connected to properties of microstructural features like grain boundaries, phase boundaries or precipitates. They may also be connected to specific phase or precipitation reactions.

These orientation relationships are usually described by specific (low index) parallel planes and directions of two crystals in the form [202]:

$$\{h_1k_1l_1\}_\alpha \parallel \{h_2k_2l_2\}_\beta$$
$$\langle u_1v_1w_1\rangle_\alpha \parallel \langle u_2v_2w_2\rangle_\beta$$

Eq. 2.5

The directions $\langle u_1v_1w_1\rangle_\alpha$ and $\langle u_2v_2w_2\rangle_\beta$ must lie in the $\{h_1k_1l_1\}_\alpha$ and $\{h_2k_2l_2\}_\beta$ planes respectively. There may be specific variants of an OR due to the crystal symmetries of the two crystal systems. The number of these specific alignments of planes and directions depends on the symmetries of the two crystal systems and the number of symmetrically equivalents of $\{h_1k_1l_1\}_\alpha$ and $\{h_2k_2l_2\}_\beta$ as well as $\langle u_1v_1w_1\rangle_\alpha$ and $\langle u_2v_2w_2\rangle_\beta$. The names of the most common orientation relationships observed in steels, their parallel planes and directions and numbers of variants are given in Table 2.4. It has to be noted, that there are some relationships between these ORs: The GT' OR is the inverse of the GT OR. This results in equivalent intervariant misorientations. The same is the case for the Pitsch OR and the NW OR. Therefore the Pitsch OR could be called the inverse NW OR [203].

Orientation relationship	Short name	Parallel planes	Parallel directions	Number of variants
Kurdjumov-Sachs [204]	KS	$\{111\}_\gamma \parallel \{110\}_\alpha$	$\langle 110\rangle_\gamma \parallel \langle 111\rangle_\alpha$	24
Nishiyama-Wasserman [114], [205]	NW	$\{111\}_\gamma \parallel \{110\}_\alpha$	$\langle 112\rangle_\gamma \parallel \langle 110\rangle_\alpha$	12
Greninger-Troiano [206]	GT	$\{111\}_\gamma \parallel \{110\}_\alpha$	$\langle 5\ 12\ 17\rangle_\gamma \parallel \langle 17\ 17\ 7\rangle_\alpha$	24
Greninger-Troiano' [206]	GT'	$\{17\ 17\ 7\}_\gamma \parallel \{5\ 12\ 17\}_\alpha$	$\langle 110\rangle_\gamma \parallel \langle 111\rangle_\alpha$	24
Pitsch [207]	P	$\{100\}_\gamma \parallel \{011\}_\alpha$	$\langle 011\rangle_\gamma \parallel \langle 111\rangle_\alpha$	12
Bain [208]	B	$\{001\}_\gamma \parallel \{001\}_\alpha$	$\langle 100\rangle_\gamma \parallel \langle 110\rangle_\alpha$	3

Table 2.4: Orientation relationships commonly observed in steels.

Kurdjumov and Sachs [204] described an OR determined by XRD for steels in their paper from 1930. They did also propose a mechanism by which a fcc unit cell could be transformed into a bcc unit cell using two simple shear distortions. They also stated that their experimental results do not agree with the model proposed by Bain [208]. Figure 2.5 illustrates the transformation mechanism of Kurdjumov and Sachs based on projections of the unit cell onto the $(111)_\gamma$ plane. Column (a) shows this projection of the initial fcc unit cell. Column (b) shows the first shear on the $(111)_\gamma$ plane in $[\bar{2}11]_\gamma$ direction. The second deformation illustrated in column (c) is reached by shear on the $(21\bar{1})_\alpha$ in the $[111]_\alpha$ direction. The final bcc/bct unit cell of the transformation product is shown in column (d). Kurdjumov and Sachs also stated that these shear deformations would not occur consecutively but rather simultaneously. They also stated that their model minimizes the distances the atoms have to be moved. The model proposed by Nishiyama [114] is conceptually very similar to this mechanism including shear on the $(111)_\gamma$ plane in $[\bar{1}\bar{1}2]_\gamma$ direction followed by a stretch deformation [114]. The models of Kurdjumov-Sachs and Nishiyama-Wassermann are both based on shear on $(111)_\gamma$ planes. Figure 2.6 compares both models and shows the differently oriented unit cell of the martensite. It has to be noted that both mechanisms were later rejected by Nishiyama in favor of the PTMC [114] (cf. Chapter 2.1.8.8).
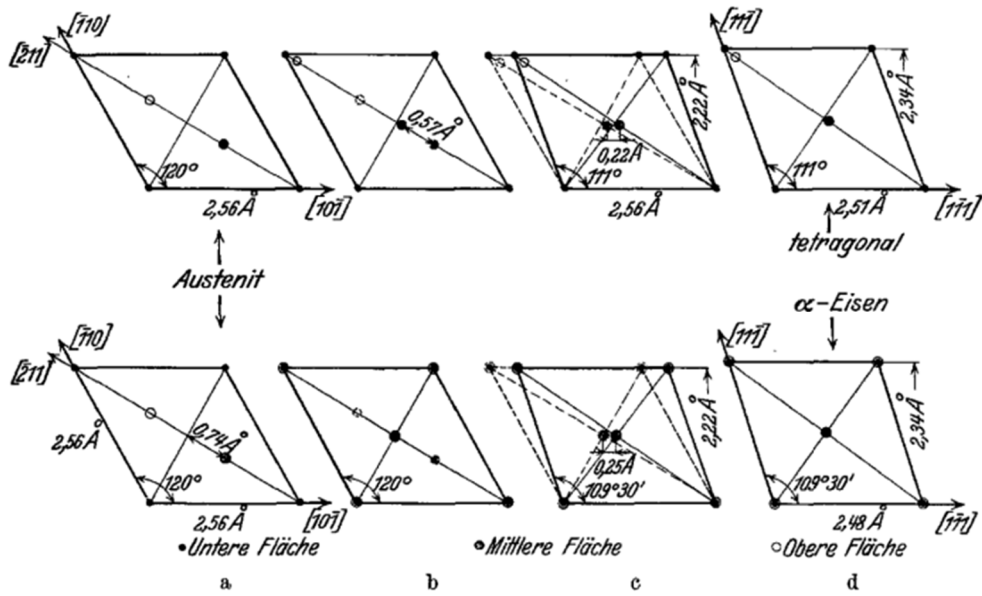
Figure 2.5: Model of the martensite formation from austenite proposed by Kurdjumov and Sachs. a) shows a projection of the austenite unit cell onto the (111) plane. b) shows the result after a first shear deformation and column c) shows the result after the second shear deformation. Column d) shows the dimensions and angles of the resulting α' unit cell.

The intervariant misorientations play an important role for the characterization of martensite [122], [129], [209]–[211]. These misorientations are the dominant misorientations of a martensitic microstructure [212], [213]. The intervariant misorientation angles of the well established ORs are listed in Table 2.5. It can be seen that variants 2, 3 and 5 of the KS OR exhibit a CSL 3 (Coincidence Site Lattice) misorientation to variant 1. Similar special intervariant misorientations can be observed for other ORs.

Intervariant misorientations are a characteristic feature of a single fixed OR. However, in most steels a continuum of misorientations can be observed ranging between the ORs listed above except for the Bain OR which is usually not observed. The origin of this continuum is unknown. It may be a result of the transformation strains which deform the austenite matrix prior to or the martensite during/after transformation. Alternatively, one could envision a reaction coordinate where the start and end point are the NW OR and the Pitsch OR. The ORs in between would then be the consequence of a more or less "complete" transformation. Both ideas are discussed in literature [203], [211], [214]–[217].
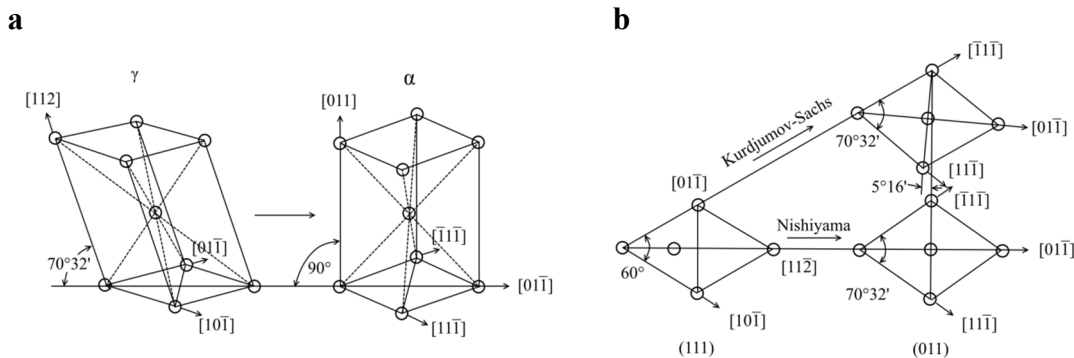
Figure 2.6: a) shows the KSN model. **b)** shows a comparison of the projected unit cells of the KS and the NW transformation product. After [114].

The listing of intervariant misorientation angles of the ORs are dependent on the numbering of the variants. There are 24! ($6.2 \cdot 10^{23}$) ways of numbering and thereby arranging the variants of the KS OR. A certain order of the variants is followed in most of the literature. This numbering scheme refers to a publication of Morito et al. [218] in which the variants of the KS OR are listed and applied to EBSD scans of different martensite microstructures. This order leads to a defined sequence of intervariant misorientation angles.

Variants can be grouped in different ways. One is connected to the Bain OR: Clusters of orientations formed by the ORs located close to the corresponding orientations arising from the Bain OR are called Bain groups. There are three Bain groups since the Bain OR has three variants. This classification has however no crystallographic motivation. The common feature is the low misorientation between the variants which belong to one cluster.

Variant	KS	NW	GT	GT'	P	B
1	0.000	0.000	0.000	0.000	0.000	0.000
2	60.000	60.000	54.279	54.279	53.691	62.799
3	60.000	60.000	51.915	60.000	53.691	62.799
4	10.529	19.471	11.279	5.721	19.471	
5	60.000	53.691	51.915	60.000	50.046	
6	49.471	53.691	50.828	60.174	62.799	
7	49.471	13.760	60.000	50.828	13.760	
8	10.529	53.691	5.721	17.256	53.691	
9	50.510	50.046	50.183	55.568	60.000	
10	50.510	13.760	57.516	50.183	13.760	
11	14.880	50.046	14.100	14.100	50.046	
12	57.213	53.691	50.031	50.031	53.691	
13	14.880		57.516	50.183		
14	50.510		14.100	14.100		
15	57.213		55.568	57.516		
16	20.605		49.592	49.592		
17	51.729		19.813	11.279		
18	47.113		59.699	51.915		
19	50.510		50.183	55.568		
20	57.213		50.031	50.031		
21	20.605		17.256	19.813		
22	47.113		55.568	57.516		
23	57.213		59.699	51.915		
24	21.058		19.953	19.953		

Table 2.5: Intervariant misorientation angles (in degree) of the ORs listed in Table 2.4. The corresponding crystallographic definition of the variants of these ORs can be found in Chapter 11.1.

The variants that belong to one CPP (close packed plane) packet are variants that share a common $\{110\}_\alpha$ plane which is parallel to one $\{111\}_\gamma$ plane. There are four CPP packets because there are four $\{111\}_\gamma$ planes in the fcc system. The variants which belong to one CPD (close packed direction) packet are variants sharing a common $\langle 111 \rangle_\alpha$ axis which is parallel to one $\langle 110 \rangle_\gamma$ direction. There are 36 variant pairings of the 276 total possible combinations for the KS OR that produce a CSL3 relation. Both variants of all of these pairs always belong to the same CPP packet but never to the same Bain group.

2.1.8.6 Martensite Variant Selection

As mentioned above, there are different well-established ORs that describe the misorientation between parent and product phase. ORs are often defined in terms of the parallelism of certain crystallographic plains and directions of parent and product phase. These can be written in the form listed in Table 2.4. A different number of symmetrically equivalent planes and directions (i.e. variants) may result due to symmetries of the phases α and β. All of the variants should be evenly distributed after the displacive phase transformation. The term "variant selection" means that certain variants are preferred in the transformation.

The study of variant selection is challenging from experimental and theoretical side. The use of an alloy with a M_S temperature below 0 °C is one experimental approach to study this effect. Bokros and Parker [219] studied the transformation of a single crystal of a Fe-31.7Ni (wt.%) alloy after plastic tension and sub-zero cooling. They concluded that variants exhibiting a habit plane perpendicular to the active slip plane of the austenite are favored. A similar model based on the similarity of the 24 slip systems of the crystal plasticity model by Bishop and Hill [220], [221] and the 24 $\langle 112 \rangle$ rotation axes of the KS OR was proposed by Sum and Jonas [222]–[224]. Other models based on considerations of residual stresses and shape change were proposed by Patel and Cohen [117] and extended by Kundu et al. [225], [226] based on the PTMC. Alloying for sub-zero quenching may however affect variant selection and even the morphology of martensite [227].

Most of the approaches described above are either based on experiments on single crystals or aim for a prediction of transformation textures. The latter are focused on a more qualitative description of the transformation product without spatial resolution. Another experimental approach is based on the presence of retained austenite in the martensite microstructure [245]–[248]. The austenite serves as reference and enables the identification of martensite variants but this can again only be used for certain alloys. Gong et al. [248] found that variants with close-packed planes parallel to the active slip planes of austenite are preferred.

Dominating influence	Mechanism	Ref.
Stresses and strains in parent γ	Correspondence between slip systems and variants	[224], [228]–[231]
	Strain energy and shape of martensite	[232]
	Strain energy, based on Bain strain	[233]
	Shear along $\{111\}\langle211\rangle_\gamma$	[234]
	Relation between habit plane and slip planes	[235]
Grain shape	Parallelism between habit plane and γ grain boundaries	[236]
	Growth direction and pancaked γ grain shape	[237]
Texture of parent phase	Elastic anisotropy of parent phase	[238]
	Elastic interaction between martensite blocks by shape strain	[239], [240]
	KS OR with two or more parent grains	[241]–[243]

Table 2.6: Various variant selection models which are discussed in the literature. The models are grouped by the most dominating influence on variant selection. Adapted from [244].

More recent studies are based on the reconstruction of the austenite microstructure starting from EBSD maps of the martensite microstructure. The Prior Austenite Reconstruction (PAR) algorithms which have been developed are described in the section 2.1.8.9. The use of such a program enables the study of variant selection without the need for special alloying with the aim of lower M_S temperatures or retained austenite. Miyamoto et al. [235] studied variant selection in a Fe-0.15C-3Ni-1.5Mn-0.5Mo (wt.%) alloy after compression based on this approach. They reported that variants are favored if their habit plane is parallel to the dominant slip plane of the austenite. This is a similar result as the one presented by Gong et al. but contradicting to the model proposed by Bokros and Parker. An overview of the different variant selection models and mechanisms which are discussed in the literature is given in Table 2.6.

2.1.8.7 Microstructure of Lath Martensite

The microstructure of lath martensite is strongly correlated to the structure of the parent austenite [249]. Parent austenite grain (PAG) boundaries are usually not affected by the transformation. A hierarchical structure can be observed for lath martensite [185], [189], [218], [249]–[251]. This hierarchical structure is schematically depicted in Figure 2.7: An austenite grain is divided into packets by the transformation. These packets can be further divided into blocks which again consist of laths which are aligned parallel to each other. This structure is of great importance for the mechanical properties of the final alloy [121], [252], [253].
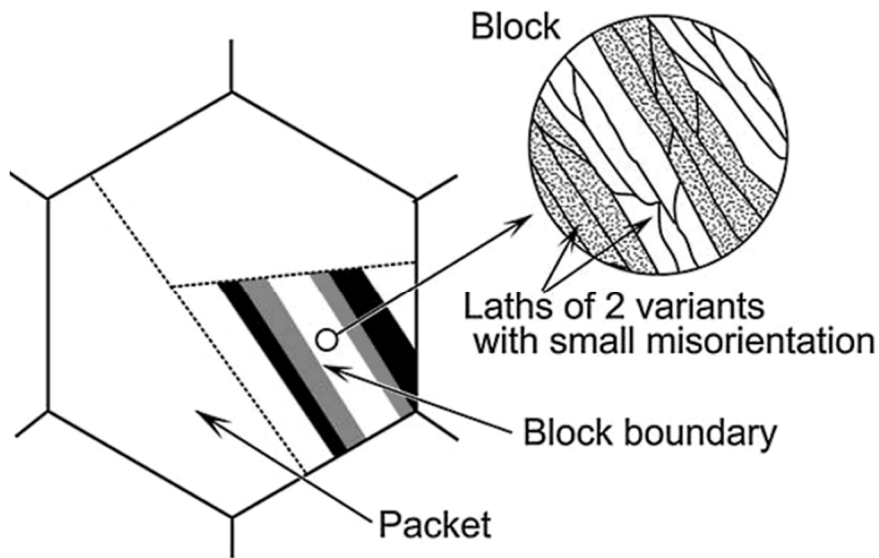
Figure 2.7: Illustration showing the hierarchical structure of lath martensite (most clearly observed in FeNi alloys) consisting of packets, blocks and laths inside a PAG, from [125].

Packets are formed by groups of blocks sharing the same $\{111\}_\gamma$ plane in the austenite. The laths in a packet are parallel to each other and therefore share a common habit plane. For low carbon steels, blocks are aggregates of laths belonging to variants which exhibit small intervariant misorientation angles (~10°). Laths are martensite single crystals containing a high density of dislocations. In this way a maximum of four different packets can form inside one austenite grain due to the four $\{111\}_\gamma$ planes available and a maximum of six different blocks can be found inside a single packet.

2.1.8.8   The Phenomenological Theory of Martensite Crystallography (PTMC)

The glissile interface envisioned to transform austenite into martensite must consist of only one single type of dislocation to enable its motion at low driving forces. This requires a coherent interface between parent and product phase which stays undistorted and unrotated i.e. an invariant plane. The essential assumption of the PTMC resulting from experimental observations is that the habit plane is an invariant plane of the shape deformation.

The motion of the interface consisting of Shockley partials leads to both, a change of crystal structure and a change in shape of the crystal [113]. These basic assumptions are combined in the Bain model [208] which describes the transformation of austenite into martensite on a crystallographic basis. The Bain correspondence can be seen in Figure 2.8a: Two fcc unit cells are shown from which a bct unit cell can be constructed without the motion of any atoms. The dimensions of this hypothetical bct unit cell are not correct and the strains which are needed for the formation of the martensite unit cell out of this bct cell are called Bain strains. This Bain strain does not fulfill the requirement of the invariant plane [254] which is required for the cooperative motion of the austenite-martensite interface. Therefore a rigid body rotation R is needed to maintain this condition. This is illustrated in Figure 2.8b. The same product (c) can equally be reached by an invariant plane strain [120], [186] (IPS) P_1 followed by a simple shear P_2 [255]. As these processes result in the correct (martensite) structure but do not lead to the observed shape an additional shear $P = P_2^{-1}$ is needed which does not affect the crystal structure i.e. a lattice-invariant deformation which compensates P_2 [28]. This may be slip (e) or twinning (d).
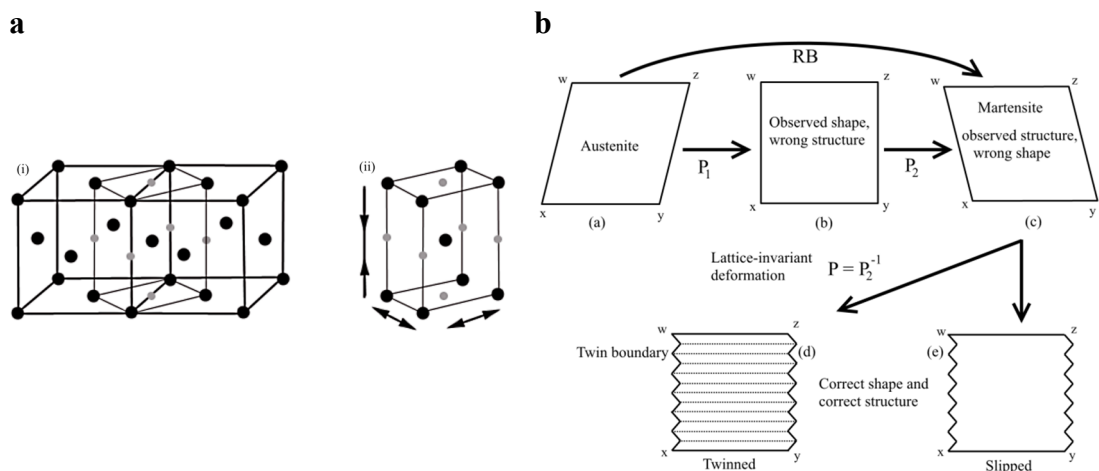
a **b**

Figure 2.8: a) (i) Visualization of the Bain correspondence. Black spheres show the positions of Fe atoms and gray spheres show the (potential) positions of carbon atoms. (ii) Illustrates the Bain strain needed to form a martensite unit cell. From [216]. **b)** Graphic illustration of the basic concept of the PTMC, following Bhadeshia [28], [255].

This completely phenomenological approach was developed by Wechsler and Lieberman [256] as well as Bowles and Mackenzie [257]–[260] independently. The theory is only considering the initial and the final state but does not help to elucidate the transformation process itself due to its phenomenological nature [217], [261].

2.1.8.9 Prior Austenite Reconstruction from Martensite

Austenite grain sizes and orientations in the hot state during processing are very difficult to assess during heat treatments. Great efforts have been made to determine these parameters by PAR algorithms because the product of the transformations during the heat treatment of steels and the properties of the final product are directly influenced by the austenite microstructure [262]–[278]. These algorithms need an Orientation Mapping (OM) of the martensite/bainite microstructure and (in most cases) an OR as input data.

Most of these algorithms are based on spatial clustering of martensite orientations with the aim of finding a parent orientation common to the martensite orientations in the cluster. This is illustrated in Figure 2.9: An EBSD map that was clustered into spatial domains is shown in Figure 2.9a. These domains may be based on orientations or they may represent single EBSD measurement points. This is then translated into a graph which is shown in Figure 2.9b. Such a graph is used to effectively find subdomains which belong to one single austenite orientation. This can be achieved based on the orientations of the domains itself (the vertices) or their relationship to each other (the edges). These correspond to the orientations of the domains or to the misorientations of neighboring domains. These rough descriptions shows that not only different methods may be used for the reconstruction but that the result is also affected by input parameters: These may be the threshold for the algorithm used to generate spatial domains in the EBSD scan of the martensite microstructure, the tolerance angles used for clustering in the graph and if an optimized or a fixed OR (and which OR is used). The methods used and described in literature range from algorithms based on single EBSD measurement points, preceding grain reconstruction, random walk approaches, clustering based on variant orientations and on intervariant misorientations.
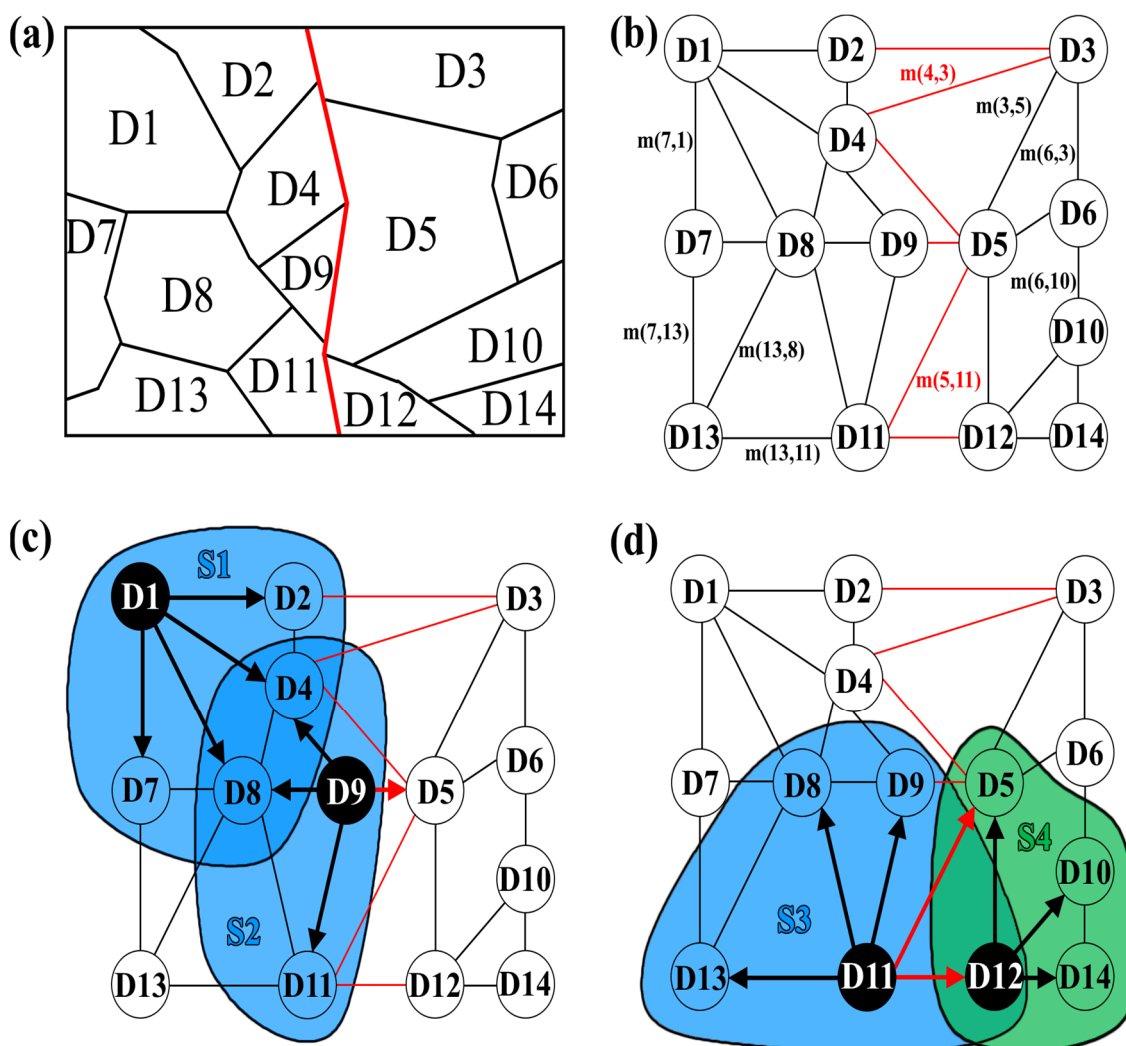
Figure 2.9: Illustration of the basic concept of parent austenite reconstruction from martensite, adapted from [279]. **(a)** Shows a schematic EBSD map of a martensite microstructure. Domains which belong to one variant are outlined with black lines and labeled D1…D14. The red line marks a boundary between two austenite grains. **(b)** Shows a graph representing the martensite microstructure shown in (a). Neighboring domains which belong to one austenite grain are connected by black lines. Red lines mark neighboring domains which belong to different austenite grains. Misorientations m(a,b) are connected to each line. **(c)** Subdomains S1, S2 are formed around domains D1, D9 and the domains included can be linked to one single parent orientation. D5 cannot be included into S2 because it belongs to another parent austenite grain. **(d)** D12 can be assigned to S4 by the algorithm if overlapping subdomains (S3, S4) are formed.

A graph theory approach and a not fixed OR is used by Bernier et al. [271] for the identification of these clusters. A similar approach was taken in the development of the algorithm by Miyamoto et al. which uses a pixel-wise iterative method without a fixed OR. An approach featuring the OR fitting of Miyamoto et al. [280], [281] based on intervariant misorientations was implemented in the MTEX toolbox by Nyyssönen et al. [213]. Another algorithm was developed by Germain et al. [279], [282]–[284] and Humbert et al. [285] using an OR that is not fixed and a simple clustering algorithm. An approach based on Bain groups was taken by Abbasi et al [276], [286], [287] for their PAR algorithm based on a fixed OR and simple clustering. An algorithm based on the summation of mutual misorientation angles was developed by Tari et al. [288] using a fixed OR. A random walk algorithm based approach was taken by Gomes et al. [289] based on an optimized OR. Cayron et al. [262], [263] use a "nucleation and growth" algorithm for which a fixed OR can be selected for the reconstruction.

PAR algorithms have become the standard method for the determination of the austenite microstructure, the determination of martensite variants and the calculation of packets. However, it is problematic that these algorithms usually cannot provide an error estimate for their results and that a critical examination and comparison of their results to the corresponding real austenite microstructure is missing. Some studies with focus on austenite grain sizes and grain shapes were performed using different etching techniques which were compared to the reconstruction [271], [290]. Only one study did consider shape and orientations of austenite grains and compared them to reconstructed mappings using a Fe-30Ni alloy and subzero-quenching treatment [291] but no studies on austenite microstructures and heat treatments closer to application level were found. The comparisons conducted in the aforementioned studies showed a good agreement of the results of PAR algorithms to the morphology of the real austenite microstructure. The austenite orientations used for the determination of martensite variants were all determined using the methods mentioned above. The errors for the determination of the orientations, the shape and position of grains and in particular twin boundaries that may arise from the PAR algorithm chosen are usually not discussed in the publications of these studies.

2.2   Investigation of Phase Transformations

Due to their overwhelming importance for the improvement of material properties numerous tools and methods have been developed in the past for the study of solid-state phase transformations. These methods include hot stage light microscopy (LM), laser scanning confocal microscopy (LSCM), X-ray diffraction (XRD), scanning electron microscopy (SEM), thermionic emission microscopy, differential scanning calorimetry (DSC), dilatometry, transmission electron microscopy (TEM) and Electron Backscatter Diffraction (EBSD). These techniques can be classified by different criteria. Some of them can be used to study the dynamic aspects of phase transformations, some can only be used to study the effects of phase transformation on the surface of the sample etc. Depending on the physical principles of the method and the measurement strategy these methods may be applied *ex* or *in situ*: On one hand, *in situ* measurements are usually more challenging from the instrumental perspective than *ex situ* experiments but on the other hand they can provide a more detailed observation of the processes that occur during transformation.

A selection of methods used for the study of solid state transformations is reviewed in the following section focusing on the measurement strategies.

2.2.1   *Ex situ* Techniques

For ex situ characterization of phase transformations usually the initial state of a sample is compared to the final state of the sample after a modification (heat treatment, mechanical processing). Several, non-destructive methods such as LM, SEM, EBSD, XRD, focused ion beam (FIB). can be used to investigate the microstructure. The heat treatment may be accomplished in a production line or simulated in a thermo-mechanical simulator (often a dilatometer is used). Using a sophisticated measurement strategy including heat treatments under an inert atmosphere and markers on the surface of the sample can enable the comparison of the same location on the sample before and after heat treatment. This allows for the observation of the microstructural evolution [292]. Similar experiments include quasi *in situ* experiments in which the heat treatment is interrupted in order to "freeze" the microstructure of the sample for characterization. It is however questionable how the "frozen" state of the sample compares to the actual state at high temperature. These approaches are only suitable for the study of phases that are stable at ambient temperature. This is, for example, rarely the case for austenite. This shortcoming was already circumvented by alloying at elevated temperature: The high temperature phase was therefore stabilized by suitable alloying elements such as nickel or chromium e.g. by Brückner et al. [26]. Unfortunately, this leads to the question how the alloying elements may influence the microstructure.

Another approach designed to overcome this problem is the reconstruction of the austenite microstructure from an EBSD scan of the martensite microstructure. This technique can only be applied if a displacive phase transformation takes place during austenite decomposition. Here, the quality of the results of the reconstruction algorithms may be questionable especially if the location of grain boundaries and twins shall be exactly determined (cf. Chapter 2.1.8.9).

2.2.2 *In situ* Techniques

In situ techniques allow for the characterization of phases and transformation processes which are not stable at ambient temperatures as well for the observation of dynamic processes. These techniques are technically more challenging and can present substantial challenges to equipment and design of experiments.

2.2.2.1 X-ray Powder Diffraction

X-ray diffraction is a very versatile method for *in situ* experiments to study phase transformations. The requirements for the experimental setup are usually relatively simple (if access to a high intensity source is available). The high time resolution combined with a multitude of information which can be extracted from the diffraction data using advanced methods [293], [294] make this method ideal for *in situ* experiments. A large number of experiments with varying measurement strategies were performed on different phase transformations in steels up to date [295]–[300]. A broad overview of *in situ* XRD techniques and combinations with other characterization techniques can be found in two books by Kannengiesser et al. [301], [302]. The major drawback of most of these experiments is their low spatial resolution. Only integral information from the interaction volume of the diffracted beam is accessible.

2.2.2.2 TEM

In situ techniques for the transmission electron microscope provide a very high spatial resolution. Phase transformation can be either investigated *in situ* using a high temperature heating stage or mechanically induced using a tensile or indentation stage [303]–[305]. Investigations on the motion of transformation interfaces in steels were performed for different austenite decomposition reactions [306]–[312] *in situ* using TEM. Transformation interfaces, orientation changes and misorientations can be observed with high spatial and angular resolution. The drawback of TEM is the sample size: The low thickness which is required by this method and the small volume of the sample result in a low number of individual observations and relatively poor statistics. A further problem arising from the low thicknesses of the samples is the relevance of the observed processes for bulk materials. For example, significant differences were reported for recrystallization [313].

2.2.2.3 LSCM

In Laser Scanning Confocal Microscopy, the surface of an object is scanned by laser light. Only the light from the focal plane is registered on a charge-coupled device (CCD) sensor through the use of a confocal pinhole. The contrast mechanism for the observation of phase transformations is therefore based on thermal grooving at interfaces. This allows for a real time observation of moving interfaces on the surface of the sample at different temperatures. Experiments for the study of phase transformations in steels using LSCM were performed by Shibata et al. [314]–[317] and Phelan et al. [19], [62]. The experiments are usually conducted under an inert gas atmosphere using a halogen furnace. LSCM allows for the observation of the progression of phase transformations at high magnifications in real-time for large surfaces (5 mm x 5 mm). The conceptually simple instrument allows for fast heating and quenching. A drawback of this method is the lack of information on crystal orientation. It is not possible to conduct phase identification, to measure the orientation of grains or misorientations at interfaces. A combination of LSCM with other techniques can partially mitigate this shortcoming. This is however restricted to post-mortem characterization of the final microstructure. Experiments of this type were performed for the study of martensite formation in steels by Nambu et al. [130] and Zhang et al. [318].

2.2.2.4 EBSD

Electron Backscatter Diffraction (EBSD) is a tool which is suitable for the study of phase transformations: Detailed crystallographic information can be obtained with a very high spatial and angular resolution for large surface areas with relatively simple sample preparation. A comprehensive general review on the study of phase transformations using EBSD was given by Gourgues-Lorenzon [319], [320]. *In situ* methods using EBSD were developed for tensile and compression experiments [321]–[323] and heating experiments. The latter were for example concerned with recrystallization [324]–[327], twin growth [328] and phase transformations [329]–[334] in various materials. *In situ* heating experiments inside the SEM additionally allow for the use of other methods available in the device which may be combined with the EBSD results such as secondary electron (SE) [335] and backscattered electron (BSE) detectors and focused ion beam microscopy (FIB). Compared to other methods, this method combines high spatial resolution with local crystal orientation data. It allows for the investigation of relatively large surface areas and many different imaging modes of the SEM can be used.

The main limitations of EBSD for the observation of phase transformations is the limited spatial resolution for the characterization of nanometer-sized phases, the time-consuming acquisition of EBSPs, and the fact that only information from regions close to the sample surface is available. These limitations and experimental difficulties concerning *in situ* high temperature EBSD caused the results to fall short of expectations [329], [332] despite the development of SEMs dedicated for *in situ* HT experiments [336]. The main problems arise from drift of the heating stage [331] and problems with accurate temperature measurement. This led experimenters which had access to *in situ* heating equipment to perform EBSD measurements only after the sample was cooled down to room temperature [326], [327]. Successful uninterrupted *in situ* EBSD heating experiments focusing on phase transformations were performed on the α/γ-transformation for different steels: Lischewski et al. [22]–[25] investigated the α-γ-α phase transformations in the intercritical regime using a laser powered *in situ* heating stage [337]. They mainly investigated variant selection during ferrite/austenite nucleation and growth. Similar experiments were performed by Fukino et al. [20], [338] focusing on the influence of grain boundaries, triple points and their misorientation on the ferrite-to-austenite transformation.

Fundamental differences between the conditions at the surface and in the bulk of the sample should also be considered for phase transformations observed by EBSD:

- Stress relaxation at free surface

- Influence of surface energies

- Smaller number of defects due to closeness of surface

These differences in boundary conditions and their influence on phase transformations may be best assessed by applying the same temperature treatment path to a bulk sample of the same composition using a dilatometer. The resulting microstructures can then be compared to the microstructures obtained in the *in situ* experiments. Alternatively, the microstructure at the surface may be compared to the microstructure in the bulk by cross sectioning or by removing the surface (polishing).

Difficulties regarding the realization of high quenching rates in these experimental setups impede the study of martensite in steels close to realistic heat treatments. Experiments using custom made additions for *in situ* quenching by Hansen et al. [339], [340] which were based on a preceding *in situ* high temperature (HT) EBSD study of phase transformations in a HSLA steel by Enstad [341] were not successful due to surface degradation by the formation of oxides. Similar experiments were carried out by the author of this thesis in collaboration with M. Wenk resulting in the first successful quenching experiment from high temperatures (ca. 900 °C) without surface degradation [342].

3   Experimental

The experimental techniques used for the studies of this thesis are described in this chapter. In this work an already existing experimental setup was improved. Technical aspects and measurement strategies that were developed are explained and discussed. Particular attention is paid to the accurate temperature measurement and control of the *in situ* HT EBSD setup. This includes a short introduction into pyrometry and its calibration.

3.1   *In situ* High Temperature EBSD/SEM Setup

The *in situ* button heater used in this thesis was already used by S. Schreijäg [343] and M. Wenk [342]. The most important element of the setup is a button heater with a diameter of ca. 6 mm. A schematic of the heater is shown in Figure 3.1b. The button heater consists of a molybdenum body which is filled with pure alumina potting. The heat is generated by a molybdenum wire embedded in the alumina potting. The hollow stem of the heater that is located in the center of the button heater holds a thermocouple. This thermocouple is in direct thermal contact with the backside of the molybdenum plate on which the sample is mounted. This enables a relatively accurate measurement of the temperature of the button heater at the top of the device. Experiments in collaboration with M. Wenk showed that the following issues had to be improved:

- The varying thermal conductivity between heater and sample causes major issues for the measurement of the temperature on the sample.

- A precise control of the temperature of the sample by a simple manual adjustment of the power of the heater using a laboratory power supply cannot provide the required accuracy.

- Logging of the temperature during heat treatments and quenching is necessary to allow for a meaningful interpretation of its effect on microstructure and properties.

- Markers on the surface of the sample are necessary for the reliable spatial correlation of sequences of EBSD/SEM measurements.

Therefore, a system for controlling the temperature of the button heater was developed within the scope of this thesis. A LabJack [344] multifunction data acquisition device is used for measurement and control. The LabJack device is connected to a PC by the USB port. The input and output signals of the LabJack are processed by a LabVIEW [345] program which was developed for this purpose. Temperature measurements from different thermocouples can be connected to the LabJack board and all measurement data can be automatically written to a log file using the LabVIEW program.

The heating stage is connected to the output of a Gossen Konstanter 44 T 20 R 10 lab power supply via a special feed-through in the SEM chamber. The output voltage of this power supply can be controlled by a control voltage (0…10 V). This input line of the power supply is connected to an output channel of the LabJack device. A proportional-integral-differential (PID) control was implemented in LabVIEW application to control the output of the power supply using this setup. The PID input signal is based on the temperature measured inside the button heater. In this way a temperature set point can be defined and the PID will then control the power supply to reach this value based on the temperature measurement inside the button heater.

The parameters for the PID were determined through experiments with the setup. The possibility for a fast change of a whole set of parameters was implemented into the LabVIEW application. This allows to adapt the characteristics of the PID to the specific heat treatment path.

The parameters of the PID control were optimized for two conditions: First for minimizing the difference between the current set point and actual temperature for the accurate execution of changes of the temperature during the heat treatment and second for minimizing fluctuations of the temperature during hold sequences. The latter set of parameters is essential for EBSD measurements at high temperatures. Small changes in the temperature of the button heater lead to thermally induced drift which will disturb the measurement. Fluctuations in the temperature of the button heater can be reduced to a minimum by changing the PID parameter set in the software with the click of a button. A screenshot of the LabVIEW application is shown in Figure 3.1a.
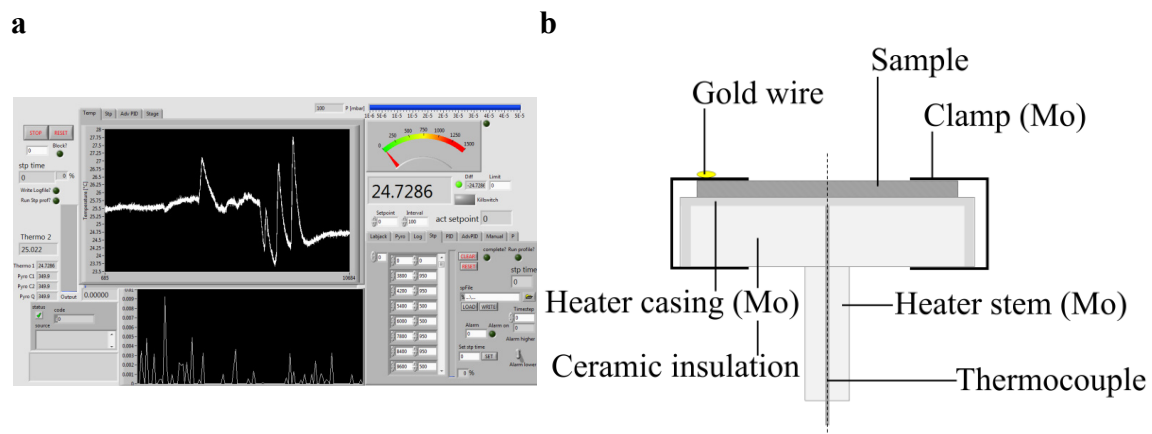
Figure 3.1: a) Screenshot of the user interface of the LabView program used for controlling the *in situ* setup. **b)** Schematic sketch of the heating part of the *in situ* heating setup.

Another important feature of the software is the possibility to design heat treatment procedures using a list of temperature setpoints and times. These heat treatment procedures can consist of up to 256 set points and can be stored in a heat treatment procedure file. This enables the definition of complex heat treatment routines including multiple ramps and holding sequences.

Two molybdenum clamps are used to mount the sample onto the button heater. In this way temperature gradients which could occur due to poor thermal contact are reduced. The possibility of temperature gradients on the surface of the sample and its magnitude was analyzed by M. Wenk [342]. In this analysis he assumed thermal contact of the sample to the heater at only one point due to the use of one Mo clamp. He concluded that the magnitude of temperature gradients on the sample is connected to the ratio of its surface area to its thickness. The temperature difference resulting for a sample with a thickness of 0.2 mm was calculated to be 23 K. This value was with 5 K significantly smaller for a sample thickness of 1 mm. Due to the fact that thick samples and two Mo clamps were used in all experiments it seems safe to assume that the thermal gradients on the sample surface were negligible.

A variety of clamps were machined for different sample thicknesses. The surface of the Mo clamps cannot be used as "orientation markers" (cf. 4.4 at p. 42) due to surface degradation at elevated temperatures. Therefore, tiny pieces of gold bond wire were mounted onto the Mo clamps via diffusion bonding (during heating with the heater). The crystal orientations of selected grains of the gold wire were then used for the correction of orientations that occurred due to slight real space orientation changes of the heater within the SEM at different temperatures. A measurement of the orientations on the gold wire is not necessary if parts of the microstructure are not affected by the heat treatment. Orientation measurments of grains tha are not affected can also be used to track sample tilt. A comparison of orientation measurements on the gold wire and on non affected grains showed that the gold wire did not move at elevated temperatures. Reproducability of tilt angles and axes could not be found suggesting that the tilt is mostly affected by the fixation of the button heater on the stem. The rotation angles of the tilt were found to be usually smaller than 3°. The whole setup of the button heater including sample, Mo clamps, thermocouple and gold wire is schematically depicted in Figure 3.1b.

Other features were also implemented into the LabVIEW application such as the measurement of the temperature of the SEM stage and an option for an automatic shut off if the temperature of the stage reaches critical values. The LabVIEW program reads all the data such as the temperatures measured by thermocouple inside the heater and on the SEM stage as well as the pressure in the vacuum chamber. It adds a time stamp to those data and writes them to a text file.

A "remote" switch was connected to a digital IO of the Labjack device to switch the heater off because the quenching valve is situated behind the SEM and has to be operated manually. The quenching sequence can be started by opening the quenching valve and simultaneously operating the switch causing the LabVIEW application to shut off the power supply for the button heater. An overview of the basic technical data on the performance of the setup is given in Table 3.1.

Performance	Value
Maximum temperature	1200 °C
Temperature measurement rate	10 Hz
Maximum heating rate	50 K/s
Maximum cooling rate (without He)	ca. 25 K/s
Maximum quenching rate	ca. 300 K/s
Accuracy of temperature control	0.1 K

Table 3.1: Basic technical data on the performance of the *in situ* heating stage.

The temperature measurement using the thermocouple was found to be lacking accuracy due to heat losses between the heater and the sample. No reproducible clamping of the sample was possible. This affects the thermal conductivity between heater and sample so that the transformations appeared to occur

at different temperatures for the same material. This can only be prevented by measuring the temperature directly on the surface of the samples. After experiments with a thermocouple directly spot welded onto the sample surface had failed, a contactless temperature measurement method was conceived.

The solution consists of a Sensortherm Metis M322 [346] two-color pyrometer which is equipped with a suitable optical fiber. It is connected to a glass fiber high vacuum feed through for the SEM chamber. The read out of this device was also implemented into the LabVIEW program using a RS322 interface. A fixture for the optics at the end of the optical fiber was designed. With this the end of the fibre can be afixed to the inside of the door of the chamber in the SEM. An adjustable mirror system was built for the optics due to the limited space inside the SEM chamber. This is based on an uncoated gold mirror that deflects the thermal radiation from the sample surface into the lens at the end of the glass fiber. The pilot laser of the pyrometer can be used to adjust the position of the optics and the mirror relative to the position of the sample before the experiment.

3.2 Pyrometry and Calibration

The study of phase transformations requires a precise measurement of the sample temperature [292]. Most *in situ* setups use a thermocouple fixed inside or on top of the heater [21], [24], [329]. This measurement method is problematic due to the non-ideal heat transfer between the heater and the sample. Experiments with very thin (0.25 mm) thermocouples spot welded onto the sample showed that the temperature of the sample is affected by the heat transfer caused by the thermocouple itself. This is particularly problematic at higher temperatures where thermal radiation is the major path of heat loss. The thermocouple locally cools the sample due to its relatively large radiating area [347]. The temperature is lowest at the point of attachment causing a gradient which is increasing with rising temperature and decreasing sample dimensions. To overcome these problems a contactless measurement of the surface temperature of the sample is necessary.

3.2.1 Pyrometry

Every object with a temperature above 0 K emits electromagnetic radiation from its surface. The wavelength peak of this radiation is proportional to the temperature of the object for perfect emitters of thermal radiation (black-bodies). This relationship is described by Wien's displacement law (which can be derived from Planck's law):

$$\lambda_{max} \cdot T = 2897.8 \, \mu m \cdot K \qquad \text{Eq. 3.1}$$

With the peak wavelength λ_{max} of the spectral radiance of black-body radiation and the temperature T of the black-body. The total emission of a black-body can be calculated by integrating Planck's law yielding the Stefan-Boltzmann law:

$$M(T) = \sigma T^4 \qquad \text{Eq. 3.2}$$

With the black-body radiant emittance $M(T)$ and the Stefan-Boltzmann constant σ. The radiation of real objects $M(T)$ differs from that of a black-body $M_{BB}(T)$. The emissivity ε is used to account for this discrepancy. The emissivity of an object is dependent on the material, the wavelength, the temperature, the surface structure, the viewing angle and the geometry of the object [348]–[351]. In general applications the total hemispherical emissivity is used for measurements omitting all dependencies except temperature:

$$\varepsilon(T) = \frac{M(T)}{M_{BB}(T)} \qquad \text{Eq. 3.3}$$

For objects with very low emissivities, the determination of exact values of $\varepsilon(T)$ can be difficult. Additionally, emitted radiance can be low (e.g. at low temperatures) and reflected radiance may be high. In order to circumvent these difficulties measurement principles were developed which try to minimize or exclude the influence of emissivity. One approach is based on the simultaneous measurement of radiance L_1 and L_2 in two spectral bands (here short λ_1 and λ_2) and the calculation of the surface temperature from their ratio $R(T)$:

$$R(T) = \frac{L_2(\lambda_2)}{L_1(\lambda_1)} = \frac{L_{BB}(\lambda_2, T_1) \cdot \varepsilon(\lambda_2, T_1)}{L_{BB}(\lambda_1, T_1) \cdot \varepsilon(\lambda_1, T_1)} \qquad \text{Eq. 3.4}$$

For objects with an emissivity independent of the wavelength and temperature (gray-bodies) this approach enables accurate temperature measurement without knowing the emissivity [352]. The measurement of the ratio of emissivities at the two spectral bands is easier than the measurement of absolute emissivity. The two-color (wavelength) approach further has the advantage that the measured temperature is not affected if the object does not completely fill the instrument's field of view.

A Sensortherm Metis M322 Pyrometer [346] was used in the *in situ* setup to monitor the surface temperature of the sample on the heating stage. The pyrometer is equipped with two InGaAs detectors measuring IR intensities in the range of 1.65 µm – 1.8 µm (channel 1) and 1.45 µm – 1.65 µm (channel 2). Temperatures from 400 °C to 1600 °C can be measured. The device is connected to the PC which is also used for controlling the heating stage power.

The device is situated outside of the SEM. It is connected to the optics inside the SEM by glass fiber and a glass fiber UHV feed through. The optics is moved along with the stage if it is tilted (i.e. for EBSD) but does not move if the stage is moved in x, y, or z because it is mounted on the inside of the chamber door of the SEM. It consists of a focusable optics and an adjustable mirror. The adjustment of the mirror is accomplished with the aid of the built-in laser targeting system of the pyrometer. This pilot light is switched on and the mirror is tilted and rotated until the laser beam points directly onto the sample that is mounted on the button heater. The measurement of the surface temperature upon quenching using the pyrometer was not possible because the sample has to be positioned under the gas injection system for quenching so that the surface is not anymore within the field of view of the pyrometer.

3.2.2 Calibration

The calibration of temperature measurements using pyrometry is challenging for surfaces with high reflectivity. A calibration routine was developed in order to determine the emissivity ratio corresponding to the measurement bands of the pyrometer in combination with the polished surface of the sample and to determine the accuracy of the setup. A thick DP600 steel sample with a fine hole suitable for a mantle thermocouple was manufactured and mounted onto the heater stage of the *in situ* setup (cf. Figure 3.1b). In this way the temperature inside the button heater and the temperature inside the sample can be monitored.

The surface of the sample was partially covered with carbon by applying a carbon black suspension (Bonderite L-GP 386 Acheson [353]: graphite in butanol, butyl acetate, ethyl alcohol) to generate a sample region that exhibits black body characteristics ($\varepsilon = 1$). The sample position inside the SEM chamber was varied so that the measurement spot of the pyrometer was located on the carbon coated side of the sample in position 1 and on the uncoated side in position 2. The pyrometer was calibrated by monitoring the temperature of the heater T_h, the temperature inside the sample T_s , the pyrometer temperature on the black side T_{pb} and the pyrometer temperature on the uncovered side of the sample T_{ps} at different temperatures in a range from 450 °C to 700 °C.

The result of this procedure is shown in Figure 3.2. It shows that a good agreement of T_s with T_{pb} can be observed for the pyrometer without additional calibration (calibration from the manufacturer). The device is calibrated from the manufacturer using a black-body radiation source. This is confirmed by the observed agreement of the temperature inside the sample and the temperature measured by the pyrometer on the coated side of the sample. The calibration on the uncoated surface of the sample was then performed in accordance to the description provided by the manufacturer. The software "SensorTools" which was provided with the pyrometer was used to adjust the dark offset and the quotient of emissivities. The calibration procedure takes influences of the feedthrough, the glass fiber and the optics into account.
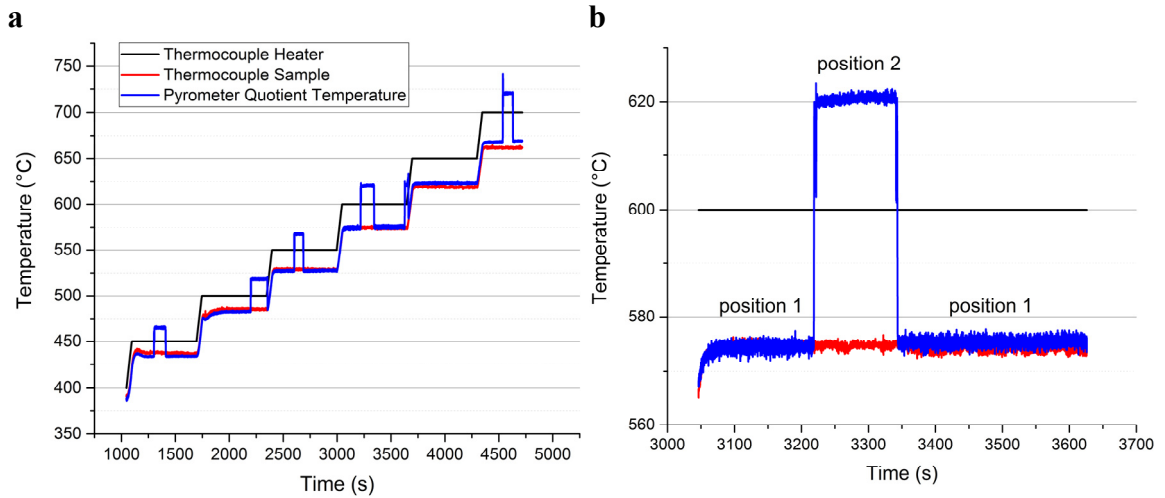
Figure 3.2: a) Temperature curve during the calibration procedure of the pyrometer using a partly carbon black coated polished steel sample. The temperature of the heater is changed in 50 K steps from 450 °C to 700 °C. **b)** Temperatures for the calibration step at 600 °C. The stage is first moved to position 1, to position 2 and back to position 1. The curve shows that the temperature measured inside the sample and on the carbon black coated surface of the sample are equal.

A very slow (0.1 K/s) heating and cooling of a DP600 sample was performed in order to verify the accuracy of the calibration and to test if changes on the surface at elevated temperatures will affect the measurement.

The results in Figure 3.3a show that a good agreement of the temperature measured using a thermocouple inside the sample and from the pyrometer on the sample can be found. The ratio of the emissivities $\varepsilon_1/\varepsilon_2$ was calculated to test the influence of surface effects on the emissivities. Figure 3.3b shows that this ratio is not much affected by surface effects at high temperatures as the curves for heating and cooling nearly lie on top of each other. A deviation of the curves between 800°C and 900°C and a small hysteresis for the whole curves can be observed suggesting that the emissivities change but the effect on the measurement is insignificant. This change could either be caused by the formation of grain boundary grooves and the accompanying change of surface roughness, which affects emissivity [354] or by oxidation.
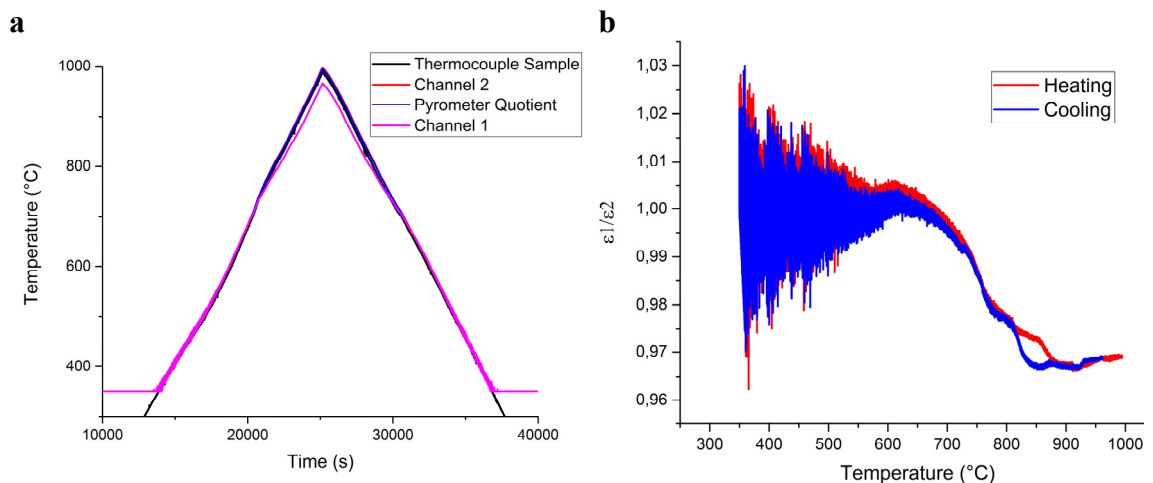

Figure 3.3: a) Test of calibration of the pyrometer using a slow heating/cooling procedure. **b)** Ratio of emissivities calculated from the apparent temperatures at the two channels (1.65 μm – 1.8 μm, 1.45 μm – 1.65 μm) for heating (red) and cooling (blue).

3.3   Quenching inside the SEM

Very fast cooling of a sample inside the SEM is necessary for the simulation of many technologically relevant heat treatment paths. In particular, this is necessary for the simulation of quenching processes which are required for the formation of martensite in low alloyed steels. A solution for this experimental problem is challenging especially because further requirements need to be fulfilled:

- Very fast controlled reduction in temperature from 1200 °C to room temperature.

- No degradation of the surface of the sample, e.g. no oxidation or other reactions on the surface.

- Ideally no vacuum break in the SEM chamber.

- No (only minimal and/or controlled) changes in the position of the sample relative to the EBSD detector.

- All components of the cooling apparatus have to be compatible with high vacuum/ultra-high vacuum (HV/UHV).

These requirements are rather difficult to fulfill. Simply switching the heater off results in a relative high cooling rate but this high cooling rate can only be maintained as long as thermal radiation is the dominant heat path (1200 °C to ~500 °C). Below this temperature range, the quenching rate becomes very low due to the lower contribution of thermal radiation. In this situation convection and conduction are too low to further reduce the temperature at sufficient rates. Resposible are the low pressure in the SEM chamber and the design of the hot stage which is designed for minimal heat loss by conduction.

The only method which can result in a high quenching rate and simultaneously does not lead to surface degradation of the sample is quenching by an inert gas. A comparison of the thermal properties of the gases which are suitable for quenching can be seen in Table 3.2. The quenching rate of a cylinder with diameter d is proportional to the heat transfer coefficient h which can be described by [355]:

$$h = 0.023 \frac{k}{d} \left(\frac{d v_{max} \rho}{\mu} \right)^{0.8} \cdot \mathrm{Pr}^{1/3} \qquad \text{Eq. 3.5}$$

with the gas conductivity k, the maximum gas velocity v_{max} the gas viscosity μ, the density ρ and the Prandtl number Pr. The density ρ is proportional to the pressure. The heat transfer coefficient for a given diameter and gas velocity is mostly influenced by the thermal conductivity k and to a lesser extent by the pressure because Prandtl number and gas viscosity differ only slightly when argon and helium are compared [356]. This results in a heat transfer coefficient which is roughly ten times higher for helium than for argon for the same diameter and gas velocity. Even higher rates can be achieved through the use of gas mixtures [357]. Eq. 3.5 does also show that the influence of the maximum gas velocity and the density i.e. gas pressure on the heat transfer coefficient are of the same magnitude. The pressure, however, is limited by the fact that the vacuum chamber is not designed for overpressure: The door of the chamber will open as soon as a pressure higher than atmospheric pressure is reached leading to the oxidation of the sample.

A quenching system was built that can be mounted to the SEM. It mainly consists of a UHV feedthrough and a ball valve. The outside end of the feedthrough is directly connected to the pressure relief valve which is attached to the helium gas cylinder. A quenching nozzle for the section inside the chamber of the

SEM was manufactured from copper tubing with a diameter of 10 mm. The quenching nozzle and its location inside the chamber of the SEM are depicted in Figure 3.4b.
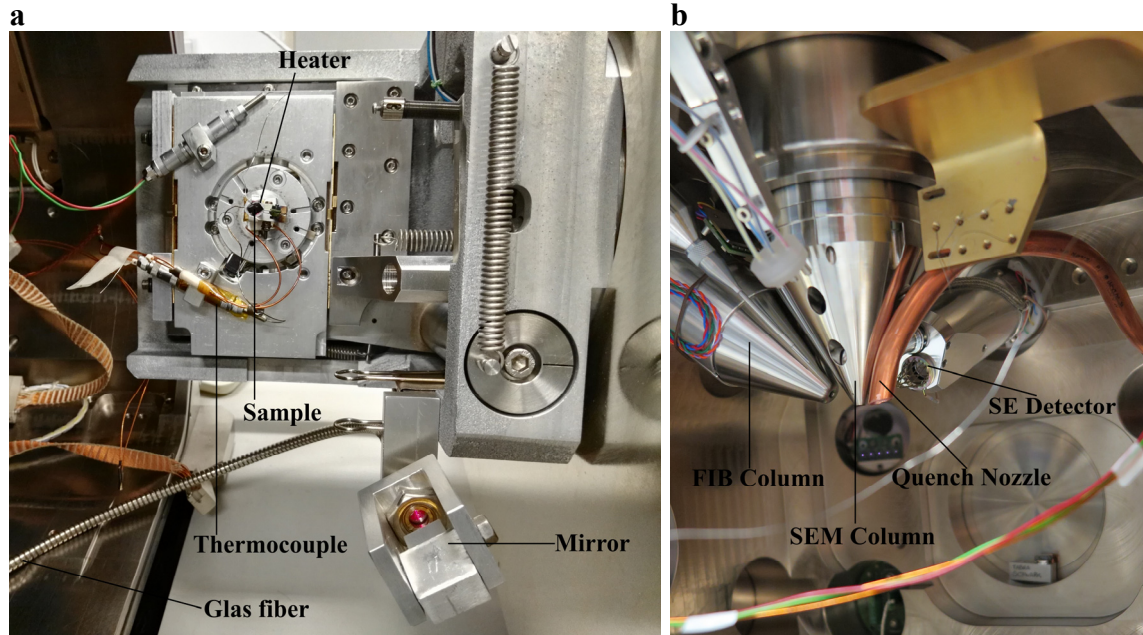

Figure 3.4: a) The opened SEM chamber equipped with the *in situ* setup consisting of heating stage, thermocouples and pyrometer system (glass fiber, optics, adjustable mirror). The pilot light is switched on and the sample can be seen on the heater. **b)** The SEM chamber equipped with the quenching gas tube which is held in its position by a thin metal wire. Outside of the vacuum chamber, the copper tubings are connected to a helium gas cylinder.

The copper tubing can be attached to the feedthrough inside the SEM chamber. It was bent in a way that it is affixed to a block (yellow coated piece in Fig. 3.4b) that is rigidly mounted to the chamber. In this position the gas outlet is located directly beneath the pole piece and the gas is expected to hit the sample roughly in the direction of the normal of its surface. Before quenching, the sample is moved underneath the gas outlet. The helium gas then flows directly onto the sample when the valve is opened. This breaks the vacuum but the noble gas prevents surface degradation by oxidation. The vacuum system of the SEM had to be modified so that all valves of the system (chamber and column valves) were kept shut during the quenching procedure. Further, the SEM additionally is put into gas quenching mode so that the power of the turbomolecular pump is turned off and the roughing pump is still fully operating.

	k $[\text{Wm}^{-1}\text{K}^{-1}]$	ρ $[10^{-4}\text{g}\cdot\text{cm}^{-3}]$	μ $[10^{-4}\text{gcm}^{-1}\text{s}]$	Pr $(=\mu c_p/k)[-]$
Ar	0.0180	1.78	2.23	0.68
He	0.1411	1.79	1.96	0.71
N₂	0.0237	1.25	1.76	0.72

Table 3.2: Thermal conductivity k, gas viscosity μ, density ρ and Prandtl number Pr of inert quenching gases at room temperature and $p = 1.013$ bar which were under consideration for the quenching experiments. Data from [358].

The pressure of the helium was limited to 3 bar by the pressure relief valve. Experiments with different pressures and flow rates showed that the position of the sample relative to the quenching nozzle has a much stronger influence than quenching gas pressure or quenching gas flow rate. These experiments also

showed that a manual regulation of the He flow into the chamber lead to relatively poor reproducibility of the quenching temperature curve. Therefore, the chamber valve was always fully opened or closed.

The standard procedure for quenching inside the SEM consists of the following steps:

- Disable the automatic ventilation system of the SEM using the manual switch which was built in for this purpose.

- Switch off the turbomolecular pump, the backing pump remains running.

- Fully retract the EBSD detector.

- Tilt the stage to 0°.

- Move the stage to position the sample underneath the quench nozzle.

- Wait for the turbomolecular pump to reach 60% of the maximum rotating speed.

- Switch off the heater.

- Open the quenching valve.

- The pressure inside the chamber is monitored using the additional pressure gauge until room temperature is reached.

- The roughing pump is switched off.

- The quenching valve is closed, the door opens and the chamber is flushed several times with nitrogen to prevent damage to the ion getter pumps from helium.

A modular design of this setup was chosen to enable the use of the setup on another vacuum chamber. Therefore, all components were mounted on a 4-way vacuum standard cross fitting. The 4-way standard cross fitting mounted on the SEM chamber is shown in Figure 3.5b. The feedthrough for the quenching gas, the feedthrough for the pyrometer and the feedthrough for two pressure gauges, one for the rough (Pirani) one for the high vacuum range (Penning) were mounted onto this cross. The setup can be easily mounted on any vacuum chamber which must at least be equipped with two electrical feedthroughs (2 x 2 wires). An interface for the Penning pressure gauge was added to the LabJack device and implemented into the LabVIEW program. This enables to log the pressure and to start heat treatments only after a pressure threshold is reached.
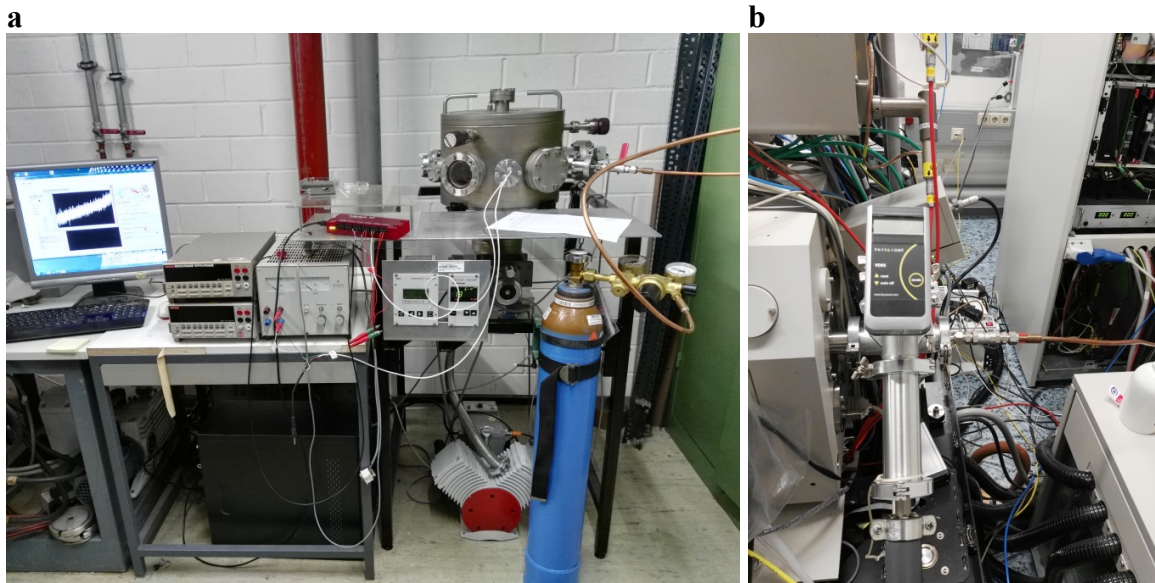
Figure 3.5: a) Shows the ex situ setup consisting mainly of a vacuum chamber and pumps. **b)** Shows the 4-way flange with instruments and feedthroughs attached to the SEM/FIB.

Time on the SEM is limited and in order to perform heat treatments under conditions comparable to the *in situ* experiments an *ex situ* setup was developed and used. The *ex situ* setup is based on an UHV chamber equipped with a turbomolecular, a scroll pump, and several electrical feedthroughs. The *ex situ* setup is shown in Figure 3.5a. The 4-way flange described above was attached to the UHV chamber. The same button heater which was used for the *in situ* experiments was mounted onto an aluminum block inside the chamber. A fixture for the pyrometer optics including the mirror was added. The 4-way flange equipped with all instruments and feedthroughs for the measurements can also be attached to other vacuum chambers.

3.3.1   Measurement Strategy

1. Combination of EBSD maps using spatial and orientation markers

OM maps at the same location of one sample are combined to quantify and characterize microstructural changes in between two scans. Markers created by FIB are used for spatial correlation. Either microstructural features not affected by microstructural changes or a gold wire afixed to the sample are used for the correlation of crystal orientations and of real space sample orientation during the experiments. A detailed description of this procedure is given in Chapter 4.

2. Combination of EBSD and SE data for the observation of dynamic processes

EBSD is not (yet) suitable for the observation of dynamic processes due to its relative long measurement time. Therefore, SE images of the surface in between EBSD scans were collected in order to capture the dynamic changes of the microstructure. This was possible with some materials because of pronounced thermal grooving at interfaces and for martensite formation due to the relief formed during the transformation. The combination of these SE images with the EBSD scans of initial and final microstructure allows for the identification of the character of the interfaces on the basis of the EBSD scans. The basic idea of this procedure is schematically outlined in the diagram in Figure 3.6.

Outline of the measurement procedure:

1. EBSD scan of initial microstructure

2. Change of temperature

3. Observation of surface using SE detector (high scan rate)

4. EBSD scan of final microstructure (low scan rate, if RT is reached)
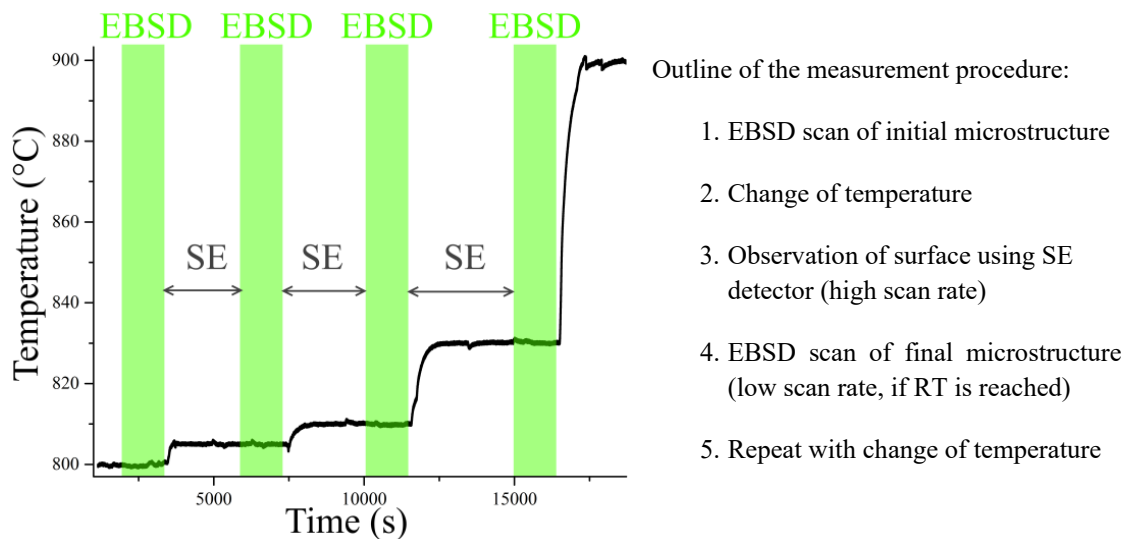
5. Repeat with change of temperature

Figure 3.6: Scheme of the measurement strategy for the combination of EBSD measurements with SE image sequences.

4 Combining EBSD Maps

This Chapter introduces a novel method for the combination of EBSD datasets. This method was developed for a better interpretation of the EBSD data which was collected in the *in situ* experiments. The method does not require *in situ* methods and is not restricted to phase transformations. It is useful for the analysis of repeated EBSD mappings of a certain surface area during microstructural changes.

The method and its limitations are presented in the first few sections of this chapter and the subsequent sections are intended to show the potential of this method. Here novel computational tools for the analysis of combined orientation mappings are presented. These tools are used further on in this thesis for the characterization of different phase transformations. Most of the tools were developed specifically for the study of martensitic transformations.

4.1 Introduction

A combination of EBSD maps of the same location on a samples surface can be used to study processes which affect the microstructure of the sample. This method enables the study of microstructural changes in a quantitative way compared to other approaches.

The relevant literature often focuses on microstructural statistical analyses (calculation of GND densities, change of texture, grain sizes, phase fractions etc.) concerning a single EBSD scan. A significant advantage of the EBSD technique is lost using this approach which is the high spatial resolution. So far the only approaches towards an analysis with high spatial resolution are based on a simple superposition of images of the EBSD scans. This enables only a very limited comparison due to drift and differences in the reference system between the scans.

A direct and quantitative comparison of EBSD data of a sample in different processing steps therefore requires at least two prerequisits:

1. Correction of crystallographic orientations: This requires to account for changes of the orientation of the sample between the measurements so that all crystallographic orientations from the measurements are based on the same reference system.

2. Correction of spatial orientation: This requires that the measured data has to be aligned to ensure that corresponding data points of the datasets fall on top of each other.

Methods to achieve this direct comparison of different EBSD data sets developed in this thesis are described in the following Chapter 4. These methods are not restricted to *in situ* experiments: It can also be used for *ex situ* experiments regardless of the experimental technique (as long as a high spatial resolution is possible).

The technique has however some restrictions concerning the experimental conditions. Some of these arise from the use of the EBSD technique:

1. Measurements can only be performed on the surface of the sample

2. The processes observed should be slower than the measurement time

Other limitations are a result of the technique used for the analysis of the measurements:

1. Markers on the surface of the sample have to be used to enable spatial correlation

2. Parts of the microstructure must not be affected by the processes between measurements or an "orientation marker" has to be used

The combination of a set of EBSD maps requires a correction or adjustment of the spatial and crystallographic orientations of the maps. These corrections or adjustments are not independent: Changes in the orientation of the sample relative to the EBSD detector will cause a change of crystallographic orientations but also a change of the spatial orientation and distortion of the field of view.

The conceptually simple technique introduced here enables the study of microstructural changes at a high spatial resolution giving access to the crystallographic orientations and their relationships. This enables a through-process characterization of the microstructure of a sample. It can be used for the study of phase transformations, recovery and recrystallization, plastic deformation and combinations of these processes.
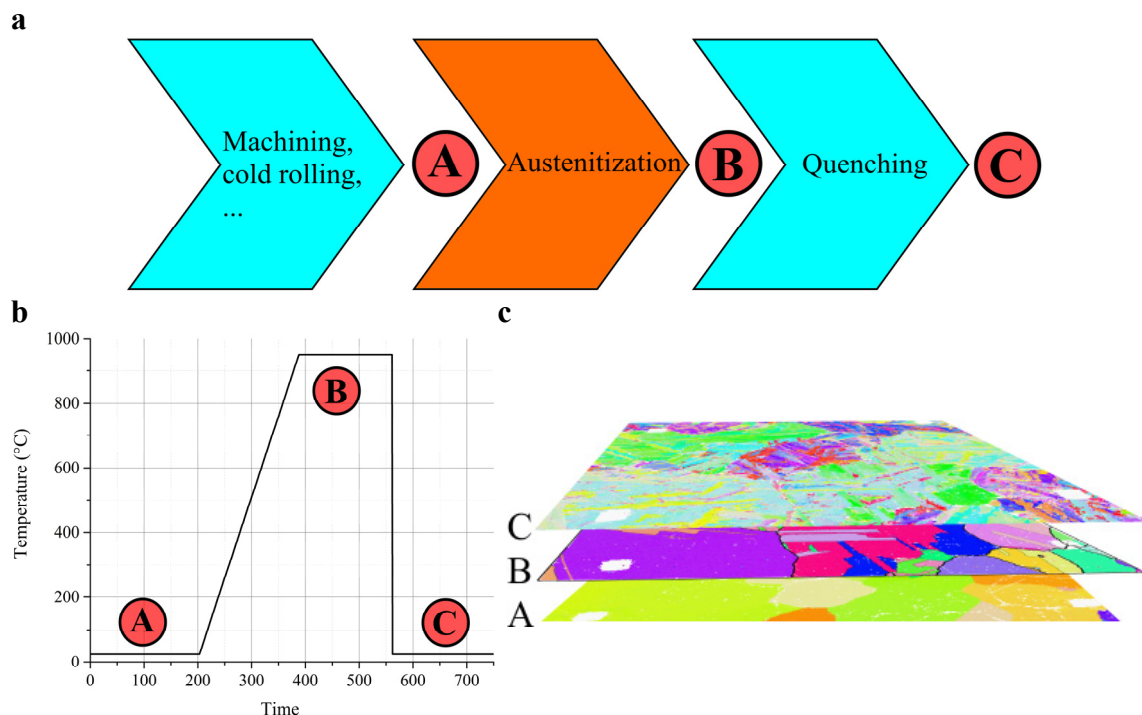

Figure 4.1: a) Schematic representation of the different processing steps and their products in a very simple processing chain. **b)** The heat treatment curve for the processing chain shown in Figure 4.1a. **c)** Illustration of the combination of EBSD maps of the different microstructural states which are a result of the processing steps shown in Figure 4.1a,b.

Accurate microstructural information about such processes is not only essential for a deeper understanding of their driving forces, crystallographic mechanisms and kinetics but also for their optimization. These processes are often important parts of a consecutive production chain. The microstructure and thereby the properties at every processing step influences the microstructure and properties of every following processing step. A very simple example is shown in Figure 4.1a. In a first step the material (steel) is deformed by machining. An austenitization treatment with a certain holding time follows. Here the first phase transformation from ferrite to austenite is involved. The material is quenched after the austenitization time is finished causing the second phase transformation from austenite to martensite. The corresponding temperature curve is shown in Figure 4.1b.

This shows that microstructural information about the past processing steps should be included for a more thorough description of a material. Therefore, a combination of EBSD scans of the microstructure at different processing steps would be desirable. Every measurement point would then contain an x- and y-coordinate as well as the phase and its orientation of the corresponding measurement point along the processing coordinate. This is schematically illustrated in Figure 4.1c where a superposition of three EBSD scans (corresponding to the three processing states) is shown. The scans were made after the different processing steps and refer to the corresponding points in the temperature curve shown in Figure 4.1b and the process chain in Figure 4.1a.

4.2   MTEX Matlab toolbox for EBSD data analysis

MTEX [359] is a free Matlab toolbox for analyzing EBSD data. The MTEX toolbox (MTEX 5.1.1) was used in this thesis for the analysis of all measured EBSD data. The open and flexible architecture of the toolbox and the generalized treatment of orientation data enable the development of complex routines for specific purposes. A large number of extending functions concerning in general crystallographic relations between parent and product phase and in particular ORs and variant identifycation between austenite and martensite were developed for this purpose in this thesis. This concerns all methods that are described inside this chapter (Chapter 4).

A simple adaption of the definition of the KS variants in accordance to Morito et al. [218] into the MTEX framework was not possible because it produced symmetrically equivalent orientations/misorientations (cf. Chapter 2.1.8.5 and Table 2.1). Therefore, the variants of all ORs were defined in the framework of the MTEX MATLAB toolbox and then ordered to achieve the sequence of misorientation angles following the definition of Morito et al. This procedure reduced the number of possible arrangements drastically. The definition of the KS variants used in this work were then selected by comparing the pole figures of the remaining variant arrangements to the ones in literature. A similar procedure was used for the NW OR (based on Kitahara et al. [122]). The variants of the other ORs were arranged in an analogous way as there is no predominant numbering of the variants present in literature. The definition of the variants can be found in Chapter 11.1.

4.3   Adjustment of Spatial Orientation

An adjustment of the spatial orientations of two EBSD scans is needed before a meaningful combination of the crystallographic information can be performed. This adjustment can be done by shifting one of the maps on top of the other. Microstructural features (grain boundaries, particles, twins) which are not affected by the changes occurring on the sample are required to determine if a good fit is achieved. Markers (e.g. made by FIB milling) have to be used if drastic changes of the microstructure are expected. However, this adjustment does not take thermally induced volume changes and volume changes arising from a phase transformation into account.

A set of MATLAB applications was created in which corresponding points can be selected on the two EBSD maps which shall be aligned. An efficient function for the calculation of the goodness of fit was developed by calculating the distance of these corresponding point pairs. A non-linear optimization algorithm (Nelder-Mead simplex direct search) is used to find the optimum shift of the EBSD map. Further capabilities of these applications include the adjustment of rotations of the sample surface in space. An alignment of the step sizes of the different maps is also necessary if different step sizes were used in the acquisition of the maps. This alignment is also automatically accomplished using the same algorithms as described above.

4.4   Adjustment of Crystallographic Orientations

Changes of the orientation of the sample relative to the EBSD detector can occur due to tilting of the stage, limited accuracy of stage positioning or if the sample was manipulated in between measurements. The rotations connected to those changes have to be determined in order to correct the orientations in the EBSD map. This can be done if no microstructural changes occur in between measurements or parts of the microstructure are not affected. The calculation of the rotation between two maps can be achieved by

the calculation of orientation distribution functions (ODF) from the maps and their comparison if no microstructural changes occured. Alternatively, individual corresponding microstructural features (grains, twins, particles etc.) common to both maps can be selected and their orientations can be compared. The rotation can then be calculated from the misorientation between the orientations of these microstructural features (crystal symmetries have to be taken into account). This solution of the problem is shown in Figure 4.3.
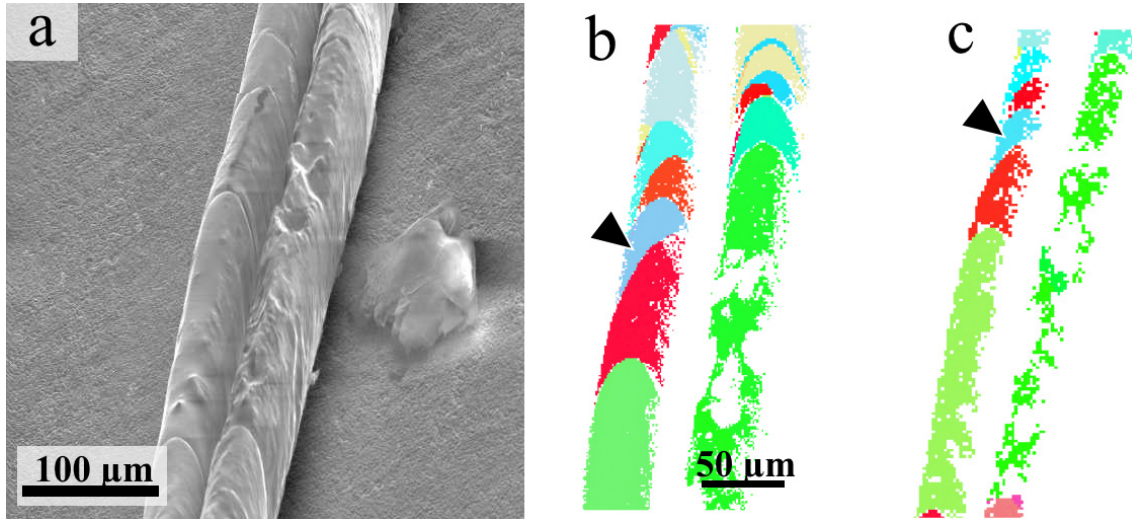

Figure 4.2: a) SEM image of two gold wires on a molybdenum clamp that are used to fix the sample on the heater. The wires are used to measure reference orientations. **b)** EBSD map of a section of the gold wires at room temperature. The grain whose orientation is used as a reference is marked by a triangle. **c)** OM of the same section of the gold wire at 900°C. The grain which corresponds to the grain highlighted in b is marked with a triangle.

If all orientations on the sample change (e.g. due to phase transformation(s), recrystallization) a reference orientation is needed: In this work a gold wire was afixed to the surface of the Mo clamp which is used to mount the sample onto the button heater. The crystallographic orientations of the same section of the gold wire were determined by EBSD prior to each EBSD scan of the sample surface. An example for this procedure is shown in Figure 4.2. An SEM image of a section of the gold wire attached to the Mo clamp is shown in Figure 4.2a. The images in Figure 4.2a and Figure 4.2b show results of the orientation mapping at this location at room temperature and at 900 °C. Black triangles indicate which microstructural features were selected for the comparison (a single grain). The misorientation is calculated by comparing the orientations of the selected grain of the gold wire of the scans at different temperatures:

$$R_{25\,°C\rightarrow900\,°C} = O_{Au}^{-1}(25\,°C) \cdot O_{Au}(900\,°C) \qquad \text{Eq. 4.1}$$

This misorientation $R_{25\,°C\rightarrow900\,°C}$ can then be applied to the orientation map at elevated temperatures. This can be used to compensate tilting of the heating stage which is a result of inhomogeneities in the thermal expansion of the setup.

4.5 Combined Adjustment

Changes of the spatial orientation of the sample with respect to the EBSD detector will not only affect the orientations measured on the surface of the sample but will also affect the spatial orientation of the orientation map due to a different projection into the 2D SEM image. This will not only affect the position of the map relative to another map but also the distances between the measurement points on a single map if the sample is not only shifted or rotated but also tilted.

An example is shown in Figure 4.3: Two EBSD scans were performed at the same location on a steel sample. The sample was manually rotated by some degrees in between the two scans. This leads to a change of the crystallographic and spatial orientations in the second EBSD scan. The misorientation which was used for the adjustment procedure was calculated from the mean orientations of the same grain marked with a triangle in Figure 4.3a and Figure 4.3b. The rotation connected to this misorientation is then applied to the crystallographic orientations in Figure 4.3b. This rotation is then additionally applied on the x- and y-positions of the measurement points resulting in the map shown in Figure 4.3c.
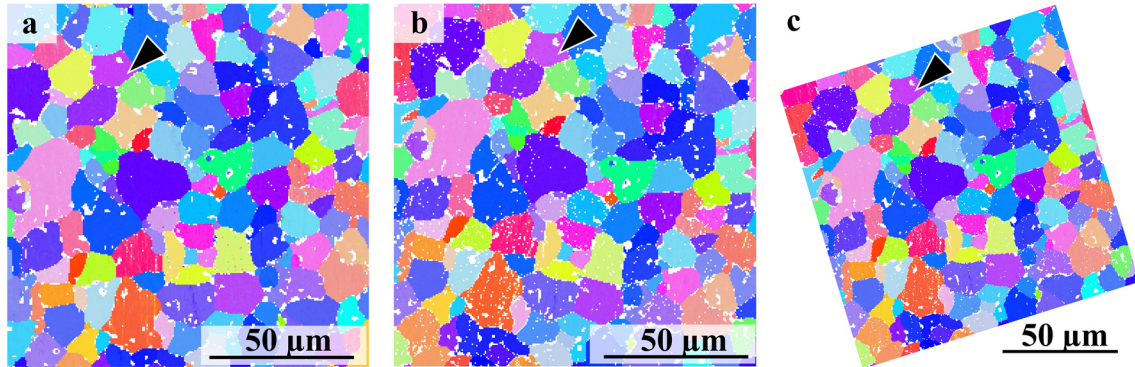

Figure 4.3: Example illustrating the spatial alignment from the comparison of crystallographic data. **a)** EBSD scan of a steel sample. **b)** OM of the same sample at the same position but rotated. The sample was rotated manually in the SEM. From the mean orientation of the grain marked in a) and b) the misorientation is calculated which is applied to the orientations measured in b) and to the positions of the measurement points. **c)** Shows the same scan as b) after the adjustment methods were applied. The crystallographic orientations and the spatial orientations are adjusted to fit to the one of scan a).

The stretching/compression necessary in the case of tilting can be calculated from the misorientation and can be applied to the measurement grid. The projection of the measurement grid is affected by this misorientation as the sample is already tilted by 70° for the EBSD measurement. The matrix of the rotation corresponding to the misorientation can be calculated. The corrected positions x_c can then be calculated from the measured positions (x, y) with respect to a rotation R using:

$$x_c = xR\begin{pmatrix} 1 \\ 0 \\ 0 \end{pmatrix} + yR\begin{pmatrix} 0 \\ \cos 70° \\ \sin 70° \end{pmatrix} \qquad \text{Eq. 4.2}$$

The position of the rotation axis in the reference frame of the EBSD map is unknown and hard to determine. If the alignment of the maps is good as in the example shown in Figure 4.3 and the rotation is relatively small, the center of the map can be used as the rotation axes.

Due to these complications a more general approach was chosen: An optimization procedure similar to the one outlined in section 1 is applied using markers or unchanged microstructural features. The misorientation measured on the gold wire is used as a starting value for this optimization.

4.6 Interpolation

A direct comparison of the orientations of two EBSD scans is only possible if the step sizes of the measurements are equal. The starting points of the scans will not be equal if the spatial orientation had to be adjusted (restricted to translational adjustment). The distances in x and y have to be integer multiples of the step size for a direct comparison.

The step sizes will be inhomogeneous if other adjustments were applied. Moreover there may be two EBSD maps which exhibit different step sizes. This is often the case for the martensitic transformation: On the one hand, there is the coarse microstructure of austenite that exhibits minimal granular orientation spread. This microstructure usually does not require a low step size and thereby reduces measurement time. On the other hand, there is the fine-grained martensite microstructure exhibiting strong orientation gradients. This microstrucre can only be accurately characterized by EBSD if small step sizes are used.

In these cases, an interpolation step is needed to combine the maps onto a regular, common grid. It may not be necessary to apply the adjustment procedures (for the spatial rotations) onto the grids of all EBSD scans of a set of measurements. The grids of the EBSD scans exhibiting larger step sizes were adjusted to fit onto the grid of the measurement with the lowest step size in order to reduce computation time. In the interpolation approach chosen here, the adjusted coarser map is interpolated onto the map exhibiting the smaller step size. Therefore, the distance of every point of the adjusted map to every point of the other map is calculated to find the closest points. The attributes of the coarser map are then applied to the measurement points of the map with the smaller step size. The distance between the points is also stored as an attribute of the points of the combined map. This serves as a measure of the error introduced by the interpolation.

4.7 Inheriting Orientations

MTEX treats EBSD datasets as lists. The elements of these lists have attributes. A standard EBSD dataset has for example the attributes id, x, y, φ_1, Φ, φ_2 which denote the position in the list, the x-coordinate, the y-coordinate and the Euler angles φ_1, Φ and φ_2, respectively. There are additional attributes such as band slope (BS), band contrast (BC), the mean angular deviation (MAD), the number of bands fitted to the EBSP etc.
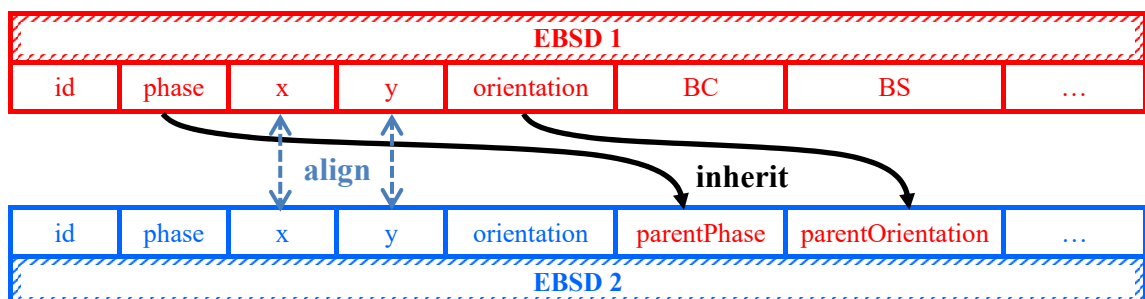

Figure 4.4: Illustration of the combination of EBSD datasets by generation of new orientation properties through spatial correlation/alignment and interpolation.

This list of attributes can be extended. The additions to MTEX developed in the scope of this thesis for the combination of maps and the study of the martensitic transformation are mainly based on the modification (for the adjustment procedures) and extension of these attributes. The main feature is the "inherit" command which performs the interpolation step described above and adds a new attribute to the map which is transferred from the map from which the interpolation is performed. For example, this enables to have two orientations connected to one single data point (e.g. orientation and parentOrientation).

4.8 Calculating Variants

The orientation pairs generated using the procedure outlined in the sections before can be used to determine properties of the phase transformations which occur between two measurements. In the case of the martensitic transformation for example the martensite variants can be determined with high spatial resolution. The procedure used for this calculation is outlined in Figure 4.5. The starting point is the austenite orientation O_γ measured at elevated temperatures. The orientation of the transformation product may be predicted using an OR:

$$O_{\alpha,i} = O_\gamma C_i M_{OR}^{\gamma \to \alpha} = O_\gamma M_{OR}^{\gamma \to \alpha}(i) \qquad \text{Eq. 4.3}$$

Where $O_{\alpha,i}$ is the orientation of product variant i, $M_{OR}^{\gamma \to \alpha}$ is the misorientation matrix representing the OR between γ-phase and α-phase and C_i is a symmetry operator accounting for the n equivalent crystallographic orientations (n is determined by the symmetries of parent and product phase and $M_{OR}^{\gamma \to \alpha}$). For the KS OR this leads to 24 misorientations $M_{KS}^{fcc \to bcc}(i)$ with $i = 1 \dots 24$ corresponding to the 24 variants.
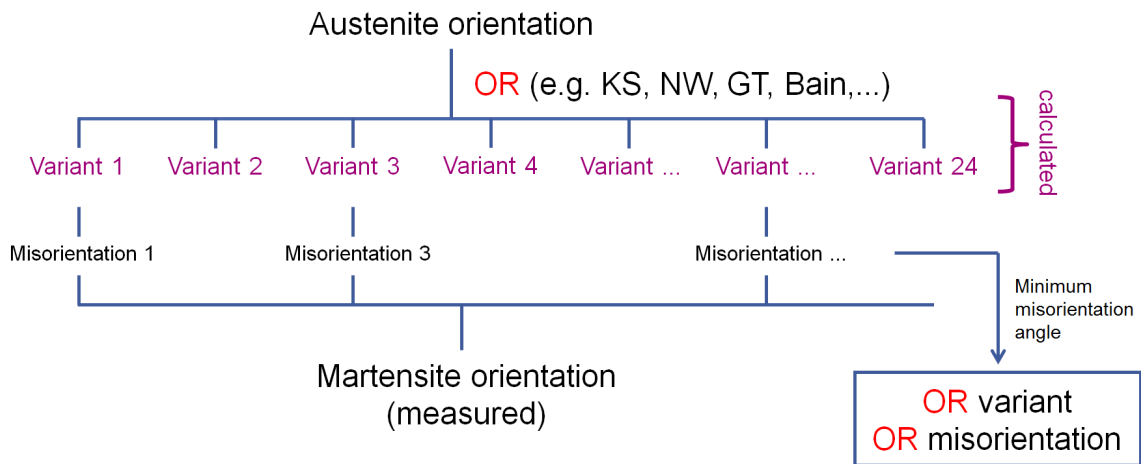
Figure 4.5: Schematic illustrating the calculation of variants and their misorientation angles from orientation pairs. The OR actually consists of n misorientations. This method is applied for every OR considered here.

These misorientations are then applied to the parent orientation resulting in a theoretical product orientation for every variant. The theoretical product orientations are then compared to the measured product orientation. The theoretical product orientation exhibiting the smallest misorientation angle to the measured product orientation can then be regarded as the variant that was formed at this point. This leads to new attributes in the EBSD data structure like ksvar, nwvar, gtvar etc., referring to the number of the KS, NW or GT variant respectively. The smallest misorientation angle calculated between the theoretical orientation and the measured orientation can be regarded as a measure of how good the specific OR

applies to the transformation at this point and is also added as an attribute to the map (ksmis, nwmis, gtmis). These calculations can be formulated as:

$$v_{OR} = \arg\min_i \left| O_{bcc}\left(M_{OR}^{fcc \to bcc}(i) \cdot O_{fcc}\right)^{-1} \right| \qquad \text{Eq. 4.4}$$

$$\Delta\theta_{OR} = \text{angle}\left(\min_i \left| O_{bcc}\left(M_{OR}^{fcc \to bcc}(i) \cdot O_{fcc}\right)^{-1} \right|\right) \qquad \text{Eq. 4.5}$$

With v_{OR} the variant number and $\Delta\theta_{OR}$ the misorientation angle towards the closest variant. These calculations are applied to every data point of the EBSD map. This is shown for an example in Figure 4.7: The martensite orientations are shown in Figure 4.7a. The corresponding parent (austenite) orientations are shown in Figure 4.7b. The variants calculated from these orientation pairs using the KS OR are shown in Figure 4.7c and the misorientation angle towards the closest theoretical transformation product is mapped in Figure 4.7d.

Information is lost if only the magnitude (angle) of the misorientation is analyzed. Therefore also the misorientation $R_{min,OR}$ which is the misorientation between measured product orientation and closest theoretical product orientation should be taken into account. This misorientation is therefore calculated and stored in the combined EBSD data:

$$R_{min,OR} = O_{bcc}\left(M_{OR}^{fcc \to bcc}(v_{OR}) \cdot O_{fcc}\right)^{-1} \qquad \text{Eq. 4.6}$$

Significant effort was put into an efficient (in terms of calculation time) implementation of these methods into MATLAB/MTEX resulting in a fast and easy to use extension of the MTEX toolbox for advanced combination of EBSD maps and the subsequent study of phase transformations.

A list of the variant numbers can be extracted from the combined EBSD map. This list can be statistically analyzed to assess the distribution of variants in the sample. This procedure is commonly used in literature to illustrate the occurrence of variant selection. Histograms are usually used to visualize this data in a comfortable way. An example of a typical variant histogram is shown in Figure 4.6a. This type of visualization is repeatedly used in this thesis. It can qualitatively illustrate the degree of variant selection and unveil which variants are generally preferred in the transformation product.

Additionally, the mean misorientation angle for each variant number is plotted in the same diagram. This can help to assess how well the variants are represented by the chosen OR and/or if certain variants are shifted to different orientations. This value is usually higher for variants with low frequencies.

4.9   Quantifying the Degree of Variant Selection

The martensite variants should show uniform distribution if no variant selection mechanisms are active. However, sometimes particular variants are favored due to some factors such as external stresses, strains etc. which is called variant selection (cf. Chapter 2.1.8.6).

Variant histograms are used throughout this thesis to illustrate whether variant selection takes place or not. This may give a detailed but only qualitative assessment of the degree of variant selection. An approach for the definition of such a metric was not found in the literature. Therefore, a quantitative measure for variant selection strength (VSS) is suggested in this thesis. In order to introduce this quantitative

measure for the degree of variant selection, the divergence (or distance) of the probability distribution $P_{OR} = \{p_1, \ldots, p_m\}$ (with $m = 1 \ldots 24$ for P_{KS}) of the crystallographic martensite variants, as calculated by a certain OR, from the uniform distribution $U = \left\{\frac{1}{m}, \ldots, \frac{1}{m}\right\}$ is determined. Here the values of P_{OR} are the relative frequencies of the variants.

This distance may be calculated using the Kullback-Leibler divergence [360] or Wasserstein metric etc. which are usually [361] used to calculate distances between probability distributions. The total variation distance was chosen in this approach. The advantages are that the function is always defined and ranges between 0 and 1. The variant selection strength factor (k_{VSS}) is thus here defined as:

$$k_{VSS}(OR) = \frac{\frac{1}{2}\sum_{i=1}^{m}|P_{OR,i} - U_i|}{1 - \frac{1}{m}} \qquad \text{Eq. 4.7}$$

With k_{VSS}, the variant selection strength factor which becomes 0 for uniformly distributed variants and 1 for the hypothetical case of a martensite microstructure consisting only of a single variant. This means that a value of k_{VSS} close to 1 corresponds to strong variant selection and a value close to 0 indicates weak variant selection. The value m is the number of variants of an OR which is equivalent to the number of symmetrically non-identical misorientations arising from the OR. An overview of the different expressions used to qualitatively describe the degree of variant selection is schematically depicted in Figure 4.6b.

a   **b**
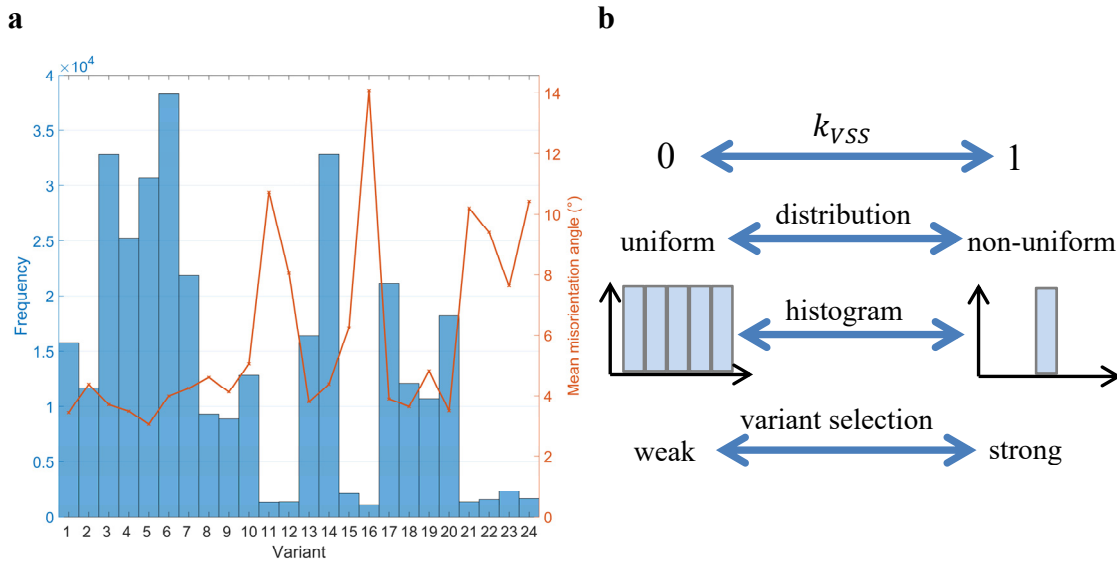
Figure 4.6: a) Example of a typical variant histogram for the case of KS variants. **b)** Illustration of the meaning of the variant selection strength and different terms for the qualitative description of the magnitude of variant selection.

Another value which can be used for the characterization and description of variant selection are the mean granular variant selection strength (mVSS). This is equivalent to the VSS calculated per prior austenite grain. Further the average number of different martensite variants $\overline{n_{var}}$ which were formed in a PAG can be calculated.

4.10 Calculating Variant Maps

The description of the martensite microstructure from orientation mapping in the literature is always focused on an approach which is based on the measurement grid. Lath martensite consists of a hierarchical microstructure. Martensite laths usually consist of a single crystallographic product variant. Therefore, a simplified description of the microstructure is possible and an algorithm for the calculation of a variant map was developed. This concept is analogous to the definition of grain maps in which a certain orientation was measured in a certain area. The grain map therefore consists of the boundaries of these areas and contains information on the enclosed area.
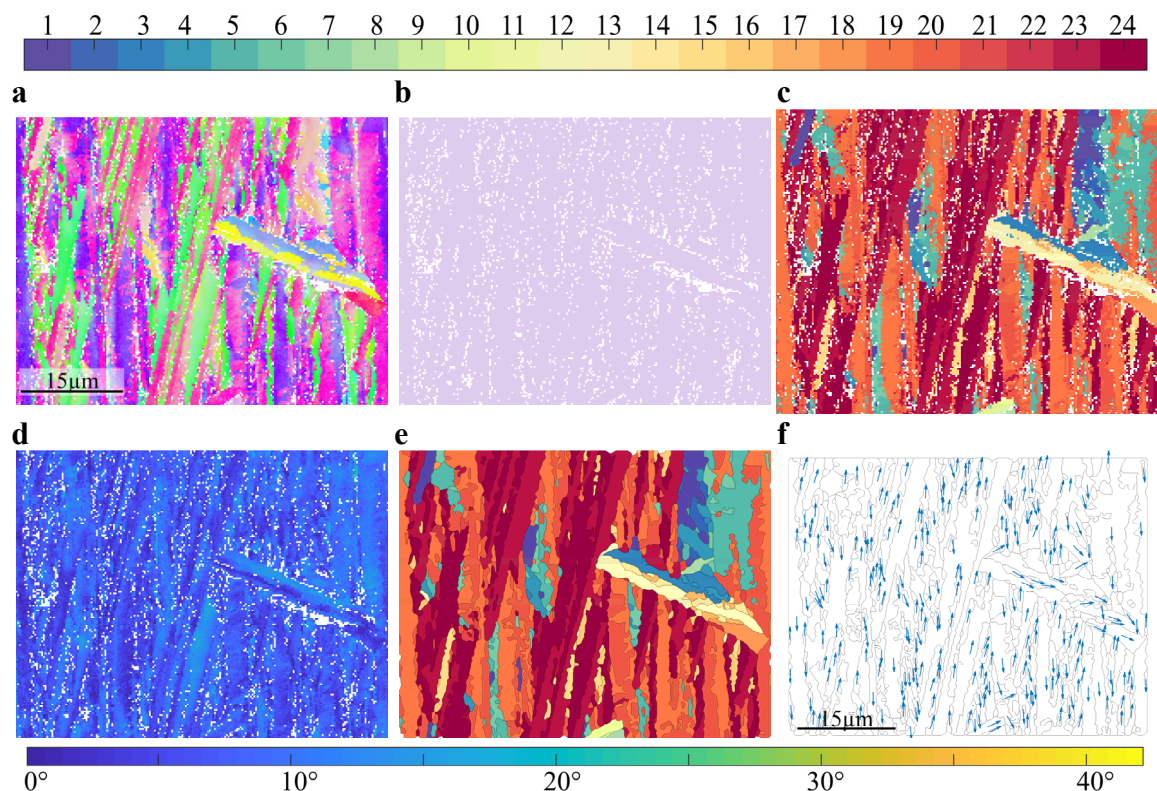

Figure 4.7: Mapping of different properties of a combined EBSD map. **a)** OM of product orientations. **b)** Corresponding OM of the parent orientations. **c)** Map of the KS variant number calculated from the product orientations and parent orientations. **d)** Map of the smallest misorientation angle of a calculated KS variant based on the parent orientation towards the measured product orientation. **e)** KS variant map. This map is based on the mapping of the KS variant number and was calculated using the MTEX grain reconstruction algorithm. **f)** Map of the boundaries of the KS variants shown in **e)** and the long direction of the martensite lath (indicated by blue arrows).

Variant maps consist of areas enclosed by boundaries in which all points belong to one martensite variant. The calculation of the martensite variant map is based on the grain reconstruction algorithm which is implemented in MTEX [362]. This algorithm basically performs a Voronoi decomposition of the EBSD grid. Voronoi cells which belong to the same phase and exhibit a misorientation angle smaller than that chosen by the user are joined together. This algorithm can be applied to different properties of the EBSD map. Instead of misorientations, the KS (or NW, GT, GT', Bain, Pitsch) variant number is used as input for the reconstruction algorithm. The result is a map that consists of areas which share the same KS variant number. An example, which is based on the mappings shown in Figure 4.7a-d, can be seen in

49

Figure 4.7e. One element of a variant map consists of a list of vertices, the variant number and the mean misorientation angle to the closest KS variant.

This approach allows for a more comprehensive statistical analysis of martensite microstructures in comparison to the approach solely based on measurement points. It is also possible to access the properties of the variant boundaries allowing for a quantitative analysis of variant pairing.

4.11 Calculation of Variant Pairing

Further characteristic statistical data which can be used to describe the martensite microstructure in more detail can be extracted from variant maps. In this thesis, the calculation of variant pairing is based on variant maps. Variant pairing describes the tendency of certain variants to form next to each other. Variant pairing is frequently described and discussed in literature but is mostly treated qualitatively on the basis of individual observations. A quantitative analysis and visualization of variant pairing is necessary for a better understanding of this phenomenon.

The variant boundaries of variant maps are analyzed using a MATLAB/MTEX script. Variant pairs can be extracted from each variant boundary segment. The pairs are sorted and ordered and then counted. As many samples exhibit rather strong variant selection a weighted bivariant histogram is calculated from the list of pairs:

$$r_{ij} = \frac{n_{ij}}{n_i \cdot n_j}$$

<div align="right">Eq. 4.8</div>

n_{ij} is the frequency of a pairing of variants i and j. n_i and n_j are the frequencies of variant i and j respectively and r_{ij} is the relative frequency of a pairing of variant i and variant j. The 24 KS variants result in $\binom{24}{2} = 276$ possible relative pairing frequencies r_{ij}. For the 12 NW variants $\binom{12}{2} = 66$ combinations are possible.

The result of the calculation described above may be influenced by the misorientation between austenite grains prior to the transformation. Neighboring variants across prior austenite grain boundaries may not be a result of the variant pairing effect. Therefore, the variant pairing is calculated for each austenite grain individually. The information if a variant belongs to an austenite grain is included in the variant maps using the "inherit" command. The resulting frequencies for the single austenite grains are then combined.
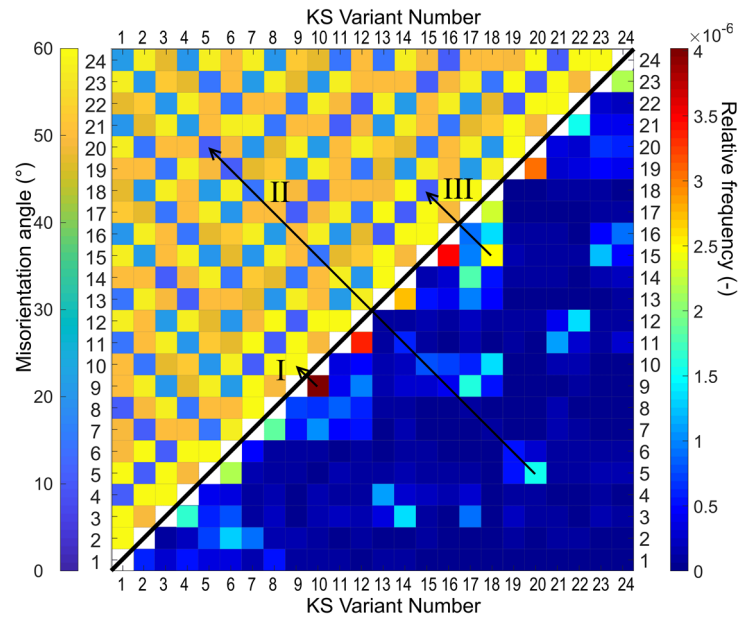
Figure 4.8: Example explaining the use of a combination of bivariant histograms and the plotting of intervariant misorientation angles for the visualization of variant pairing used throughout this thesis.

A diagram for the visualization of the variant pairing data is proposed in this thesis. So far, no quantitative studies can be found on pairing in literature containing or describing visualizations of variant pairing (an exception is the study by Stormvinter et al. [209]). Therefore, a bivariant histogram is created for the representation of variant pairing. It consists of 276 fields (for the KS OR) which are colored according to relative frequency of the respective variant pair i.e. the value of r_{ij}. This results in a triangular diagram because $r_{ij} = r_{ji}$. These diagrams are combined with a diagram of the intervariant misorientation angle throughout this thesis. An example is shown in Figure 4.8. The black line shows the division of the diagram in its two parts: The lower right triangle shows the bivariant histogram for all variant pairings for the KS OR. The upper left triangle shows the intervariant misorientation angle for all variant pairings for the KS OR. The black arrows show how this diagram can be read: the corresponding square mirrored at the black line shows the intervariant misorientation angle for a certain variant pairing. The highest relative frequency can be found for the pairing V10-V9 (marked as I). The corresponding intervariant misorientation angle can easily found to be 60° indicating that the variants V9 and V10 are twin-related. A relative high relative frequency can be found also for the pairings V5-V20 (marked as II) and V15-V18 (marked as III): In both cases the intervariant misorientation angle is 10.53°.

4.12 Calculation of Orientation Relationships from Combined EBSD Maps

An OR can be calculated from one single pair of parent and product orientation. A large number of such orientation pairs are usually available if EBSD is used for the study of phase transformations. These orientation pairs either may result from measurement points from both sides of a phase boundary or from the combination of two EBSD maps recorded before and after the transformation. A method for the calculation of an OR from a large amount of orientation pairs was developed in this thesis: A misorientation density function (MDF) is calculated from the orientation pairs. A kernel density estimation via Fourier series with a 5 degree kernel is used to calculate the MDF in order to achieve a reduction of calculation time [363]–[365]. Therefore, a de la Valee Poussin kernel is used. Then the maximum of this MDF is calculated resulting in the most dominant misorientation. This is shown as an example for an austenite-to-martensite transformation in Figure 4.9a. A part of the total number of misorientations is plotted and the maximum of the MDF calculated from all misorientations is marked. This misorientation is then fitted onto parallel planes in the parent and product phase producing two parallel crystallographic planes and two parallel directions of parent and product phase. The variants of the OR are then calculated by applying the symmetries of parent and product phase onto the misorientation resulting in 2304 single misorientations (for cubic symmetry). The unique variants are then extracted from these misorientations by searching all non-equivalent misorientations.

4.13 Quantitative Estimation of the Habit Plane

A statistical approach can be used for the estimation of the habit plane of the martensite microstructure based on martensite variant maps. Therefore, the spatial orientation of the martensite laths needs to be determined. This is accomplished in the MATLAB/MTEX application which was developed for this purpose with the aid of principal component analysis. This results in the length of the short and long axis of the laths as well as the orientation of the lath within the surface of the sample. The orientation of the long axis of the martensite laths of the example microstructure are shown in Figure 4.7f as an example. The inclination angle α can be used to calculate the spatial orientation of the trace of the habit plane on the surface. The parallel crystal plane m can be obtained from the orientation of this trace using the local austenite orientation O_{fcc}:

$$m = O_{fcc}^{-1} \cdot \begin{pmatrix} 1 \\ \tan \alpha \\ 0 \end{pmatrix} \qquad \text{Eq. 4.9}$$

The inclination of the habit plane in z-direction cannot be obtained without cross-sectioning the sample. Instead all possible normal vectors (perpendicular vectors of the austenite crystal plane parallel to the trace of the habit plane) are calculated. This results in a circle on the unit sphere of the stereographic projection for every martensite lath. An example is given in Figure 4.9b for a martensitic microstructure. If this analysis is performed for many laths, the orientation of the habit plane can be estimated if areas of high density of intersection points appear on the unit sphere. These vectors are then the most probable normal vectors of the habit plane. They can be calculated by searching the common orthogonal vector to the crystal plane parallel to the traces of the habit plane of the martensite laths. This may be accomplished by finding the eigenvector with the smallest eigenvalue to the poles of the planes.
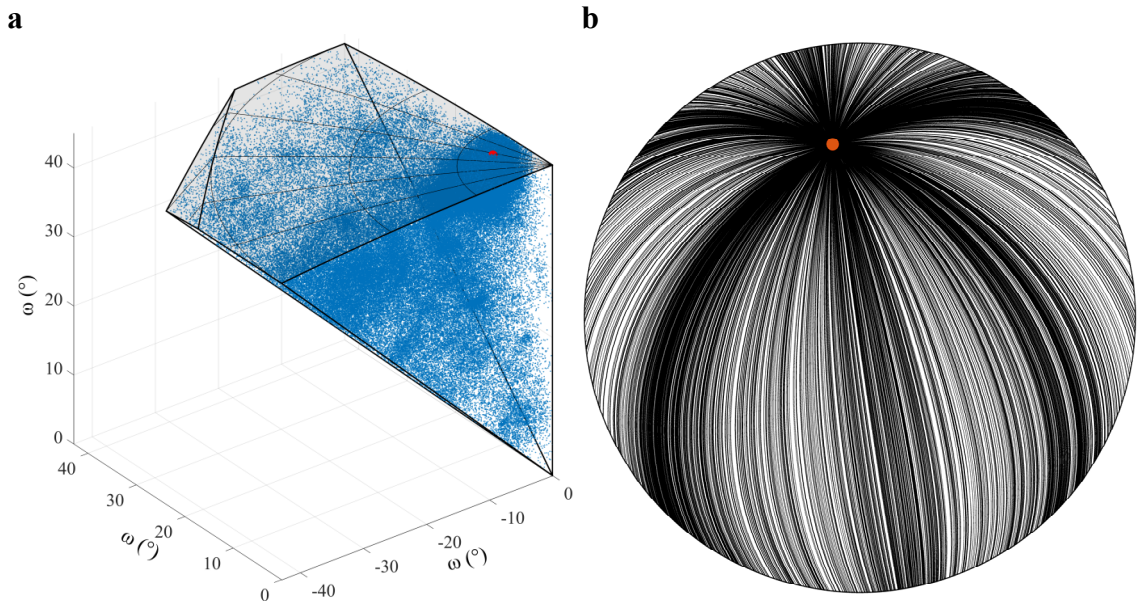
Figure 4.9: a) Plot of misorientations from more than 170 000 measurement points calculated from the combination of austenite and martensite orientations in 3D misorientation space. The red dot marks the maximum of the corresponding MDF. **b)** Circles on a unit sphere representing all vectors orthogonal to the crystal direction parallel to the habit plane trace. The common point to all circles i.e. the point with the highest density of intersections is marked with a red dot. This point represents the most probable habit plane vector of the martensite laths.

This method is very sensitive to scatter of the austenite plane parallel to the habit plane trace and can therefore only be applied if the scatter is relatively small. Therefore, a more robust approach was developed. This algorithm tries to find the maximum density of intercepts of the circles on the unit sphere which are formed from the perpendicular vectors with respect to the habit plane trace. This is done by the calculation of n vectors $\vec{p_i}$ which are perpendicular to the austenite vector $\vec{v_j}$ parallel to the habit plane trace. These vectors $\vec{p_i}$ are equally distributed around the perpendicular vector $\vec{v_j}$. This is accomplished by calculating one arbitrary vector $\vec{p_1}$ which is perpendicular to $\vec{v_1}$. This vector is then rotated around $\vec{v_1}$ in $\frac{360°}{n-1}$ steps resulting in n vectors perpendicular to $\vec{v_1}$. This procedure is then repeated for all $\vec{v_j}$ and the maximum of the density of vectors $\vec{p_i}$ is calculated which is the most probable habit plane normal vector.

5 Quantification of Orientation Relationships

Heat treatments are often used for the optimization of material properties. The microstructure of the material is affected by the heat treatment resulting in changes of its properties. These microstructural changes are often caused by phase transformations which are induced by the heat treatment. One important aspect of a (solid to solid) phase transformation is the orientation relationship of parent and product phase. This relation has to be known in order to predict the properties of the product phase i.e. when the texture is considered. The orientation relationship introduces a general description of the change of crystallographic orientations during the transformation.

5.1 Introduction

Several ORs were suggested since the beginning of the study of crystallography. These are connected to certain phase transformations or precipitation reactions. Most of the well-established ORs were determined at the beginning of the 20th century. The approach used at that time was qualitative. XRD measurements before and after the heat treatment of single crystalline samples revealed a constant relationship between parent and product phase orientations. However, it was not known if the OR found was valid for the complete sample or if variations of the OR existed throughout the sample.

With the advent of modern diffraction techniques such as EBSD, a quantitative approach becomes possible. Another method for the determination of ORs was taken with the development of the TEM: The orientations of neighboring phases were determined with the help of local electron beam diffraction experiments. Conclusions on the dominant OR were frequently made after a small number of observations disregarding the possibility that these orientations may not be representative for the sample as a whole. Therefore, an estimation of the probability of a random occurrence of orientations within certain proximities of a special OR has to be made beforehand. Only based on that, the statistical relevance of the observed OR can be assessed.

5.2 Comparison of Misorientation Data to Orientation Relationships

The determination of the OR requires knowledge of the orientation O_a of the parent phase and the orientation O_b of the product phase. The OR is equivalent to the misorientation $M_{a \to b}$ of these two orientations:

$$M_{a \to b} = O_b \cdot (O_a)^{-1}$$
<div align="right">Eq. 5.1</div>

The OR can be calculated from the orientations measured before and after the phase transformation. This is frequently done in the literature using XRD or TEM for a small amount of measurements. With the use of EBSD a large number of pairs of orientations from the parent and the product phase can be determined.

If the dominant OR from various established ORs has to be determined based on measured orientation pairs another approach is usually taken: Theoretical product orientations O_{th} are calculated from measured parent orientations $O_{a,m}$ using these known (well established) ORs.

$$O_{th} = O_{a,m} M_{a \to b} \qquad \qquad \text{Eq. 5.2}$$

The misorientation M_{OR} between calculated and measured orientation is then used to decide which OR fits best to the measurement data:

$$M_{OR} = O_{a,m}(O_{th})^{-1} = O_b \left(O_{a,m} M_{a \to b} \right)^{-1} \qquad \qquad \text{Eq. 5.3}$$

A large number of parent and product orientation pairs are taken into account for the quantitative determination of the dominant OR based on EBSD scans. The calculations described before are applied to all of these pairs. A quantitative measure of the degree of fit of a certain OR can be given by a mean misorientation angle:

$$\overline{\Delta\theta_{OR}} = \frac{\sum_n^1 |M_{OR}|}{n} \qquad \qquad \text{Eq. 5.4}$$

This angle is affected by the volume of the material that transforms according to the OR. It only gives a significant measure of the fit of the OR if the whole area of the EBSD scan took part in the transformation. A better measure is the number of orientation pairs that fulfill Eq. 5.5 for a given tolerance angle ω:

$$|M_{OR}| < \omega \qquad \qquad \text{Eq. 5.5}$$

The fraction of measurement points fulfilling this criterion is then given by the number of points fulfilling Eq. 5.5 divided by the number of measurement points that took part in the transformation:

$$f_{OR}(\omega) = \frac{n(M_{OR}(|M_{OR}| < \omega))}{n(M_{OR})} \qquad \qquad \text{Eq. 5.6}$$

This angle ω can be imagined as the radius of circles around the poles connected to the theoretical product orientation on the surface of the unit sphere of the stereographic projection. If measured orientations of the product phase fall into these circles they are counted. The percentage of orientations meeting this criterion can be calculated for all ORs under consideration, revealing the dominant OR. This approach is usually taken in literature [366], [367].

Caution has to be taken for the comparison of these values: Depending on the symmetries of the crystal systems of parent and product phase and the definition of the OR several non-equivalent variants can result in a single OR. A direct comparison of the fraction of points f for the Bain OR (3 variants) and the KS OR (24 variants) will introduce a systematic error because a random orientation will eight times more likely fall into one of the circles arising from the KS OR than into one of the circles connected to the Bain OR. A similar analysis was done by Ryder, Pitsch and Mehl [368], but as a rough estimate (simply by using the factor 8).

The probability of a random orientation to fall into one of the circles around the poles arising from an OR is proportional to the surface of all these circles on the unit sphere. This correction factor $f_{OR,norm}(\omega)$ has to be taken into account for the comparison of the relative frequencies $f_{OR}(\omega)$.

$$f_{OR,c}(\omega) = \frac{f_{OR}(\omega)}{f_{OR,norm}(\omega)}$$

Eq. 5.7

The value $f_{OR,norm}$ is dependent on the tolerance angle ω and the OR considered. It is the probability of random orientations to fulfill the condition of Eq. 5.5. The value $f_{OR,c}$ describes the relative frequency of the orientation to be found to fulfill Eq. 5.5 compared to a completely random orientation pair i.e. the relative frequency in multiples of random. The value of $f_{OR,norm}$ is proportional to the area covered by the circles around the poles arising from an OR. These correction factors are calculated for the well-established ORs in the following sections Chapter 5.3 and Chapter 5.4.

5.3   Limited Analytical Solution

The circles around the poles form domes because they are situated on a sphere. The surface of these domes can be calculated as planar circles ignoring the spherical distortion only for small angles ω (Legendre's theorem).

For an exact value, the surface of these domes can be calculated using an analytical equation:

$$A_{dome} = 2\pi(1 - \cos\omega)$$

Eq. 5.8

For the fraction of the unit sphere which is covered by these domes this results in:

$$f_{OR,norm} = \frac{N_V}{2}(1 - \cos\omega)$$

Eq. 5.9

N_V is the number of variants which result from a given OR. For the KS OR with $N_V = 24$ this results in:

$$f_{KS,norm} = 12\,(1 - \cos\omega)$$

Eq. 5.10

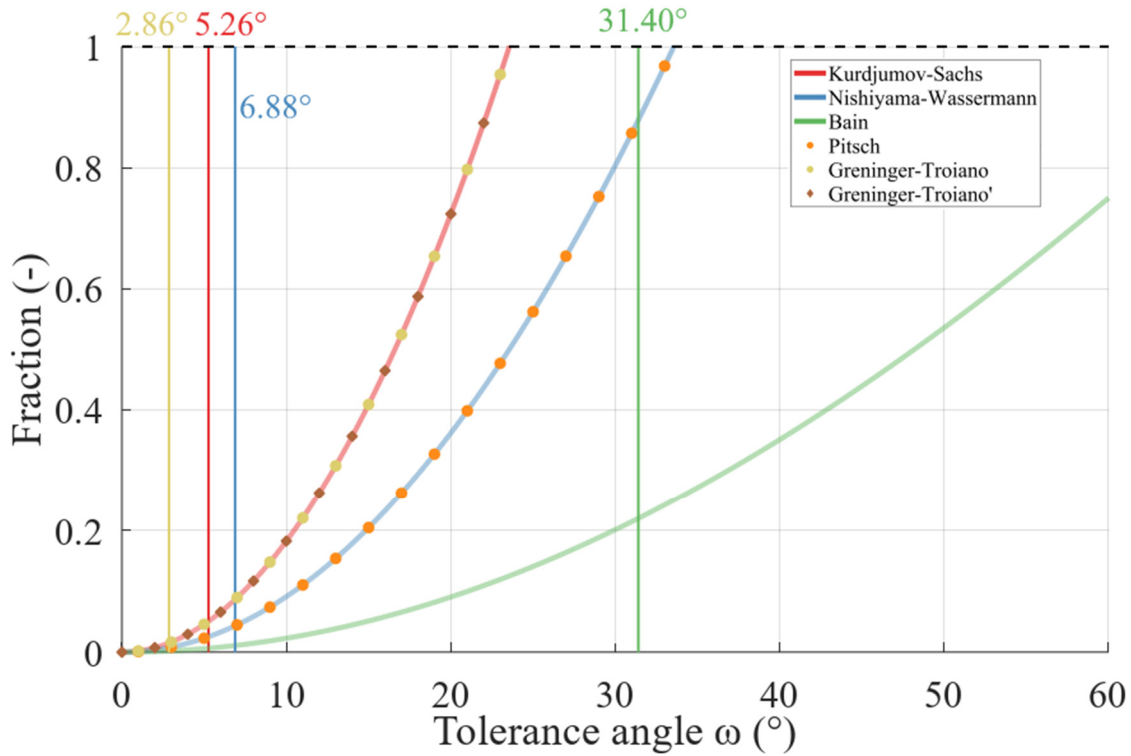A plot of the resulting values is depicted in Figure 5.1.

Figure 5.1: Plot of the result of geometric calculation for the fraction of orientations as a function of the tolerance angle based on Eq. 5.9 (or Eq. 5.10 and Eq. 5.11). The angles up to which these results are valid are marked using the corresponding colors. Both ORs and the KS OR result in the same probabilities. The NW and Pitsch OR do also produce the same probabilities which are valid for tolerance angles up to 6.88°.

This equation is only valid for $f_{KS,norm}$ if the tolerance angle ω is smaller than half of the minimal intervariant misorientation angle (i.e. 5.25°). The domes start to overlap for tolerance angles larger than that angle. It can also be applied for the GT and the GT' OR but the tolerance angles are then restricted to angles smaller than 2.86°. The corresponding equation for the NW and Pitsch OR with $N_V = 12$ can then be calculated by

$$f_{NW,norm} = 6\,(1 - \cos\omega) \hspace{3cm} \text{Eq. 5.11}$$

for tolerance angles smaller than 6.88°. A plot of these functions for all ORs considered here is shown in Figure 5.1. It can be seen that the result for the different OR is only dependent on the tolerance angle and the number of variants N_V which may be formed by the OR. This results in the same curves for the KS, GT, GT' OR. The same is the case for the NW and Pitsch OR.

5.4   Monte Carlo Approach

The situation becomes more complex for larger ω: The variants of most ORs are clustered (e.g. for the KS OR in Bain groups). Therefore, the intervariant misorientation angle is often relatively small for a group of variants ($\sim 10.5°$ for KS). This causes the domes on the unit sphere to overlap, so that no simple analytical expression (counting the areas of the domes) can be found for the total surface formed by these overlapping domes. Figure 5.2 shows a pole figure of random orientations that fulfill Eq. 5.5 for a tolerance angle ω of 2° (a) and 10° (b).

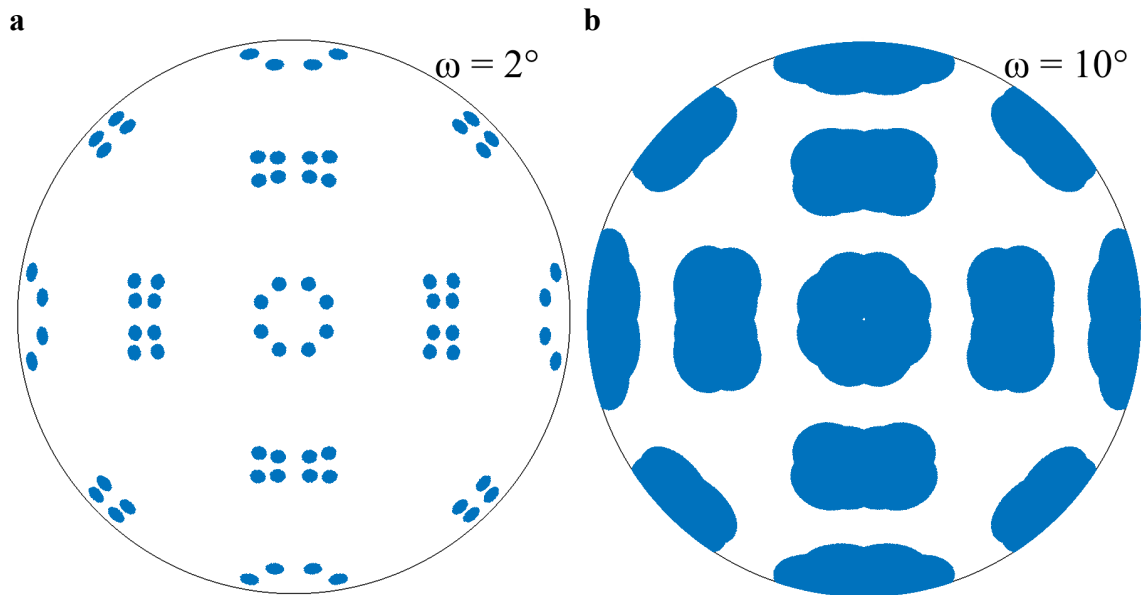**Figure 5.2: a)** Orientations fulfilling the KS OR assuming a tolerance angle of $\omega = 2°$. **b)** Orientations fulfilling the KS OR assuming a tolerance angle of $\omega = 10°$ calculated from random orientations. The tolerance angle is larger than 5.25° causing the circles around the poles to overlap.

In order to circumvent the complications arising from the domes overlapping a more general approach was taken for the calculation of these probabilities: The criterion defined above in Eq. 5.5 was applied to a random uniform texture for several well-established ORs and varying ω. Random orientation pairs (α and γ) were generated and the criterion was applied. This was done for several tolerance angles. The calculation of theses probabilities was performed using an MTEX feature which produces random orientations. The abort criterion for this Monte-Carlo (MC) algorithm needs to account for the fact that the convergence of the resulting probability is dependent on the tolerance angle ω. Therefore the abortion criterion was defined by limiting the number of orientations fulfilling the criterion to 10^6. This results in low calculation times for large tolerance angles (seconds) and very long calculation times for low tolerance angles (up to several days).

The resulting probabilities are shown in Figure 5.3. It shows that the fraction of orientations fulfilling Eq. 5.5 strongly depends on the OR considered and the tolerance angle ω. It further shows that the probabilities for the KS OR are larger than those for the other ORs for all tolerance angles. This means that the KS OR has the highest probability to be calculated from a set of misorientation data for any tolerance angle larger than the minimum intervariant misorientation angle of the ORs under consideration.

The evaluation also shows that the probabilities for the NW and Pitsch OR are the same. The reason for this is that the Pitsch OR is the inverse of the NW OR:

$$f(\omega) = \left(f(\omega)\right)^{-1} \qquad \text{Eq. 5.12}$$

The same is obviously the case for GT and inverse GT (GT') orientation relationships. A comparison between the calculation of these probabilities using the geometrical method shown in Figure 5.1 to the results using the Monte-Carlo method shows that the probabilities do not only depend on the number of variants formed by the OR but also on the intervariant misorientation angles. However, this is only the case for tolerance angles larger than half of the minimum intervariant misorientation angle.
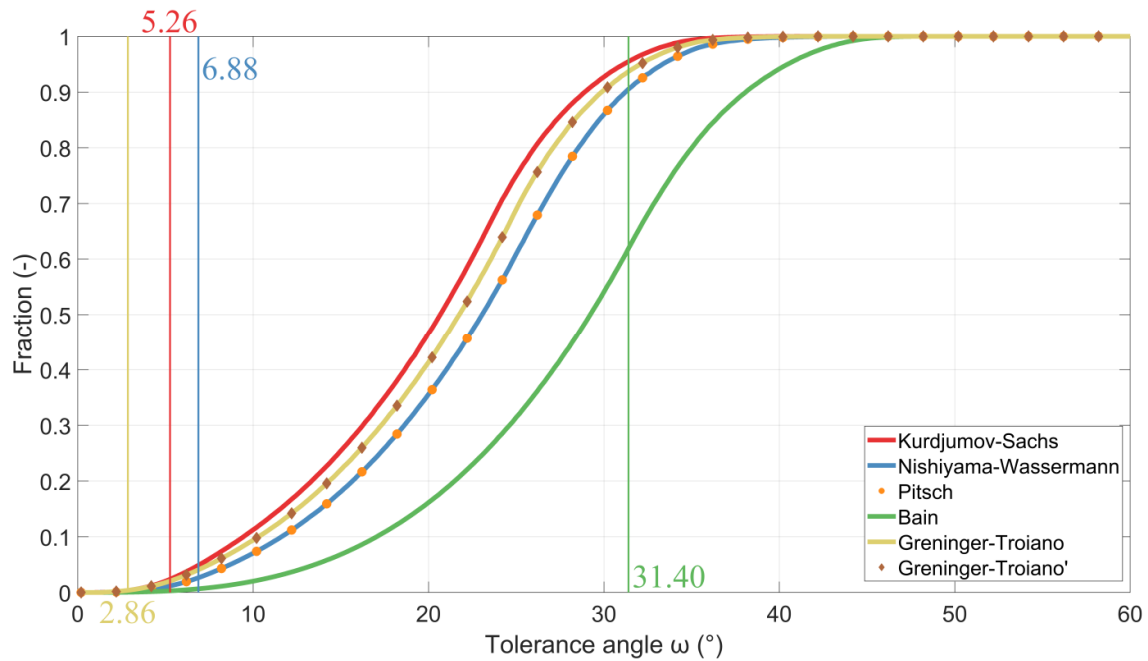
Figure 5.3: Probability of a random orientation pair to fulfill Eq. 5.5 for the KS, NW, GT, inverse GT, Pitsch and Bain OR as a function of the tolerance angle ω. The abort criterion used was 1,000,000 orientation pairs fulfilling the condition.

The probability of an OR to describe a random misorientation under a certain tolerance angle is dependent on the coverage of the unit sphere by the variants of this OR i.e. the number of variants N_V of the OR and the minimum intervariant misorientation angle.

A rather theoretical question arises from this evaluation if an OR can be found that exhibits higher probabilities than the KS OR for any tolerance angle. The requirements for this OR would be to have 24 variants and a minimum intervariant misorientation angle which is as big as possible in order to cover as much area as possible on the unit sphere.

A grid of misorientations in the $m\bar{3}m - m\bar{3}m$ misorientation space with a resolution of 0.2° was generated and ORs were calculated from these misorientations resulting in more than $1.9 \cdot 10^7$ individual ORs. The minimum intervariant misorientation angle and the number of variants N_V were then calculated for all of these ORs. The maximum angle of these intervariant misorientation angles was found to be 43.4°. The OR exhibiting maximum intervariant misorientation angle is close to:

$$\{31\bar{2}\}_\gamma \parallel \{2\bar{1}\bar{3}\}_\alpha$$
$$\langle 1\bar{1}1 \rangle_\gamma \parallel \langle 1\bar{1}1 \rangle_\alpha$$

Eq. 5.13

This OR can describe any set of scattered fcc-bcc orientation pairs equal or better than every other OR for any tolerance angle ω.
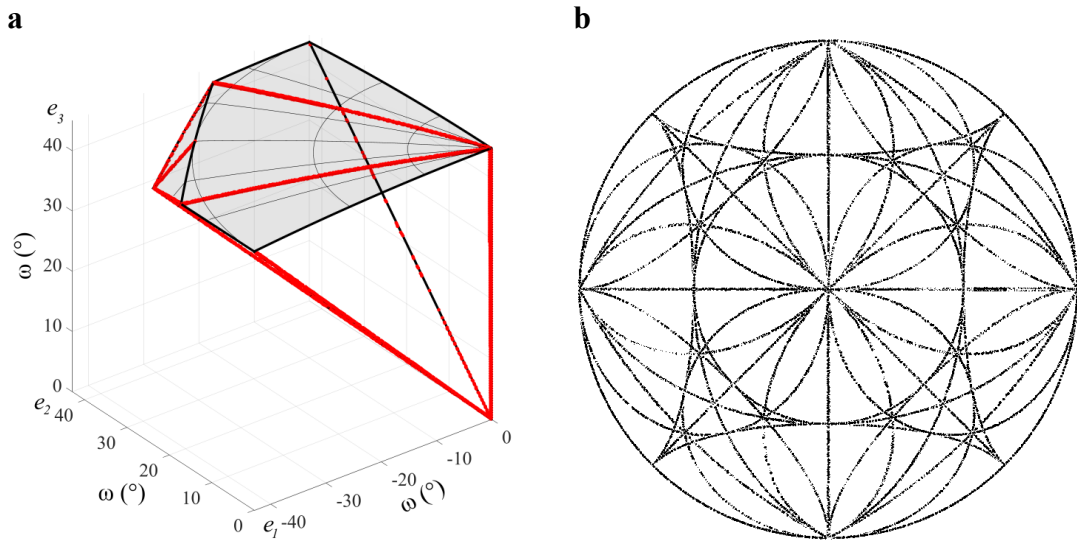

Figure 5.4: a) Complete **$m\bar{3}m - m\bar{3}m$** FZ in 3D misorientation space. The ORs marked in red result in less than 24 variants. All other ORs contained in the FZ producing 24 variants are not shown. **b)** Visualization of the same ORs on a (100) pole figure: Resulting bcc orientations which result from a fcc (001) [100] orientation.

The calculated number of variants N_V for all ORs in the 0.2° grid showed that not all ORs on the edge of the misorientation space result in less than 24 variants. Only 0.037 % of all ORs were found to produce less than 24 variants. These ORs are marked in Figure 5.4a with red dots in 3D misorientation space in the fundamental zone (FZ) for $m\bar{3}m - m\bar{3}m$. It can be seen that these ORs fall onto distinct misorientations on the edge of the fundamental zone. The number of variants formed by a certain OR is dependent on the symmetries of parent and product phase, which is constant for this evaluation. But the number of variants is also dependent on the OR itself: The number of variants is reduced if the rotation describing the OR is coupled to any of the rotational symmetry group elements which are common to those of parent and product phase [369], [370]. This is illustrated in Figure 5.4b where all ORs which produce less than 24 variants (red dots in Figure 5.4) are plotted in a (100) pole figure.

6 Martensite Formation in EUROFER Steel

EUROFER steel is a reduced activation martensitic steel which is still part of an ongoing materials development project of the European fusion materials community. It will be used as a structural material for future fusion reactors (ITER, DEMO). The alloy was optimized for resistance against irradiation damage and reduced long-term activation potential against radioactivity. A large number of various studies were performed regarding properties and processing of EUROFER steels due to the large interest of the scientific community.

The strength and ductility of these reduced activation ferritic/martensitic (RAFM) steels are direct consequences of the martensitic microstructure with its hierarchical structure. This microstructure was extensively investigated in the past using the EBSD technique. These studies focused on martensite formation, orientation relationship and Prior Austenite Reconstruction (PAR). The vast amount of studies on EUROFER steels combined with the defined condition of the lab scale production make this material a good candidate for this experiment. In addition, the low critical cooling rate for martensite formation allows for the direct *in situ* observation of the transformation. The aim of this research is a through process characterization of the microstructural development of the material during a heat treatment. In this chapter, the ferrite microstructure and the austenite microstructure as well as the final martensitic microstructure are investigated.

6.1 Experimental

The material chosen for the experimental investigation is a 8.7Cr steel of the EUROFER family. Its composition is given in Table 6.1.

Element	Fe	Cr	C	Mn	V	N	W	Ta
wt%	balance	8.7	0.0583	0.0223	0.353	0.0465	1.07	0.100

Table 6.1: Composition of the investigated steel.

The starting point for the heat treatment is a ferritic/pearlitic microstructure which was produced by very slow cooling (cooling rate ca. 12 mK/s) from austenite in the *ex situ* device (cf. Chapter 3.3). The sample was then prepared for EBSD by grinding and polishing, finishing with a vibratory polishing step. The sample was then mounted onto the heating stage. Before heating, a reference orientation on a gold wire was fixed onto the sample and measured to account for changes of the orientation of the stage due to thermal expansion (cf. Chapter 4.4). Four square shaped markers were produced on the surface of the sample using a FIB (FEI Nanolab Nova 200). Finally, an EBSD scan (313 µm x 313 µm and 1 µm step size) of the ferritic microstructure covering the markers was performed.

The sample was then heated with a rate of 1 K/s to 980 °C for full austenitization. The relative low heating rate of 1 K/s was applied to produce a homogenous microstructure. After holding the sample for 10 min at this temperature the reference orientation on the gold wire was measured again. Then an EBSD scan on a larger area (2500 μm x 2500 μm and step size 10 μm) in the vicinity of the markers was performed. After that, a detailed EBSD scan (313 μm x 313 μm and 1 μm step size) of the area between the markers was performed. Finally, the sample was quenched by setting the output of the power supply to zero causing the temperature to decrease. The whole temperature profile of the sample is shown in Figure 6.1a. The temperature development during quenching is shown in Figure 6.1b: The average quenching rate was calculated by a linear fit in the range from maximum temperature to 200 °C. The average quench rate was found to be -5.19 K/s. The maximum quenching rate was determined by differentiation and was found to be -19 K/s.

The surface of the sample was continuously observed during cooling using the SE detector. This generated a sequence of images of the surface during martensite formation. An area of ca. 510 μm x 440 μm was observed. The image sequence was stabilized (shifted to compensate for eventual drift) due to heavy drift arising from the change in temperature. This reduced the size of the observed area to ca. 470 μm x 345 μm. An EBSD scan of the martensitic microstructure was performed after the sample reached room temperature and the reference orientation on the gold wire was measured again. A detailed EBSD scan of the martensitic sample was performed in a Zeiss Merlin SEM (178.5 μm x 150 μm and step size 0.25 μm). The surface relief of the sample was measured using Laser Scanning Confocal Microscopy (LSCM) in a Keyence VK-9700 microscope.
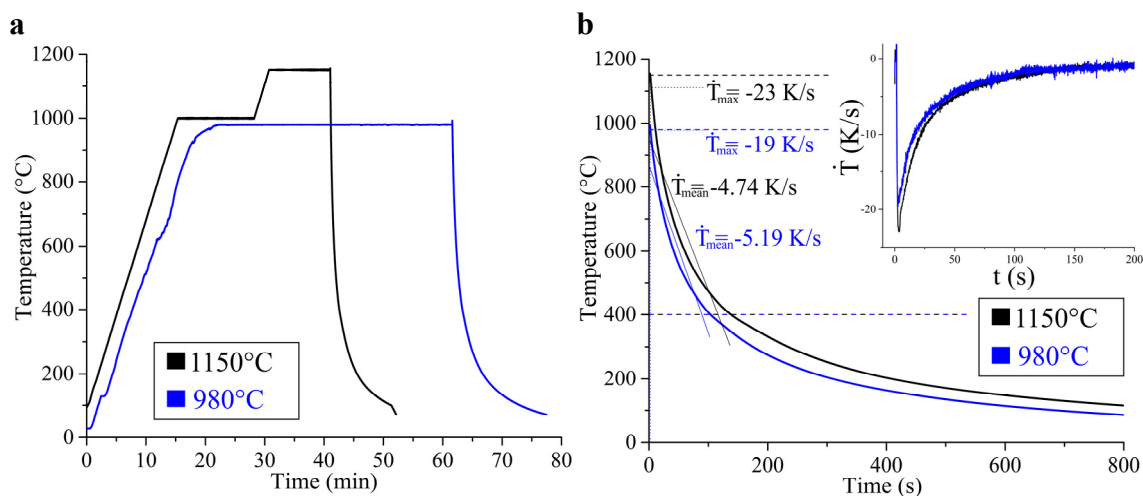
Figure 6.1: Temperature profile of thermal treatment procedures: **a)** Temperatures of the samples measured during the heat treatments for the sample which was quenched from 1150 °C (in black) and from 980 °C (in blue). **b)** Measured temperatures of the sample which was quenched from 1150 °C (in black) and which was quenched from 980 °C (in blue). The average (calculated from a linear fit from maximum temperature to 400 °C) and maximum quench rates are shown.

The temperature was monitored during the experiment using a two-color pyrometer equipped with a glass fiber feedthrough. The heater was controlled by a PID using the temperature measured by a thermocouple inside the heater. This temperature value was then corrected using the difference of the temperature measured by thermocouple and the pyrometer. This was done because of the better signal to noise ratio of the thermocouple measurement enabling an accuracy of $\Delta T < 0.1$ K for temperature control (minimizing drift).

A second experiment was conducted in order to study the influence of the austenitization temperature and austenite grain size on martensite formation. The sample had the same composition but was heated with a heating rate of 1 K/s first to 1000 °C and after 13 min to 1150 °C. Pronounced grain growth was observed at this temperature. This was evident from the motion of grain boundary grooves on the surface which was observed using the SE detector. An EBSD scan of a larger area (1000 µm x 1000 µm) was performed at this temperature (step size 3 µm). The sample was then quenched as well by switching of the heater. The development of the temperature is also shown in Figure 6.1b. The average quenching rate between 1150 °C and 400 °C was found to be -4.74 K/s which is similar to the one which was achieved for the sample which was quenched from 980 °C. The maximum quenching rate was -23 K/s.

Again the surface of the sample was observed using the SE detector but it was not possible to observe the transformation sequence due to the weak relief formed on the surface. An EBSD scan of the final martensitic microstructure was conducted in the Zeiss Merlin SEM (537.5 µm x 544.5 µm and step size 0.5 µm).

TEM lamellae were prepared from both samples for more detailed characterization of the bulk microstructure. The lamellae were prepared by FIB in regions in which EBSD scans were performed before. The lamellae were characterized in the Zeiss SEM with an acceleration voltage of 30 kV in STEM mode. Additional Transmission Kikuchi Diffraction (TKD) experiments were performed for the sample which was quenched from lower temperature (5.6 µm x 4.5 µm with a step size of 5 nm).

The sample that was heated to 980 °C was carefully polished using a vibratory polisher. Subsequently, an EBSD scan of the surface was performed on the sample in the region between the FIB markers. This z-sectioning allows for the characterization of the bulk microstructure with better statistical relevance compared to the TEM lamellae. This procedure was overall repeated three times. The depth was determined each time using LSCM measurements on the FIB markers. The EBSD scan after the last sectioning could not be evaluated because it was deeper than the FIB markers so that the depth could not been measured and that the relevant region could not be found and connected to the previous scans.

6.2 Results

The initial ferrite microstructure at room temperature is shown in Figure 6.2a. It shows large ferrite grains (grain size 160.54 μm) with very low orientation gradients. The cementite of the pearlitic regions is too fine to be indexed in this EBSD scan. No distinctive texture was present in the ferritic/pearlitic sample after the heat treatment which was applied to achieve a purely ferritic/pearlitic microstructure.
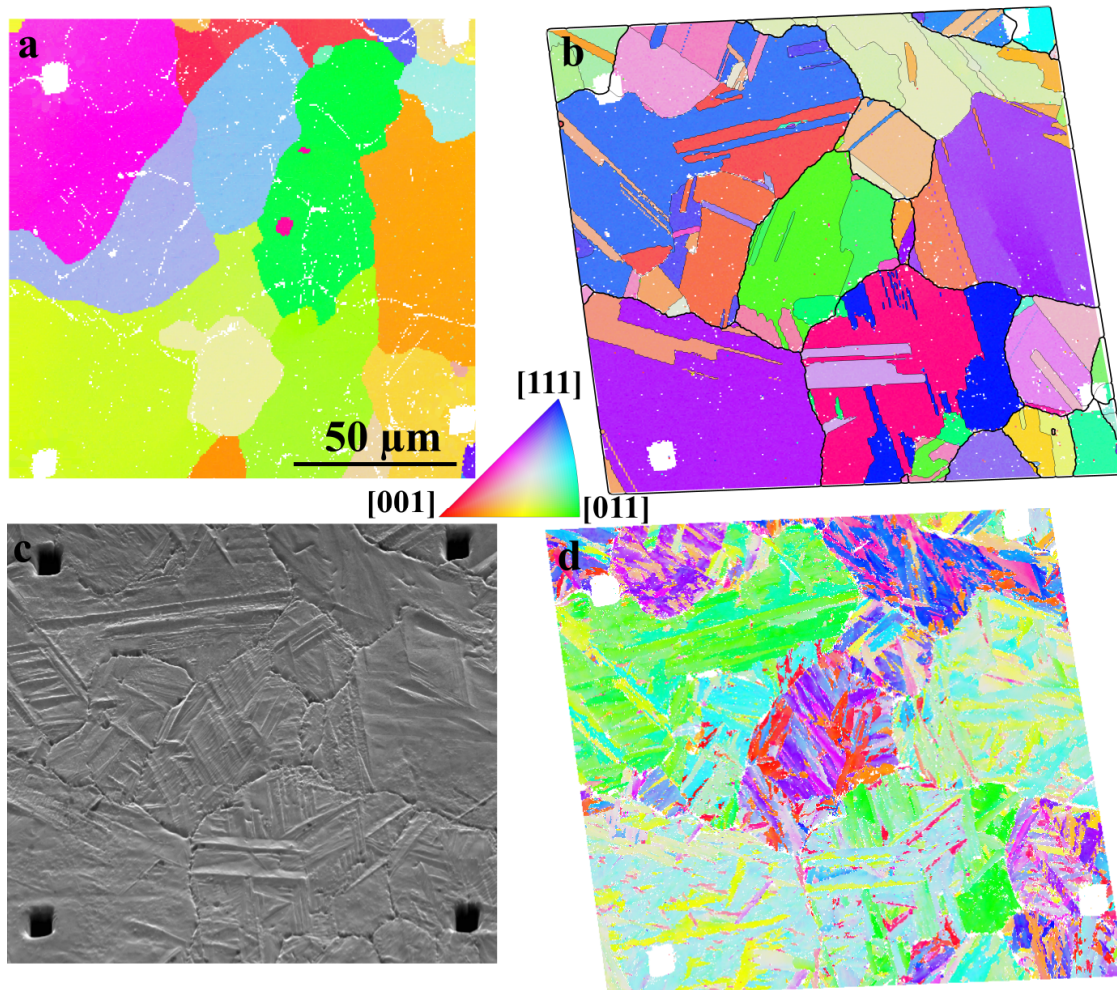

Figure 6.2: a) (001) orientation map of the ferritic sample before the *in situ* experiment. **b)** EBSD map of the same location on the sample at 980 °C. The sample has fully transformed to austenite. Twin boundaries are marked with fine black lines and grain boundaries with thick black lines. **c)** Secondary electron image of the relief on the surface of the sample after quenching to room temperature. **d)** Orientation mapping of the martensite microstructure after quenching. a), b) and d) show orientation mappings of the same location on the sample in different states.

The corresponding austenite microstructure at 980 °C is shown in Figure 6.2b. Grain boundaries are outlined by thick black lines whereas twin boundaries are marked by fine black lines. The austenite microstructure consists of large grains (grain size 93.49 μm) with very low orientation spread. All grains exhibit multiple twins that vary in size. The twins often form parallel structures and are always connected to at least one grain boundary or twin boundary. Some very fine twins exist which are at the limit of being resolved in the coarse scan. It cannot be excluded that even finer twins exist in the microstructure which could not be mapped due to the relative large step size. A similar austenite microstructure can be observed for the sample which was heated to 1150 °C: Figure 6.4a shows, that all austenite grains contain a

large number of twins. One large austenite grain formed in the center of the orientation map. This grain is surrounded by smaller austenite grains.

Figure 6.3b shows an SE image of the surface of the sample which was heated to 980 °C before quenching. The microstructure of the sample can be already recognized in the SE image: Grain boundaries are clearly visible because of thermal grain boundary grooving. The upper triangle in Figure 6.3b marks a grain boundary groove. The lower triangle highlights a groove associated to a twin boundary. These boundaries can be distinguished by the depth of the groove. The grooves connected to grain boundaries appear to be deeper than the grooves connected to twin boundaries. This is caused by the difference in interfacial energies. The twin boundaries exhibit low interfacial energies compared to grain boundaries exhibiting random misorientations.
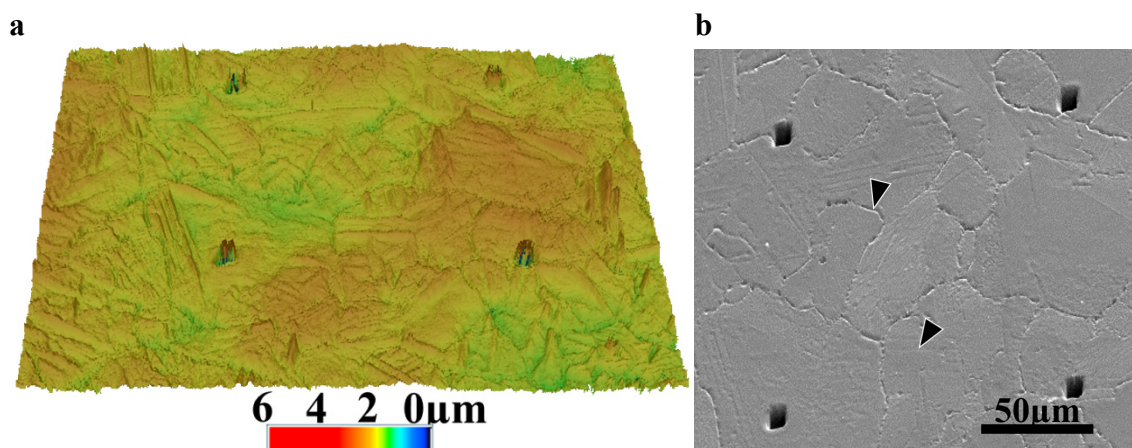

Figure 6.3: a) Height profile measured by LSCM after quenching. **b)** SE image of the surface at 980 °C. The upper triangles mark a grain boundary groove. The lower triangle marks a twin boundary groove.

The microstructure of the martensite formed at the same location on the sample after quenching is shown in Figure 6.2d. The surface of the sample is shown in Figure 6.2c. It shows a relief which is characteristic for the martensitic transformation. This relief shows the spatial orientation of the martensite laths which are also recognizable in the EBSD scan. The austenite grain boundary grooves are still visible on the surface of the quenched sample. These grooves also cause a decrease in EBSP quality close to the prior austenite grain (PAG) boundary. The PAG boundaries are easily recognizable from the EBSD scan. The martensite microstructure consists of laths which are predominantly arranged parallel to each other. Each lath exhibits a strong orientation spread perpendicular to the long edge.

The microstructure of the sample which was heated to 1150 °C exhibits a finer martensite microstructure after quenching. Very long martensite laths are mostly arranged in parallel to each other especially in the center of the scan which belongs to the large austenite grain. The locations of twins are evident from the change of the spatial orientation of the laths by 60°.

Figure 6.3a shows a 3D reconstruction of the surface of the sample obtained from LSCM. It shows that the relief connected to different martensite laths varies in height and that a maximum in height often roughly coincides with the edge of a lath. The value of the maximum height of the relief connected to the martensite laths ranges between 1 μm and 3 μm. The spikes which are visible around the FIB markers are a result of reflections at the edges of the FIB markers. The height of the surface relief of the second sample was found to be smaller than the lateral resolution limit of the LSCM.
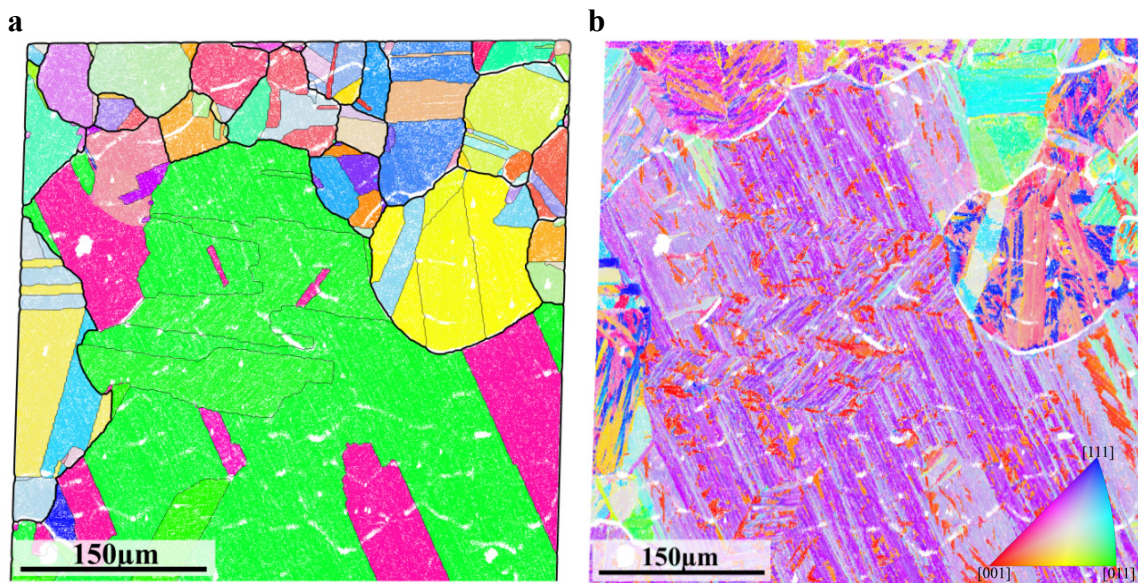
Figure 6.4: a) OM of the austenite microstructure at 1150 °C. Grain boundaries are plotted as thick black lines and twin boundaries as fine black lines. **b)** OM of the resulting martensite microstructure at room temperature after quenching.

Figure 6.5 shows selected secondary electron images of the image sequence which was obtained during the transformation after the heater was switched off. The surface relief of the sample can be already identified shortly before the martensite start temperature is reached in Figure 6.5a. This relief which is already visible before any martensite nucleates is caused by thermal grooving at the grain and twin boundaries. Figure 6.5b shows the formation of the first martensite lath which emerges from outside of the observed region. Figure 6.5c shows the formation of a surface relief outlining a martensite lath which forms first in the austenite grain during the transformation. Figure 6.5d-g show the subsequent formation of laths until the final state is reached in Figure 6.5h. The first martensite lath nucleated at 492 °C. Single isolated nucleation events occurred during further cooling in all grains. The nucleation of the first lath in an austenite grain occurred always at a twin boundary. The sequence shows, that twin boundaries are also preferred nucleation sites after martensite laths are already present in the austenite grain. At 430 °C the transformation was finished.
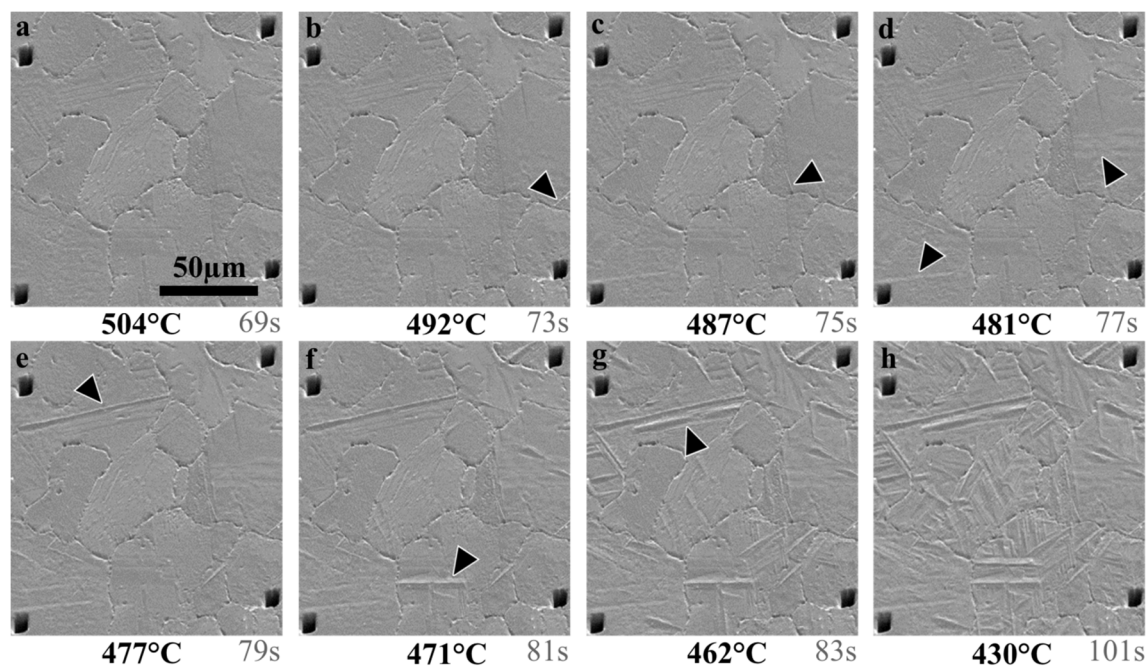
Figure 6.5: Observation of the development of the surface relief during quenching inside the SEM. The temperature and time after start of cooling is indicated. **a)** Shows the initial state before martensite start is reached. The surface relief visible here is caused by thermal grooving originating from diffusional processes at interfaces. **b)** The triangle shows the formation of surface relief caused by the first lath formed. **b)** – **g)** show the further progression of the transformation. **h)** Shows an image of the surface after martensite finish is reached.

A TEM sample was prepared by FIB milling to investigate the bulk microstructure in addition to the microstructure on the surface. The position where the lamella was cut is marked in Figure 6.6c. The area was selected just outside of the observed region to preserve the microstructure for further investigation. The FIB markers on the right side of the analyzed area are marked with arrows in Figure 6.6c. BF STEM images were captured using the STEM detector of the Zeiss Merlin SEM at 30 kV acceleration voltage. A STEM image showing individual martensite laths just beneath the surface is shown in Figure 6.6b. It shows that the laths extend from the sample surface towards the bulk of the specimen. The laths are arranged in parallel and have a thickness of ca. 500 nm. A high dislocation density present inside the laths can be seen in the BF STEM image shown in Figure 6.6d. Figure 6.6a shows a corresponding transmission Kikuchi diffraction (TKD) map of the sample at the same position as the STEM image in Figure 6.6b. The map shows that three different variants are present at the surface in this region and reveals the orientations of the martensite laths.
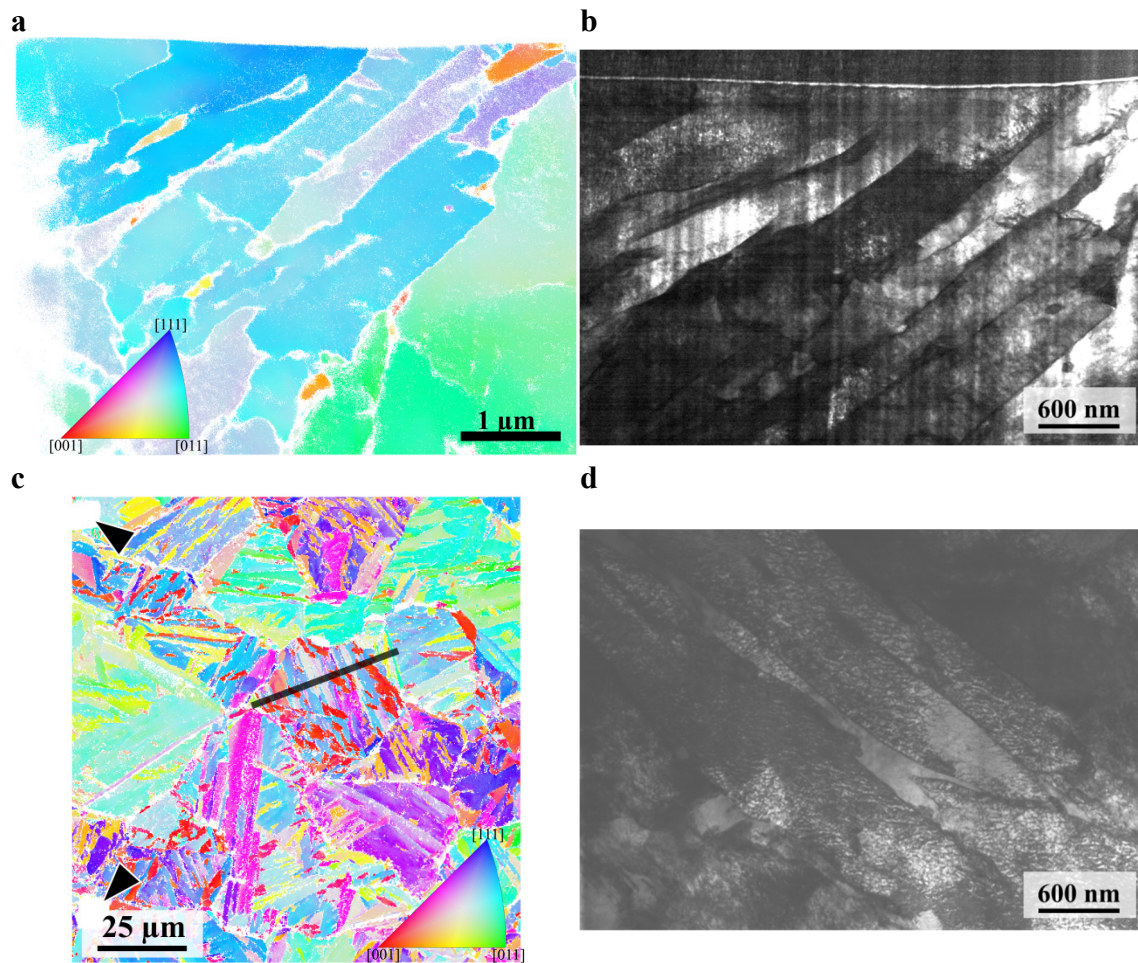
Figure 6.6: a) shows a (001) OM from a TKD scan of the lamella. **b)** Bright field STEM image of the lamella showing martensite laths. **c)** (001) OM of the location where the TEM sample was extracted. The lamella was chosen to be oriented perpendicular to the martensite laths inside the PAG. **d)** BF STEM image showing high dislocation densities inside the laths.

A second TEM lamella was prepared by FIB in order to observe the martensite morphology away from the surface of the second sample which was quenched from 1150 °C. The lamella was cut perpendicular to the martensite laths. BF-STEM images were obtained using the STEM detector of the Zeiss Merlin microscope. The resulting scans are shown in Figure 6.7. Figure 6.7a shows two groups of laths which are both arranged in parallel. The laths vary in size from ca. 10 nm to 400 nm. This could be the result of different spatial orientations of the laths inside the TEM lamella. Figure 6.7b shows one group of laths. All laths are arranged parallel to each other. A high dislocation density is evident from the tangled structures inside the individual laths.
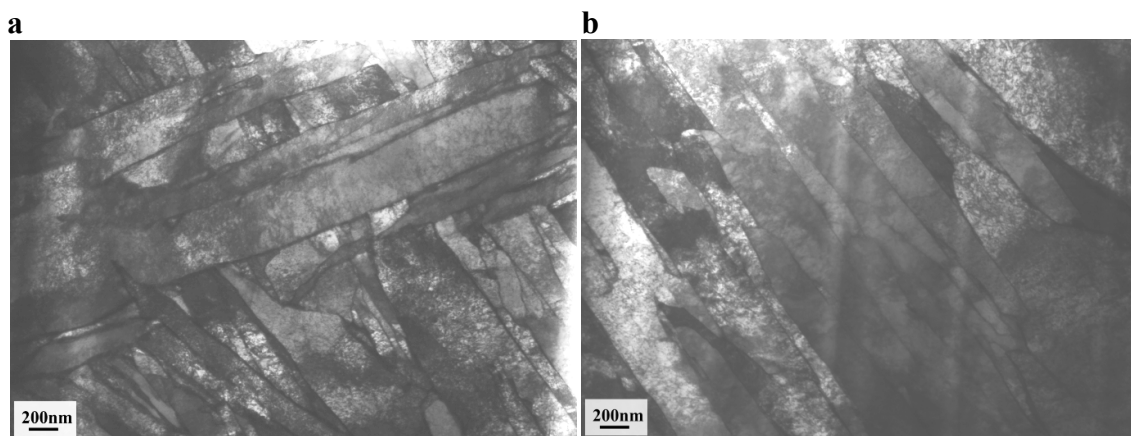
Figure 6.7: Bright field STEM images prepared from the second sample which was quenched from 1150 °C: **a)** BF-STEM image showing the arrangement of the martensite laths perpendicular to the surface. The laths form in packets of parallel oriented laths. The thickness/width of the laths seems to vary between ca. 10 nm and 400 nm. **b)** BF-STEM image showing one packet of parallel laths. The laths of this packet exhibit similar dimensions. A high dislocation density inside the laths is visible.

Three z-sections through the samples were prepared in order to study the influence of the free surface on the martensitic transformation: The result of this sectioning can be seen in Figure 6.8. The morphology of the martensite formed on the surface is not significantly different compared to the morphology which can be observed in the bulk. This is the case for the microstructure shown in Figure 6.8a and Figure 6.8b. Mainly a change of the cross section of the PAGs can be observed. This corresponds to the three-dimensional shape of the austenite grains.

Figure 6.8: EBSD scans of the sample after removal of surface layers. **a)** Orientation mapping for $z = 2$ µm. The orientations were aligned to the orientations in Figure 6.2d using a procedure outlined in the discussion. **b)** Corresponding mapping of the martensite orientations for $z = 5$ µm.

6.3 Discussion

The results of the *in situ* experiment are discussed in the following sections. Therefore, the EBSD scans of the sample in different states are al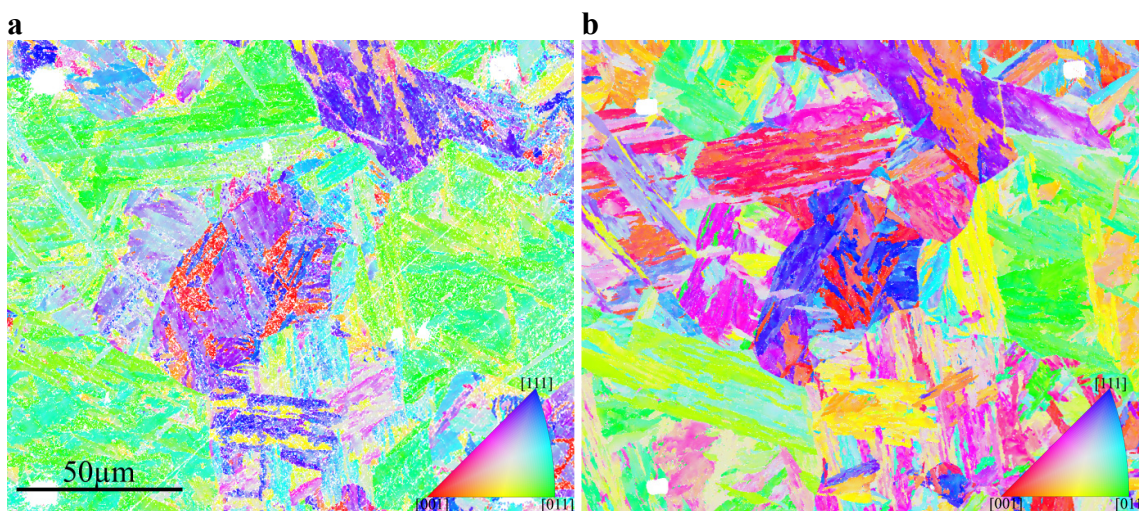igned using the FIB markers (cf. Chapter 4.3) and the rotations calculated from the reference orientations of the gold wire (cf. Chapter 4.4). An interpolation step (cf. Chapter 4.6) is used to account for the different step sizes of the scans. Orientations and parent orientations can be connected to each EBSD data point using this procedure (cf. Chapter 4.7). The orientation pairs generated are used in the following discussion to calculate the dominating orientation relationship, variants and their misorientations. The technical details of these methods have been outlined in Chapter 4.

6.3.1 Austenite Microstructure

A surprisingly low number of EBSD studies on the austenitic microstructure of steels can be found in the vast literature on the topic of ferritic steels. The author of this study is only aware of three studies [20], [24], [332] which mainly focus on the α-γ-α transformation. Therefore, the austenite microstructure is shortly discussed here. The grain size of the austenite microstructure was found to be smaller than the ferrite grain size even when twin boundaries were ignored. This grain size is larger than the grain sizes achieved by Danon et al. [371] with a similar alloy and a similar heat treatment but starting from a martensite microstructure. The resulting austenite grain size achieved in this work appears to be surprisingly low taking into account the grain size of the material at the start of the experiment. This effect may be caused by the stabilization and pinning effect of TaC and VN precipitates which are reported to segregate to austenite grain boundaries [372], [373]. This pinning effect is also retarding austenite grain growth effectively so that no significant grain growth was detected during the holding time at 980°C. Further heating to temperatures above 1150°C results in the dissolution of TaC precipitates and rapid grain growth [374]. This was observed for the second sample. Figure 6.4b shows lines of non-indexed measurement points in the upper region of the map. These lines are the result of thermal grooves caused by austenite grain boundaries suggesting that the large grain at the bottom of the map grew at the expense of the smaller grains in the top of the map.

Figure 6.2b shows that the microstructure contains a large amount of twin boundaries. The fraction of twin boundary length amounts to 74.8 % of total interface length. The size of the twins exhibits a large variation: Some very large twins are located at grain boundaries. But also very fine twins are present exhibiting thicknesses that are close to the step size of the EBSD scan. The austenite grains exhibit a very low orientation spread resulting in a mean granular orientation spread smaller than 0.01°. The texture index (equal to 1 for random texture and →∞ for single crystal) determined from the ODF which was calculated from the large EBSD scan was found to be 1.028 indicating that the austenite phase does not exhibit any distinct texture.

6.3.2 Martensite Microstructure

The combination of the austenite orientation map with the martensite orientation map enables an in-depth characterization of the martensite microstructure. The calculation method for martensite variants was already described in detail in Chapter 4.8.

The calculation is performed for every measurement point of the EBSD grid and for all of the established ORs (Bain [208], KS [204], NW [375], Pitsch [207], GT [206], GT' [206]). The result of the calculation of the KS variant number can be seen in Figure 6.9a and the result of the calculation of the corresponding misorientation angles (misorientation angle between the measured product orientation and the closest theoretical product orientation according to the KS OR) is shown in Figure 6.9b for the sample which was

heated to 1150 °C. Measurement points corresponding to a single variant form elongated domains which correspond to martensite laths in the mapping of the variant number. A mapping of the KS variant numbers for the sample which was heated to 980 °C is shown in Figure 6.11a. Domains sharing the same KS variant number tend to be longer for the sample which was quenched from 1150 °C compared to the same mapping for the sample which was quenched from 980 °C.

A statistical evaluation of the frequencies of these variants is shown as a histogram in Figure 6.10a for the sample which was heated to 980 °C and Figure 6.10b for the sample which was heated to 1150 °C. It reveals that the 24 variants of the KS OR are not equally distributed. This effect is called variant selection. The variant selection strength k_{VSS} was calculated from the distribution of KS variants. A description of the definition of this value can be found in Chapter 4.9 (p. 47). The variant selection strength was found to be $k_{VSS} = 0.362$ for the first sample that was quenched from 980 °C. The variant selection strength for the sample that was heated to 1150 °C is $k_{VSS} = 0.469$.

This shows that stronger variant selection occurred for this sample than for the sample which was heated to 980 °C during transformation. As there are no mechanical stresses applied to both samples, the cause for this variant selection can only be explained by the presence of the free surface. Variants enabling the accommodation of transformation strains perpendicular to the free surface will be favored. This minimizes plastic and/or elastic accommodation effects that are not directed out of the surface.

The differences in the degree of variant selection between the two samples can be attributed to the larger austenite grain size of the second sample. The longer martensite laths (cf. Chapter 2.1.8.2) lead to a more efficient accommodation of transformation strains through variant selection hence more pronounced variant selection is observed.
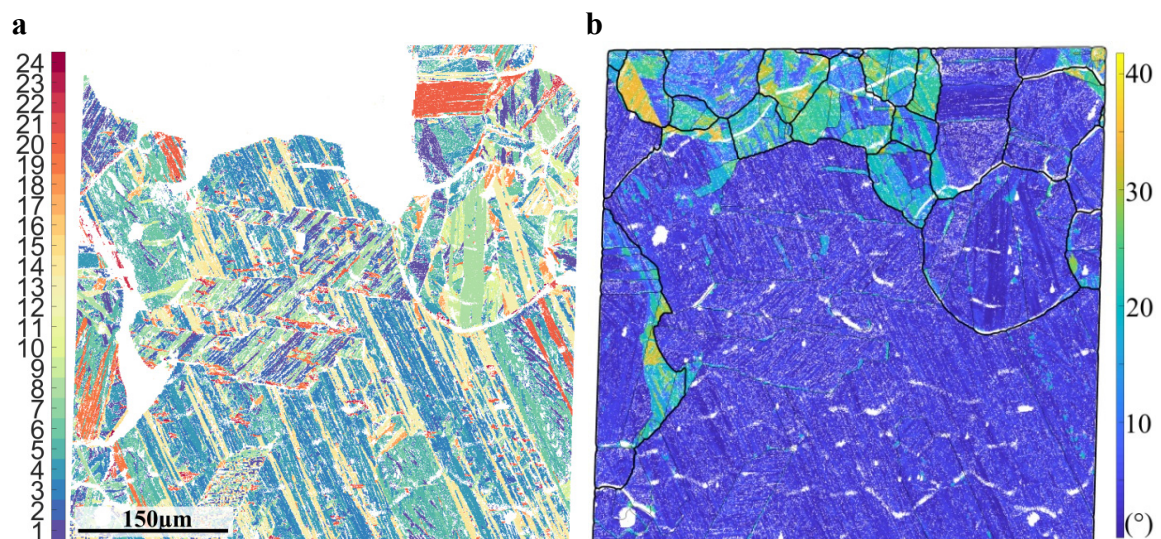
Figure 6.9: a) Mapping of the KS variant number corresponding to the austenite-martensite orientation pair for the sample which was heated to 1150 °C. **b)** Map of the misorientation angle of the martensite orientation to the closest theoretical transformation product variant.

This assumption is further supported by the arrangement of the martensite variants as shown by the variant map in Figure 6.9a: One group of variants which all belong to one CPP packet is predominantly formed. Variants belonging to another CPP packet are situated in between groups of the dominant variants. A direct comparison of the histograms for both samples shows that the qualitative trend of variant selection is very similar.

The differences in variant selection for the two austenite grain sizes suggest that a more pronounced variant selection can be observed for larger austenite grain sizes. The very low height of the surface relief of the sample with more pronounced variant selection additionally implies that variant selection is preferred over the formation of a relief for the accommodation of transformation strains. This indicates that variant selection is preferred over plastic deformation as a way of accommodating transformation strains. The efficiency of variant selection seems to be affected by the geometrical constrains imposed by the austenite grain boundaries.

a

b

Figure 6.10: Histograms showing the frequencies of the KS variants. The red curve shows the mean misorientation angle of the calculated martensite variant based on the austenite orientation to 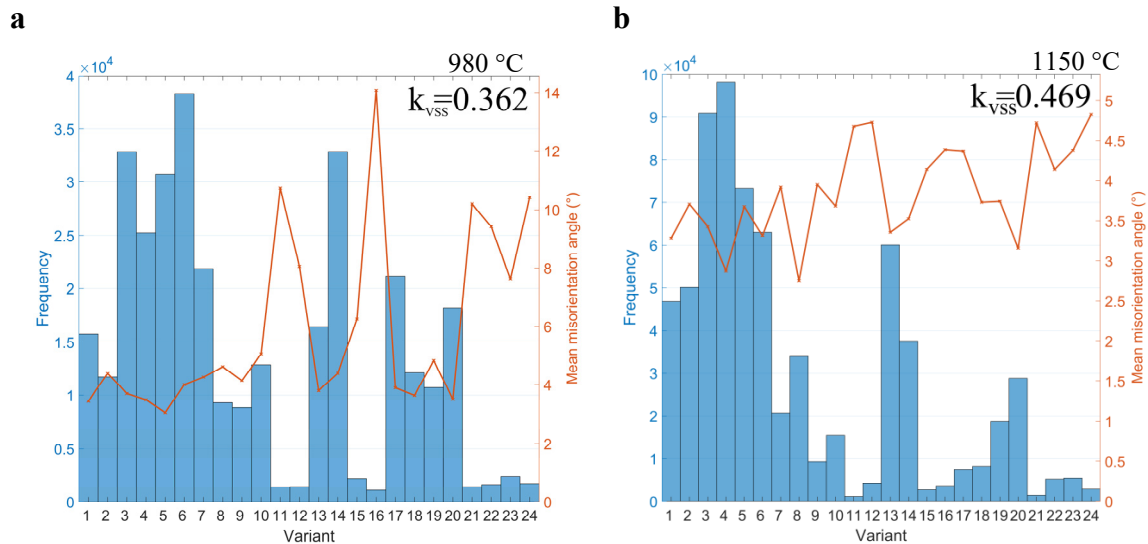the measured martensite orientation for all measurement points of that variant. **a)** shows the histogram for the sample which was heated to 980 °C and **b)** shows the histogram for the sample which was heated to 1150 °C.

Abnormal austenite grain growth of the second sample at 1150 °C did continue in the time between the last HT EBSD scan and quenching. This abnormal austenite grain growth is reflected in the calculation of the misorientation of the transformation product orientation to the closest theoretical transformation product orientation based on the local austenite orientation and the OR (the KS OR was used here). A large misorientation angle, in comparison to the inner regions of the large grain, indicates that the austenite grain grew into these directions. This can be seen in Figure 6.9b where this misorientation angle is mapped. It shows a low misorientation angle of less than 3° for large parts of the map but also regions with high misorientation angles of more than 20°. This indicates that the grain grew towards the top of the map consuming some of the grains above the large grain (cf. Figure 6.4a) in the time between the last EBSD scan and quenching. A second area exhibiting large misorientation angles can be seen on the left side of the large grain indicating that the grain also grew into this direction. The low misorientation angles around the austenite twins and (more importantly) the change of the spatial orientations of the laths show that, contrary to the grain boundaries, the twin boundaries did not move but remained at their positions.

The grain reconstruction algorithm of the MATLAB/MTEX toolbox [362] was used to generate spatial clusters of single martensite variants resulting in a variant map. In this way a map of regions sharing the same OR is calculated. This procedure enables variant reconstruction without the use of a grain reconstruction algorithm for the martensite microstructure so that the results are not dependent on a threshold angle for the definition of grain boundaries. A detailed description of this procedure can be found in Chapter 4.10. The resulting map is shown in Figure 6.11b: The martensite laths tend to form parallel arrangements consisting of different variants. A comparison between the austenite microstructure and the

martensite variant map shows that the spatial orientation of the laths within this arrangement is determined by austenite twins present in the vicinity of the laths before the transformation. The laths are arranged parallel to these twins in most cases. The variant map shows that they often span the length of the parent austenite grain (PAG). The accommodation of the transformation strain of subsequent laths can be achieved effectively by forming a parallel arrangement.
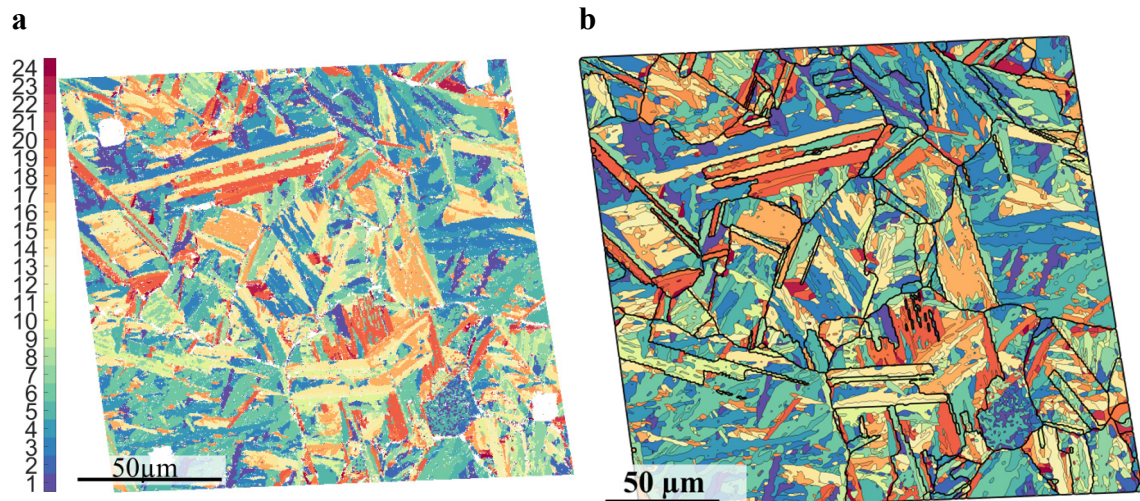

Figure 6.11: a) Map of the KS variant number calculated from the austenite-martensite orientation pairs for the sample which was heated to 980 °C. **b)** Variant map calculated from the austenite martensite orientation pairs using the KS OR. Variant boundaries are plotted as fine black lines and previous austenite grain boundaries are plotted as thick black lines.

An interesting behavior can be observed at parallel austenite twins exhibiting the same orientation: This is illustrated with a section from the variant map (cf. Figure 6.11b) and the corresponding austenite orientation map shown in Figure 6.12a. Each of the laths formed at these twins belong to the same KS variants albeit they form at different temperatures independently of each other. Subsequent laths formed in parallel to these laths also belong in each case to the same variant indicating that a reproducible transformation sequence can occur if the same crystallographic conditions prevail.

Figure 6.12b shows the bivariant histogram of the relative frequency of KS variant pairings for the sample which was quenched from 980 C. Variant pairing analysis for the sample which was quenched from 1150 °C shows the same trend. The calculation procedure for variant pairing analysis is described in detail in Chapter 4.11. The analysis of variant pairing shows two predominant variant pairing tendencies: The first one is a preferred pairing of variants exhibiting a twin relationship resulting in a misorientation angle of exactly 60°. The second one is a preference for minimal misorientation angles. The misorientation angles between the KS variants are shown in Figure 6.12b in the upper triangle. The misorientation angles fall into two groups: One group contains angles between 10.53° and 21.06° and the second contains angles between 47.11° and 60°. The angle of the preferred pairings falls either on the smallest angle of group one or the largest angle of group two (mostly Σ3). The result of the variant pairing analysis is not in accordance with earlier studies by Stormvinter et al. [209] focusing on FeC alloys but closer to the results of a study of variant pairing performed on a 13Cr5Ni steel by Liu et al. [376]. It has to be mentioned that the austenite orientations used for the calculation of martensite variants in these studies (Stormvinter et al. and Liu et al.) were determined solely on the basis of PAR algorithms. The similarity of the variant pairing in this study to the results of the study on a steel with similar composition may indicate that the pairing of variants is strongly influenced by the chemical composition of the alloy.
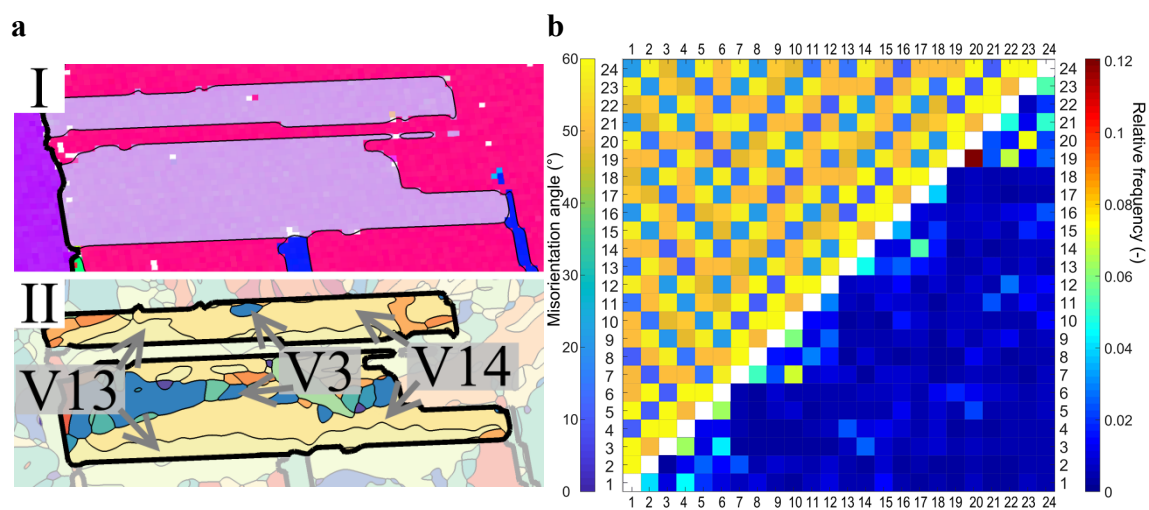
Figure 6.12: a) Shows a section of the austenite orientation map in I) containing two larger twins. II) shows a variant map of the same section after transformation **b)** Color-coded bivariant histogram showing the relative frequency of pairings of martensite variants in the lower right hand side triangle. The upper left hand side triangle shows the misorientation angles of the KS variants and can be used to read the bivariant histogram by using the x=y axis as a mirror plane.

The variant reconstruction approach used in this work allows for an accurate statistical analysis of the martensite microstructure. The mean size of the laths was investigated by principal components analysis. Ellipses are thereby fitted to the laths and the length of the short and long axis as well as an angle describing the orientation of the laths is calculated. Figure 6.11a shows that there are some areas were the orientations cannot be assigned to one or the other variant very well leading to some very fragmented areas. The principal components analysis was therefore applied only to laths exhibiting an aspect ratio larger than 10. The mean lath thickness was found to be 330 nm and the mean lath length 7.2 µm.

6.3.3   Martensite Nucleation

The observation of the transformation sequence for the sample which was quenched from 980 °C on the surface suggests that the martensite start temperature M_S is 492 °C for an alloy of this composition, austenite grain size and the specific applied cooling rate. The martensite finish temperature M_f was found to be 423 °C. No new laths were formed at the surface after this temperature was reached. Raju et al. [377] performed a detailed DSC study on the martensite formation kinetics on an EUROFER steel. They found martensite start temperatures ranging between 387 °C and 507 °C and martensite finish temperatures between 355 °C and 235 °C for an alloy of similar composition. The martensite start temperature is affected by the chemical composition of the alloy but also by austenite grain size and quenching rate. A further contribution to the chemical free energy change during transformation can arise from the free surface: Klosterman and Burgers [378] suggested that for a Fe-Ni alloy martensite at the surface forms 5 K to 30 K above the M_S temperature that was determined for the bulk material. It is evident that the presence of a free surface will lead to a reduction of the driving force due to a reduction of the strain energy associated with the accommodation of transformation strains for the martensite laths. According to Bhadeshia [379] this reduction is in the range of 600 J mol^{-1}.

The location of the nucleation of the first lath in an austenite grain was found to be strongly heterogeneous: every isolated nucleation event occurred at an austenite twin. Nucleation events that did not occur in the vicinity of an austenite twin boundary were connected to previously formed martensite laths and are caused by the autocatalytic effect (cf. Chapter 2.1.8.3) arising from the stress fields of laths that were formed earlier. Some groups of laths were also observed to form instantaneously within the time resolu-

tion of the observation. The observations suggest that twin boundaries act as preferred nucleation sites during martensite formation. This is illustrated in Figure 6.13.
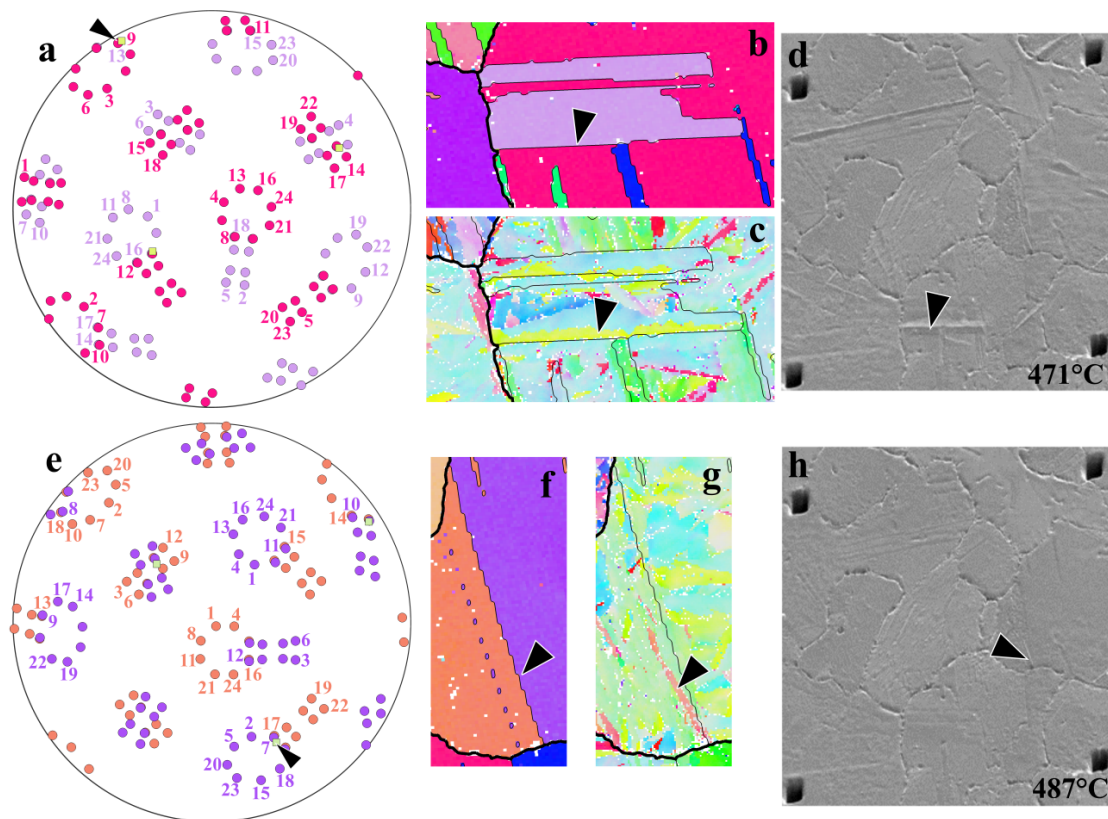

Figure 6.13: Orientation analysis of two nucleation events during the martensitic transformation. **a)** and **e)** Comparison of the orientation of the lath formed at a twin boundary to the KS variants of the crystals connected to the same. **b)** and **f)** show the austenite microstructure around the twin where the lath nucleated in detail. **c)** and **g)** Show the corresponding martensite microstructure formed at this location. **d)** and **h)** SE images of the nucleation events and the relief caused by the formation of the martensite lath.

This strongly heterogeneous nucleation suggests that there may be an effect of the orientations of the twinned crystals on the orientation of the nucleating variant due to the special crystallographic character of the twin interface. The orientations of the variants that nucleate were compared to the theoretical KS products of the two orientations connected to the twin related crystals in order to elucidate any variant selection mechanism active during nucleation. Figure 6.13 shows this comparison for two selected examples. Figure 6.13a and Figure 6.13e depict a comparison of the KS variants of the two twin related austenite crystals with the orientation of the martensite lath nucleated at this twin boundary. The markers indicating the KS variants of the twins are colored according to the orientation of the austenite grains using the same color key as in Figure 6.13b. The small square marker highlights the orientation of the lath formed at this position (marked with a black triangle in Figure 6.13a). The triangles in Figure 6.13b and Figure 6.13f indicate the twins on the austenite orientation maps where the nucleation takes place at 471 °C and 487 °C, respectively. Figure 6.13c and Figure 6.13g show the corresponding section of the final martensite microstructure. Both laths formed in the nucleation events are marked by black triangles. The relief related to the nucleation is shown in Figure 6.13d and Figure 6.13h. It reveals that the lath in Figure 6.13d is not formed alone. A second lath parallel to the first one formed together with it. The formation of the first martensite lath located parallel to an austenite twin was observed for the majority of the first nucleation events in austenite grains. Laths often formed in groups sharing the same spatial orientation. This suggests that the formation of more than one lath enables a more effective accommoda-

tion of transformation strains. A comparison of the orientations in Figure 6.13a and Figure 6.13e shows that the variant which nucleated at the austenite twin boundary exhibits a KS orientation relationship to both twin related orientations neighboring the twin boundary.

This nucleation condition was found for all nucleation events which were observed (i.e. the first nucleation in every austenite grain). The orientation of the lath formed in Figure 6.13c is very close to KS variant 13 of the twin and KS variant 9 of the matrix next to the twin. These KS variants of both sides of the twin boundary result in the same bcc orientation (which is also the case for 15&11, 18&8, 16&12, 17&7 and 14&10). The misfit angle between the orientation of the lath and the common orientation of variants 13 and 9 is lower than 1°. Similar low misfit angles were observed for all other isolated nucleation events. This nucleation condition reduces the number of possible variants (i.e. bcc orientations) which can form with respect to the KS OR from 42 (24 for both orientations at the twin boundary minus 6 common orientations) to only 6 possible orientations.

The same crystallographic nucleation condition was observed by Luo and Weatherly [380] for the precipitation of Cr-rich bcc phase from a binary Ni-45 wt% Cr alloy. They found that the precipitates exhibited KS OR between matrix and twin. A similar observation was made by Ameyama and Maki [236], [381] for a Fe-25%Cr-6%Ni duplex steel: Austenite particles precipitated primarily at ferrite deformation twins upon annealing after compression. They also found that these precipitates are KS variants of both matrix and twin. Later, this nucleation condition was discussed by Furuhara and Maki [382] as a means for "variant metallurgy" but in this case only for diffusive phase transformations.

Nucleation of martensite at twin boundaries may be preferred because of several reasons: The $\Sigma 3$ interface itself may lower the energy needed for the formation of a lath especially if the twinning interface can act as the martensite habit plane. The habit plane of lath martensite is reported to be close to $(557)_\gamma$ which would be 9.45° off of the twinning plane $(111)_\gamma$. However, variations of the habit plane in lath martensite are reported in the literature [126], [127], [189], [383], [384] ranging between $(111)_\gamma$ and $(557)_\gamma$. This suggests that the lath formed at a twin boundary should be oriented parallel to the twinning plane maximizing the common interface area of lath and twin. This behavior is indeed observed for most nucleation events investigated.

The twin boundary may act as a source of dislocations for the formation of martensite nuclei. The formation and structure of these nuclei is described by a model developed by Olson and Cohen [156]. They discuss a nucleation mechanism based on the Bogers-Burgers model [159] which proposes the formation of bcc/bct structured domains by the spread of Shockley partial dislocations over several planes in an fcc crystal (cf. Chapter 2.1.8.3). In an review of experimental work by Dash and Brown [161] they suggest the incoherent part of twins as an suitable source for dislocations of this type. An alternate and more general approach suggests that Intrinsic Grain Boundary Dislocations (IGBDs) [164] may facilitate the nucleation of martensite if they fulfill the requirements arising from the Bogers-Burgers model.

The experimental evidence presented in this work shows that twin boundaries are generally preferred over grain boundaries as nucleation sites. Furthermore, the results suggest that the intersection of the twinning boundary with the grain boundary acts as the dominant nucleation site: These special triple points can provide the Shockley partials and may act as a location of coherency stress that locally lowers the energy barrier for martensite nucleation. It is not yet clear if the presence of the free surface promotes this mechanism or if it is even a prerequisite for enabling this nucleation mechanism and/or the observed clear preference for $\Sigma 3$ boundaries. It is difficult to answer this question based on experiments because the locations of the austenite twins are very difficult to detect in the bulk.

The observed nucleation mechanism, statistical analysis of variant selection and variant pairing call for a more differentiated discussion of the term "variant selection". Two types of variant selection will occur

during transformation: Variant selection during nucleation and variant selection during growth. The analysis of martensite nucleation revealed that a very strict variant selection mechanism is active during nucleation. The nucleated variant or group of martensite laths will influence further variant selection which may then occur during growth i.e. the habit plane and stress field of the variant(s) nucleated first will influence which variants will subsequently form. This implies that the properties of existing austenite twins will determine, together with the shape and size of the prior austenite grains, the martensite microstructure (if no additional, external stresses are present). This is schematically illustrated in Figure 6.14: The case of an austenite grain which contains a twin boundary embedded in a fully austenitic microstructure is depicted in Figure 6.14a. The nucleation of the first martensite lath is governed by crystallographic constrains by the nucleation condition at the austenite twin boundary (cf. Figure 6.14b). The crystallographic variant selected here determines the habit plane and to some extent the stress field of this lath. These two factors play a role in the the variant selection during growth of subsequent laths. This is illustrated in Figure 6.14c. The stress field of the lath, which forms first, will lower the driving force for the nucleation of further martensite laths (i.e. the autocatalytic effect). Further factors which will influence variant selection during growth are the geometrical constrains imposed by the size and shape of the PAG. This is schematically illustrated in Figure 6.14d. Martensite laths tend to minimize their aspect ratio (cf. Chapter 2.1.8.2) resulting in laths that are as long as possible in order to minimize their strain energy. The PAGBs hinder this growth of the martensite laths resulting in higher transformation strains. Simultaneously, martensite growing in different directions will similarly impose constraints upon each other.
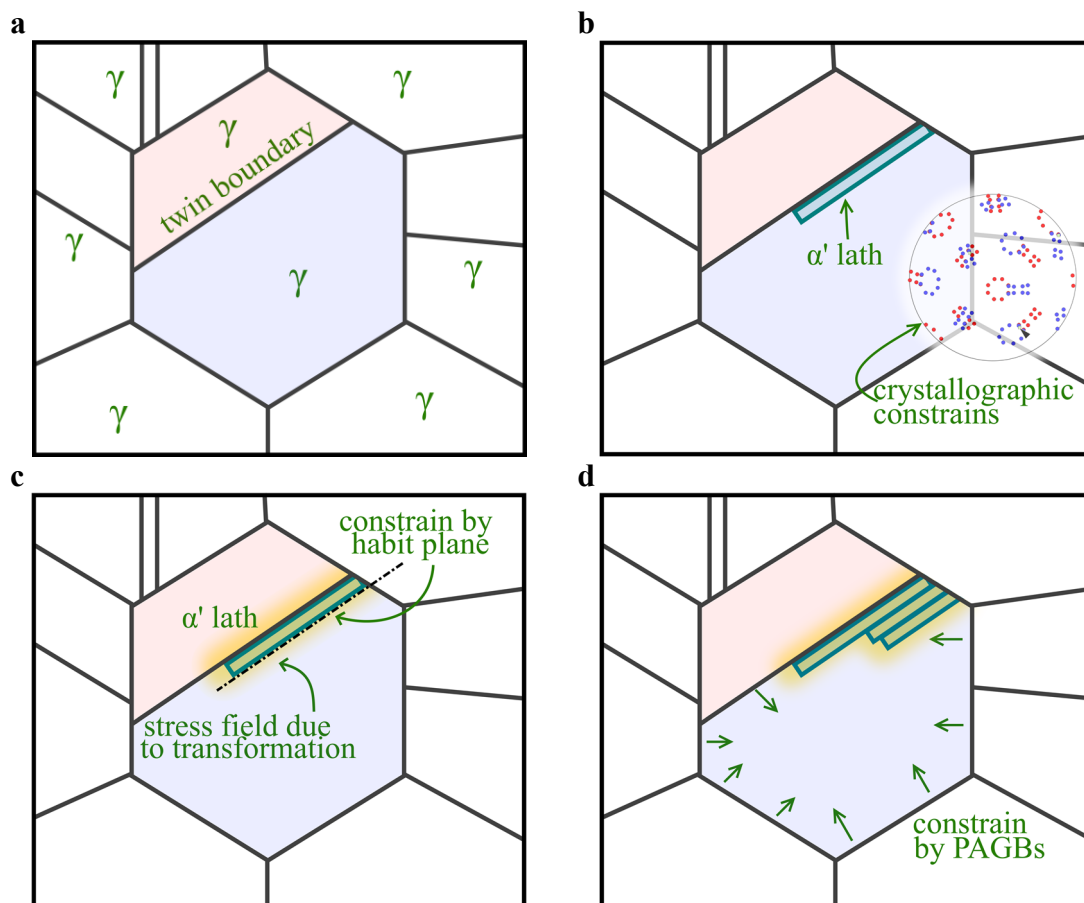
Figure 6.14: Illustration of factors influencing martensite variant selection and their interrelation. **a)** shows a schematic representation of the austenite microstructure. **b)** shows the nucleation of a martensite lath at an austenite twin. **c)** depicts the influence of the stress field and habit plane of this martensite lath on the formation of consequent laths. **d)** illustrates the constraining effect of PAGBs on variant selection.

6.3.4   Martensite Transformation Sequence

The series of images which was recorded during the martensitic transformation was compared to the variant map shown in Figure 6.11b to assess the transformation sequence quantitatively. The results are depicted in Figure 6.15a as a transformation temperature map. This map visualizes the temperature at which a specific lath formed. The information is combined into the variant map as a property of the individual laths. It indicates that parallel laths tend to form at the same temperatures generating packets of parallel laths. Laths forming in such packets belong to the same close packed plane (CPP) group.

The size of the laths that nucleate first exhibit a similar size distribution as the final martensite micro-structure. Morsdorf et al. [194] suggested that coarse laths exhibit a lower dislocation density because they were formed earlier than smaller laths. In contrast to the indirect analysis of the transformation sequence (based on carbon content measured by atom probe tomography (APT)) performed by Morsdorf et al., a preference for the formation of larger martensite laths in the early stage of the transformation was not found. The differences in dislocation density in the martensite laths may be caused by another effect: Laths that correspond to variants which are preferred under the local stress state will grow in a more unrestricted manner compared to laths that correspond to variants that do not fit to the local stress state. However, this is not necessarily influenced by the point of time when they nucleated. The analysis of nucleation shows that the variants that form first are restricted by the specific crystallographic variant selection mechanism at austenite twins. In the same manner, this variant selection mechanism will restrict the habit plane and spatial orientation of the laths which form first. The lower dislocation density is therefore a direct consequence of the local stress state which favors the formation of a specific variant and influences its size. To some degree it may be independent from the transformation sequence.

The transformed fraction can be calculated by integration of the area of the martensite laths corresponding to each temperature. It has to be mentioned that this method cannot include information about the bulk material and is solely based on the transformed fraction on the surface. The result of this analysis is plotted in Figure 6.15b. It shows that the transformation occurs between 492 °C and 423 °C and the maximum transformation rate is reached at 457 °C.
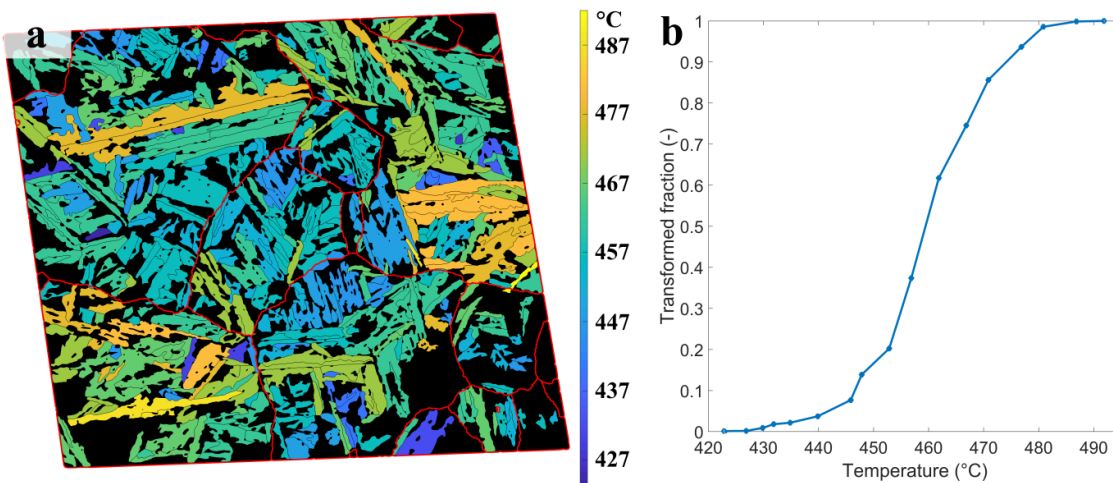

Figure 6.15: a) Mapping of the transformation temperature of individual martensite variants. The variants in the black areas are too small or the transformation temperature was not recognized. PAG boundaries are plotted as red lines. **b)** Transformed fraction of the mapped and registered area plotted against the temperature showing the progression of the transformation.

6.3.5 Quantitative Analysis of the Martensite Habit Plane

The most common direct way for the determination of the habit plane reported in literature is performed by TEM [124], [218], [383], [384]. The closest lattice vector with respect to the lath interface is determined and then from orientation measurements of retained austenite or by using an OR, the corresponding plane in the parent crystal is determined. This does not enable a statistical evaluation of the habit plane for a larger surface area or volume. Similar approaches using EBSD are also limited by the method by which the parent orientations are identified.

A statistical approach was developed for the determination of the habit plane and used with the parent orientations measured at 980 °C. The variant map shown in Figure 6.11b was used for this evaluation. This has the advantage that regions corresponding to a single martensite variant are defined. The method for the estimation of the martensite habit plane is described in detail in Chapter 4.13. This procedure was performed for every parent (austenite) grain in order to account for variations of the habit plane. The resulting orientations of the habit plane are plotted in Figure 6.16. The variation of the habit plane is surprisingly large. The vectors of the habit plane commonly reported in literature are plotted in red in Figure 6.16 for comparison.

For the sample which was quenched from 980 °C it can be seen in Figure 6.16a that the $(259)_\gamma$ habit plane fits best but that also regions can be found where the habit plane is closer to $(225)_\gamma$ or $(557)_\gamma$. The mean habit plane orientation was identified to be close to $(348)_\gamma$. The resulting habit plane orientations for the sample which was quenched from 1150 °C exhibit also a large scatter but are shifted away from the [111] direction. The mean habit plane was here found to be $(214)_\gamma$ which is ca. 6° away from $(348)_\gamma$. It is not clear if the large scatter of the habit plane is caused by surface effects or by effects connected to the transformation misfit. This assumption would imply that the scatter of habit plane orientation will decrease if elastic and/or plastic accommodation of transformation strains are reduced. It could also be reasoned that this scatter may be caused by the presence of the free surface and the accommodation of transformation strains perpendicular to the free surface. There are not many reports on studies of the habit plane with a similar statistical approach that can serve for comparison. Otte et al [384] concluded that the observed scatter of the habit plane is not a result of measurement errors but is real. They also concluded from comparison of the habit plane on the surface and in the bulk that the habit plane measured on the surface is also valid for the bulk.
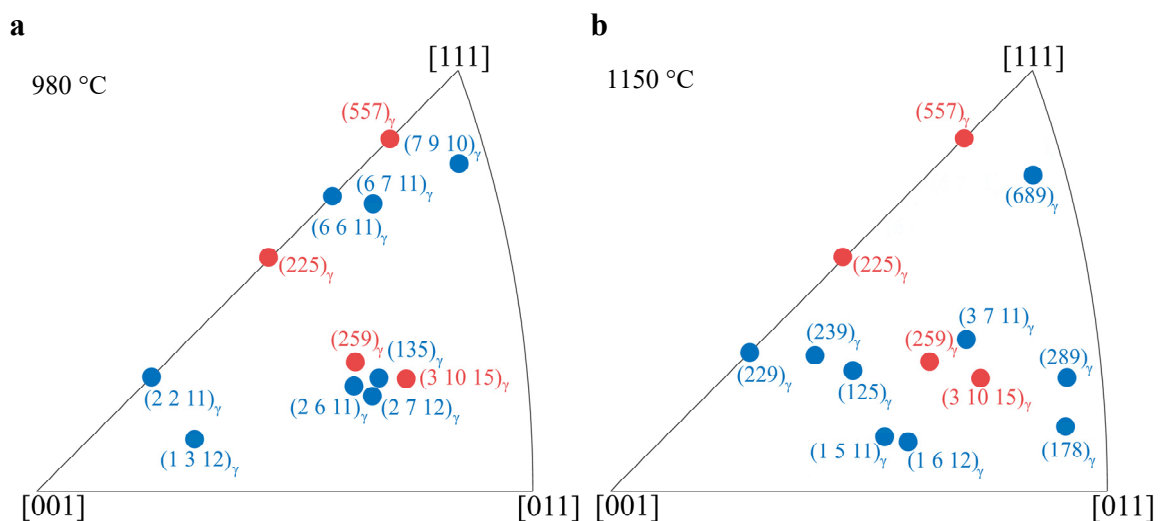

Figure 6.16: Inverse pole figure showing the most common habit planes calculated for the martensite microstructure. The most common habit planes found in literature are marked in red. **a)** for the sample which was quenched from 980 °C. **b)** for the sample which was heated to 1150 °C.

6.3.6   Comparison of Surface and Bulk Microstructure

TEM lamellae were prepared from the material by FIB milling for a more detailed comparison of the observations made on the surface to the microstructure of the bulk material. The result of a Transmission Kikuchi Diffraction (TKD) scan on the lamella extracted from the sample which was heated to 980 °C is shown in Figure 6.6a. The top of the scan corresponds to the surface of the sample. The orientations at the top of the TKD scan were compared to the orientations measured by EBSD on the surface at the exact location were the lamella was extracted. This was done to align the orientations measured by TKD to the orientations which were measured on the surface. These orientations and the orientations of the austenite grain which were measured at 980 °C by EBSD at this position were used to calculate the KS variants and the misorientation angle to the closest KS variant assuming that the austenite grain extended far enough into the bulk. Figure 6.17a indicates that this misorientation angle is low also beneath the surface of the sample. This suggests that the austenite grain extended deeper than the depth of ca. 4 μm examined by the lamella. In particular, this proves that no surface layer formed which could exhibit different properties than the bulk material.
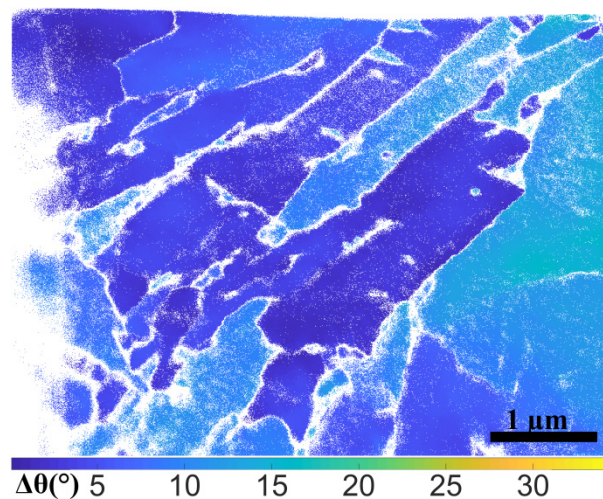
Figure 6.17: TKD mapping of the misorientation angle to the closest KS variant. It shows that there is no significant change of OR present from the surface towards the bulk of the sample.

As mentioned above it can be assumed that the transformation is influenced by the presence of the free surface. It is very difficult to perform a similarly detailed and accurate analysis of the bulk of a specimen. Therefore, the influence of the free surface has to be examined. This requires depth information about the microstructure of the sample. Otherwise it cannot be ruled out that only a thin layer of martensite formed on the surface or that the microstructure at the surface is completely different from the bulk microstructure. Therefore, cross sectioning of the sample via polishing was carried out. Two EBSD scans of the microstructure at $z \approx 2$ μm and $z \approx 5$ μm were performed. This does not only enable the examination of the influence of the free surface on the transformation but also changes in martensite morphology and crystallography from surface to bulk.

A correction of the orientations measured on the polished surface is needed to allow for a direct comparison of measured orientations in the bulk of the sample to the ones measured on the surface at 980 °C: The determination of the misorientation between the EBSD scan shown in Figure 6.2 and the EBSD scan after the removal of the surface layer is difficult due to possible orientation gradients in the martensite microstructure which can therefore not be used as reference orientations. Instead, an indirect alignment of the orientations was performed: The PAR algorithm of Cayron et al. [262], [263] was used to obtain an estimation of the prior austenite microstructure. The misorientation between both austenite maps was then

calculated by comparing several orientations of the austenite grains on the map measured at 980 °C to orientations of the austenite grains on the reconstructed map. Thereby a one to one comparison of the OM underneath the surface to the EBSD scan at 980 °C is possible if it may be assumed that the austenite grains reach deeper than the depth of 3 μm that was removed from the surface. The TKD results obtained from the TEM lamella close to the area under consideration above supports this assumption. An indicator that can be used to further confirm this hypothesis is the misorientation angle towards the closest KS variant (cf. Figure 6.17). However, a careful test of this method revealed that the reconstructed orientations did not fit to the orientations of the HT EBSD scan: It was not possible to find a rotation which aligned all orientations of the reconstructed grains of the different z-levels.

Figure 6.18a shows a map of the misorientation angle of the martensite to the closest KS variant calculated from the austenite orientations which were measured on the surface of the sample. It can be seen that all misorientation angles are relatively small. This is not the case for the corresponding maps further inside the bulk that are depicted in Figure 6.18b and Figure 6.18c. The KS misorientation angles are only very small for the PAG in the middle of the map because the orientation of this grain was used for the alignment. It is surprising that the other austenite grains exhibit relatively high misorientation angles. This could only be explained by the following considerations:

1. Orientation gradient in z-direction in the austenite grains.

2. Very flat austenite grains so that the martensite laths measured in $z > 0$ belong to different austenite grains.

3. Rotation of the austenite grains due to the martensitic transformation.

4. Change of the OR between surface to bulk.

5. Deformation of austenite by transformation strains of martensite formed in its vicinity.
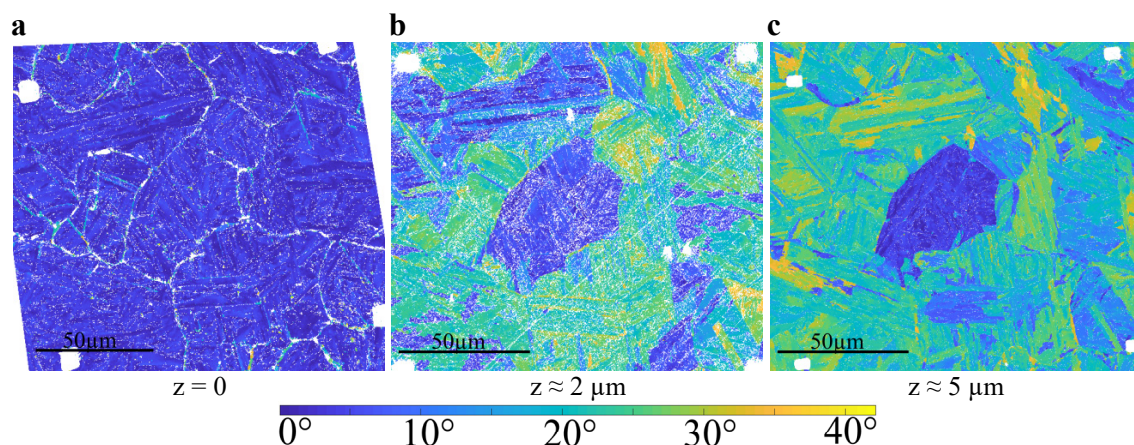
Figure 6.18: Map of the misorientation angle of measured martensite orientations towards the closest calculated KS variant. **a)** shows the mapping of the surface. Measured austenite orientations were used to calculate the orientations of the KS variants. **b)** and **c)** show the misorientation mapping for $z \sim 2$ μm and $z \sim 5$ μm respectively. The austenite orientations used for the calculation of the KS variant orientations were taken from a PAR algorithm. The orientation of the resulting map produced by the algorithm was corrected using the grain in the middle of the map.

These considerations are discussed in the following section:

1. From the EBSD scans of austenite at elevated temperature it does not appear to be sensible to assume orientation gradients inside the bulk. The OM of austenite at high temperatures shows that it is very unlikely that orientation gradients should be present in austenite grains in z-direction. Additionally, the TKD OM of the TEM lamella of the same sample did not reveal indications that support this assumption.

2. The assumption that the austenite grains are very flat and that the grain does not extent deeper than 5 μm into the bulk can be ruled out by a simple comparison of the grain shapes of the reconstructed PAGs to the austenite grains measured on the surface: It can be seen that the grain boundaries do not extent perpendicular to the surface into the bulk but new grains (i.e. new austenite orientations) do not appear. Even several austenite twin boundaries extending almost perpendicular into the surface can be seen in the martensite microstructure for z ≈ 5 μm.

3. A rotation of complete austenite grains would result in a uniform misorientation for a single PAG in the misorientation maps. But the regions of uniform misorientation angle in Figure 6.18 do not correspond to PAGs but to martensite laths. This suggests that the observed effect must be a result of a mechanism acting on the microstructural level of individual laths.

4. & 5. The last two considerations are hard to separate but are the most plausible ones for an explanation of the observed misorientations: The OR compares the orientations of the parent and product phase. However, plastic deformation due to the transformation misfit will also contribute to the misorientation between the parent and product phase. The definition of the OR must include these contributions or an "apparent OR" has to be defined. This last assumption seems to be the most plausible one: Variant selection will change due to the changed stress state in the bulk material. Therefore, stresses acting not perpendicular towards the surface are more pronounced in the bulk in comparison to the surface. It may also be assumed that martensite first forms at the surface and penetrates into the bulk. During this propagation, the stress states will change resulting in more plastic deformation of austenite in the vicinity of growing martensite laths leading to a change of austenite orientations.

The orientation of an individual austenite grain was aligned to allow for martensite variant analysis of one single austenite grain. The grain in the center of the map depicted in Figure 6.8 was chosen for the analysis. The KS variants calculated from the aligned maps for this grain are plotted in Figure 6.19. The comparison shows that the martensite habit plane does not significantly change with increasing depth. Most of the laths are still parallel to the laths that formed on the surface of the sample. A statistical analysis of the lath length indicates that it decreases with increasing depth from 7.2 μm at the surface to 5.1 μm at 2 μm depth and to 4.9 μm at 5 μm depth. The width of the laths is less affected. The thickness at the surface was 330 nm, at 2 μm depth 260 nm and also 260 nm at 5 μm depth.
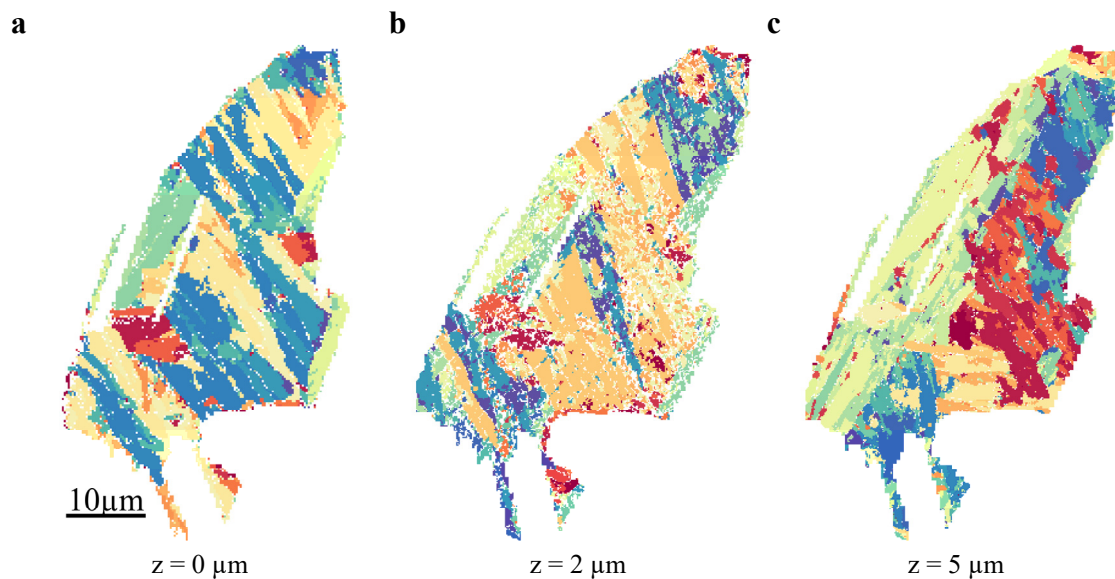
Figure 6.19: Comparison of martensite variants in a selected PAG in different depths. **a)** shows a mapping of the KS variants at the surface. **b)** shows the corresponding mapping at a depth of z = 2 µm and **c)** shows the mapping of the KS variants at a depth of z =5 µm. The corresponding color key can be found in Figure 6.12a.

6.3.7 Orientation Relationship

Figure 6.20a shows the (100) pole figure of the orientations measured in the large EBSD scan of the austenite microstructure at 980 °C. It does not exhibit a specific texture but distinctive maxima due to the relative small sample size. Figure 6.20b shows the corresponding (100) pole figure for the orientations of the martensite that formed at the same location. The martensite orientations exhibit two distinct maxima. This is a result of variant selection. The pole figure does also exhibit a circle of very low intensity which formed around a center with higher intensity.

Figure 6.20c shows a representation of the OR between the austenite and martensite orientation pairs measured in the area depicted in Figure 6.2. The austenite orientations were therefore rotated to one common (001)[100] austenite orientation. The same rotations needed to accomplish that were also applied to the corresponding martensite orientation in the same regions. The resulting pole figure of the rotated martensite exhibits distinct intensities close to the orientations of the variants of the KS OR which are marked in the pole figure by blue dots. The OR is very sharp and the intensities of the different variants are not equal.

Figure 6.20: a) (100) pole figure of austenite orientations at 980°C measured in the large EBSD scan. **b)** corresponding (100) pole figure of the martensite microstructure after the transformation. **c)** (100) pole figure calculated from the austenite/martensite orientation pairs representing the orientation relationship between the two phases. The orientations of the KS variants are marked with blue dots and the orientations of variants of the OR calculated for this material are marked with black dots.
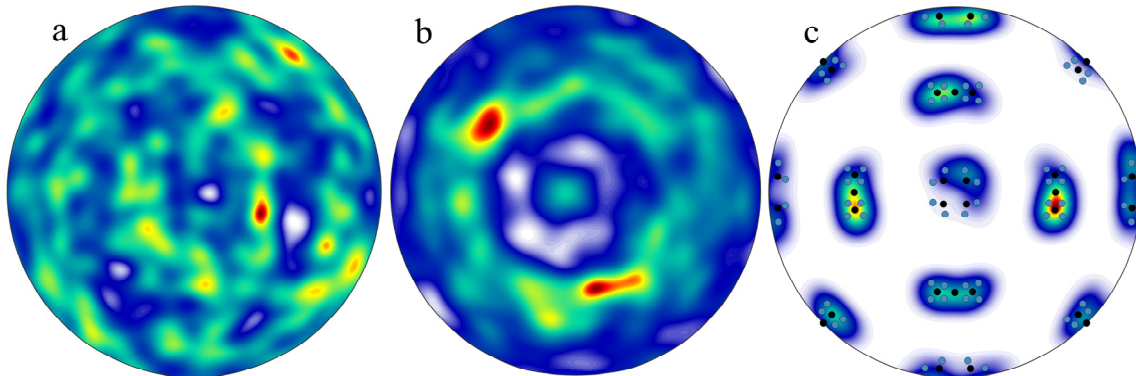
The actual OR for this material was determined by calculating the Misorientation Density Function (MDF) [385]–[388] using a de la Vallee Poussin Kernel with a halfwidth of 5° [389] from the fcc/bcc orientation pairs. As there may be some uncertainties connected to the alignment of the high temperature and low temperature maps the points considered in this analysis were restricted. Only orientation pairs having a minimum distance of at least 2 μm to the closest PAG boundary were considered for the calculation of the OR. The maximum of the MDF was calculated and from this misorientation the common parallel planes and directions were calculated. A detailed description of this method can be found in Chapter 4.12. The resulting OR for the sample that was quenched from 980 °C is close to the KS OR and represents the orientations produced by the martensitic transformation very well (cf. Figure 6.20). The OR which was calculated can be described as:

$$\{20\bar{1}\}_\gamma \,||\, \{22\bar{1}\}_\alpha$$
$$\langle 0\bar{1}0 \rangle_\gamma \,||\, \langle 1\bar{1}0 \rangle_\alpha$$

Eq. 6.1

This OR (subsequently called OR1) is less than 10° away from the KS, NW, Bain, Pitsch, GT and GT' OR. The minimum intervariant misorientation angle of this OR is 10°. The variants of the resulting OR are marked by black dots in Figure 6.20c. It shows that the KS OR can be used as a good approximation of the actual OR found in the material but that the misorientations exhibiting the highest frequencies are not located on any of the variants of the KS OR but can be found in between those. The calculated OR is closer to the maxima of the pole figure. The OR calculated for the sample which was quenched from 1150 °C is very close to the OR calculated above and it does also produce 12 variants. The misorientation angle between the ORs for the two samples is smaller than 1.6°. This is in the range of the accuracy of the EBSD method. This suggests that despite the differences in martensite morphology of both samples, the OR is not affected.

Here, the considerations made in Chapter 5 are applied to assess the accuracy of the different ORs quantitatively. This analysis is based on the orientation pairs which were measured for the sample which was quenched from 980 °C. The OR calculated from these orientation pairs is also included into the analysis as "OR1". The fractions of measurement points fulfilling the different ORs are listed in Table 6.2. This analysis demonstrates that the KS OR fits best for tolerance angles larger than half of the minimum intervariant misorientation angle of the KS OR (i.e. 5.26°). The GT' OR fits best for tolerance angles smaller than that.

ω (°)	KS	NW	Pitsch	GT	GT'	Bain	OR1
7	0.9518	0.8687	0.7740	0.9465	0.9498	0.0414	0.8407
5	0.7966	0.6007	0.3344	0.7428	0.8494	0.0028	0.5410
3	0.3670	0.2277	0.0664	0.2855	0.5008	0.0002	0.1633

Table 6.2: Fractions of bcc-fcc orientation pairs between austenite and martensite fulfilling an OR under a certain tolerance angle ω. The most common ORs from literature and the OR described above are compared. Three tolerance angles were selected for the comparison.

The relative frequencies corresponding to the fractions for completely random samples need to be calculated for a valid comparison of the ORs. The $f_{OR,norm}(\omega)$ values from Chapter 11.2 were used to calculate normalized frequencies $f_{OR,c}(\omega)$ in multiples of random. The results of the calculation are listed in Table 6.3 for 7°, 5° and 3°.

ω (°)	KS	NW	Pitsch	GT	GT'	Bain	OR1
7	18.67	31.23	27.86	22.23	22.38	5.96	33.89
5	39.29	59.15	32.94	41.45	47.41	1.09	53.21
3	83.67	104.02	30.27	65.15	114.40	0.35	74.39

Table 6.3: Frequencies of the occurrence of ORs between austenite and martensite under a tolerance angle ω in multiples of random. The most common ORs from literature and the OR described above are compared. Three tolerance angles were selected for the comparison. The corresponding absolute frequencies can be found in Table 6.2.

The values of the relative frequencies expressed as multiples of random change the trends that were observed for the absolute frequencies. The best fit to the experimental data can be found for the inverse GT OR for the smallest tolerance angle of 3°. The fit of the NW OR and even KS OR are better than for OR1 which was calculated from the experimental data.

This effect is probably caused by the variant selection which can be observed for this measurement: The method for the determination of the OR considers the absolute maximum of the MDF which is calculated from the experimental data. It does not consider a certain tolerance angle. This could be achieved by an algorithm that searches for a sphere in misorientation space with radius ω corresponding to the tolerance angle in which a maximum number of measurement points can be found. The inverse GT OR performs worse than the NW OR and OR1 for a tolerance angle of 5°. For the highest tolerance angle considered here (7°) the best fit can be found for OR1 followed by the NW OR and the Pitsch OR.

Similar investigations were performed by Barcelo et al. [366], [390] using EUROFER steels, among others. Unfortunately, they did not take into account the differences for random orientation frequencies of the ORs under consideration but instead used the absolute frequencies to quantify the ORs of the martensite. The austenite orientations used in these studies were calculated using a PAR algorithm for which neither sufficient data on its success rate nor its accuracy is available. Similar analysis of different steels by different research groups [367], [391], [392] did also not consider the occurrence of random orientation of the different ORs. The quantitative analysis of ORs without these considerations may lead to false conclusions about the predominant OR connected to the investigated phase transformation.

Although the considerations described in Chapter 5 were included into this analysis, the question of the predominant OR remains difficult. The evaluation above shows that the analysis of the frequencies of certain ORs in a large number of diffraction experiments can remain ambiguous despite the use of relative frequencies.

Visualization in the axis-angle space [393] is chosen to show the relation of the OR reported here to the well-established ORs. Two projections of this three-dimensional representation are plotted in Figure 6.21. It reveals that the OR calculated for this material is in between the well-established ORs. It is located at the edge of the fcc/bcc misorientation space. This leads to the formation of only 12 variants (c.f. Chapter 5.4). The OR can be found in between the Pitsch OR and the NW OR. It is 2.6° away from the NW OR and 6.9° away from the Pitsch OR. The proximity of the measured OR to the established ORs is in agreement with similar observations made in martensite based on residual austenite. A relative large spread of the OR between the well-established ORs was observed [203], [215], [217]. The OR found for this material is however relatively sharp compared to the ORs observed in the literature. The spread of the OR is often discussed to be a consequence of transformation strains deforming the untransformed matrix during the transformation. If this is the case an "apparent OR" would be a more appropriate term for the measured OR.
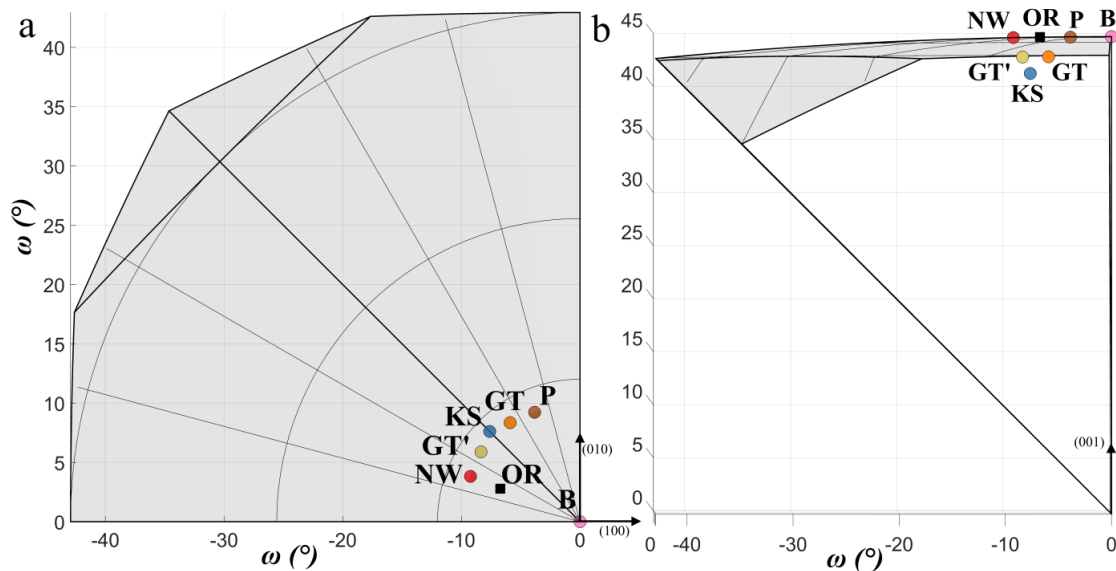
Figure 6.21: Representation of the OR calculated for EUROFER and the well-established ORs in axis-angle space. **a)** shows the projection parallel to (001) and **b)** shows the projection parallel to (010). The NW, GT, GT', Pitsch, KS and Bain OR are represented as red, orange, beige, brown, blue and pink dots. The OR calculated here is marked with a black square.

From the literature it is not clear how the free surface may influence the transformation and if these influences would also affect the orientation relationship. Differences in the observed OR may be caused by different degrees of plastic/elastic accommodation of transformation strains for the bulk and material close to the surface and due to the accommodation of transformation strains perpendicular to the free surface. However, the reasons for this shift away from the well-established ORs is not clear. Different ORs were mainly proposed for steels of different compositions. The KS OR was first observed in FeC alloys [204] whereas the NW OR was mostly observed in FeNi alloys [205], [375]. The crystallographic mechanism involved in the transformation determines the resulting structure and thereby the OR. Furthermore, the transformation mechanism and in particular the motion of individual atoms is mostly not discussed and remains unknown to great extent. This cooperative movement during the transformation is the process in which alloying elements may influence the pathways of the atoms and thereby also the

structure of the transformation product. All models that are currently discussed regarding the martensitic transformation in steels also omit the role of carbon atoms and the atoms of other alloying elements. This shows that the influence of the parameters governing the transformation such as transformation temperatures, alloying composition, transformation strains, grain sizes, chemical potentials, crystallographic structure are heavily interconnected and not completely understood regarding the mechanism of the transformation.

6.3.8 Austenite Reconstruction Benchmark

The literature on ferritic steels and in particular the literature on the martensitic transformation shows a surprising lack of data on the microstructure of austenite at elevated temperatures close to the temperatures achieved during heat treatments. In order to compensate this lack of experimental data, several algorithms for the reconstruction of the austenite microstructure from martensite OMs have been developed [211], [263], [271], [276], [286], [394], [395] (cf. Chapter 2.1.8.9). So far, these algorithms were not extensively tested using relevant heat treatments and materials in the literature [290], [291] and the calculated orientations of the austenite have not been verified except for steels transforming at very low temperatures.

The experimental data based on EBSD maps of austenite and the resulting martensite at the same location presented in the previous chapters makes a comparison of reconstructed and measured austenite OMs possible. The methods for the alignment of OMs and the combination of multiple crystallographic datasets into one EBSD map allow for a direct point-by-point comparison.

Two approaches and algorithms were chosen (due to availability) for this comparison: The first reconstruction approach used in this comparison was developed by T. Nyyssönen [213]. It does not use a fixed OR but uses the KS OR as a starting point for an iterative optimization of the OR. The resulting OR is then used for the reconstruction. It is not based on a point-to-point analysis but is instead based on the misorientations at grain boundaries produced by a grain reconstruction applied to the martensite mapping. The local misorientations at these boundaries are the input data for the calculation of the OR using inter-variant misorientations.

The second reconstruction approach was developed by C. Cayron [263] and is based on a point-to-point misorientation analysis. Several start parameters for the program (ARPGE) based on this approach were tested and the KS OR was chosen for the reconstruction. Multiple reconstructions were produced and the best reconstruction was selected for comparison. The two austenite microstructures resulting from the two austenite reconstruction algorithms are plotted in Figure 6.22. The map in Figure 6.22c is the result of the algorithm developed by T. Nyssönen. It exhibits a relatively good match with the actual austenite microstructure. Problematic microstructural features are austenite twins: the algorithm often fails at twin boundaries although some twin boundaries are recognized correctly. The orientation of the austenite grains is not uniform. This artefact is caused by the calculation of martensite "grains" during the reconstruction. Figure 6.22d shows the reconstruction based on the algorithm of C. Cayron. The austenite grains exhibit a uniform orientation and the microstructure is similar to the real austenite microstructure if only austenite grain boundaries are considered. This algorithm did also struggle to reconstruct austenite twins.
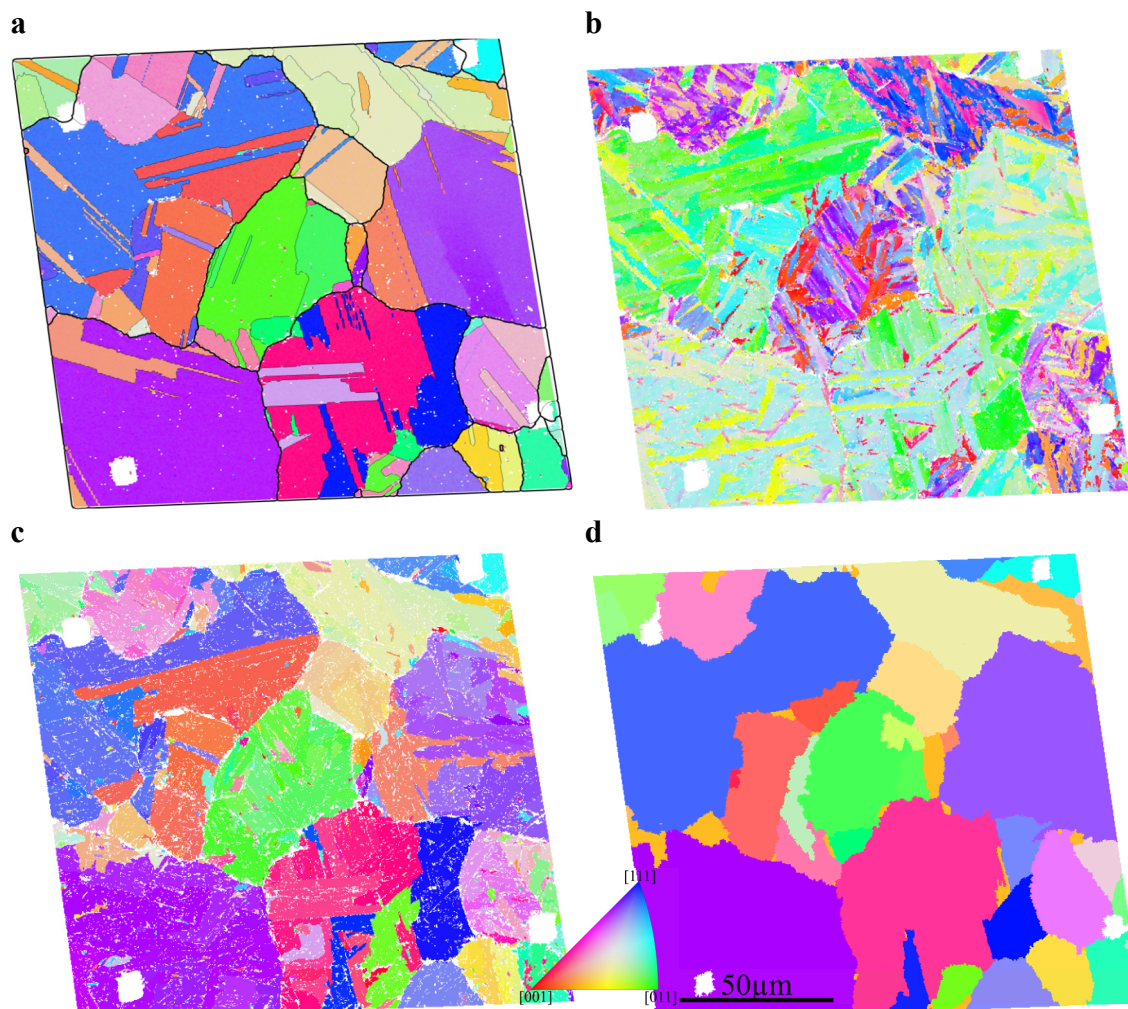
Figure 6.22: Comparison of reconstructed austenite orientation maps. **a)** shows the austenite OM from measurement at elevated temperatures for better comparison. **b)** shows the EBSD scan of the final martensite microstructure which is used as input for PAR. **c)** shows the result of the reconstruction procedure developed by T. Nyssönen et al. **d)** shows the result of the reconstruction procedure developed by C. Cayron et al. (ARPGE)

A map of the misorientation angle between reconstructed austenite orientations and measured austenite orientations is depicted in Figure 6.23a for the algorithm of T. Nyssönen and in Figure 6.23b for the algorithm of C. Cayron. Both maps exhibit the same trend: Both algorithms fail at twin boundaries or fail to reconstruct the orientation of the twin. This is a consequence of the intervariant misorientations being often very close to Σ3 misorientation. It is surprising that the algorithm of T. Nyssönnen (Figure 6.23a) which does not rely on a fixed OR is also not able to reconstruct the austenite twins properly. In particular, the two markers show two twins (interfaces that may be interpreted as twin boundaries) that were reconstructed in the wrong location. This is a consequence of the inhomogeneous distribution of variant pairings: Variants with low misorientations and twin related intervariant misorientations are preferred in this sample. The formation of multiple variants with parallel spatial orientation does also contribute towards this tendency.

In order to compare the two algorithms, the mean misorientation angle per point was calculated. For the algorithm of Cayron et al. a mean misorientation angle of 16.52° and for the algorithm of Nyyssönen et al. a mean misorientation angle of 15.22° was found. It has to be mentioned again that only the best result (the result that showed the best agreement to the measured austenite orientation mapping) of the algorithm of C. Cayron was chosen for this comparison and analysis. Several different prior austenite recon-

struction maps were calculated based on the same martensite EBSD data depending on the input parameters for the algorithm (OR, tolerance angle for grain identification, tolerance angle for parent grain nucleation, tolerance angle for parent grain growth, minimum accepted grain size).
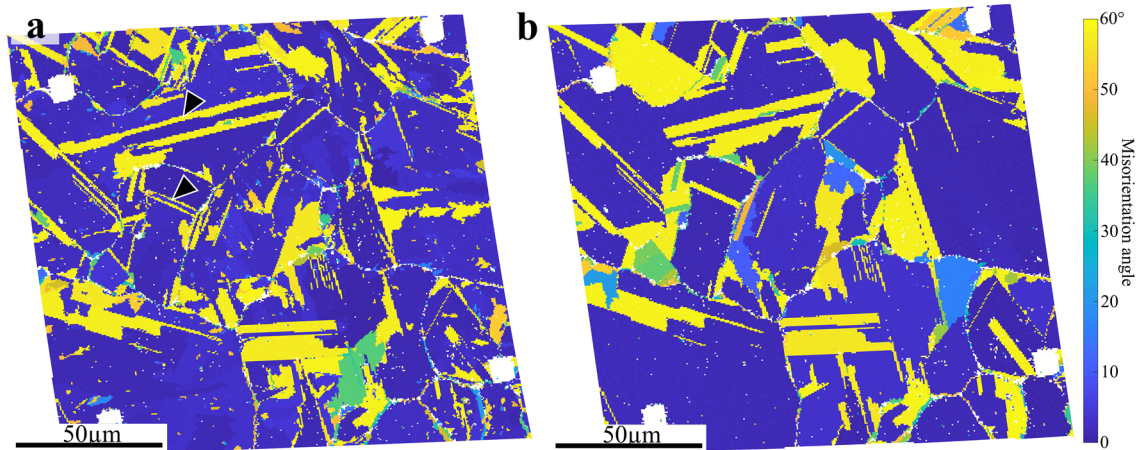

Figure 6.23: Map of the misorientation angle of the reconstructed austenite orientations (based on the martensite orientations measured on the same location) to the measured austenite orientations. **a)** Misorientation map for the austenite reconstruction using the algorithm developed by T. Nyssönen et al. **b)** Misorientation map for the austenite reconstruction using the algorithm of C. Cayron et al.

It is reasonable to assume that this mean misorientation angle can increase drastically if a higher density of annealing twins is present in the austenite. An increase in the density of twin boundaries in the austenite phase could be caused by the deformation of the austenite in processes like hot forming. The reliability of the result of the PAR algorithm is affected by the density of twin boundaries in the austenite microstructure. Other factors that will have negative impact on the quality of the PAR are the austenite grain size and the strength of variant selection.

The results of this comparison highlight the importance of a more critical approach towards prior austenite grain reconstruction algorithms and their results. These algorithms generate impressive results and are easy to use but have to be treated with caution. Their results for prior austenite grain sizes seem to be reliable but special interfaces cannot be reconstructed reliably. A review of the literature on martensite formation and variant selection in ferritic steels shows that the calculations there are entirely based on the orientations produced by PAR algorithms if no retained austenite is present after the transformation. A closer look at the reconstructed austenite orientation maps in these publications reveals that twins are rarely predicted [275], [289], [396]–[399]. Therefore, the results and conclusions based on these calculations (variants, variant pairings, etc.) have to be treated with caution.

6.4   Summary

The formation of martensite from fully austenitic EUROFER steel was investigated using the *in situ* setup. The EBSD scans at elevated temperatures showed that a stable (low grain coarsening) austenite microstructure can be observed at 980 °C. A second sample which was annealed at higher temperatures exhibited pronounced austenite grain growth above 1150 °C due to the dissolution of carbides above this temperature. All austenite orientation maps at elevated temperatures showed low granular orientation spread and a high density of austenite twin boundaries.

EBSD scans of the product martensite microstructure revealed that the spatial orientation of martensite laths is mostly determined by the spatial orientation of austenite twin boundaries as martensite laths tend to form in parallel to prior austenite twin boundaries. Comparison of martensite variant selection between the samples quenched from different temperatures indicates that the degree of martensite variant selection is influenced by the prior austenite grain size: Larger austenite grains exhibit lower geometrical constraints for the formation of martensite laths. This enables a more efficient accommodation of transformation strains through martensite variant selection. Detailed statistical analysis of martensite variant pairing indicated a preferred pairing of variants which exhibit minimal misorientation angles or twin related variants independent of the annealing temperature.

The tracking of the transformation sequence by the observation of surface relief formation indicated a strongly heterogenous martensite nucleation mechanism. Martensite laths nucleated at austenite twin boundaries by a strict crystallographic variant selection mechanism: The orientation of the first lath has to be a variant common to both austenite twin and matrix. This reduces the number of possible variants under the assumption of the KS OR from 42 to only 6 variants. Martensite variant selection in the final martensite microstructure may be significantly determined by austenite twins if it is assumed that martensite variant selection during further martensite growth is mainly influenced by the stress fields of the first laths (which are again determined by variant selection during martensite nucleation). This is supported by the observation of a reproducible martensite variant selection at two separate twin boundaries of the same type inside a single austenite grain.

TEM lamellae and cross-sectioning of the samples revealed that no abrupt change of martensite microstructure can be observed from surface to bulk. The orientation maps of the cross-sections indicated that an austenite orientation gradient may be present from surface to bulk. Unfortunately it is not clear if this gradient is real or may be attributed to a gradient in the OR from surface to bulk. It may alternatively be attributed to the different stress state of the surface and the fact that less plasticity is required there for the shape changes resulting from the displacive transformation.

The orientation relationship calculated from the maximum of the misorientation density function that was obtained from all austenite/martensite orientation pairs was found to be close to the KS OR. The calculated OR leads to 12 variants and is close to the well established ORs (KS, NW, Pitsch, GT, GT').

Prior austenite reconstruction algorithms were developed by different groups in the past to reconstruct the austenite microstructure from the martensite microstructure with the aid of orientation relationships. In this work, the combination of orientation maps of austenite and martensite microstructure at the exact same location was used as a test of the prior austenite orientation reconstruction algorithms. The results of two available algorithms were directly compared to the results from the measurements. This revealed that the reconstructed microstructure and the orientations show reasonable agreement with the measured orientation maps. Both algorithms failed at the reconstruction of austenite twin boundaries producing results which indicate that a twin boundary may be present were in reality no twin boundary exists and omitting twin boundaries where twin boundaries were present. This observation shows that the results of

prior austenite reconstruction must be treated with caution and that analysis of variant selection based on PAR results are prone to errors. The observed martensite variant selection upon nucleation further demonstrates the importance of austenite twin boundaries: The martensite microstructure is to large extent determined by the location of prior austenite twin boundaries.

7 Intercritical Annealing of EUROFER Steel

The ferrite-to-austenite transformation is the first transformation to occur in the standard heat treatment of EUROFER steels. The austenite microstructure is heavily influenced by the characteristics of this transformation. This transformation belongs to the class of diffusive transformations. In these transformations no strict crystallographic relation between parent and product phase is observed. To investigate this transformation in detail, EBSD scans are performed during intercritical annealing.

Eventually, quenching was performed from the intercritical regime. The direct observation of the transformation sequence starting with the two phase microstructure allows for a detailed observation and, with the computational tools described in Chapter 4, analysis of the quenching process from the intercritical annealing regime. Dual-phase EUROFER steel is used here because of its low critical quenching rate for martensite formation.

A comparison of the martensitic transformation is made for the same material with two different microstructures as starting points: The transformation from a fully austenitic microstructure is described in Chapter 6. In this chapter, the analysis of the transformation from an austenite/ferrite microstructure is performed with particular focus on martensite nucleation and the interaction of the intercritical ferrite with the martensitic transformation.

7.1 Experimental

Ferritic/pearlitic EUROFER steel was produced in the laboratory by slow cooling (12 mK/s) after a homogenization treatment. The chemical composition of the sample is the same as for the material which was already used in this thesis (cf. Chapter 6.1). After the heat treatment, the sample was ground, polished, and finally vibratory polished. The sample was mounted onto the heating stage and heated up into the two-phase region. The austenite phase fraction was altered by varying the temperature.

Several EBSD scans (500 µm x 500 µm with a step size of 2 µm) of the austenitic/ferritic microstructure were performed in the two-phase region. A scan of the gold wire afixed to the Mo sample clamp was performed before every scan. The orientations from these scans were not used for crystallographic alignment. Instead, the mean orientations of several ferrite grains which could be tracked through the whole experiment were used. The sample was heated to 850 °C in a first heating step. The temperature was then lowered to 800 °C to reduce the austenite phase fraction. Further EBSD scans were performed at 910 °C, 900 °C, 890 °C and 870 °C. The sample was finally quenched by switching off the heater after a phase fraction of roughly 50% was reached. The quenching which resulted in a martensitic/ferritic microstructure was observed in real time using the SE detector and an image sequence of the surface during the martensitic transformation was captured. The images were registered to account for drift due to the rapid change in temperature of the heating stage.

A discontinuous oxide layer consisting of islands of small flakes formed on the surface of the sample in the lower temperature range of the two-phase region and caused a degradation of the EBSP quality. The oxide layer exclusively formed in ferritic regions. It dissolved slowly as the temperature increased and these regions transformed into austenite. After the heating and quenching experiment, the sample was carefully polished using a vibratory polisher in order to remove the oxide islands on the ferritic regions. A detailed EBSD scan of the dual-phase sample was performed in the Zeiss Merlin SEM (ca. 230 μm x 260 μm and step size 0.2 μm). Simulatenously EDX spectra were recorded for the characterization of the oxides. A TEM lamella was prepared by FIB (FEI Nova NanoLab 200). This lamella was cut into the region where the detailed EBSD scan was performed before. The location was chosen to allow for a characterization of the ferrite-martensite interface. STEM and TKD was performed on the lamella in the Zeiss Merlin SEM using an acceleration voltage of 30 kV.

7.2   Results

The starting microstructure of the sample was produced by slow cooling from the austenitic state producing a ferrite/pearlite microstructure. The corresponding orientation map is shown in Figure 7.3a. The starting grain size of the ferritic microstructure was 92.8 μm. An overview showing temperatures and measurment times is given in Table 7.1. The two-phase region was reached in the first heating step at 850 °C. The result of the EBSD scan at this temperature is depicted in Figure 7.1a. It consists of 83 % austenite with a high density of twin boundaries. The average grain size is 61.6 μm. Austenite transformed into ferrite during cooling to 800 °C resulting in an austenite phase fraction of 42 %. The γ-α back transformation also led to coarsening of the microstructure resulting in an average grain size of 82.4 μm. Large areas of non-indexed measurement points can be seen predominantly in the ferritic grains in the phase map shown in Figure 7.1b. This low indexing rate is caused by an oxide film forming on the ferrite grains which causes a decrease of quality of the EBSP. An EDX analysis of this layer after the *in situ* experiment revealed that it consists of chromium and vanadium oxides. In a next step, the temperature of the sample was increased to 910 °C resulting in the growth of austenite to a fraction of 64 % and dissappearance of the oxide layer. The resulting phase map is shown in Figure 7.1c. A stepwise decrease of the temperature resulted in a slow growth of ferrite until reaching an austenite phase fraction of 41 % at 870 °C. The corresponding phase map is shown in Figure 7.1f. The austenite grains show a very low granular orientation spread (GOS) i.e. each grain exhibits one sharp orientation. Differences in the orientations measured within one grain are smaller than the minimal angular resolution which can be achieved by EBSD. An interesting feature of the ferrite phase fraction is the formation of subgrains. In contrast to the austenite grains, ferrite grains frequently exhibit larger orientation gradients resulting in a higher GOS for the ferrite phase compared to the austenite phase. Once formed, these subgrains and the orientation gradients are stable during the intercritical annealing.

T [°C]	850	800	910	900	890	870
t [min]	37	106	242	295	357	405

Table 7.1: Temperatures and times at which the corresponding EBSD scans were finished. The times are measured relative to the starting point (t = 0) when the first set point was reached (850 °C).

Almost all of the austenite grains that formed during intercritical annealing contain twin boundaries. The twin boundaries (CSL3) in austenite are marked by yellow lines and twin boundaries in ferrite are marked by white lines in the phase maps in Figure 7.1. Independent of the temperature, about 20% of the accumulated phase boundary length exhibits a misorientation close (tolerance angle ω < 5°) to the KS OR. These special phase boundaries are marked by green lines in the phase maps in Figure 7.1.
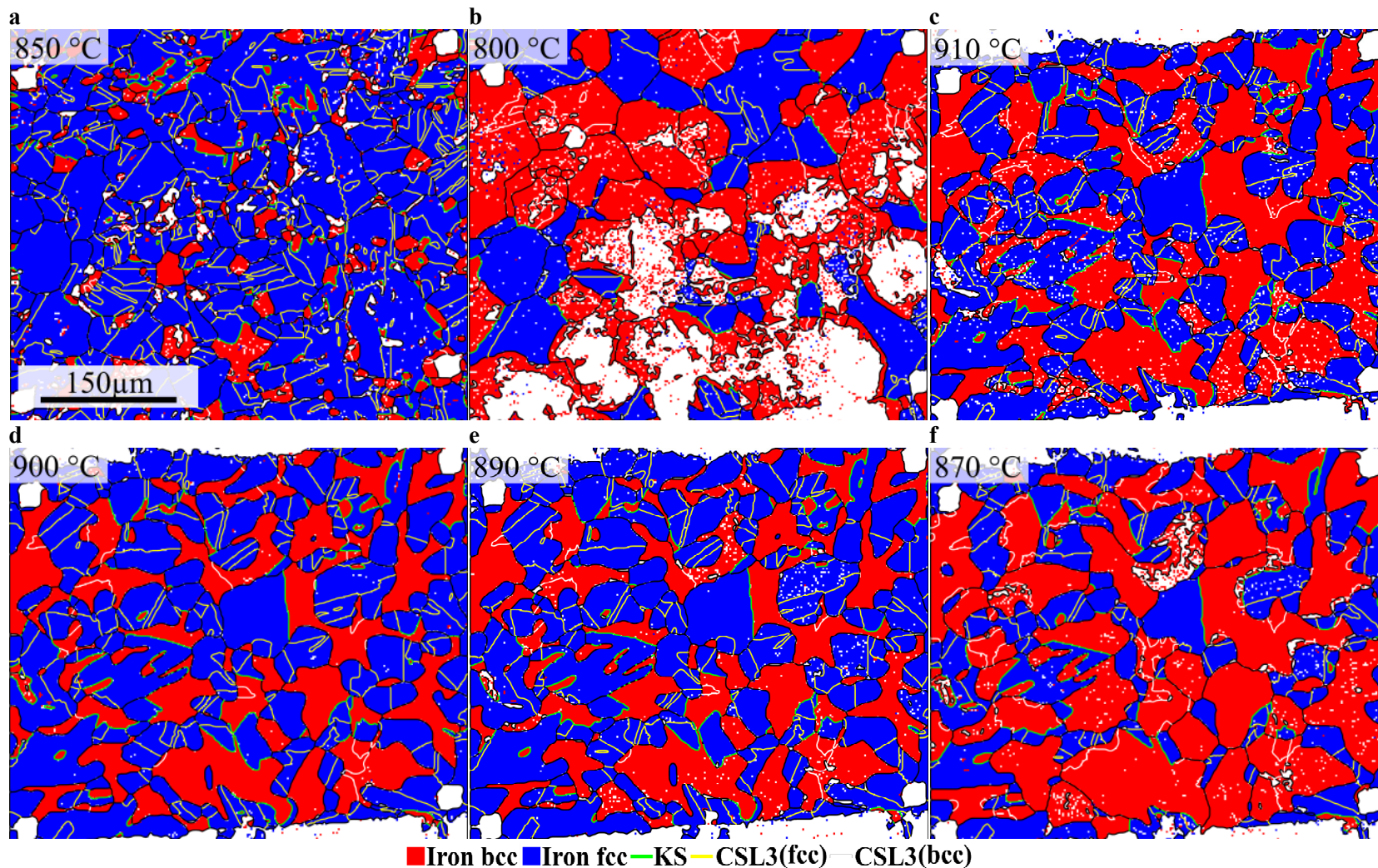
Figure 7.1: Phase maps of the EUROFER sample in the two-phase region. The blue colored areas correspond to austenite and the red colored to ferrite. Phase boundaries exhibiting a misorientation close (tolerance angle ω < 5°) to the KS OR are colored in green. Twin boundaries (CSL3) in the austenite are colored yellow. Twin boundaries (CSL3) in the ferrite are colored white. **a)** shows the microstructure at 850 °C, **b)** corresponds to the phase map at 800 °C, **c)** at 910 °C, **d)** at 900 °C, **e)** at 890 °C and **f)** at 870 °C just before quenching.

The last EBSD scan on the sample in the two phase region at 870 °C is shown in Figure 7.3b. The phase map of the sample at 870 °C is also added as a guide for the eye in Figure 7.3c. The ferrite phase fraction determined from this EBSD scan was 58.8 %. The sample was quenched by switching off the heater. An image sequence of the surface was captured using the SE detector. Changes on the surface of the sample in the same region for which the OMs were performed were observed by SEM. The progeression of the transformation is visible due to the formation of a surface relief caused by the displacive character. Selected images of this image sequence can be seen in Figure 7.2. Nucleation events are marked by black triangles. The first martensite lath appeared at 481 °C. Transformation continued until ca. 395 °C.
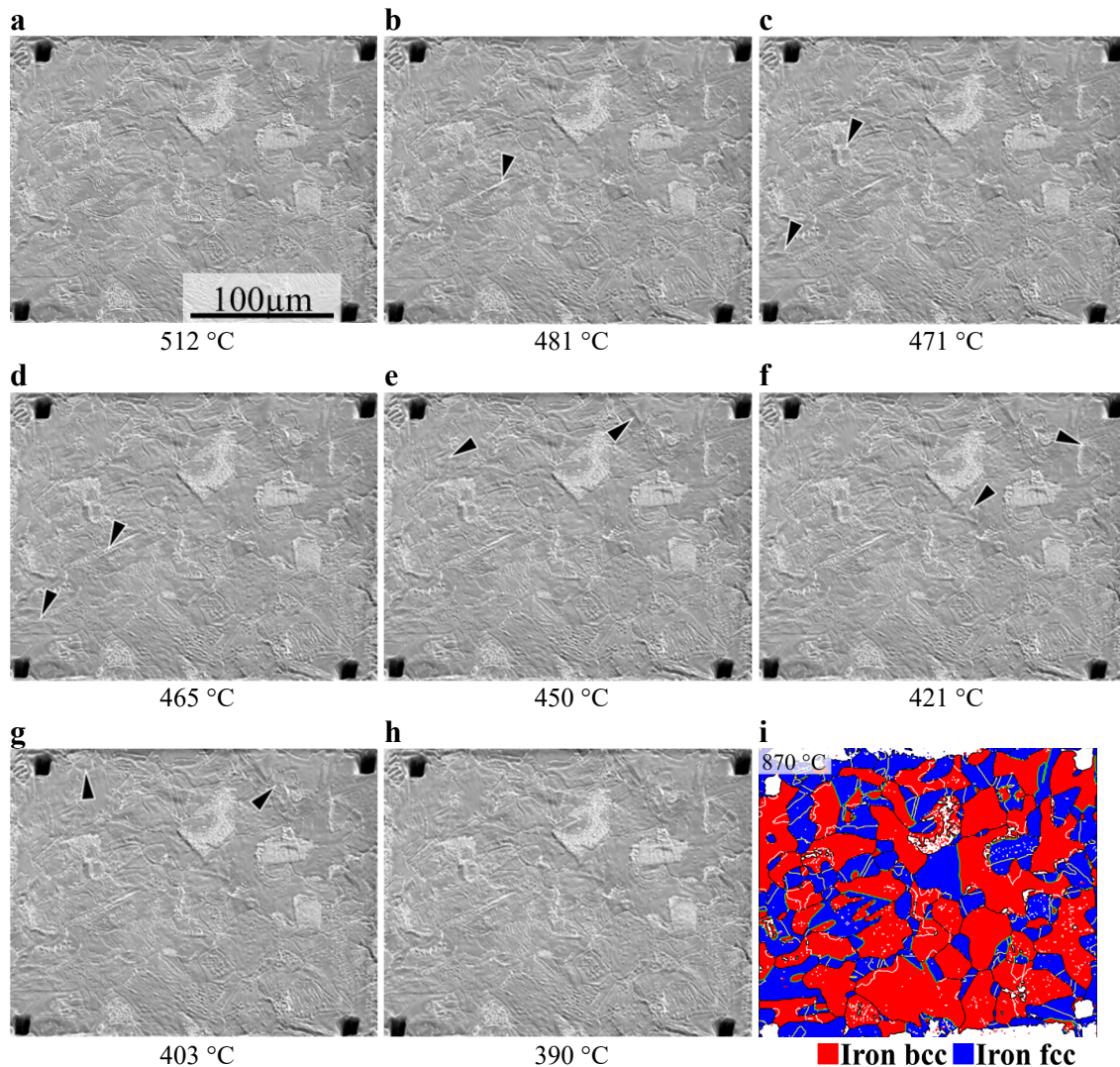
Figure 7.2: Image sequence showing the relief associated to the martensitic transformation observed during quenching. **a)** shows the initial state of the surface and **h)** the final state. Image **i)** shows the last EBSD phase map just before quenching as a guide for the eye. Selected nucleation events are outlined in the SEM images with black triangles.

The orientation map of the resulting ferritic/martensitic microstructure is shown in Figure 7.3d. It shows large ferrite grains exhibiting relative low GOS compared to the neighboring martensite islands. Some ferrite grains exhibit orientation gradients resulting in a subgrain structure. Some of these large ferrite grains are surrounded by small ferrite grains. These grains, which are grouped around a larger ferrite grain, share one common orientation. One example is highlighted by triangles in Figure 7.3d.

The phase map of the sample at 870 °C shows that those small grains already formed during intercritical annealing (cf. Figure 7.3c). The martensite formed from intercritical austenite consists of fine laths exhibiting strong orientation gradients.

A comparison of the last measurement taken in the intercritical regime with the measurement recorded at room temperature shows that large areas of the former austenite transformed into martensite. The phase fraction of martensite calculated from this EBSD scan is 28.0 %. It can also be seen that some regions of the austenite transformed into epitaxial ferrite (EF) which originates exclusively from the growth of neighboring ferrite grains.
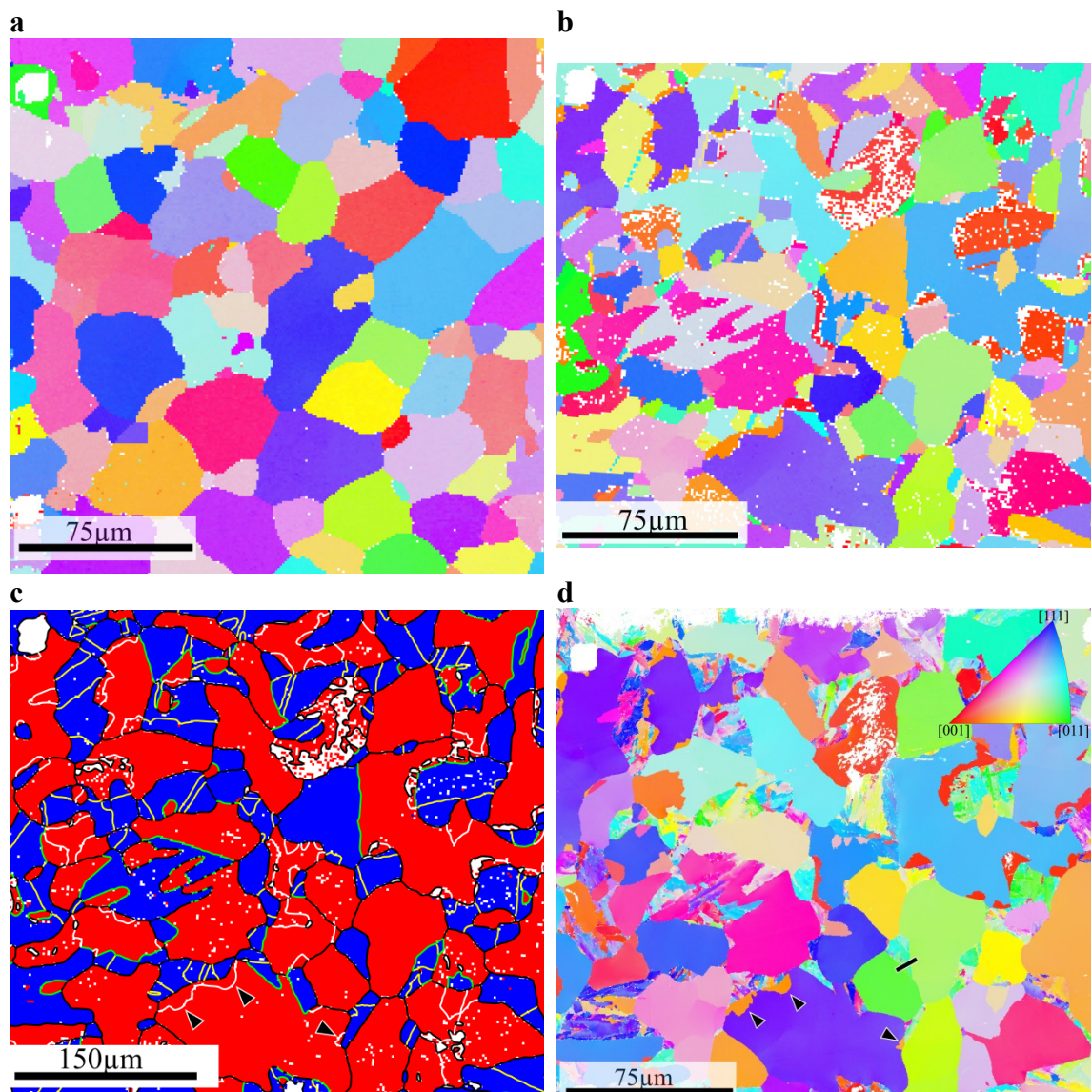
Figure 7.3: a) OM of the sample before the experiment. The sample is fully ferritic/pearlitic. **b)** Orientation map of the last EBSD scan of the intercritical annealed sample before quenching. **c)** Shows the corresponding phase map for the same measurement. **d)** Shows the orientation map for the dual-phase (ferrite/martensite) microstructure after quenching. Twin-related grains formed during intercritical annealing are marked with black triangles. The location where a TEM lamella was extracted is marked by a black line.

A TEM lamella was extracted from the marked location in Figure 7.3 in order to examine if the observations on the surface are representative for the bulk. The location of the lamella was chosen so that the ferrite grain, the martensite island and the interface could be examined. STEM and TKD OM were performed to investigate the structure of this part of the microstructure focusing on the ferrite/martensite interface. The resulting OM is shown in Figure 7.4a. A part of the ferrite grain can be seen on the right and a section of the martensite island can be seen on the left. The TKD scan shows that the martensite was not only formed at the surface but that the martensite microstructure extents into the depth of the material. It shows the presence of relative large martensite laths of mainly one martensite variant which are arranged parallel to each other. Smaller laths of other variants seem to be oriented parallel to the ferrite/martensite interface. The corresponding STEM image in Figure 7.4b shows the interface between the ferrite and martensite islands which is oriented almost perpendicular to the surface. The black spots which can be seen in the martensite island on the left suggest that carbides formed during quenching.

a

b

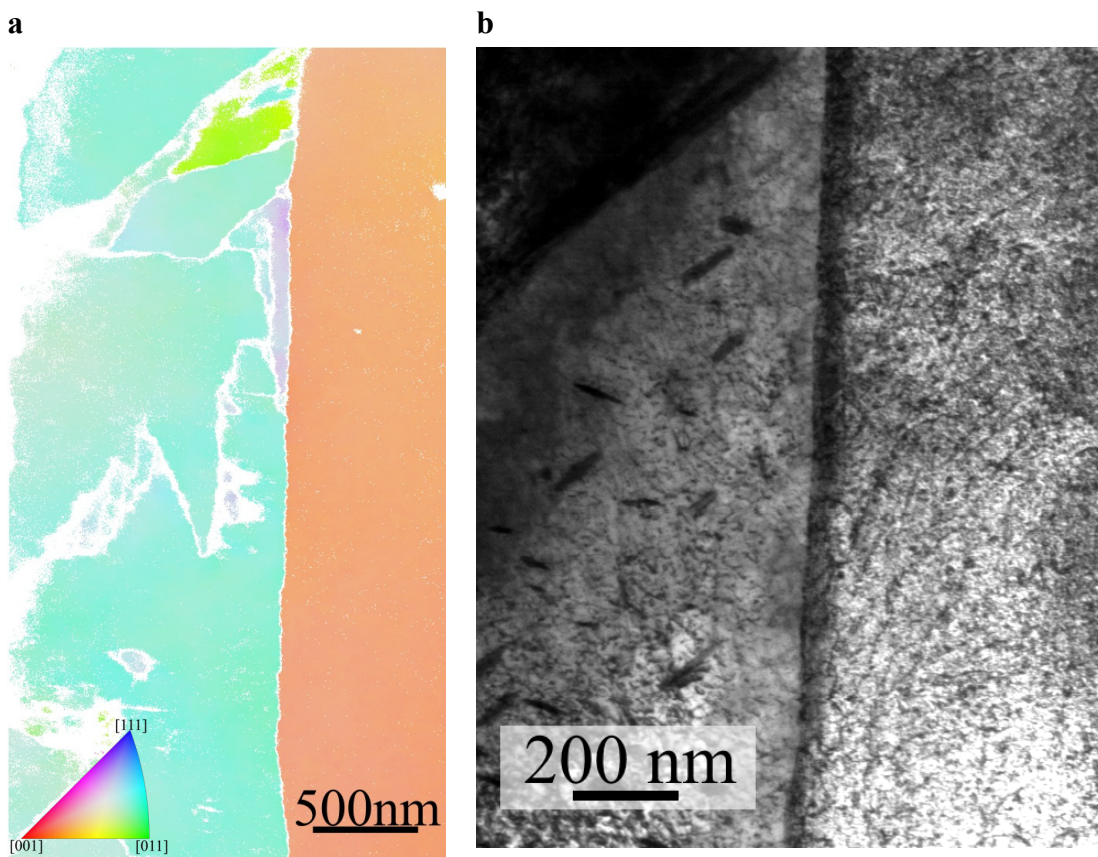**Figure 7.4: a)** TKD orientation mapping of the TEM lamella extracted from the location marked in Figure 7.3d. The left side shows the region inside the martensite island. The right side is located in a single ferrite grain. **b)** Bright field STEM image of the same region showing the interface between the ferrite and the martensite islands. The black spots inside the martensite suggest that carbides formed during quenching.

7.3 Discussion

7.3.1 Intercritical Annealing

The formation of austenite from a ferritic/pearlitic microstructure can be separated into three stages connected to different diffusive processes which affect the phase transformation [400]. Rapid growth of austenite is followed by slower carbon diffusion controlled austenite growth into ferrite. The third and last stage is controlled by the diffusion of substitutional alloying elements and is therefore rather slow. The alloying elements in this material that govern the kinetics of the last stage are mostly chromium and tungsten. Typical annealing times which are still governed by diffusion of substitutional alloying elements are reported to be in the range of several hours for manganese [400]. This illustrates that the phase maps shown in Figure 7.1 do not represent an equilibrium state (with regard to these slow diffusive processes) at least for the first EBSD scans.

The observation of changes of grain morphologies during annealing reveals that the predominant direction of curvature of the phase boundary changes during the experiment. The phase boundaries of the ferrite are convex if the temperature decreases and ferrite grows. This can be seen in Figure 7.1b. The phase boundaries become concave for the opposite case of austenite growth during an increasing temperature, which can be observed by comparing Figure 7.1b and Figure 7.1c.

Figure 7.1 shows that non-indexed EBSD measurement points can be almost exclusively found in ferritic areas. This is due to the formation of a layer consisting of oxide flakes. EDX analysis revealed that these flakes are V- and Cr-rich. The oxide layer formed in a certain temperature window between 800 °C and 850 °C. The formation of the oxide may be caused by a change of the chemical activities of these alloying elements due to the phase transformation. This change of activity may cause Cr and V in ferrite to be more prone to oxidation at the surface.

7.3.1.1 OR Between Ferrite and Austenite

The phase maps depicted in Figure 7.1 suggest that large parts of the austenite-ferrite phase boundary exhibit misorientations close to the KS OR. Therefore, misorientations at the phase boundaries of all HT phase maps were combined to analyze the exact OR of the austenite-ferrite interface. The result is shown in Figure 7.5 as a (100) pole figure. The orientations of the corresponding KS variants are marked with black dots. It shows that the OR at the phase boundary is very close to the KS OR but exhibits a broad scatter. It can also be seen that the maxima in the pole figure do not correspond to any of the KS variants but are situated in between the KS variants. Overall, only 20% of the phase boundary segments are in agreement with the KS OR if a tolerance angle of 5° is chosen.
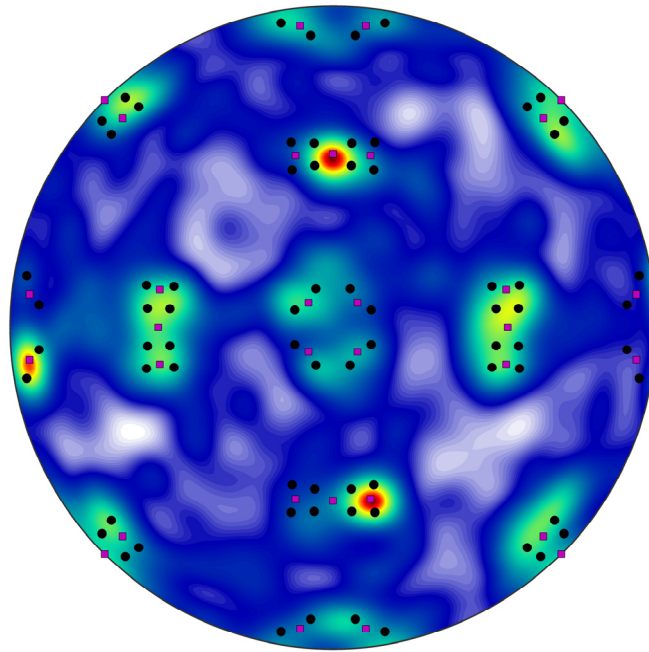
Figure 7.5: (100) pole figure calculated from the austenite/ferrite orientation pairs at the phase boundary representing the orientation relationship between the two phases. The orientations of the KS variants are marked in black. The variants of the OR calculated for intercritical annealing of EUROFER (cf. Eq. 7.1) are marked by red squares.

The dominant OR at the phase boundary between ferrite and austenite was calculated. In order to do so, the Misorientation Density Function (MDF) was calculated from the misorientations at the phase boundaries. The maximum of the MDF was then determined and parallel plane/direction pairs were fitted to the resulting misorientation (cf. Chapter 4.12). The OR was found to be:

$$\{001\}_\gamma \parallel \{011\}_\alpha$$
$$\langle 210 \rangle_\gamma \parallel \langle 211 \rangle_\alpha$$

Eq. 7.1

The closest OR from literature to the calculated OR above is the NW OR [20], [21], [23], [24], [26], [27], [401]. The calculated OR is 1.0° away from the NW OR and 6.2° away from the OR (OR1) found in Chapter 6. It has to be noted that OR1 describes an OR for a displacive transformation (austenite → martensite) while in this case a diffusive transformation (austenite ↔ ferrite) is considered.

7.3.1.2 Formation of Ferrite Twin Boundaries

The phase map of the last intercritical annealing step in Figure 7.3c and the orientation map of the transformation product in Figure 7.3d show that small grains of Intercritical Ferrite (IF) formed in the periphery of larger ferrite grains. For each single large ferrite grain, these grains share a common orientation. One example is marked with triangles in Figure 7.3c and Figure 7.3d. The same effect can be observed for other larger ferrite grains throughout the observed region. The phase map in Figure 7.3c reveals that these small ferrite grains are twin-related (CSL3, grain boundary marked in white) to the large ferrite grain which they surround.

This effect can be observed for all of the smaller ferrite grains which formed in the last annealing steps. It suggests that ferrite grains that nucleate at an austenite-ferrite phase boundary tend to select orientations which are twin-related to the ferrite grain at which they nucleate. The shapes of the twin boundaries observed in the austenite and in the ferrite differ strongly. The austenite twin boundaries are very similar

to "classical" annealing twins which exhibit a straight more or less coherent boundary. The twins in the ferrite phase are less straight than in the austenite phase. The occurrence of twin boundaries in the ferrite phase upon back-transformation from austenite was also observed by Lischewski [25]. He explained the formation of these twins as a result of the preferred nucleation of KS-related ferrite grains and their impingement upon growth. This may result in a ferrite twin if the KS variants that nucleate at austenite triple points exhibit a CSL3 relationship. Lischewski observed this formation of twins in a full transformation from ferrite to austenite and again to ferrite. The results obtained here show that the formation of ferrite twins may also occur without the impingement of growing KS related ferrite grains because the twin boundaries formed without a complete austenite-to-ferrite transformation. The twin-related smaller ferrite grains situated around a larger ferrite grain also exhibit usually the same orientation independent of the orientation of neighboring austenite. These observations contradict the interpretation of Lischewski albeit the same morphology of ferrite twins (smaller grains of common orientation surrounding CSL3-related large grain) observed here can be seen in the EBSD maps of Lischewski [25].

The orientation maps recorded at elevated temperatures suggest that this OR (CSL3) for ferrite nucleation at phase boundaries is prevalent for this material. These boundaries could alternatively be explained as "classical" annealing twins in the ferrite phase. The first notion has some implications for boundaries between ferrite grains which are not twin-related: These boundaries must then be the result of impingement of two growing ferrite grains which nucleated either at different ferrite grains at a phase boundary or at other interfaces in the austenite.

7.3.1.3 Ferrite Subgrain Formation

The formation of ferrite subgrains can be observed in Figure 7.3b. Several large ferrite grains exhibit distinct orientation gradients. These gradients tend to spread over the whole grain. One grain was selected as an example and is shown in detail in Figure 7.6 at 800 °C, 910 °C and 870 °C. It can be seen that an orientation gradient is present at all temperatures. The same trend was also observed in other ferrite grains but never in austenite grains. These ferrite grains freshly formed from austenite after the first decrease in temperature from 870 °C to 800 °C. This shows that the formation of subgrains in ferrite may be connected to the phase transformation. For example, they may be a product of the coalescence of smaller ferrite grains that nucleated during the transformation. Bengochea et al. argue that two mechanisms may be responsible for ferrite coarsening behind the transformation front: The first is normal grain growth; the second is coalescence of grains with similar orientations [402]–[404]. Similar considerations were made by Furuhara et al. [382]. According to them, the low misorientation may be caused by the nucleation condition of the single grains: Nucleation of similarly oriented ferrite grains can be expected if it is assumed that ferrite grains nucleate at austenite grain boundaries and that the orientations of these ferrite grains are close to the KS OR to at least one of the austenite grains [20], [23], [24], [338]. Low misorientation angles will then only be found if the KS variants to which these ferrite grains belong are situated on a single Bain circle. This would result in a minimal misorientation angle of 10.53°. The misorientation angles between the different subgrains in the grain depicted in Figure 7.6 lie between 1.2° and 3.4°. Analysis of orientation gradients in several ferrite grains showed that the misorientation angles of the orientation gradients are always lower than the minimal misorientation angle of 10.53° (for the KS OR). Suitable variant selection during the nucleation process can therefore be ruled out as the reason for the observed subgrain formation.
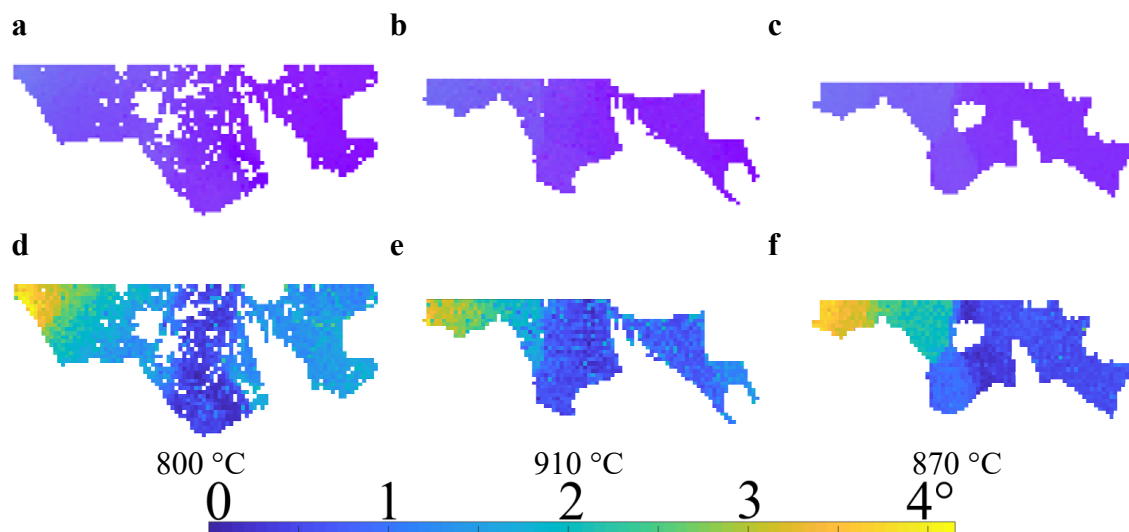
Figure 7.6: a), **b)**, **c)** orientation maps of one selected ferrite grain which can be seen in Figure 7.3b in the top left corner (the grain is rotated here by 90°) at 800 °C, 910 °C and 870 °C, respectively. **d)**, **e)**, **f)** misorientation angles relative to the mean orientation of the grain to visualize the orientation gradient inside the grain.

Therefore it seems more reasonable to consider a more general explanation for the formation of these orientation gradients: The evaluation of the EBSD scans at different temperatures shows that the gradients are often observed for ferrite grains which grew into multiple austenite grains exhibiting different orientations. This leads to different ferrite growth conditions at those interfaces depending on the local misorientation to the neighbors. The effect of this misorientation on ferrite growth may lead to a minimization of interfacial energy or to the formation of misfit dislocations which are then left behind the moving transformation front. This will subsequently lead to the formation of orientation gradients in the developing ferrite phase.

The last measurement shown in Figure 7.6c and f at 870 °C was performed about 5 h after the first measurement at 800 °C which is depicted in Figure 7.6a and d. The subgrains were observed to be very stable at elevated temperatures even for long annealing times. The observation of the stationary gradients is important for the interpretation of microstructural features after quenching: The presence of these orientation gradients in Intercritical Ferrite (IF) could be mistaken for traces of the deformation of the ferrite matrix due to the transformation misfit of neighboring martensite during transformation. The detailed observation of the microstructural evolution before quenching allows to rule out such false assumptions.

7.3.2   Formation of Epitaxial Ferrite

A distinction between IF which forms during intercritical annealing and Epitaxial Ferrite (EF) which forms during quenching after intercritical annealing is difficult. Santofimia et al [71], [76], [405], [406] applied different etching solutions to reveal the boundary between IF and EF. With some etchants they were able to reveal the interface between IF and EF as weak fine lines. Several further studies proposed different EBSD based methods for an automated distinction of the microstructural constituents in multi-/complex-phase steels [407]–[409]. Zaefferer et al. [410] conducted a study on the transformation processes in the production of a low alloyed TRIP steel using a combination of OR mapping and TEM analysis. On the one hand, the approach based on OR mapping is prone to errors: It must be assumed that the probability of EF to exhibit a KS OR towards neighboring austenite is high. The evaluations discussed

above for the intercritical regime show that this is often, but not always the case. On the other hand, TEM analysis may be a useful method to distinguish both constituents but is very time-consuming.

The location and the amount of martensite that formed during the transformation and the location and the amount of austenite have to be known in order to enable the reliable identification of EF. Combining high-temperature EBSD maps before quenching and maps after quenching can reveal the amount and location of EF that formed during quenching. Therefore, the austenite-ferrite phase map of the last inter-critical annealing step is used for such an analysis. This map can be superimposed onto the EBSD map of the transformation product. Unfortunately, this would not allow for a clear distinction between EF and martensite. This can be accomplished indirectly by considering band slope of the EBSP. The band slope is significantly lower in martensitic areas compared to ferritic regions [411]–[416]. Figure 7.7a shows a map produced by overlaying the band slope map after quenching and the phase map at 870 °C. The locations at which EF formed are clearly visible as yellow areas.

The austenite phase area fraction calculated from the EBSD scan performed at 870 °C just before quenching was 41 %. The martensite phase fraction after quenching was found to be 28 %. The difference of 13 % of austenite which did not transform into martensite formed EF. This means that 68 % of the austenite transformed into martensite and 32 % transformed into EF.
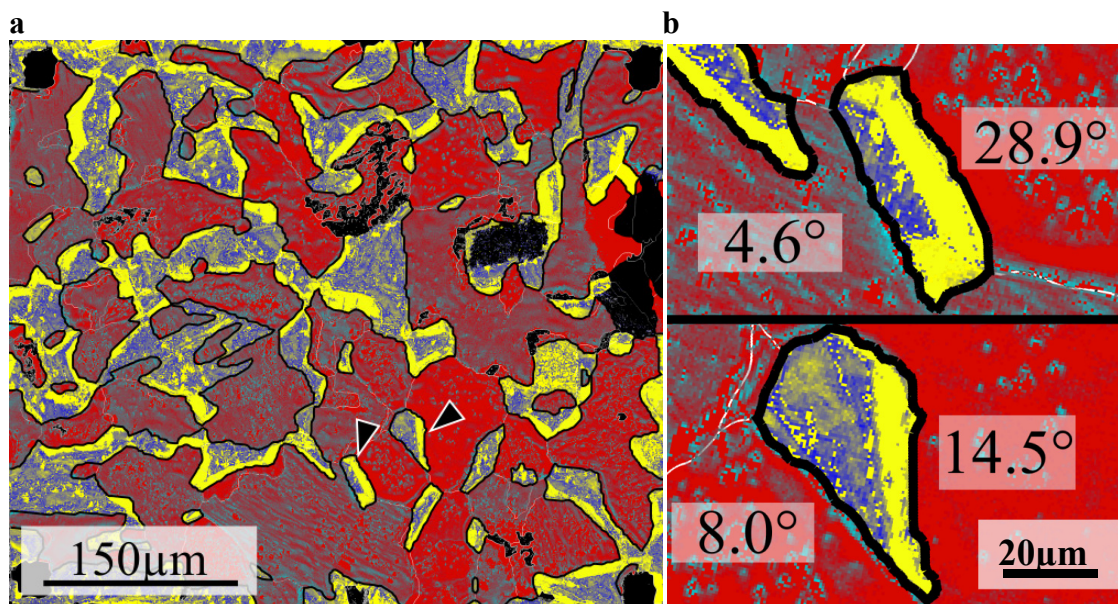
Figure 7.7: a) Overlay of phase map of the sample at 870 °C and a map of the band slope at RT after quenching. Phase boundaries are outlined as thick black lines. The areas in red are IF, the areas in blue are martensite formed from austenite during quenching and the areas in yellow are EF formed during quenching. Black regions are points were no indexing of the EBSP was possible. **b)** Detailed maps of selected regions that are marked by black triangles in (a). The numbers in the ferrite grains show the misorientation angle towards the KS OR at the phase boundary before quenching.

Two martensite/EF islands are marked in Figure 7.7a: These formed from small austenite grains with at least two neighboring ferrite grains. The amount of EF formed in these grains is not evenly distributed between the neighboring grains: This implies that the character of the phase boundary determines if and how much EF forms during quenching. Therefore, the misorientations between the austenite grains and its neighboring ferrite grains were analyzed. This shows that significantly more EF was formed at phase boundaries which exhibit the larger misorientation angle to the closest KS variant calculated from the austenite orientation.

This is demonstrated for the two austenite grains marked in Figure 7.7a: The two regions around these grains are shown in detail in Figure 7.7b. The misorientation angles of the ferrite grain orientation towards the closest KS variant calculated from the orientation of the austenite grain is noted in the neighboring ferrite grains. The upper example in Figure 7.7b shows that almost no EF formed from the ferrite grain on the left but a substantial amount of EF formed from the ferrite grain on the right of the previous austenite grain. This is the case because the minimum misorientation angle of the possible KS variants towards the orientation of the ferrite grain on the right is much larger (28.9°) than towards the orientation of the ferrite grain on the left (4.6°). The same effect can be observed for the other example: Significantly more EF forms from the ferrite grain which exhibits the larger misorientation angle (14.5°) towards the closest possible KS variant of the austenite grain orientation. This misorientation angle towards the orientation of the ferrite grain on the left is much smaller (8.0°) and therefore almost no EF formed from this ferrite grain (at this phase boundary segment). This can also be observed for all other austenite grains on which substantial amounts of EF appeared during quenching. Austenite grains which are surrounded by two non KS related ferrite grains develop more EF from the ferrite grain which exhibits the larger misorientation angle to the closest KS variant.

The formation of EF takes place during quenching before the martensitic transformation is finished i.e. before M_f is reached if nucleation of martensite inside the grain at a twin boundary is assumed. This requires a high mobility of the austenite-ferrite phase boundary. The mobility of the phase boundary depends on the misorientation. The mobility is larger for interfaces which exhibit a high misorientation towards the KS OR (cf. Chapter 7.3.1). This means that EF will predominantly form at phase boundaries exhibiting a misorientation far away from KS. The amount of EF that forms during quenching depends on the misorientation of the ferrite to the closest KS variant of neighboring austenite. A further argument that can explain the different amounts of EF is based on the competition between martensite and EF. Phase boundaries which exhibit a misorientation close to the KS OR can act as nucleation sites for martensite (cf. Chapter 7.3.3). In this case martensite easily forms and the time available for EF formation is smaller (i.e. the time before M_S is reached) compared to phase boundaries at which nucleation of martensite does not take place.

7.3.3 Formation of Martensite

All martensite islands formed from intercritical austenite consist of several martensite variants. This is illustrated in an example shown in Figure 7.8a. The martensite variants tend to form parallel in elongated laths. These are shown in Figure 7.8b with respect to the KS OR. An interesting point is the number of variants present within a single martensite island. Du et al. [274] observed that the number of variants in martensite islands of dual phase steel is reduced in comparison to a completely martensitic microstructure. They also observed that the number of CPP packets present in the martensite in the dual-phase microstructure is reduced.

It may be assumed that transformation strains can be effectively accommodated in the relative soft ferrite matrix surrounding the martensite. This would provide an additional way for the accommodation of transformation strains which is not available in the case of a completely martensitic microstructure. Depending on the effectiveness of the accommodation mechanism, this could reduce the degree of accommodation by variant selection. Therefore, a reduced number of variants would be expected inside such a martensite island.

This effect cannot be observed for the sample investigated here. The number of variants is still high inside a single martensite island and moreover all CPP packets are present. A map of the CPP packets is shown in Figure 7.8c. It shows a higher frequency for the CPP variants 1 and 3 but nevertheless all packets are present.
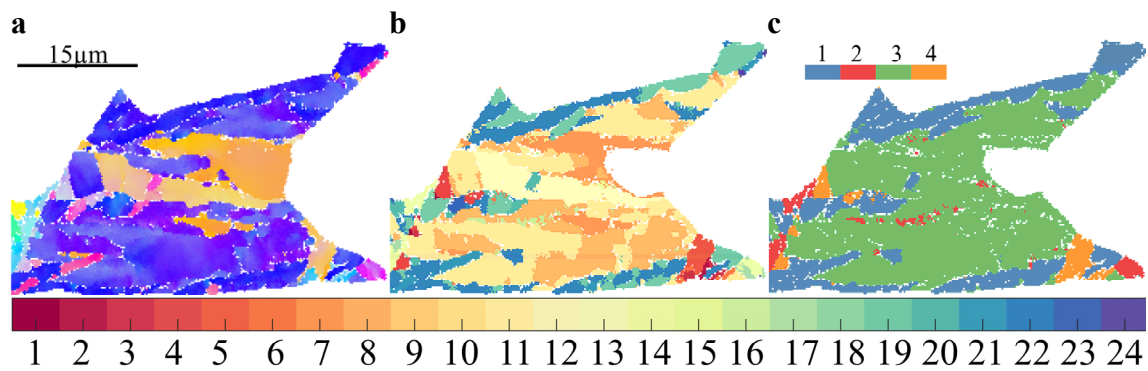
Figure 7.8: a) Orientation map of a martensite island marked in Figure 7.3c. **b)** Shows the corresponding map of the KS variants. **c)** Map of the CPP packets to which the martensite variants belong.

A lower martensite start temperature is found from the temperatures connected to the observation of the transformation sequence compared to the fully martensitic material which was discussed in Chapter 6. The martensite finish temperature was also found to be lower for the dual-phase material and the difference $M_S - M_f$ is larger compared to the fully martensitic sample. This change is quite likely caused by the higher carbon concentration in the austenite phase due to the lower solubility in the ferrite phase fraction and resulting partitioning.

By calculating the MDF from the martensite–austenite orientation pairs and finding its maximum, the OR between the martensite and the austenite phase was calculated. The OR for the martensite in the dual phase microstructure was found to be the same as the one found for the fully martensitic microstructure in Chapter 6.3.7. The combination of the HT EBSD map and the room temperature EBSD map included martensite and epitaxial ferrite as the transformation products of the austenite phase. The much lower band slope of the martensite islands was used to only select martensite for the calculation of the OR. A (100) pole figure showing the OR between austenite and martensite can be seen in Figure 7.9a. The misorientation angle of the EF and the martensite that formed during quenching relative to the orientation of the austenite is mapped in Figure 7.9b. The areas in which EF formed can be clearly recognized in most cases by their high misorientation angle towards the theoretical KS product orientation. However, this is not the case if a phase boundary exhibiting a KS OR was present in the intercritical regime.
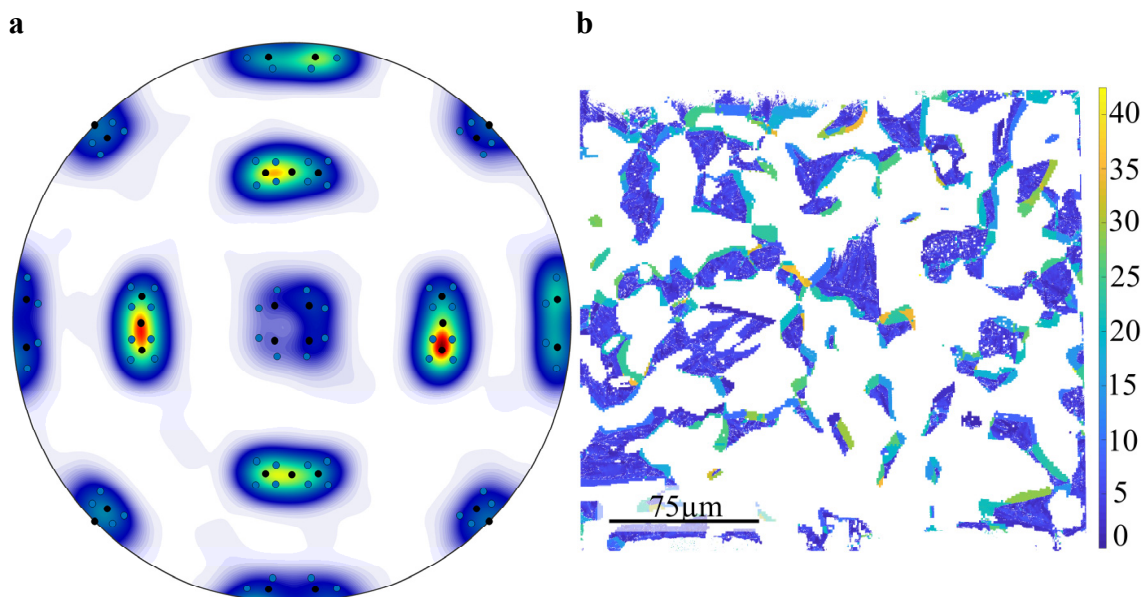
Figure 7.9: a) (100) pole figure calculated from the austenite/martensite orientation pairs representing the orientation relationship between the two phases. The blue dots represent the corresponding KS variants. The black dots are the variants resulting from the OR from Chapter 6.3.7. **b)** Map of the misorientation angle between the EF and martensite orientations and the closest KS variant calculated from austenite orientation.

Another aspect of the martensitic transformation is the variant selection: Transformation strains may be reduced by the selection of favorable variants. A histogram showing the frequency of the 24 KS variants is shown in Figure 7.10a. It shows that variant selection does occur during transformation. The variant selection strength factor k_{VSS} was found to be 0.152 for the martensite in the dual-phase microstructure. This is significantly lower in comparison to the variant selection strength calculated (k_{VSS}= 0.362) for the fully martensitic microstructure in Chapter 6. The weaker variant selection could be a consequence of the availablility of the additional way to accommodate transformation stresses by the deformation of the surrounding soft ferrite.

Similar tendencies can be observed for variant pairing: The bivariant histogram describing variant pairing is shown in Figure 7.10b: It shows that certain pairings exhibit larger frequencies than others. This behavior was described in the previous chapter for this steel. For the fully martensitic sample the prevalence of two types of pairings was found: Intervariant misorientation angles close to 60° (CSL3) and variant pairings with minimal misorientation angles were preferred. For the case of the dual phase microstructure of this chapter a different behavior is found: The histogram shows that variant pairings with high misorientation angles (CSL3) are only weakly preferred. A strong prevalence for pairings with minimal intervariant misorientation angles exists. This change in variant pairing cannot be attributed to the described additional nucleation condition (nucleation at phase boundaries with KS OR) in comparison to the fully martensitic microstructure because austenite twins are still preferred and the amount of pairings affected by this is negligible.

This suggests that transformation strains may be mostly accommodated by the combination of variants exhibiting minimal misorientation angles and by deformation of the surrounding matrix. The accommodation by the combination of variants with high misorientation angles seems to be less effective and/or energetically less favorable and these variants pairings are avoided.

Another possible reason for the change of the variant pairings observed in the dual phase microstructure compared to the fully martensitic sample is the altered chemistry of the austenite and thereby the martensite. Annealing in the two phase region leads to partitioning of alloying elements between the two phases. This means that the austenite in the intercritically annealed sample must contain higher levels of carbon, chromium and tungsten compared to the austenite which developed into the fully martensitic microstructure in Chapter 6. This not only leads to changes of the transformation temperatures but also to changes of the stacking fault energy (SFE) which affects the martensitic transformation. These differences probably also affect the pairing of the martensite variants.
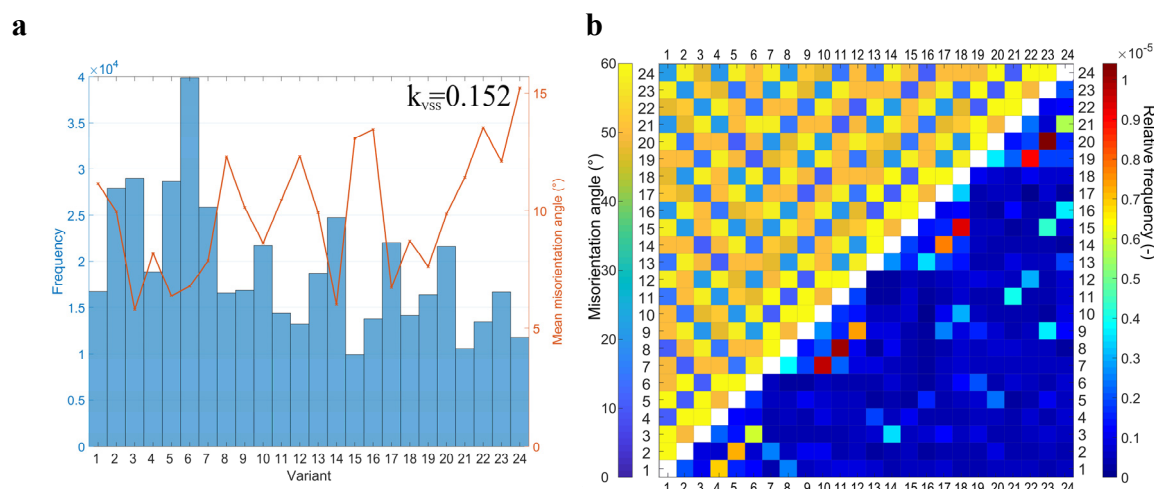

Figure 7.10: a) Histogram of the 24 KS variants. The mean misorientation angle of the variants with respect to the theoretical orientation is plotted in red. **b)** Bivariant histogram showing the frequency of KS variant pairings. The histogram is normalized using the frequencies of the variants.

7.3.4 Influence of Neighboring Ferrite on Variant Selection

A closer examination of the martensite islands inside the dual phase microstructure reveals that in some cases, the martensite variants exhibit similar orientations as their neighboring ferrite grains. This is shown for two examples in the EBSD scans in Figure 7.11. Figure 7.11a shows a martensite island which is surrounded by four ferrite grains. The ferrite grain f1 features an orientation which is one of the product orientations of the neighboring austenite grain if the KS OR is assumed. The martensite laths next to ferrite grain f1 which formed from this austenite grain have orientations very close to the orientation of ferrite grain f1. The misorientation angle between the martensite laths and the ferrite grain is smaller than five degrees. The martensite laths seem to "emerge" from ferrite grain f1. They are all oriented at an angle of ~25° towards the straight boundary of ferrite grain f1. It is clear that martensite variants that formed from an austenite grain will exhibit a misorientation close to intervariant misorientation of the KS OR towards a neighboring ferrite grain if the austenite and ferrite grain exhibited a misorientation close to the KS OR before transformation. This indicates that the observed effect must be connected to the variant selection and/or martensite nucleation at the phase boundary segment exhibiting a KS OR. The latter case would suggest that austenite-ferrite phase boundary segments exhibiting misorientations close to the KS OR may be preffered sites of martensite nucleation inside austenite grains and that the nucleated variants tend to have the same orientation as the ferrite at the phase boundary.
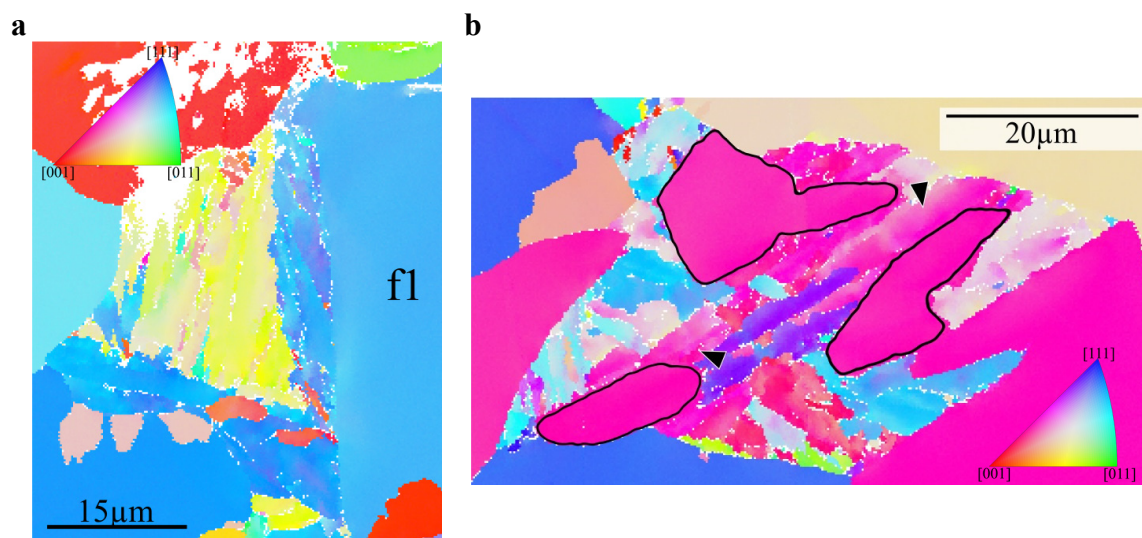
Figure 7.11: a) Orientation map of a martensite island in which martensite variants formed which exhibit low misorientations to one neighboring ferrite grain. **b)** Shows the orientation map of a martensite island containing ferrite grains. The ferrite grains inside the island are outlined. Two martensite laths featuring a low misorientation angle towards the orientation of these grains are marked with triangles.

A similar observation can be made in Figure 7.11b: The ferrite grains inside the now martensite islands exhibit a KS OR towards the surrounding austenite before quenching. These ferrite grains were already present before quenching (cf. Figure 7.3d). The orientation map shows several martensite laths featuring a very low misorientation angle towards these ferrite grains. Two of these laths are marked with triangles. This influence of neighboring ferrite was described in a more generalized way by Yoshida et al. [417]. They reported a special OR between ferrite and neighboring martensite. The martensite and the ferrite were reported to belong to the same CPP packet. This is also the case for the austenite grains described above but can also be observed for all of the observed martensite islands. In contrast to Yoshida et al. the influence of neighboring ferrite on variant selection seems to be stronger in these observations: The variants that formed do not only belong to the same CPP packet but even exhibit the same orientation as neighboring ferrite if a phase boundary with misorientation close to the KS OR was present before quenching.

One distinct feature that is clearly visible in the orientation maps of the two selected examples in Figure 7.11 is that the martensite laths formed at the phase boundary appear to "have grown out" of the ferrite grain. This is a result of a misorientation gradient: The misorientation towards the orientation of the ferrite grains is low close to the ferrite grain and increases towards the end of the laths (away from the ferrite).

This gradient suggests the possibility of a continuous mechanism: EF grows into the austenite until M_S is reached at which a continuous change of the transformation mechanism to martensite may be initiated. A similar mechanism was already proposed by Zafferer et al. [410] for Bainite. One could alternatively argue that the ferrite may grow in a displacive manner. However this would contradict the findings connected to the formation of EF (relief, dislocation density). Moreover, a clear distinction between the ferrite islands and adjacent martensite of the same orientation can be made by observation of band slope and GOS.

7.3.5 Martensite Nucleation in Dual-Phase Microstructure

A further question arising from the discussion concerning the influence of neighboring ferrite on variant selection is martensite nucleation: Are austenite-ferrite phase boundaries preferred martensite nucleation sites? Do phase boundaries that exhibit a KS OR play a special role concerning the martensitic transformation?

The transformation sequence starting from intercritical annealing was tracked by capturing SE images of the surface of the sample during quenching. The evaluation of the transformation sequence showed a preferred nucleation at austenite twins. One of these nucleation events can be seen in Figure 7.2c. The triangle in the upper part of the image marks an austenite twin at which the first martensite lath in the austenite grain forms. Two similar nucleation events at austenite twins which are also outlined using triangles can be observed in Figure 7.2e. The local crystallography of the austenite twin and the martensite lath formed at the twin were evaluated for all cases where the nucleation was clearly visible in order to verify the nucleation condition described in Chapter 6.3.3. All nucleation events observed at austenite twins did follow this condition. The laths which formed first in an austenite grain nucleated at an austenite twin and always showed a misorientation close to the KS OR towards both, the matrix and the twin. Other events of martensite formation not connected to austenite twins can be seen in Figure 7.2d marked by the upper black triangle in the image. For this type of nucleation event the neighboring martensite is characteristitc which nucleated earlier and triggers the autocatalytic effect (cf. Chapter 2.1.8.4). These types of nucleation events were already observed in Chapter 6.3.3. Here, a new nucleation mechanism was identified in grains featuring a phase boundary which exhibits a misorientation close to the KS OR. Nucleation events of this kind can be seen in Figure 7.2c marked with the lower triangle and in Figure 7.2f in the middle of the image.

The nucleation of martensite at phase boundaries exhibiting non-KS misorientation was rarely observed. One single case is marked in Figure 7.2f with a triangle in the upper right area of the image. There martensite nucleated at a phase boundary exhibiting a misorientation of 29.7° towards the closest KS variant calculated from the orientation of neighboring austenite. The first nucleation of a martensite lath was observed there despite the presence of a twin boundary in this specific grain. The only rather weak condition observed in this nucleation event is that the martensite and the ferrite grain next to the phase boundary where the nucleation occurred belong to the same CPP packet.

These observations show that neighboring ferrite influences the nucleation of martensite: Austenite-ferrite phase boundaries can act as additional nucleation sites. However, a preference for phase boundaries over austenite twin boundaries concerning martensite nucleation was not observed. The evaluated sequence suggests that phase boundary segments exhibiting a misorientation close to KS are preferred over phase boundary segments with random misorientations. The observed cases of nucleation events connected to KS boundaries were also evaluated with respect to the influence of neighboring ferrite on variant selection. This evaluation showed that in all these cases an influence as described in the previous section was found.

The microstructural features at which martensite nucleation events were observed in the dual phase microstructure in order of prevalence are:

- Austenite twins

- Austenite-ferrite phase boundaries with KS OR

- Austenite-ferrite phase boundaries with non-KS OR

The interfacial energies of these microstructural features differ [418]: The lowest interfacial energy may be assumed for the austenite twin boundary. The interfacial energy connected to the phase boundary featuring a KS OR may be second and the largest interfacial energy is connected to a phase boundary with random misorientation. This classification of interfacial energies can be observed on the SE images of the surface: Thermal grain boundary grooves exhibit the highest depths for phase boundaries with random misorientation whereas phase boundaries with misorientation close to the KS OR feature shallower grooves. The smallest thermal grooves can be observed at twin boundaries. Martensite nucleation is therefore not strongly influenced by the interfacial energy at the nucleation site as the twin boundaries, which feature the lowest interfacial energy, are mostly preferred over grain boundaries that exhibit a random misorientation.

Therefore, the influence of the local misorientation and thereby the structure of the interface must play a decisive role for nucleation. The martensite nucleation model of Olson and Cohen [156] relies on dislocation arrays for the formation of a bcc embryo. The preferred nucleation sites should act as a source of suitable dislocations for the formation of such embryos. Furthermore, a structural similarity between austenite twins and austenite-ferrite interfaces featuring a KS misorientation may be assumed from these considerations.

In combination with the formation of the EF discussed above, these observations give a more comprehensive understanding of the transformation products in dual phase microstructures. This is schematically illustrated in Figure 7.12: The local misorientation at the phase boundary governs the transformation product: EF will only form if a high misorientation towards the KS OR is present. The magnitude of this misorientation determines the mobility of the interface and with that how much EF will be formed. Martensite will form if the misorientation at the phase boundary is close to KS. These interfaces exhibit lower mobilities. The martensite variants that form in this case will tend to feature a low misorientation angle towards the orientation of the neighboring ferrite. However, this will only occur if martensite does not nucleate at other microstructural features (austenite twins) than the phase boundary.
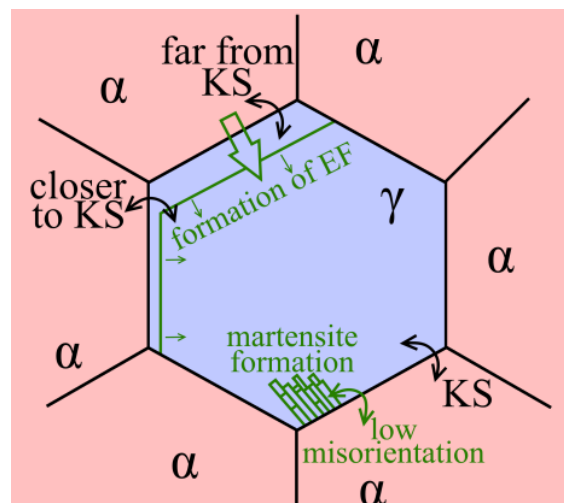

Figure 7.12: Schematic illustration of the transformation mechanisms starting from an intercritical annealing microstructure.

7.3.6 Influence of the Martensitic Transformation on Neighboring Ferrite

The transformation strains caused by the martensitic transformation may be accommodated in different ways i.e. by the selection of suitable variants, formation of a relief (if a free surface is available), or by elastic/plastic deformation of the neighborhood of the austenite/martensite. One additional way for the accommodation of transformation strains which is only available for transformations from the intercritical regime is the elastic or plastic deformation of the surrounding ferrite. The local misorientation angle towards the granular mean orientation of ferrite grains is plotted in Figure 7.13a in order to assess if plastic deformation of the ferrite by the transformation of neighboring austenite occurs. This local misorientation can be assumed to be a good measure of the deformation (stored dislocations) in the grains. The map shows clear evidence of deformation in the ferrite grains close to martensitic islands. The origin of accumulated misorientation in ferrite far away from martensite islands (long range gradients in orientation) has been discussed in Chapter 7.3.1 and is not related to the martensitic transformation.
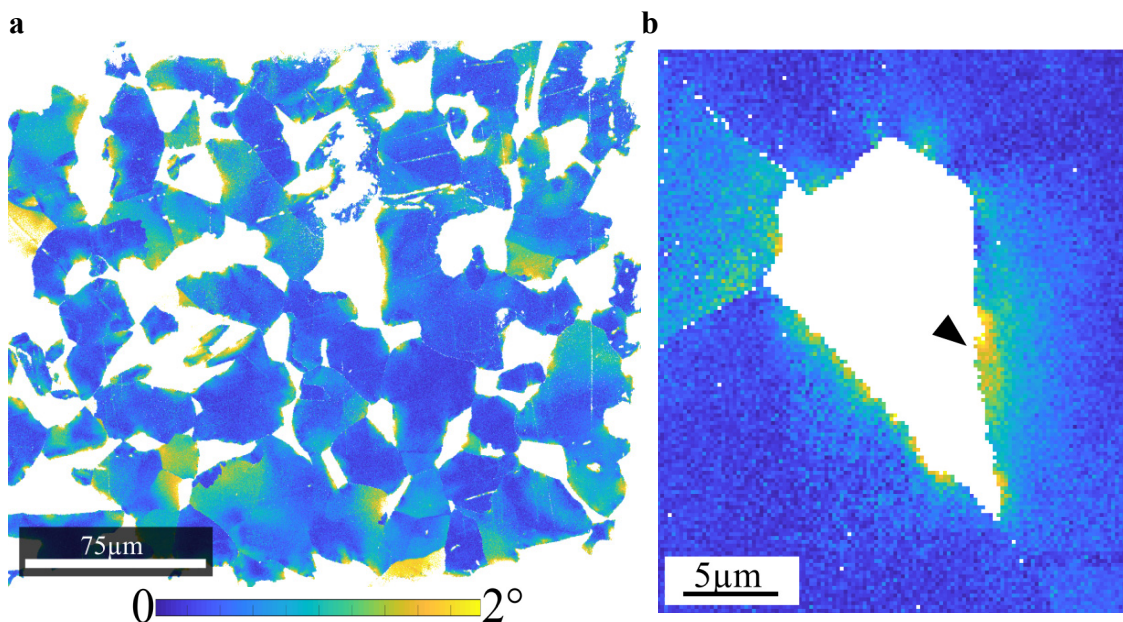
Figure 7.13: a) Mapping of the local misorientation angle towards the granular mean orientation for the ferrite grains. b) Shows a detail of the map shown in **b)** depicting the ferrite grains surrounding the martensite island formed from a single austenite grain.

The map in Figure 7.13b shows the misorientation in the ferrite grains surrounding the martensite island formed from a single austenite grain. This section of the map was already discussed with focus on the formation of EF. The map of the misorientation shows that all neighboring ferrite grains deformed as a result of martensite formation. The effect in the two larger grains is more pronounced. The EF which is located at the right side of the martensite island was more affected by the transformation strains than the other grain at which the martensite nucleated (cf. Figure 7.7b). The stronger deformation of the right grain may have different reasons:

- The stress field of the martensite island is unknown. The transformation strains may be directed to the right side of the martensite island due to the orientation of the austenite grain.

- The ferrite grain on the right may exhibits a higher Schmid factor.

- The EF which was predominantly formed on the right side is softer than IF on the left side.

EF formed during quenching is supersaturated by alloying elements. Partitioning of these alloying elements into the austenite is very limited due to reduced temperatures and the onset of martensite formation. Therefore, the chemical compositions of EF and Intercritical Ferrite (IF) are different. EF is more similar to martensite than to IF regarding its chemical composition. This suggests that the hardness of EF is higher than the hardness of IF. It may be concluded that the higher deformation in the EF is not a consequence of its formation mechanism but has to be caused by the transformation sequence of the martensitic in its vicinity.

An evaluation of the SE images of the transformation sequence indicates that the nucleation of martensite occurred at the phase boundary on the left side of the austenite grain under consideration. An explanation for the higher level of deformation on the right side of the ferrite matrix could then be that it is the result of the growth direction during martensite formation. Transformation strains of the first few martensite laths that formed on the left side of the austenite grain could lead to a deformation of the surrounding austenite. Upon reaching the right side of the grain no more austenite is available (no more accommodation by variant selection or deformation of austenite) and the surrounding ferrite will be deformed to accommodate the transformation stresses.

A striking feature of the map in Figure 7.13a is the very low misorientation in IF that formed during slow cooling at the phase boundary despite the large misorientation in the larger ferrite grains surrounding these smaller grains (cf. analysis in Chapter 7.3.1.3) induced by transformation strains of neighboring martensite.

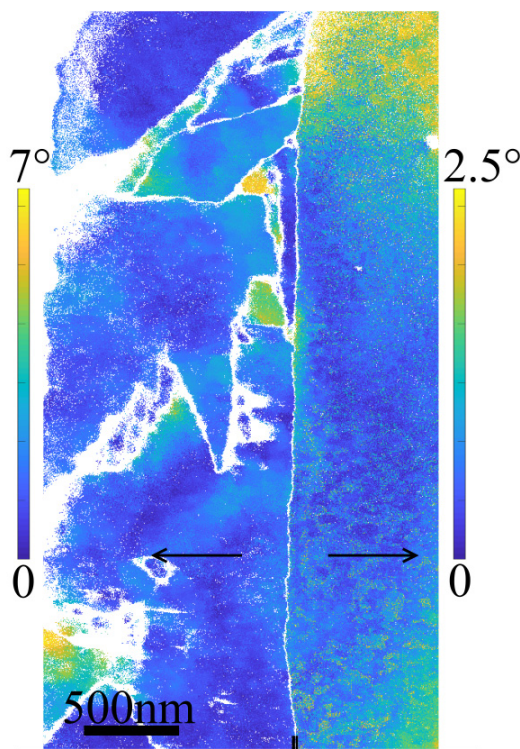**Figure 7.14:** Map of the misorientation angle towards the granular mean orientation corresponding to the TKD OM shown in Figure 7.4a. The left side corresponds to the martensite island and the right side to a single ferrite grain. The vertical line in the middle of the scan is the martensite/ferrite interface. The color values on each side of the mapping correspond to different scales shown on the respective side.

A TEM lamella was extracted from the martensite island marked in Figure 7.3d in order to assess the influence of the free surface and to characterize the ferrite/martensite interface. Figure 7.3c shows that this interface did not exhibit a misorientation close to the KS OR during intercritical annealing. Additionally, Figure 7.7b shows that EF formed during quenching at this interface, which means that the ferrite next to the martensite formed during quenching. The location of the interface which was investigated using TKD is also marked by a black triangle in Figure 7.13b. The results of the TKD scan is depicted in Figure 7.4a. It can be clearly seen, that the ferrite grain shows very low intragranular misorientation. The martensite on the left side of the interface consists mostly of a single variant. These martensite laths seem to be arranged in parallel to each other. Laths of other variants are not oriented parallel to those.

The misorientation angle towards the granular mean orientation was evaluated for this TKD scan in order to assess the accommodation of transformation strains of the martensite in the ferrite through the depth of the sample. Two different scales were used for the scan because martensite regularly exhibits high misorientation angles inside individual laths. A map of this misorientation angle can be seen in Figure 7.14. It clearly shows that the deformation inside the ferrite grain is not only present at the surface of the sample

but also in the bulk. It also shows that this deformation is not homogenously distributed. This suggests that the deformation in the neighboring ferrite through transformation strains is dependent on variant selection in the martensite and/or sequence of martensite formation.

A more detailed STEM BF image is shown in Figure 7.4b. Black spots are visible inside the martensite microstructure on the left side of the ferrite/martensite interface. Such spots do not occur in the ferrite grain in the right part of the image. This observation suggests that carbides are present inside the martensite. Carbides of this size were not present in the microstructure of the fully martensitic EUROFER samples which were analyzed in Chapter 6.

7.4 Summary

The intercritical regime (coexistence of ferrite and austenite) during annealing of EUROFER steel and the subsequent martensite formation were investigated in this Chapter. This enabled the investigation of the $\alpha \rightarrow \gamma$ phase transformation and the study of the formation of martensite from a mixed-phase microstructure. The formation of martensite and epitaxial ferrite and the reciprocal influence of martensite formation on the already present ferrite were analysed.

Orientation maps at different temperatures and consequently different phase fractions revealed that the α/γ-phase boundary curvature depends on the change of temperature. It is concave when temperature is increased and austenite grows and convex when temperature drops and austenite shrinks. Orientation data gathered at the α/γ-phase boundary of all orientation maps recorded at different temperatures were analyzed to calculate the OR between ferrite and austenite. This OR was found to be not as sharp as the austenite-martensite OR observed in Chapter 6 and is located closer to the NW OR than to the KS OR.

The mixed-phase microstructure was found to be stable (low grain coarsening) during intercritical annealing. The austenite phase exhibited very low granular orientation spread (GOS) and a high density of annealing twins. The ferrite phase showed stronger GOS during intercritical annealing. These orientation gradients led to the formation of ferrite subgrains. The magnitude of the misorientation ($< 5.26°$) shows that this process can not be connected to ferrite nucleation events at the phase boundary. However, the observed orientation gradients may be a consequence of minimization of interfacial energy at the phase boundary towards differently oriented austenite grains.

Another microstructural feature which was observed during intercritical annealing is the nucleation of new ferrite grains at the α/γ-phase boundary. These new ferrite grains always had a CSL3 OR towards their neighboring ferrite grains. The origin of these grains is unclear but it can be ruled out that these ferrite grains form during quenching or that they are a consequence of the impingement of other ferrite grains that independently nucleated.

Observation of the microstructure during intercritical annealing and after quenching allowed for a very detailed investigation of the formation of epitaxial ferrite (EF) during quenching. It was found that the amount of epitaxial ferrite that formed during quenching is dependent on the misorientation between ferrite and austenite at the phase boundary. More EF forms if the misorientation at the phase boundary is further away from the KS OR. This is probably a direct consequence of the α/γ-phase boundary mobility. The mobility of the α/γ-phase boundary depends on its misorientation. The higher the misorientation between its misorientation and the KS OR, the higher is its mobility.

Martensite nucleation, variant selection and pairing were analyzed for martensite formation from the intercritical regime. A weaker martensite variant selection was observed for martensite that formed from the intercritical regime in comparison to the martensite that formed from a fully austenitic sample as

analyzed in the previous chapter. For the accommodation of transformation strains, the plastic deformation of the relative soft ferrite might be preferred over variant selection for the accomodation of martensite. The comparison of variant pairing of the fully martensitic sample with the dual-phase sample showed that prevalence for variant pairs with minimal misorientation angles can be observed in the dual-phase material. The OR between austenite and martensite was found to be very close to the OR which was observed in the previous chapter.

Preferred nucleation of martensite at austenite twin boundaries and the associated variant selection rule described in the previous chapter was also observed for the dual phase microstructure. In addition it was found that the α/γ-phase boundary is a preferred nucleation site if its misorientation is close to the KS OR. The crystallographic variant selection rule observed here is very similar to the one observed for the fully austenitic microstructure. The orientation of the martensite variant nucleated at the α/γ-phase boundary has to be close to the orientation of neighboring ferrite. This shows that martensite formation from the intercritical regime is influenced by the presence of ferrite and specifically by its orientation.

Surrounding ferrite is in turn affected by martensite formation in its vincinity. Distinct orientation gradients which were not present during intercritical annealing were found in the ferrite close to the martensite islands. These orientation gradients are a consequence of the deformation of ferrite that was caused by the formation of martensite in its vincinity. TKD orientation maps on a TEM lamella perpendicular to the ferrite-martensite phase boundary showed that the orientation gradients are not homogenously distributed from surface to bulk. They vary in a similar manner as the magnitude of the orientation gradients around martensite islands. This suggests that plastic accommodation of martensite transformation strains are dependent on the martensite variants that form.

8 Austenite Annealing Twins

The formation mechanism and the cause of the formation of annealing twin boundaries in fcc materials remained obscure for over a century and are even not completely clarified until today. The formation of annealing twins has long been observed and described but its underlying mechanisms remain unclear. Besides this fundamental scientific interest, there is technological interest: The role of these special interfaces is highlighted by the concept of grain boundary engineering (GBE) [419] as a tool for the optimization of the mechanical properties by tailored microstructures.

The results of the preceding investigations reveal and underline the role of austenite twin boundaries in the formation of martensite. The aim of this chapter is to clarify the origin of these microstructural features. Dynamic observations of microstructural changes are therefore necessary. Here a combination of EBSD scans with SE image sequences is used to analyze and observe the formation, motion and annihilation of austenite twin boundaries.

8.1 Experimental

An iron foil (99.99%) with a thickness of 2.0 mm was annealed for 20 h at 1000 °C after a carbon coating was applied and slowly cooled (cooling rate of ca. 12 mK/s) in order to achieve a regular ferritic/pearlitic microstructure. The composition of the sample was analyzed after the *in situ* experiment and the subsequent characterization. The analysis of the sample showed that the carbon content of the sample was 0.105 wt.% (analyzed by ICP-OES at IAM-AWP). The sample was ground and polished to obtain a flat surface after this annealing procedure. The last polishing step included an oxide particle suspension (OPS) using a vibratory polisher. The sample was then mounted on the heating stage inside a FEI Nova Nanolab 200 SEM/FIB using Mo clamps. A region of ca. 600 μm x 600 μm was marked by cutting four square shaped holes into the surface using the ion beam of the FIB. The orientations within this region were then mapped using the EBSD (HKL Nordlys) system with a step size of 1 μm.

The orientations of grains of a gold wire bonded to one of the Mo clamps of the heater were determined by EBSD at room temperature. A second EBSD scan of the same region was performed after the sample was heated to 800 °C. The progression of the austenitization was monitored using the SE images from the surface of the sample after increasing the temperature of the sample by 5 K. A third EBSD scan was started after the motion of the interfaces on the surface had stopped. This procedure was repeated at 810 °C, 830 °C and 930 °C. The temperature at the surface of the sample was monitored during the experiment using a two-color pyrometer connected to the SEM chamber by a glass fiber feedthrough. The measured temperatures in the intercritical regime are plotted in Figure 8.1a.

Video sequences of the surface in between the EBSD scans were captured by the SE detector. The motion of the interfaces triggered by a change in temperature could be monitored because of thermal grooving at the interfaces. The identification of the character of the interfaces was achieved by comparison of the SE images with the results of the EBSD scans that were performed before and after the change in temperature. Finally, the sample was quenched using a stream of helium gas which was directed onto the surface of the hot sample. The temperature during quenching was monitored using a thermocouple inside the heater (the gas injection system obstructed the optics of the pyrometer). The temperature curve during quenching is plotted in Figure 8.1b.
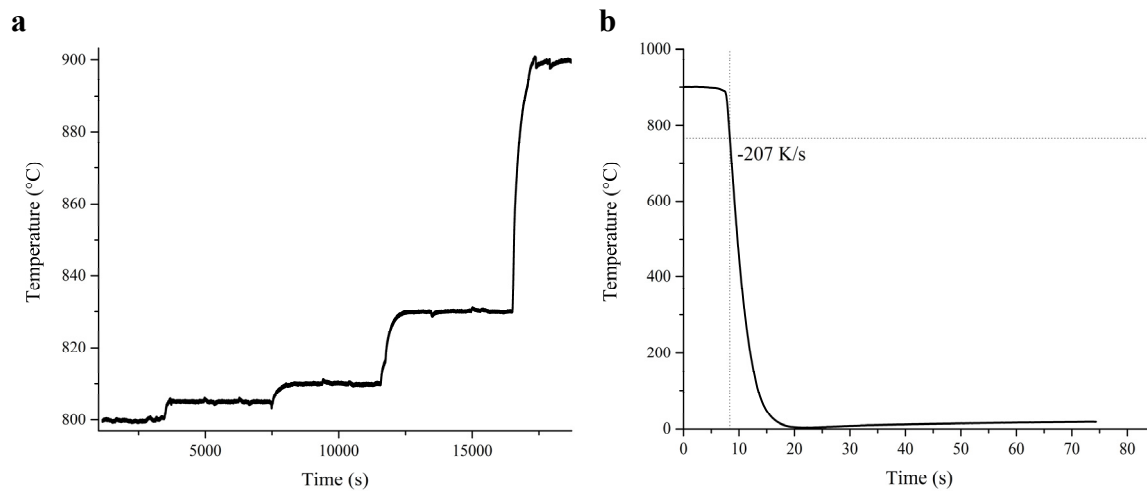
a

b

Figure 8.1: a) Temperature during intercritical annealing. **b)** Temperature during quenching with He gas. The point of maximum quenching rate (-207 K/s) is marked.

After quenching, the orientations of the resulting microstructure and the same reference grains of the gold wire on the Mo clamp were again mapped by EBSD with the same step size. An additional EBSD scan with a higher spatial resolution was performed inside a Zeiss Merlin SEM (449 µm x 397 µm step size 0.5 µm).

8.2 Results

The EBSD scans are depicted in Figure 8.2. The initial ferritic/pearlitic microstructure is shown in Figure 8.2a exhibiting a grain size of 90.5 µm. The ferrite grain size increases with sample temperature and annealing time up to 132 µm at 810 °C. The ferrite grains exhibit a very low granular misorientation independent of the temperature of the sample. A very small amount of the ferrite grain boundaries consists of bcc twins (1%). This fraction grows with increasing temperature to a fraction of ca. 7%.

A relativly constant fraction of ca. 24% of the phase boundary segments exhibits a misorientation close to the KS OR. This fraction increases to 29% at 830 °C where only very small ferrite islands are present. This is caused by the lower mobility of phase boundary segments that exhibit a misorientation close to the KS OR. Smaller austenite islands like the ones observed at 800 °C seem to exhibit a phase boundary with a misorientation close to KS more frequently than larger austenite islands.

The austenite phase at 800 °C exhibits an average grain size of 49.2 µm. The size of the austenite grains increases to 94.8 µm at 900 °C. A large fraction of austenite/austenite interfaces consists of austenite twins. The fraction of austenite twins with regard to the overall length of austenite/austenite interfaces amounts to 68% at 800 °C. This fraction decreases to 48% only after full austenitization is reached due to the disappearance of the transformation interface and the associated increase in austenite boundaries.
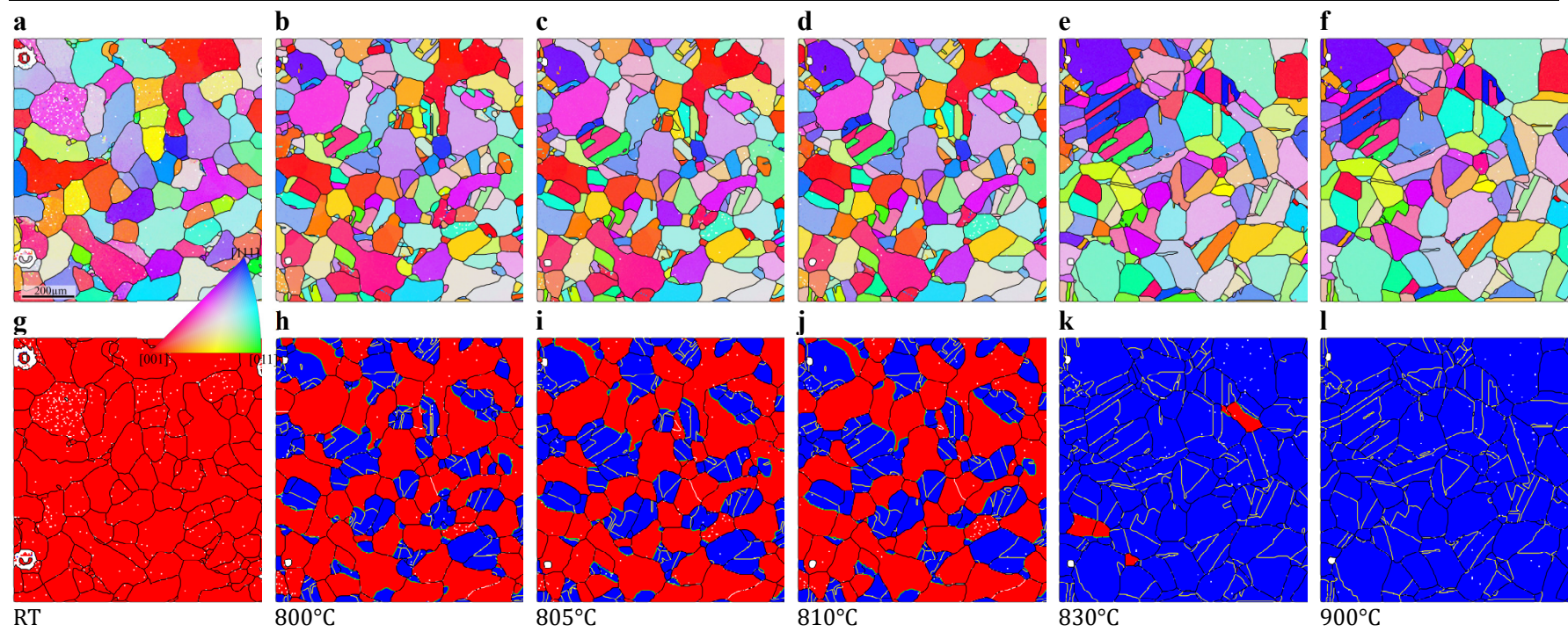
Figure 8.2: a)-f) EBSD maps showing the orientations measured on the surface of the sample at RT, 800 °C, 805 °C, 810 °C, 830 °C, 900 °C, respectively. **g)-l)** show the corresponding phase maps. Austenite regions are marked in blue and ferrite regions are marked in red. Grain boundaries are drawn in black, CSL3 boundaries in austenite and ferrite in yellow and white, respectively. Phase boundaries exhibiting a misorientation close (tolerance angle ω < 5°) to the KS OR are marked in green.

The motion of interfaces can be clearly seen in the sequence of SE images of the surface of the sample during the growth of the austenite phase fraction between 810 °C and 830 °C. A comparison of these images to the OM at 810 °C and 830 °C enables the identification of phases and orientations of grains and the character of their interfaces (grain, phase and twin boundaries). Twins typically consist of different boundaries. The coherent CSL3 boundary which has low energy and the incoherent part which conatins more lattice defects and therefore costs more energy. In the following, the long edges of the twins in the images and maps are associated with the coherent boundary while the short edges are interpreted as incoherent twin boundaries. Figure 8.3 shows one section in which the formation of new austenite twin boundary segments by the motion of the austenite-ferrite phase boundary can be observed. The phase map in Figure 8.3a shows the initial state of this section on the sample. The black triangle marks a triple junction formed by an austenite twin with the phase boundary. The phase boundary starts to move due to an increase of the temperature from the austenite grain into the ferrite grain marked in Figure 8.3b. The SE images in Figure 8.3c-e show the motion of the phase boundary which is marked by red triangles. The triple junction moves along with the phase boundary resulting in a growth of the twin boundary (i.e. of both twin related grains). Figure 8.3f shows a phase map of the result of the phase transformation. The segment of the twin boundary which was created by the motion of the phase boundary is located between the two black triangles.
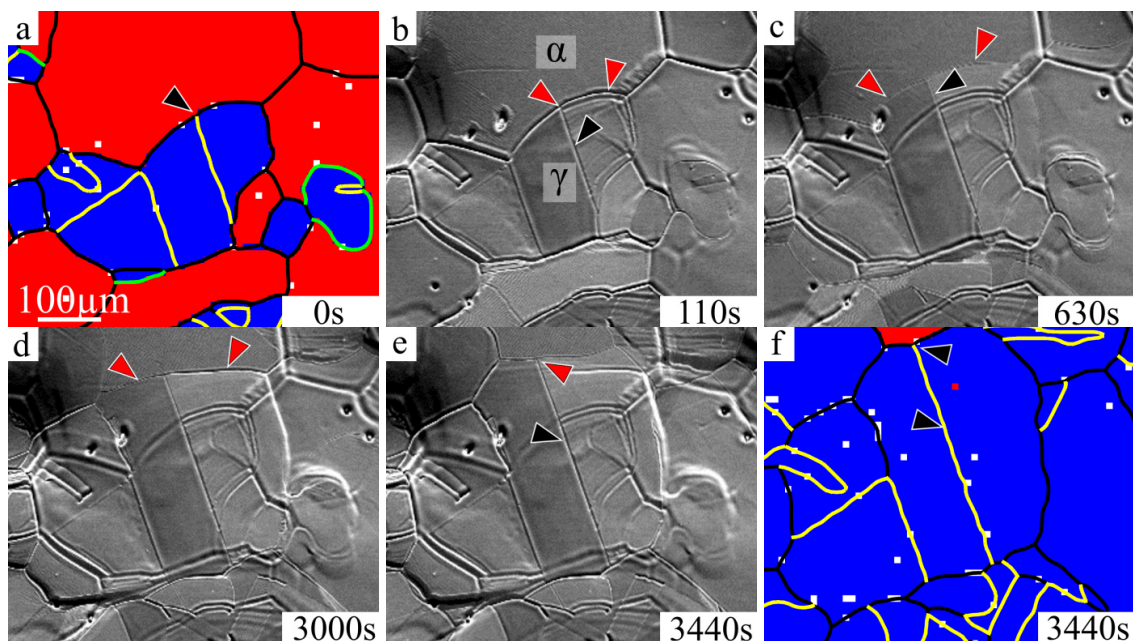
Figure 8.3: Formation of a new twin segment by the motion of the austenite-ferrite phase boundary. **a)** shows a phase map corresponding to the region depicted in the SE images. The measurement points assigned to the austenite phase are shown in blue. The ferrite phase is shown in red. Austenite twins are shown in yellow, phase boundaries with a misorientation close to the KS OR are marked in green. The triangle shows the triple junction of a twin and the phase boundary. **b)-e)** show the progression of the phase transformation by the motion of the phase boundary. The phase boundary is marked by red arrows. **f)** Shows a phase map of the same section on the sample after 3440s when equilibrium was reached.

A second example is shown in Figure 8.4. The phase boundary marked by red triangles shown in Figure 8.4b exhibits a strong curvature which can be clearly seen in Figure 8.4b marked by a black triangle. In Figure 8.4c a twin forms at the point of maximum curvature which is marked by a black triangle. The incoherent part of the twin forms first and the twin grows with the motion of the transformation front which is marked by red triangles in Figure 8.4d. The twin is highlighted by a black triangle. Figure 8.4 shows the full twin ending at an austenite grain boundary after the transformation is complete. The phase map of the final state shown in Figure 8.4f indicates that the twin grew in thickness between the end of the SE observation and the end of the EBSD scan.
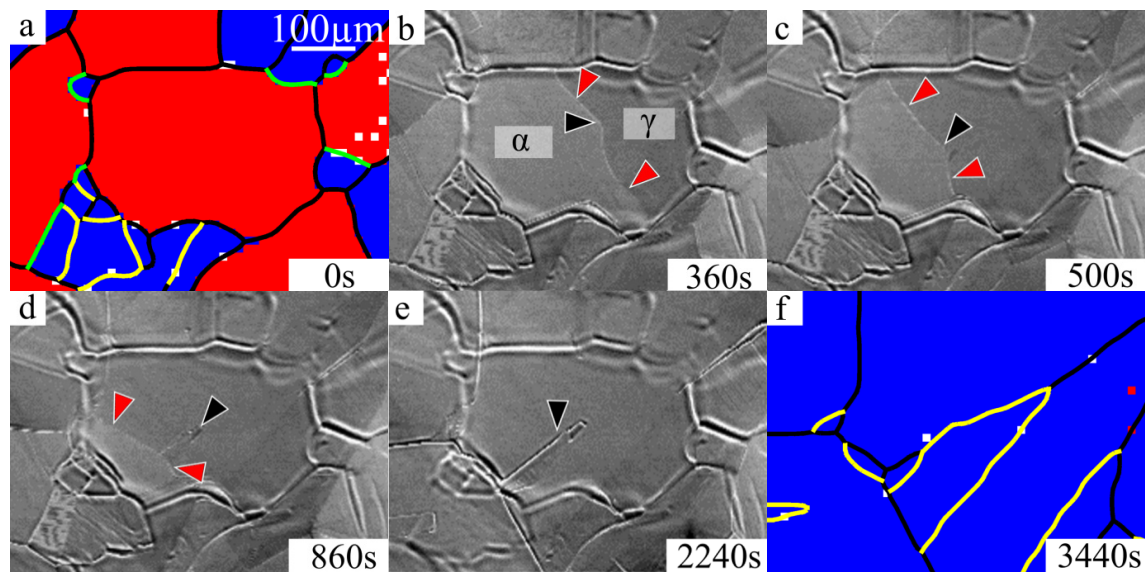
Figure 8.4: Formation of an austenite twin during the motion of an austenite-ferrite phase boundary at the point of maximum curvature. **a)** and **f)** show phase maps of the initial and final state, respectively. SE images **b)-e)** show the evolution of the surface of the sample between initial and final state.

A similar event where the formation of fresh twin boundary segments is caused by the motion of the phase boundary is shown in Figure 8.5. In contrast to the growth of an existing twin which was described above, here new twinned structures form during transformation. Figure 8.5a shows the initial state of the section before the temperature is increased. Figure 8.5b shows the motion of the austenite-ferrite interface. The interface is marked with red triangles. The first twinned grain emerging from the phase boundary is marked with a black triangle. Figure 8.5c shows the formation of a further twin adjacent to the triangular shaped small twinned grains marked with a black triangle.
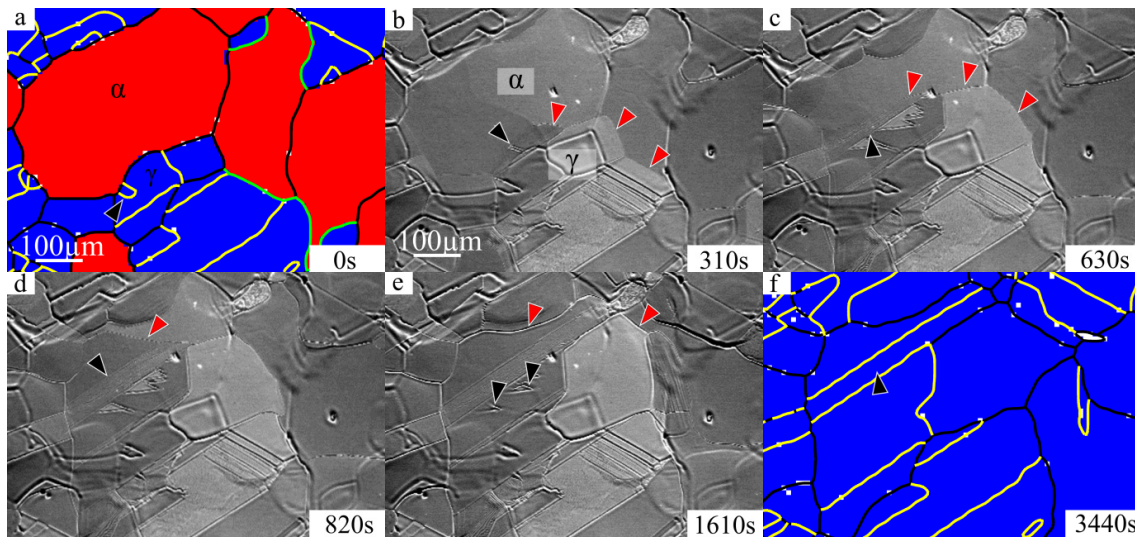
Figure 8.5: Formation of new austenite twins by the moving austenite-ferrite phase boundary. **a)** Initial state of the area. **b)** Continuation of the phase transformation by motion of the α-γ phase boundaries into the ferrite grain. The interface is marked with red triangles. The first twin formed from the interface is marked by a black triangle. **c)** shows the formation of a second twin adjacent to the first ones. **d)** shows the growth of this twin until the final state in **e)** and **f)** is reached. The black triangles in **e)** show the disappearing twinned triangular segments. The black triangle in **f)** highlights the twin which was formed.

The moving phase boundary is marked with red arrows. The further growth of this twin is shown in Figure 8.5d: The twin is marked with a black triangle and the moving interface is marked with red triangles. The disappearance of the smaller triangular twinned structures is shown in Figure 8.5e. The final state of the section is shown in Figure 8.5f. The twin lamella that formed by the motion of the transformation interface is marked by a black triangle. The smaller triangular twinned structures could not be detected in the EBSD scan.

The following two detailed figures show two processes which lead to the annihilation of austenite twins. The first one is depicted in Figure 8.6 starting with the growth of an existing twin by the motion of the phase boundary. This can be seen in Figure 8.6a and Figure 8.6b. The SE images in Figure 8.6c-e show the reduction of the size of the twin by the motion of the incoherent part of the twin towards the grain boundary at which the twin is connected. A comparison between the phase map at 830 °C and the phase map at 900 °C which are depicted in Figure 8.2k and Figure 8.2l shows that the size reduction of the austenite twin continues slowly during annealing.

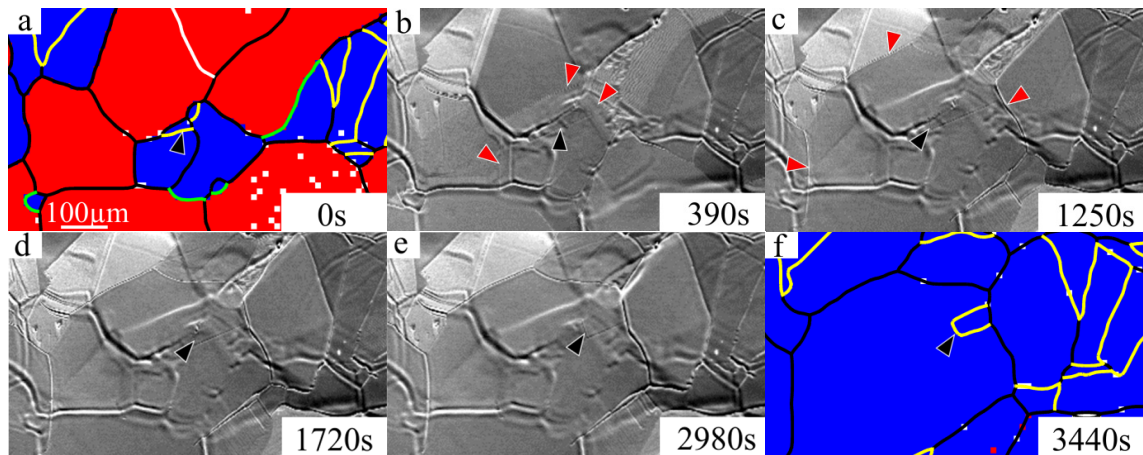**Figure 8.6:** Growth and subsequent size reduction of an austenite twin. **a)** shows a phase map of the initial state of the twin. The twin is marked with a black triangle. **b)** illustrates the growth of the twin by motion of the phase boundary. The twin is marked with a black triangle, the phase boundary is marked with red triangles. **c)** shows the state of the twin after shrinkage started. The incoherent boundary is marked by a black triangle. The phase boundary is marked by red triangles. **d)** depicts the size reduction of the twin by motion of its incoherent boundary. **e)** shows the size of the twin after further shrinkage. **f)** the final state of the austenite twin in an EBSD phase map.

Another process leading to a reduction of twin boundary length can be observed in Figure 8.7. The initial state at 805 °C is shown in Figure 8.7a. The twin boundary in this OM which is marked with a black triangle starts moving after the temperature is increased. The austenite grain in which this twin is located is mostly surrounded by ferrite grains. These phase boundary segments barely move. The same twin boundary can be seen in Figure 8.7b marked by a black triangle just before it starts to move. The motion starts once 810 °C is reached. The motion of the twin boundary can be observed in Figure 8.7b-e. It moves significantly more quickly than phase boundaries or grain boundaries in the same sample. The final state can be seen in the EBSD scan shown in Figure 8.7f. It shows that the grain changed its orientation by the motion of the twin boundary. At this point the initially small twin has consumed the whole austenite grain.
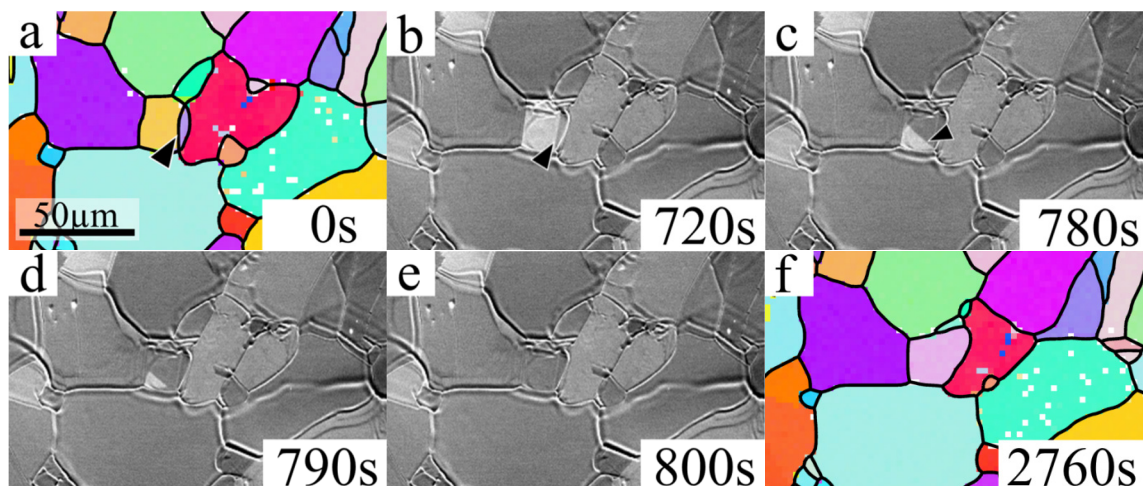
Figure 8.7: Motion of a twin boundary during the temperature change from 805 °C to 810 °C. **a)** Shows an EBSD scan of the sample before the change of temperature. The twin boundary is marked with a black triangle. **b)-e)** show SE images of the surface during the motion of the twin boundary. The boundary is marked with a black triangle in b) and c). **f)** shows an EBSD scan of the same section after no motion on the surface were detected after reaching 810 °C.

An EBSD scan of the microstructure after quenching at the same location as shown in Figure 8.2f and Figure 8.2l is shown in Figure 8.8b. The SE image in Figure 8.8a of the surface shows the formation of a surface relief which indicates the involvement of a displacive phase transformation during quenching. Some Widmanstätten structures can be seen in the EBSD scan but also some regions in which martensite/bainite formed. Different ferrite morphologies can be seen ranging from Widmanstätten ferrite to martensite.

a

b
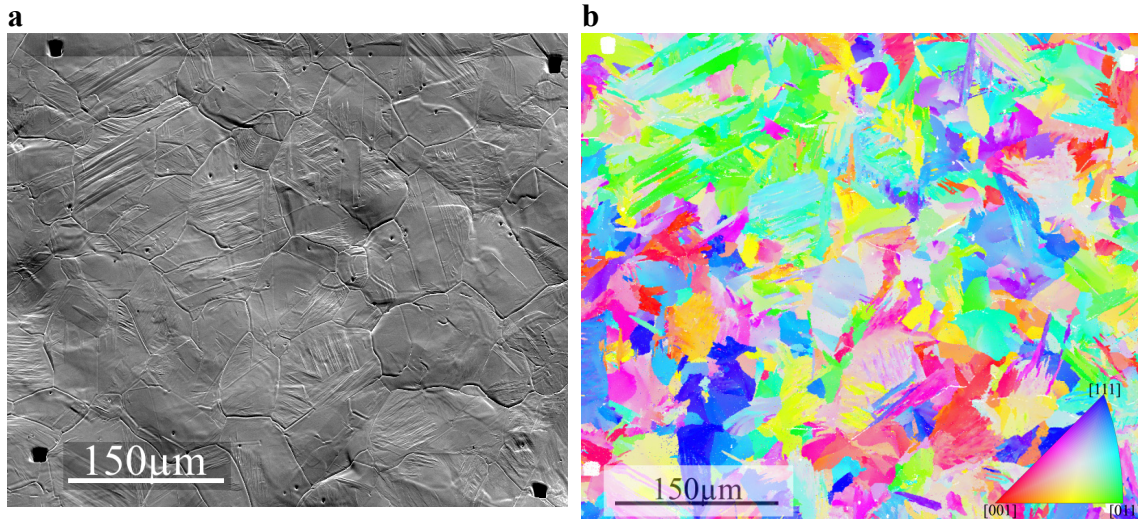
Figure 8.8: a) SE image of the surface at the same location as all prior EBSD scans after rapid cooling from 900 °C. The surface relief formed in some regions indicates displacive processes during transformation. **b)** shows the EBSD measurement of the same location corresponding to the SE image in a).

8.3 Discussion

8.3.1 OR Between Ferrite and Austenite

The characterization of the phase boundary between austenite and ferrite in the intercritical annealing step shows that the phase transformation is dominated by a misorientation at the phase boundary that is close to the KS OR. The OR between the ferrite and the austenite phase is shown in Figure 8.9a in a (100) pole figure. The superimposed orientations of the variants of the KS OR shows that the OR between ferrite and austenite in the intercritical regime is close to the KS OR but exhibits large scatter around the ideal KS OR. It also shows that the variant selection processes seem to be active.

The orientation data of the intercritical annealing steps where austenite and ferrite coexist can be used to calculate the exact OR between austenite and ferrite for this alloy. Therefore, the misorientation at the austenite-ferrite phase boundary is used. A MDF is calculated from the fcc/bcc orientation pairs. Finding the maximum of the MDF gives the dominant misorientation which can then be expressed as parallel planes and directions. The result of this calculation for all misorientations at the phase boundary for all temperatures is:

$$\{1\bar{1}0\}_\gamma \parallel \{100\}_\alpha$$
$$\langle 22\bar{1}\rangle_\gamma \parallel \langle 04\bar{1}\rangle_\alpha$$

<div align="right">Eq. 8.1</div>

This OR is 6.8° away from the KS OR and 4.3° away from the NW OR and results in 12 product variants.

A comparison of the microstructures at different temperatures shows that the velocity of phase boundaries exhibiting a misorientation close to the KS OR is very low. The highest velocities can be observed for twin boundaries which can migrate inside a grain. The motion of interfaces observed by SE images does not completely cease after a certain temperature is reached: The combined motion of twin boundaries and phase boundaries can be observed after that point until equilibrium is reached. The dynamic nature of this equilibrium is also evident from the growth of some ferrite grains upon increasing temperature.

8.3.2 Annealing Twins in Austenite

The microstructure of the austenite phase features a high density of CSL3 boundaries. A histogram of the distribution of misorientation angles at austenite-austenite grain boundaries is shown in Figure 8.9b. The untextured uncorrelated misorientation angle distribution is plotted in the same diagram as a red line for comparison. This shows that twin boundaries are the most common boundary in the austenite phase. The fraction of twin boundaries for the fully austenitic sample at 900 °C was found to be 48%. The overall twin boundary length can be observed to double from 800 °C to 900 °C. A twin boundary density may be calculated by relating the twin boundary length to the surface covered by austenite. This calculation shows that the austenite twin density decreases from 0.02 $/m^2$ to 0.12 $/m^2$ during the increase of the temperature from 800 °C to 900 °C.

a

b
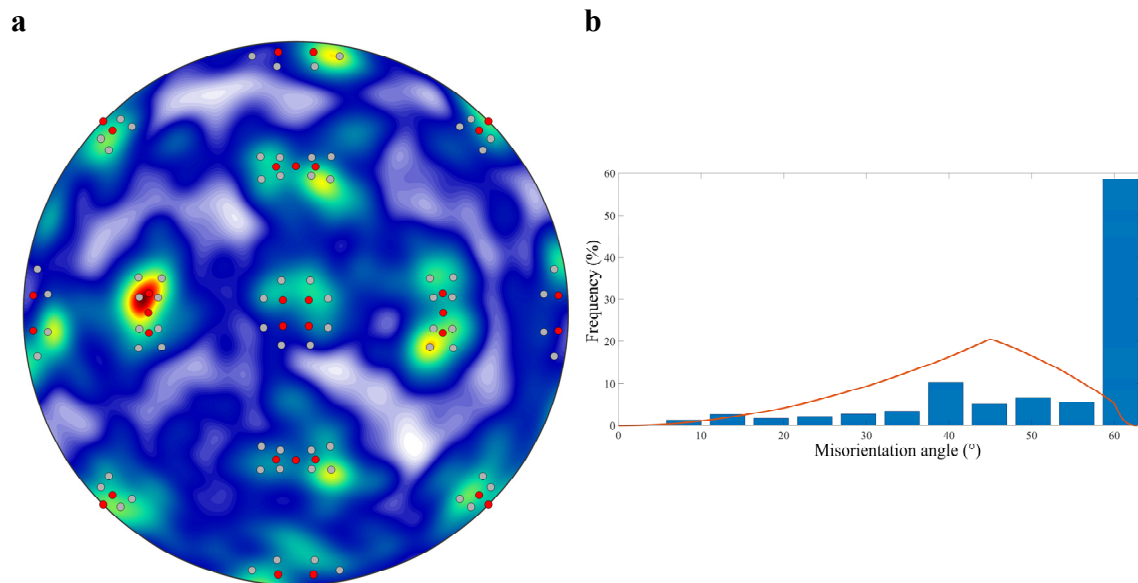
Figure 8.9: a) (100) pole figure representing the OR between austenite and ferrite at the phase boundary. The displayed misorientations are from the EBSD scans at all temperatures. The gray circles represent the orientations of the corresponding KS variants. The red marks show the orientations of the variants of the OR shown in Eq. 8.1. **b)** shows the misorientation angle distribution of austenite grain boundaries which were taken from the EBSD scans at all temperatures at which austenite was present.

The higher density of twin boundaries in the austenite phase when compared to the ferrite phase is a direct consequence of the low Stacking Fault Energy (SFE) of austenite. The stacking fault energy of austenite depends on the composition of the alloy, mainly on Mn, Ni and Cr [420], [421]. The largest change of the SFE is caused by the carbon concentration in the alloy [422], [423]. The SFE of the austenite phase in pure FeC alloys is 15-60 mJ/m^2 [424], which is lower than the SFE of copper (41 mJ/m^2 [425]).

Lischewski et al. [25] observed an increase of austenite twin boundary density with increasing austenite phase fraction in their *in situ* EBSD experiments on a 0.05C-0.28Si-0.82Mn steel. They explained this increase with the formation of growth twins during austenite grain growth after the transformation. This conclusion was solely based on EBSD scans conducted during austenitization without considering SE images from the surface of the sample.

The question that arises from this analysis is how the twins in the austenite phase form. It would be reasonable to consider these twins to be annealing twins which are reported to be formed by moving grain boundaries during recrystallization or grain growth at elevated temperatures [426]. An evaluation of the EBSD scans at 830 °C and 900 °C combined with the SE image sequence of the surface of the sample at the same location in between these temperatures shows that the austenite twins are formed or at least grow at the moving austenite-ferrite phase boundary.

8.3.3   Nucleation of Annealing Twins at the α-γ Phase Boundary

The observations suggest that all austenite twins directly form at the austenite-ferrite phase boundary. The formation of austenite twins from a moving grain boundary which is usually reported as the cause for the formation of annealing twins during annealing or recrystallization was not observed here. Three different modes were identified which lead to an increase in twin boundary length in the austenite phase.

The first mode is based on an already existing twin boundary as illustrated in Figure 8.3. A triple junction of an austenite twin boundary with the austenite-ferrite phase boundary is present in the initial state. Upon increasing the temperature, the phase boundary starts to move into the ferrite grain. The triple point moves along with the phase boundary and this leads to an elongation of the austenite twin boundary by the simultaneous growth of both twin related grains. The same effect can be observed at most triple junctions of the austenite-ferrite phase boundary and an austenite twin. It can be assumed that the sample was in a steady state during the EBSD scan because the measurement was started after no motion of any interfaces was detectable in the SEM. This implies that the angles which can be observed at triple junctions can be considered as equilibrium angles representing the relative energies of the different boundaries. This suggests that the energy of the twin boundary is negligible compared to the energy of the austenite-ferrite phase boundary. It can be clearly seen that the phase boundary is not affected by the twin boundary that it is connected to. This is also the case during the transformation. The two twinned crystals seem to grow independently. The twin boundary does not cause any drag effect in the motion of the phase boundary that is connected to them.

The second mode can be seen in Figure 8.4. The moving phase boundary which is not connected to a twin forms twins during its motion into the ferrite grains. The moving phase boundary is marked with red triangles in Figure 8.4b and Figure 8.4c. The black triangle highlights one point on the boundary where the boundary exhibits maximum curvature. It is not clear if the friction of the boundary is higher in this location or if an obstacle (carbide, particle) retards its motion. Figure 8.4c and Figure 8.4d show that an austenite twin forms at the point of highest curvature leading to a decrease of the curvature of the phase boundary. The twin nucleates by the formation of the incoherent part which later remains inside the austenite grain. In contrast to the first mode, additional twins can form by this mechanism.

The third mode can be observed in Figure 8.5: Here the formation of several twins from the phase boundary which are connected to an already present, very fine twin can be seen. This first twin is almost parallel to the phase boundary. A complex structure of three small triangular twinned austenite grains forms at the phase boundary. This can be seen in Figure 8.5b and Figure 8.5c. These crystals do not form like the ones in Figure 8.3. Instead a new crystal exhibiting a twin OR to the parent grain forms. These triangular grains are very similar to the small twinned grain which is marked by a black triangle in Figure 8.5a. The similarity in shape suggests that this twin shares the same orientation as the twinned crystals that forms at the phase boundary. Starting from these small grains a new twin grows from the phase boundary in Figure 8.5c and Figure 8.5d. This twin has the same orientation as the first twin at which the processes started. The smaller twins which formed in Figure 8.5b start to dissolve after the large twin appears and cannot be detected anymore in the EBSD scan at 900 °C.

A nucleation of an austenite twin from a phase boundary exhibiting a misorientation close to the KS OR was not observed due to the very low velocity of these interfaces. The observations do not contradict the classical description of the formation of annealing twins during grain growth or recrystallization but show an additional mechanism for the formation of annealing twins at moving phase boundaries.

Several possible fundamental mechanisms for the formation of annealing twins were proposed. Gleiter et al. [427] and others [428] described the formation of annealing twins based on grain growth accidents. Dahs et al. [429] and Meyers et al. [430] showed that twin nuclei consist of stacking fault packets. Pande et al. [431] proposed a mechanism in which the formation of annealing twins is based on the formation of Shockley partial loops on consecutive $(111)_\gamma$ planes during grain growth. Based on this, an additional model was proposed by Mahajan et al. [426] which tries to unify all of the previous models.

The structure of the austenite-ferrite interface is supposed to consist of ledges [432]–[438]. These ledges may be assumed to consist of $(111)_\gamma$ planes on the surface of the austenite crystal. According to Pande et al. [431] the probability of a growth accident to occur on this plane is proportional to the velocity of the boundary. This is in contradiciton to the observation made in Figure 8.4 because here the twin nucleates at the point where the boundary moves with the lowest velocity. The probability for a growth accident on a $(111)_\gamma$ plane may however not be directly dependent on the velocity of the interface but also on its structure i.e. the length of the $(111)_\gamma$ steps in the interface. The probability for a growth accident to occur should be proportional to the SFE and proportional to the amount of atoms transferred through a $(111)_\gamma$ ledge of the austenite ferrite interface. This would explain the formation of the twin in Figure 8.4 where the twin forms at the point of the interface which is moving with the lowest velocity. The resulting curvature may lead to a change of the structure of the interface in which the proportion of $(111)_\gamma$ ledges becomes larger increasing the probability of growth accidents. This may explain the correlation between interface curvature and twin nucleation probability.

Following the discussion of Mahajan et al. this could then lead to the formation of an annealing twin by the emission of Shockley partial loops. The significantly higher frequency of twin formation at the transformation front compared to twin formation from grain growth is a consequence of the lower mobility of the grain boundary in comparison to the relative heigh velocity of the phase boundary.

The mechanisms for twin nucleation leading to the structures observed in Figure 8.5 are complex. Multiple twinning occurs by the interaction of an already existing twin with the phase boundary. The newly formed twin nucleates after the already existing twin stopped to grow with the moving phase boundary. This indicates that the phase boundary detaching from the austenite twin leads to the nucleation of the new twin. It is also clear from Figure 8.5d (and Figure 8.4) that the moving phase boundary can contain the incoherent part of the twin.

It is not clear if transformation stresses at the interface support these processes or are even prerequisites for them. It may be assumed that diffusion will lead to a very fast relaxation of transformation stresses so that they are not active during twin nucleation.

8.3.4 Annihilation of Annealing Twins and Twin Boundary Migration During Annealing

Two different processes leading to a reduction of twin boundary length were also observed during annealing. The annihilation of twins was already described in the observations made in Figure 8.5: The smaller triangular twinned grains disappear during annealing. The same effect was observed for the twinned grain marked by a black triangle in Figure 8.5a. This may be caused by the low size and relative high amount of incoherent boundary compared to the overall boundary length of the twinned grain.

The first mechanism is illustrated in Figure 8.6: After initial growth of an existing twin, the twin started to shrink. This process commenced by the motion of the incoherent part of the twin towards the grain boundary containing the other incoherent part of the twin so that the twin lamella became shorter. The process started after the character of the grain boundary containing the incoherent part of the twin changed due to the ongoing phase transformation. The maximum velocity of the incoherent part of the twin was observed close to the beginning of its motion. From then on, the velocity of the incoherent part decreased continuously. The same twin can therefore be seen to be still present at the end of the experiment just before quenching at 900 °C in Figure 8.2k. This mechanism that consist in a decrease of the twin size by the motion of the incoherent part(s) of the twin towards each other may also be responsible for the annihilation of the twin which was observed in Figure 8.4.

A second mechanism was observed several times during annealing which can lead to a reduction of twin boundary length in the austenite phase during annealing. The migration of a twin boundary through an austenite grain, as observed in Figure 8.7, may lead to a reduction of the overall twin boundary length in the austenite phase. This motion leads to a change of the orientation of the grain at a significantly higher velocity as it would be possible by purely diffusive processes. The twin boundary was curved and therefore its motion must involve the migration of both, the coherent and the incoherent part of the twin.

It is not clear what the driving forces for the migration of the twin boundary may be. The local crystallography of the surrounding of the grain did not change during the observation, as the surrounding grains did not change significantly in size or orientation before and after the experiment. The migration of the twin boundary did not result in a shape change of the grain that would be expected. Brandl et al. [439] suggested a structural model for non-coherent CSL3 boundaries consisting of a succession of coherent twin boundary segments and incoherent steps consisting of three Shockley partial dislocations each. The existence or formation of such a structure may occur localized in the vicinity of the (non CSL3) grain boundary which forms a triple point with a CSL3 boundary. They further motivate a migration mechanism since the partial dislocations are glissile dislocations common to both adjacent crystals. A successive motion of these dislocations along the boundary can then lead to a motion of the twin boundary. A further result of this consideration is that the CSL3 boundary has a net zero Burgers vector suggesting that the shape change resulting from CSL3 boundary migration may be zero. Nucleation and emission of Shockley partial loops is necessary for this mechanism to propagate. A self-propagating mechanism would lead to the migration if the stress concentration at the triple point of the twin boundary and the grain boundary may provide the stresses necessary for the emission of Shockley partial dislocations [440], [441]. The driving force for the migration of the twin boundary may then be extremely small and the feasibility of twin boundary migration mostly dependent on the character of the grain boundaries which contain the incoherent part of the twin boundary. In contrast to the models proposed for mechanically induced twin boundary migration, there is no back stress acting on the migrating twin boundary resulting in a constant migration velocity.

8.3.5 Characterization of the Microstructure After Quenching

The goal of this chapter is to investigate the intercritical regime of this simplified steel with a focus on phase evolution and the formation of twins. Besides that, also quenching was performed and the resulting microstructure was investigated. The microstructure that this clean and conceptually simple FeC steel develops differs strongly from the EUROFER steel in chapter 6 and 7. In this section this microstructure is examined.

After quenching, the microstructure of the sample does not exhibit the typical morphology of lath martensite. The surface relief and the morphology suggest that some areas transformed by a displacive transformation. The orientations of the microstructure before and after quenching were compared. The result is plotted as a (100) pole figure in Figure 8.10a where the variants of the KS OR are marked with grey points. It shows a good agreement with the KS OR. It contains more scatter than fully martensitic samples (cf. Chapter 6.3.7). A comparison of the microstructure before and after quenching by superimposing the two OM reveals that the austenite grain boundaries acted as nucleation sites for ferrite and bainite i.e. ferrite grains can be found that extend over Prior Austenite Grain Boundaries (PAGBs). Lath-like transformation products have the tendency to be situated inside larger prior austenite grains and do not extend across prior austenite grain boundaries.

The misorientation angle of the final orientation towards the closest KS variant which was calculated from the austenite orientation measured at at a given location is mapped in Figure 8.10b. It can be used to distinguish between the different constituents of the complex microstructure observed after quenching.
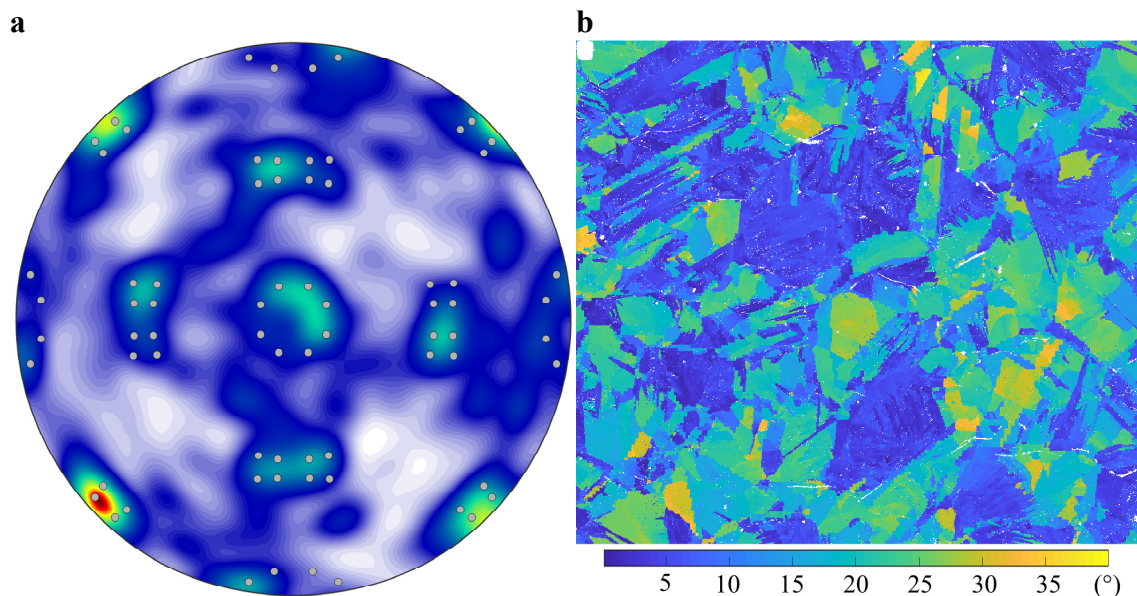
Figure 8.10: a) (100) ferrite pole figure visualizing the OR between austenite and the transformation product. **b)** map of the misorientation angle of the product orientations towards the orientation of the nearest KS variants.

This map illustrates that regions where transformation products exhibit orientations in good agreement with the KS OR and regions where the orientations of transformation products that are far away from the orientations of the KS variants can be distinguished. It shows that lath or needle-like constituents are in good agreement with the KS OR. These are bainite, martensite and Widmanstätten ferrite. An analysis of the ORs of these constituents shows that all of them maintain an OR close to the KS OR to the austenite orientation.

Figure 8.11a shows the pole figure of the transformation products inside one PAG. The OM of the transformation product is shown in Figure 8.11b. It suggests that the transformation of this PAG is dominated by diffusive processes. Large ferrite grains that exhibit characteristic orientation gradients can be seen.

Figure 8.11: Orientation analysis for the transformation products developed from one austenite grain dominated by diffusive processes. **a)** shows the (100) pole figure where the data points are colored according to the IPF map in **b)** The orientations of the KS variants calculated from the austenite orientation of the grain are superimposed in gray. **c)** Map of the smallest misorientation angle of the transformation product towards the nearest KS variant calculated from the orientation of the austenite grain. The color bar can be found in Figure 8.10b.

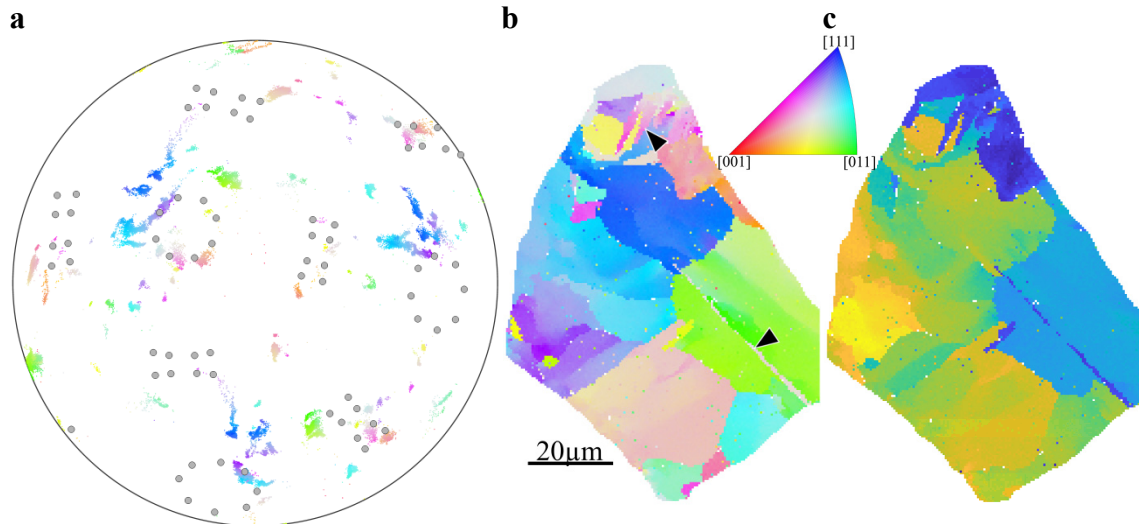The pole figure only exhibits a very weak agreement with the KS OR. This is further illustrated in Figure 8.11c where the misorientation angles between the product orientation and the closest theoretical KS variants are mapped. It shows that large parts of the misorientations between parent and product phase are not in accordance with the KS OR. Only a few smaller regions at the top and the right side show better agreement. These parts of the microstructure consist of Widmanstätten ferrite. The smaller ferrite grain at the top of the PAG exhibits an orientation close to a KS variant and developed Widmanstätten needles (marked with a black triangle in Figure 8.11b). This behavior can be observed multiple times in this microstructure. Widmanstätten needles which form as sideplates i.e. with an orientation gradient to an allotriomorphic ferrite grain are only formed if this ferrite grain exhibits a KS OR to the PAG.

The second Widmanstätten needle in the former austenite grain is not a sideplate as it is not connected to an allotriomorphic ferrite grain. This long and narrow ferrite needle which grew from the grain boundary on the right into the grain shows very good agreement with the KS OR. Allotriomorphic ferrite grains exhibit a small granular misorientation when compared to displacive transformation products. They consist of subgrains which are clearly recognizable in Figure 8.11b.

The opposite case to Figure 8.11c can be found in Figure 8.12c: The PAG shown there is almost fully in accordance with the KS OR. The pole figure in Figure 8.12a shows the KS variants which were calculated from the measured orientation of the PAG and the product orientations marked with the same color key which was used in Figure 8.12b. The pole figure shows that there is a good agreement with the KS OR. This indicates that the transformation of the grain was dominated by displacive processes. Martensite laths formed inside the grain without contact to the PAGBs. The majority of displacive transformation products are not in contact with randomly oriented PAGBs but austenite twins. However, this is not the case for Widmanstätten ferrite which grows from either PAGBs or allotriomorphic ferrite (as sideplates).
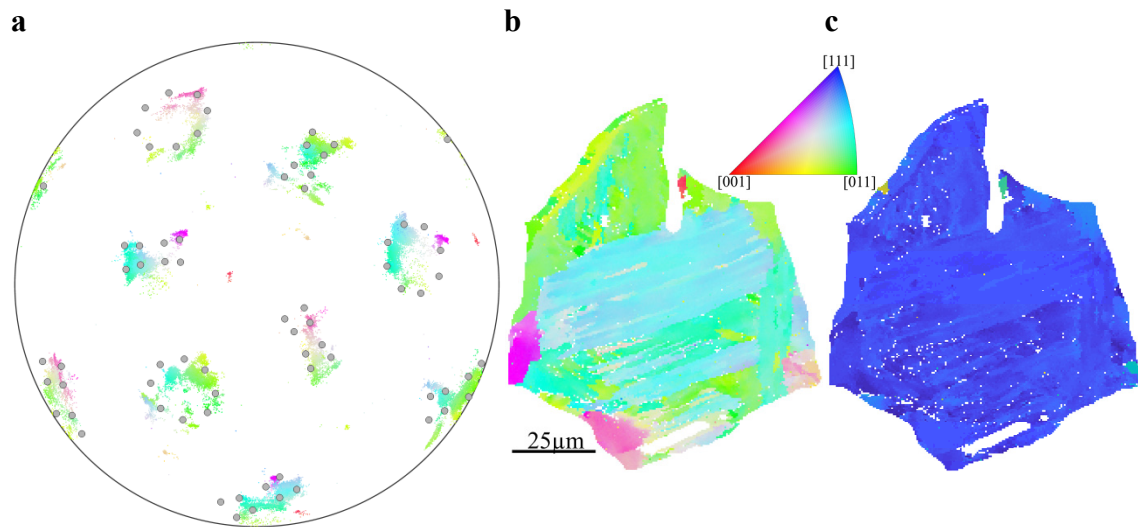
Figure 8.12: Orientation analysis for the transformation products formed from one austenite grain dominated by displacive processes. **a)** shows the (100) pole figure where the data points are colored according to the IPF map in **b)** The orientations of the KS variants calculated from the austenite orientation of the grain are superimposed in gray. **c)** Map of the smallest misorientation angle of the transformation product towards a KS variant calculated from the orientation of the austenite grain. The corresponding color bar can be found in Figure 8.10b.

Variant pairing and selection was analyzed only for transformation products for which the misorientation angle between parent and theoretical product orientation (calculated using the KS OR) is smaller than 7°. Otherwise the result would be heavily affected by the misorientations between neighboring allotriomorphic ferrite grains or other products of diffusive transformation processes. This means that no distinction between Widmanstätten ferrite and martensite could be made in this analysis. The histogram with the distribution of product KS variants is depicted in Figure 8.13b. It indicates that a low tendency towards variant selection was present during transformation. This is further confirmed by the low variant selection strength factor of $k_{VSS} = 0.251$. The k_{VSS} found here is significantly lower compared to the fully martensitic EUROFER steels (cf. Chapter 6) but higher than the variant selection strength factor found for dual-phase EUROFER (cf. Chapter 7). Variant selection is influenced by transformation stresses. The low variant selection found for this material and heat treatment indicates that transformation stresses are lower compared to the other samples or that transformationen stresses can be accommodated more effectively by deformation of the matrix. The fact that variant selection strength is higher for this FeC material compared to the dual-phase EUROFER sample suggests that the transformation stresses are lower in the FeC sample if it may be assumed that ferrite in the EUROFER alloy is stronger than ferrite in the FeC alloy due to lower strengthening by alloying elements. The observed variant pairing is shown in Figure 8.13a. It indicates a trend corresponding with the tendencies found for variant selection: It can be seen that variants with small intervariant misorientation angles are preferred (third diagonal line from the center line). These variant pairings are strongly dominating the microstructure although twin-related variant pairings are also present in the sample but to a much smaller extent. Variant pairing is supposed to be influenced by transformation stresses. Transformation misfits can also be accommodated by plastic or elastic deformation of the transformation product itself or a softer matrix. This is the case for the transformation in the present sample. Different microstructural constituents form during the transformation with different properties. This suggests that the transformation stresses of the constituents resulting from displacive transformations may be accommodated by the surrounding constituents that form by diffusive processes. Therefore, almost no twin-related variant pairing is found. This is similar to what was found for the dual-phase steel in Chapter 7.
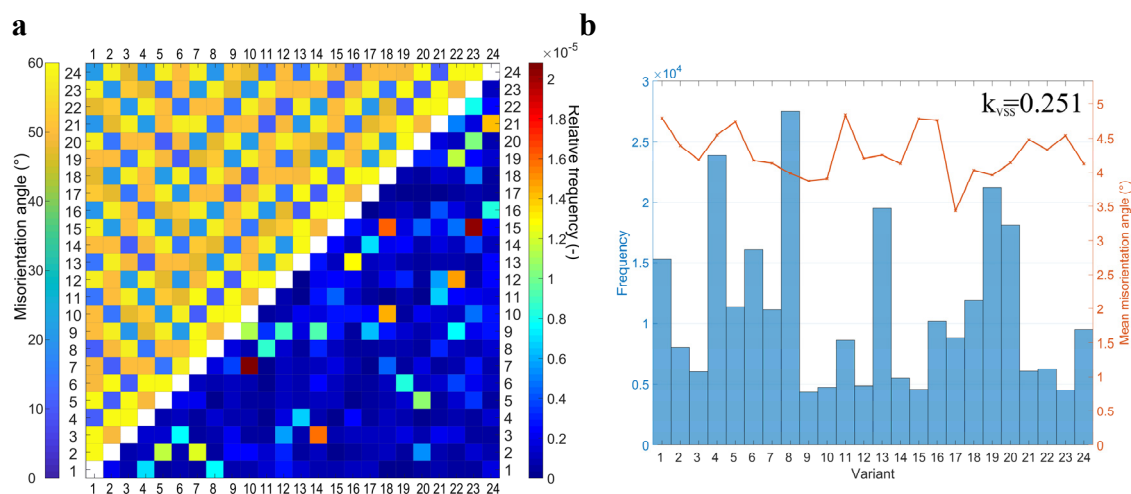
Figure 8.13: a) Representation of variant pairing in the regions of the sample in which parent and product misorientations were close (7°) to the KS OR. **b)** shows the frequency of the 24 KS variants formed during the transformation.

It was not possible to observe the surface of the sample during quenching because the vacuum was broken by the helium injection to obtain the quenching rate necessary for the occurrence of martensite in this steel. Unfortunately, therefore no information about nucleation or transformation sequence of the product microstructure is available.

Nevertheless, the variant selection criterion for the nucleation at twin boundaries (cf. Chapter 6.3.3) can be examined. The orientation of the twinned austenite grains and the orientation of the martensite formed at these locations are available from the combined EBSD map. The theoretical KS product orientations are calculated from the austenite orientations and compared to the orientation of the martensite formed there. This analysis shows that the nucleation criterion identified in Chapter 6.3.3 applies to both, martensitic and ferritic transformation products in this sample. The variant that nucleates at the austenite twin has to be a common variant of both the twin and the matrix.

8.4 Summary

Annealing twins in the austenite and their importance for the formation of martensite was one of the key findings of the previous chapters. The experiment in this chapter aimed at the investigation of the origin of austenite annealing twins. Plain carbon steel (0.105 wt.% C) was chosen for this experiment to avoid the formation of a layer which led to deterioted EBSPs of EUROFER steel at high temperature. Combinations of orientation mapping and SE image sequences during intercritical annealing were used to investigate dynamic processes leading to formation and annihilation of austenite annealing twins.

The observations clearly show that the majority of austenite annealing twins form by the motion of the austenite-ferrite phase boundaries. Formation of new austenite annealing twins was found to be connected to the curvature of the α/γ-phase boundary. Austenite annealing twin annihilation during intercritical annealing was observed to be not connected to the α/γ-phase boundary. The movement of austenite annealing twin boundaries was found to lead to changes of the orientations of smaller grains (~20 μm) with relatively high velocities (<80 s). These highly dynamic processes led to an increase of twin boundary length during the progression of the transformation to austenite but only to a weak decrease of the density of twin boundaries.

Characterization of the sample after quenching from a fully austenitic microstructure showed that a mixture of different transformation products was formed. Maps of the orientation relationship were successfully used to distinguish between transformation products that formed by displacive and diffusive processes. The variant selection strength of these displacive transformation products was found to be weaker than that of the fully martensitic microstructures (Chapter 6) and weaker than that of the dual-phase microstructure (Chapter 7).

9 Martensite Formation in Plain Carbon Steel

A high purity binary FeC alloy (0.24 wt% C) was subjected to a heat treatment to achieve large austenite grains. The heat treatment procedure led to the formation of a phase mixture consisting of martensitic islands and surrounding perlite. Thereby, the martensite islands are separated. This material allows for a study of the variant selection and pairing of martensite on a solid statistical basis due to a very large number of martensite laths.

9.1 Experimental

Iron foil (99.99%) with a thickness of 2.0 mm was annealed for 20 h at 1000 °C after a carbon coating was applied. The sample was slowly cooled (cooling rate of ca. 12 mK/s) to room temperature in order to achieve a regular ferritic/pearlitic microstructure. The composition of the sample was analyzed after the *in situ* experiment and the subsequent characterization. This analysis showed that the sample contained 0.240 wt.% carbon. This is more than two times the carbon content of the sample under investigation in Chapter 8. The heat treatment chosen for this experiment is very similar to the one in the previous chapter. The austenitization temperature was increased to 950 °C in order to obtain a larger amount of martensite.

The sample was ground and polished to obtain a flat surface after the annealing procedure. The last polishing step included an oxide particle suspension (OPS) using a vibratory polisher. The sample was then mounted onto a heating stage inside a FEI Nova Nanolab 200 SEM/FIB using Mo clamps. It was heated up to 950 °C to achieve full austenitization. The austenite microstructure was mapped by several EBSD scans at 950 °C. A rough EBSD scan with a step size of 10 µm of an area of ca. 3 mm x 3 mm was also performed. Fast cooling is necessary to achieve the cooling rate needed for the formation of martensite in pure carbon steel. Therefore, the sample was quenched by injection of helium gas directly onto the sample surface using a custom made gas injection system.

Afterwards, the microstructure of the sample was investigated in a Zeiss Merlin SEM. EBSD scans with higher spatial resolution were conducted in this microscope (ca. 400 µm x 400 µm with a step size of 0.3 µm). TEM lamellae were prepared from the martensite and the pearlite regions in order to get a clearer distinction between both constituents. The lamellae were prepared using the FIB of the FEI Nova NanoLab 200. The STEM images were taken inside the Zeiss Merlin at 30 kV acceleration voltage.

9.2 Results

The orientation map of the austenite microstructure just before quenching is shown in Figure 9.1a. The microstructure consists of large austenite grains with an average grain size of 644 µm. The austenite grains exhibit very low orientation spread. The microstructure contains a high density of austenite twins with ca. 61 % of the overall grain boundaries being twin boundaries. It cannot be excluded that smaller twins are present which were not mapped due to the large step size which was chosen to reduce meas-

urement time at high temperature. Three regions were investigated more closely: Two larger regions G1 and G2 mainly consisting of one austenite grain and a smaller region G3 was selected for a more detailed investigation of the martensite microstructure. The transformation products formed from austenite grain G2 are shown in Figure 9.1b.
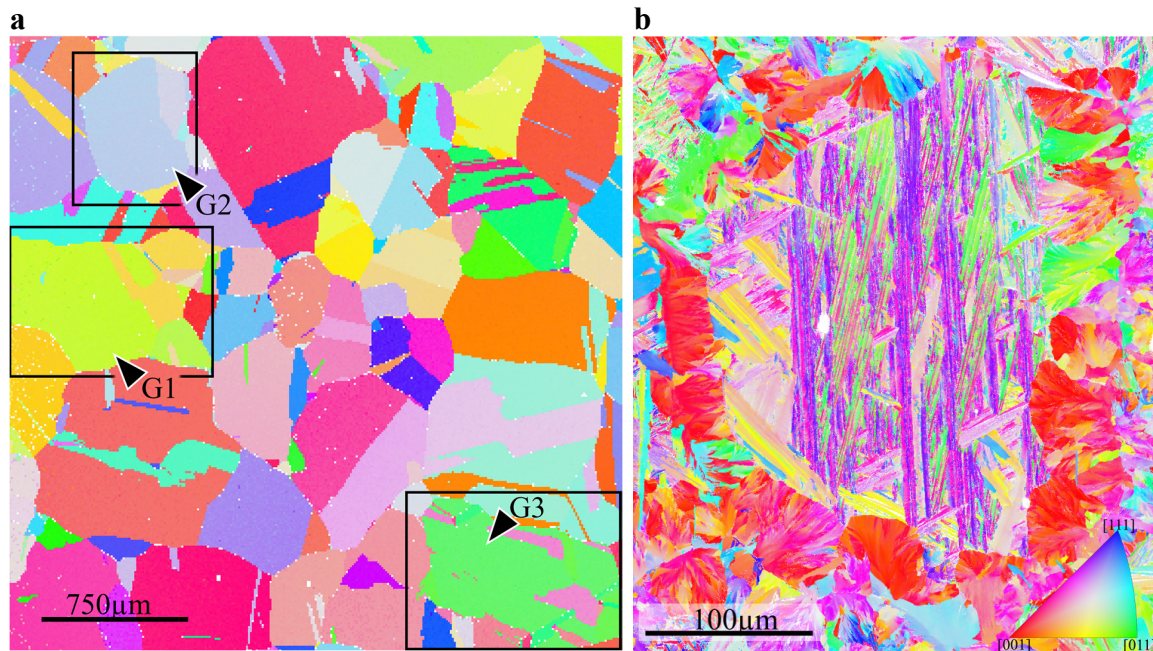

Figure 9.1: a) EBSD map of the surface of the steel sample at 950 °C. Three grains, which are shown in detail later are marked as G1, G2 and G3. **b)** Shows an OM of the austenite grain G2 after quenching.

The EBSD map reveals that the transformation product consists of two microstructural constituents: Martensite formed in the center of the PAG. Very fine pearlite nucleated mainly at the PAGB. The average grain size of the pearlite/martensite transformation product assuming a misorientation angle of at least 5° for a grain boundary was calculated to be about 53 μm. The transformation product of austenite grain G1 is shown in Figure 9.2. The EBSD scan depicted in Figure 9.2b reveals a similar microstructure as it was observed for austenite grain G1. In contrast to the martensitic regions, the pearlitic regions do not show any surface relief in the SE image which can be seen in Figure 9.2a. The ferrite orientations in the pearlitic regions exhibit strong orientation gradients. Two different kinds of pearlite colonies can be observed: The first kind is always connected to a PAGB and exhibits finger like structures which are formed by orientation gradients. The other kind also exhibits these finger-like features but they emerge from a single point and are arranged radially around this point. It can be seen from a comparison of parent and product maps that pearlite colonies may grow irrespective of PAGBs if the colonies are of the latter type. The pearlite colonies exhibit a sharp interface towards the martensitic constituent.

The martensite is mostly formed in the center of a PAG and is never in direct contact to the PAGBs. There is always some amount of pearlite between the martensite and the PAGB. The martensite micro-structure consists of very long martensite laths which form in parallel arrangements. These arrangements often consist of several variants which form a fixed sequence of variants. The laths tend to form triangular structures exhibiting angles of ca. 60° towards each other.
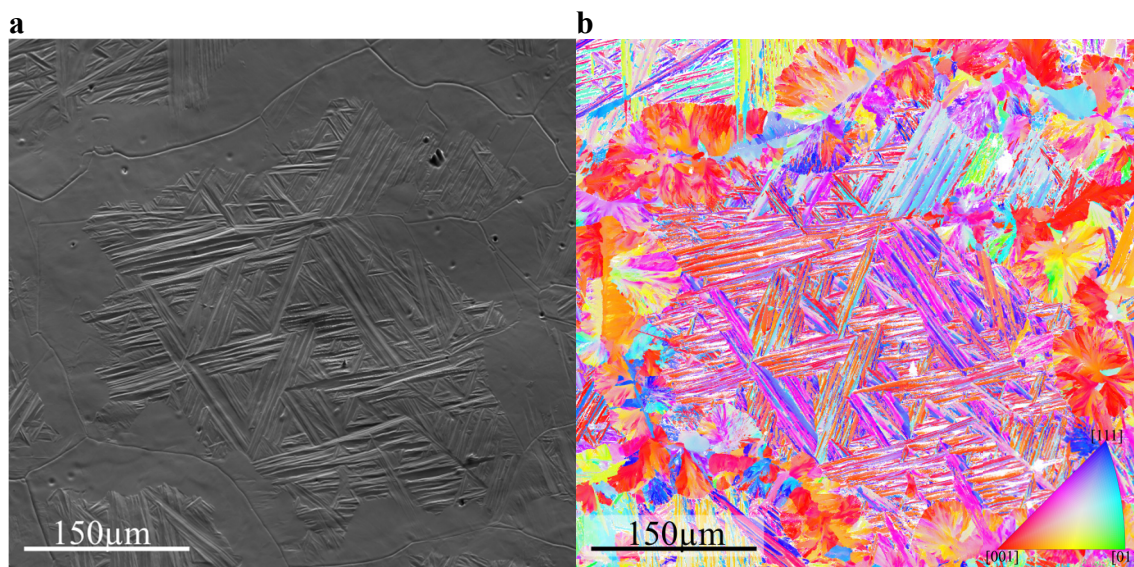
Figure 9.2: a) SE image of the surface of the sample at the location of austenite grain G1 after quenching. PAGBs can be clearly seen from grain boundary grooving. The relief arising from martensite formation is clearly visible allowing for the distinction of individual martensite laths. The areas around the PAGBs exhibit a very weak relief. **b)** shows the corresponding OM of the same region.

These triangular arrangements can be seen more clearly in the more detailed scan in Figure 9.3a. The structures are also clearly visible on the surface of the sample by the relief caused by the martensitic transformation. One pearlite colony of the second kind formed inside the PAG on the lower left side of the scan. The center of this structure appears to be a particle for which no EBSP was indexed. The SEM image shows a particle which is located at the same location.
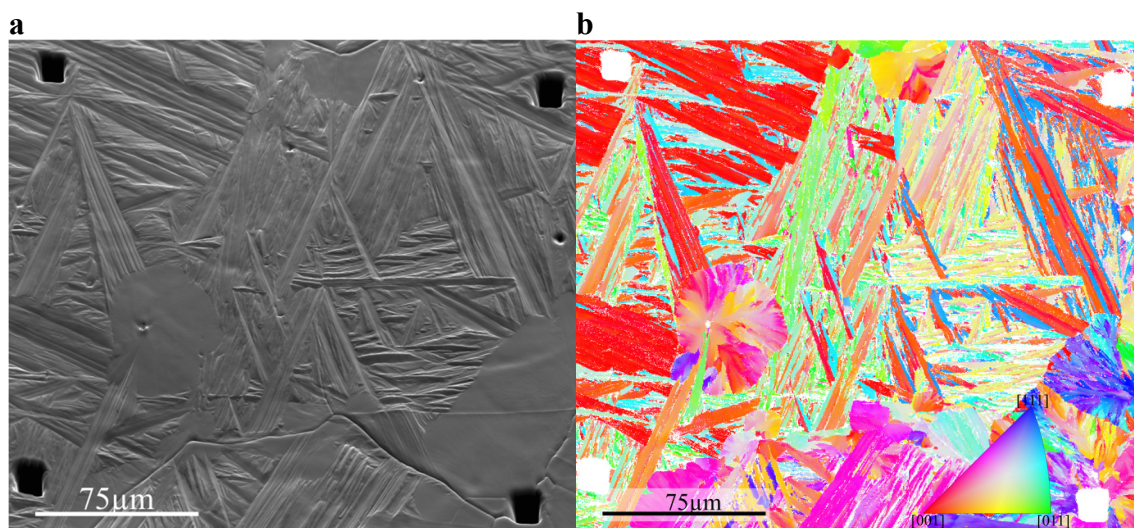
Figure 9.3: a) shows a SEM image of the surface of the sample in region G3. The martensite laths can be seen to form triangular structures on the surface. **b)** shows the corresponding OM of the same region martensite and bainite can be clearly distinguished.

Figure 9.4 shows STEM bright-field images of two TEM lamellae prepared from the martensite and pearlite microstructure respectively. The image in Figure 9.4a shows a cross section of the martensite laths. A high dislocation density can be observed. The thickness of the laths appears to be between 100 nm and 200 nm.

Figure 9.4b shows the lamella prepared from the pearlite microstructure. Finely dispersed carbide precipitates can be seen inside the ferritic/pearlitic grains. They appear to be equally orientated within the individual ferrite grains. The carbides are elongated and measure roughly 300 nm in length and 40 nm in thickness.

a   **b**
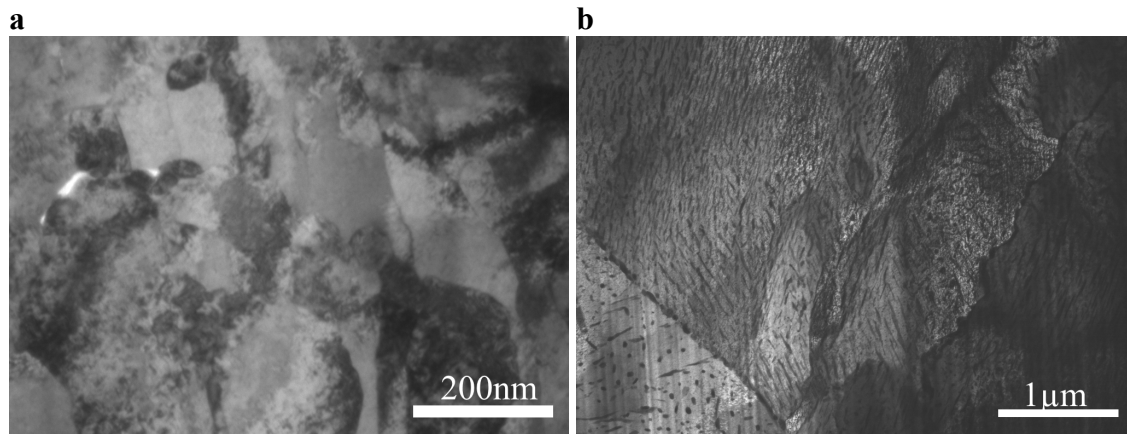
Figure 9.4: a) Shows a bright field STEM image of a lamella prepared from a martensite region perpendicular to the martensite laths. A high dislocation density and the small size of the cross section of the martensite laths can be seen. **b)** shows a STEM (BF) image of a lamella cut from the pearlitic part of the sample. It shows finely dispersed cementite which is oriented roughly in parallel.

A STEM BF image of the pearlite is shown in Figure 9.5a at higher resolution. The cementite can be clearly recognized as dark lines or dots. This cementite is dispersed in the matrix but is sometimes also arranged as a chain of cementite particles on grain boundaries.

a   **b**
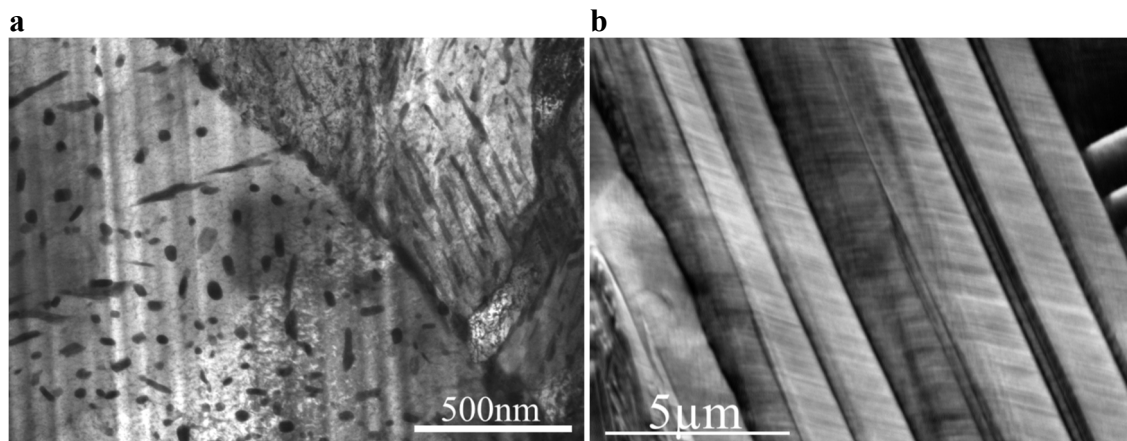
Figure 9.5: a) shows a STEM BF image of the pearlite structure showing fine cementite. **b)** shows a more detailed SE image of a bundle of martensite laths. Striations are present on the surface of the sample.

Figure 9.5b shows a detailed SE image of the surface of the sample in a region where martensite was formed. It shows that a periodic substructure is present on the subunits which form the relief and which can be connected to single martensite variants. These striations consist of a much finer relief of parallel grooves which are inclined by ca. 50° to the habit plane of the laths.

9.3   Discussion

The martensite morphology observed in this Fe-C alloy is different from the morphology observed for the EUROFER alloy in Chapter 6. The microstructure observed here consists of two different microstructural constituents which result from different phase transformations. Pearlite mostly formed by diffusive and martensite by displacive processes.

9.3.1   Distinction between Pearlite and Martensite

The mapping of the misorientation angle of the orientation of the transformation product to the closest KS variant calculated from the orientation of the PAG reveals that the orientation of martensite which formed inside the PAGs is close to the KS OR. The corresponding maps for the PAGs G1 and G2 are shown in Figure 9.6a and Figure 9.6b, respectively. These maps show that the different transformation products can be very clearly distinguished based on the misorientations relative to the product orientations based on the KS OR.
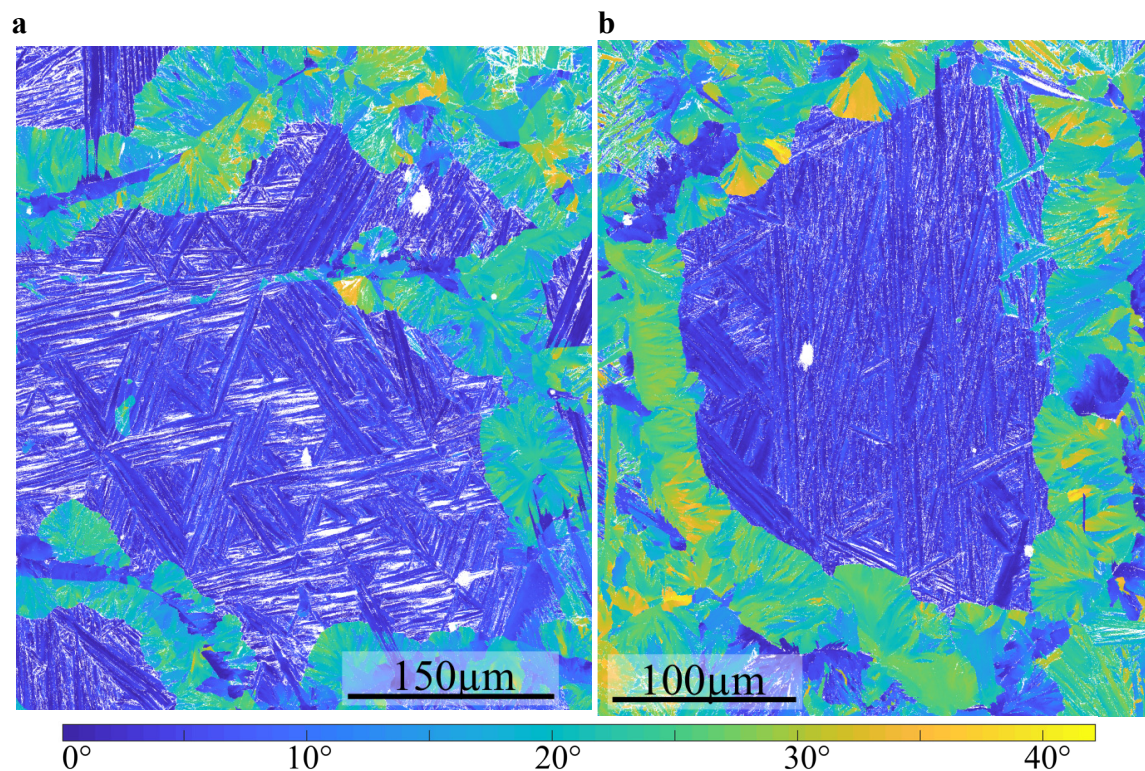
Figure 9.6: Map of the misorientation angle of the product orientation to the closest theoretical product orientation calculated using the KS OR. The maps in **a)** and **b)** show PAGs G1 and G2.

Most of the pearlite shows significantly higher misorientation angles to the KS OR compared to the martensite that formed inside the PAGs. However, this is not the case for all of the pearlite. Parts of the pearlite colonies, especially close to the PAGBs, exhibit low misorientation angles to the closest KS varaint. A statistical evaluation of the misorientation angles of all microstructural constituents towards the theoretical transformation product under consideration of the KS OR in the form of a histogram is shown in Figure 9.7.
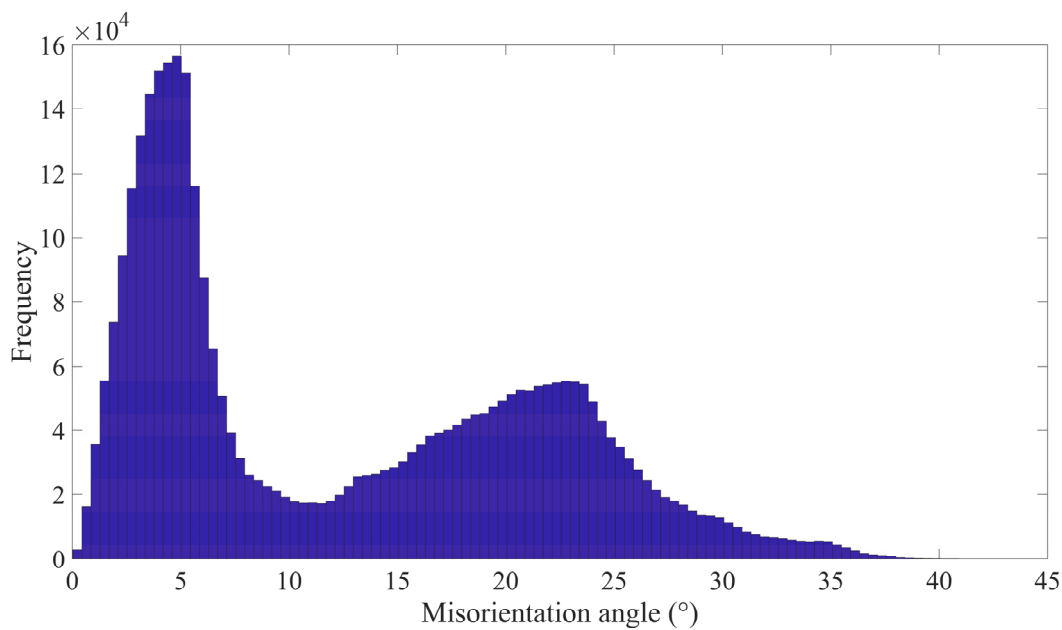
Figure 9.7: Histogram of the misorientation angle of the measured product orientation towards the calculated theoretical product orientation based on the KS OR.

This histogram demonstrates that the misorientation angle can be used to distinguish between martensite and pearlite. In a more general approach, it can be used to distinguish between microstructural product constituents that are formed by displacive processes and microstructural product constituents that were formed by diffusive processes. The observation that some of the pearlite colonies exhibit relative low misorientation angles towards the closest KS variant shows that this criterion is only necessary but not sufficient.

9.3.2   Martensite Microstructure

The martensite consists of long martensite laths which are arranged in parallel. Groups of different laths form parallel bunches. Parallel laths belong to a single martensite variant. The laths can extend from one PAGB to the other but most laths are confined between other bunches. The average length of the variants was found to be 38.8 μm and the average thickness 1.7 μm. The arrangement of several bunches create triangular structures. The angles of these structures are very similar for one austenite grain (i.e. one austenite orientation). The most frequent angle observed in PAG G1 ranges between 15° and 40° whereas the same angle for PAG G2 ranges between 50° and 70°. The variant map for the PAGs G1 and G2 are shown in Figure 9.9a and Figure 9.9b, respectively.

The variant map shows that variant selection occurs during the transformation. The variant histogram which was calculated for PAG G2 is depicted in Figure 9.8b and shows that variants 2 and 22 are preferentially formed in the transformation. The variant maps shown in Figure 9.9 further suggest that strong variant pairing tendencies are present in the martensite microstructure. A relative bivariant histogram of the variant pairing calculated from all scanned regions is shown in Figure 9.8b. It shows a strong prevalence for twin related, neighboring variants i.e. V4&V3, V6&V5, V8&V7 and so on. This can be observed for all neighboring variants except for V1&V2. An only weak tendency for the pairing of variants exhibiting low misorientation angles can be seen from the diagram but from these the variants exhibiting minimum intervariant misorientation angles e.g. V15&V18, V14&V17 etc. are preferred.
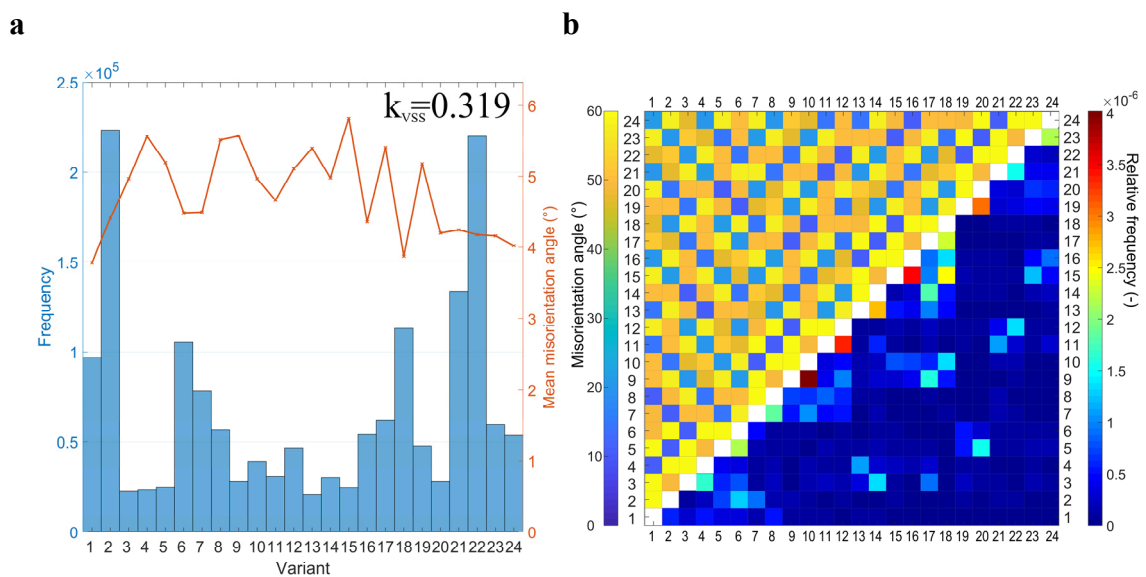
Figure 9.8: a) KS variant histogram calculated for the PAG G2. The frequency of KS variants refers to the number of EBSD measurement points which can be attributed to one KS variant. **b)** shows a representation of the variant pairing as a bivariant histogram (lower triangle). The pairings of all investigated regions were combined for the calculation of the histogram. The upper triangle represents the misorientation angles connected to the specific variant pairings.

The influence of the dual-phase morphology of the transformation product which was observed in Chapter 7 for a EUROFER alloy cannot be observed for this Fe-C alloy. A lower tendency towards twin related martensite variants would be expected following the discussion for the dual-phase microstructure for EUROFER steel in Chapter 7. This is not the case in this material. The reason for this may be due to a stronger influence of either alloy composition and/or transformation temperature on martensite variant pairing tendency.
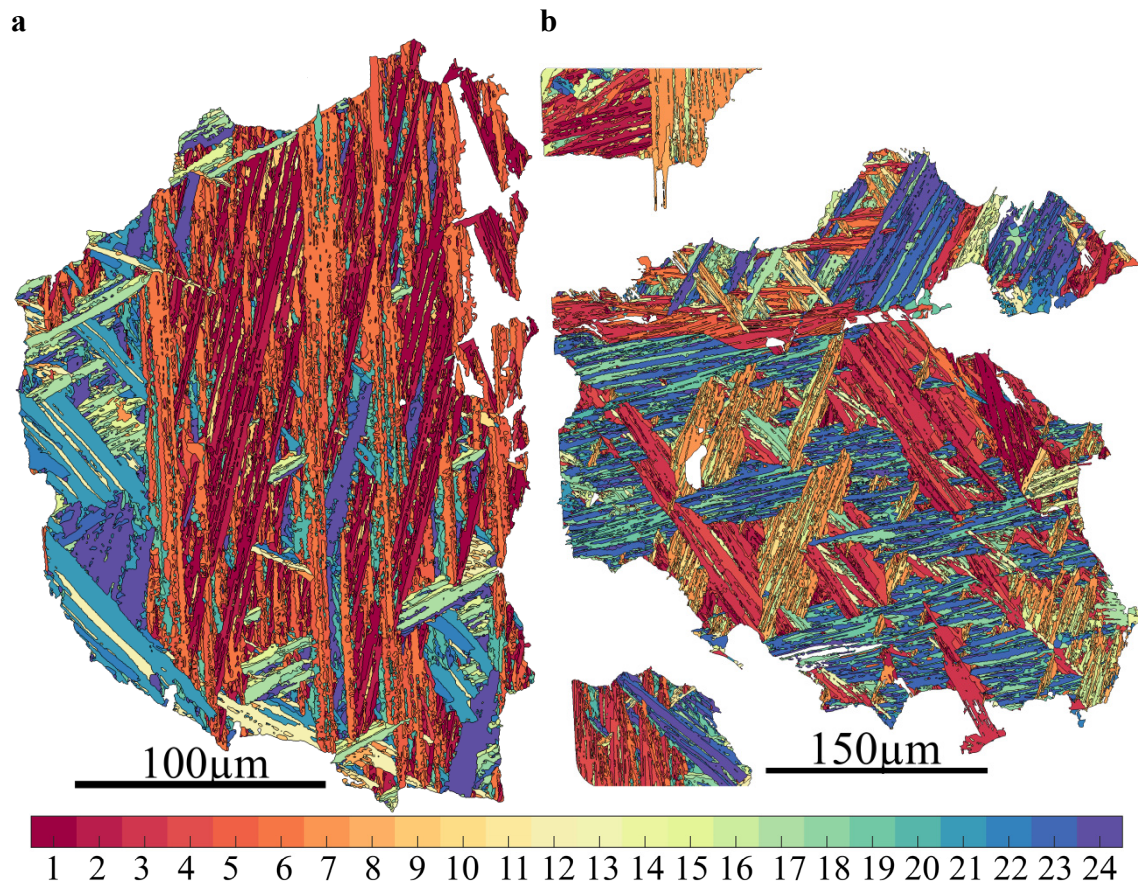
Figure 9.9: Variant maps calculated from the EBSD scans of the transformation product combined with the austenite EBSD scan using the KS OR. **a)** Variant map for the PAG G1 and **b)** Variant map for PAG G2.

Only one quantitative, experimental study on variant pairing tendencies can be found in literature: Stormvinter et al. [209] investigated the influence of carbon content on variant pairing tendencies in martensitic Fe-C alloys. They used an austenite reconstruction algorithm for the determination of the martensite variants. All previous attempts on the study of variant pairing were based on the analysis of misorientation profiles [125], [218], [415]. Stormvinter et al. found a strong influence of carbon content on the variant pairing tendency. They concluded that, especially for lath martensites, higher carbon contents promote the formation of twin related variant pairings and will simultaneously reduce the martensite start temperature.

9.3.3 Habit Plane Analysis

Martensite laths with an aspect ratio larger than 5 were taken into account for this analysis which was performed for the variant map shown in Figure 9.9b (mostly PAG G2). The trace of the habit plane was determined by principal component analysis and used to calculate the parallel lattice direction in the local austenite orientation. The details concerning the estimation of the habit plane can be found in Chapter 4.13. A relative large scatter of the habit plane was found throughout the analyzed microstructure. This scatter was relatively low for a single austenite grain but larger between different PAGs. Therefore, habit planes for all PAGs present in the analyzed area were calculated. The results are marked with blue dots in the IPF shown in Figure 9.10b. The red dots show the habit planes of martensite that are frequently discussed in the literature. This shows that the scatter found in this experiment is relatively high but that the most commonly observed habit planes are close to the $(259)_\gamma$ and the $(3\ 10\ 15)_\gamma$ habit plane. Other experimental work focusing on the habit plane in lath martensite did also find considerable scatter [384].

It should also be noted that "conventional" habit plane analysis using TEM is only able to make a very limited amount of orientation measurements. In contrast to that, here more than 17,000 laths were automatically evaluated on an area of ca. 400 μm x 400 μm. The relative large scatter shows that the habit plane of martensite is not strongly affected by the prevalent OR because the misorientation towards the OR found for this material was found to be very small. This suggests that the habit plane may be strongly influenced by varying local transformation stresses which are difficult to assess or predict.

9.3.4 Martensite Orientation Relationship

The misorientations between the austenite and the martensite orientations for every martensite measurement point in the martensitic regions were used to calculate the actual OR observed for this steel (cf. Chapter 4.12). The OR calculated from all orientation pairs from the investigated regions can be expressed as parallel planes and directions as follows:

$$\{2\bar{1}1\}_\gamma \parallel \{1\bar{3}2\}_\alpha$$
$$\langle 120 \rangle_\gamma \parallel \langle 310 \rangle_\alpha$$

Eq. 9.1

This OR produces 24 variants. This OR and the KS OR are marked in the pole figure shown in Figure 9.10a where the accumulated OR of all investigated regions is represented in a contour plot. It shows that the observed OR is very sharp and close to the KS OR. It also shows that variant selection can be observed (non uniform distribution of intensity between the variants) which may be attributed to the presence of the free surface. The OR calculated for this sample was found to be 4.2° away from the KS OR, 4.4° away from the NW OR, 3.2° away from the Pitsch OR, 2.7° away from the GT OR and 3.4° away from GT' OR. The calculated OR is in between the well-known ORs proposed in literature.
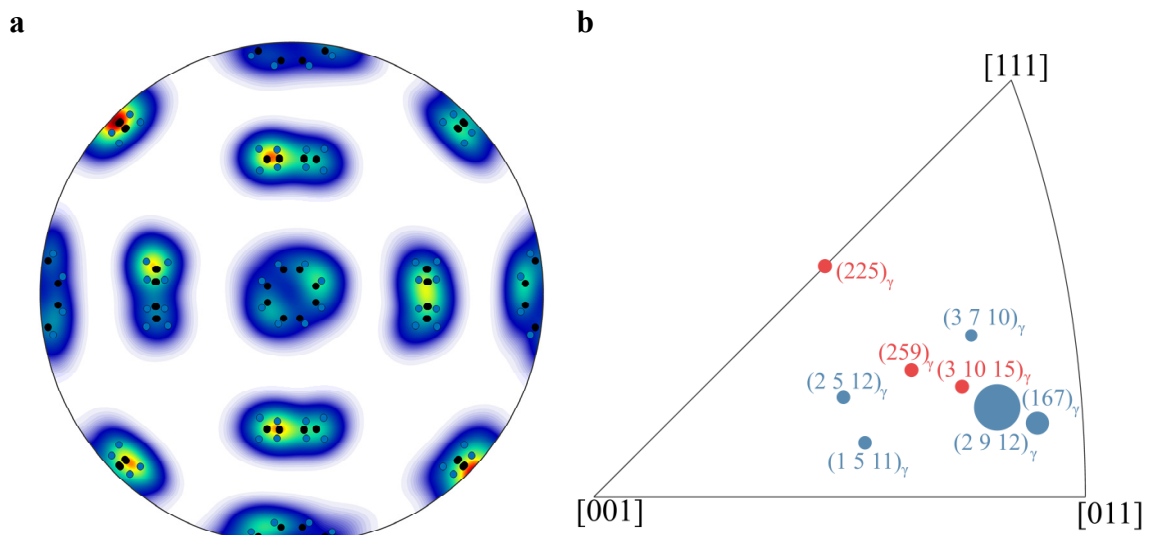
Figure 9.10: a) shows a (100) pole figure representing the OR between austenite and martensite in the sample. The data points of all investigated regions were combined for this pole figure. The corresponding orientations of the KS OR and the OR calculated for the sample are marked on the pole figure in blue and black, respectively. **b)** result of the habit plane analysis for the martensite microstructure shown in Figure 9.9b. The sizes of the blue markers correspond to the number of laths which were analyzed in the calculation of the corresponding habit plane. The red dots show the habit planes for martensite that are commonly discussed in literature. All planes are defined corresponding to the fcc austenite crystal structure.

9.3.5 Martensite Nucleation

The nucleation condition described in Chapter 6.3.3 was tested for the austenite grain G2 which contains a twin boundary. The variants which formed at the twin boundary are indeed KS variants of the two austenite orientations of the twinned crystals. However, this does not prove that these martensite laths nucleated at the austenite twin and that this nucleation was not induced by other factors since no observation of the transformation sequence for this sample was possible. Therefore, the observed correlation of the orientations is only a necessary but not sufficient condition for the variant selection on nucleation described in Chapter 6.3.3.

9.3.6 Pearlite Microstructure

The STEM images taken from the region with a very weak surface relief shown in Figure 9.4b and Figure 9.5a reveal that this region consists of finely dispersed cementite and ferrite. This cementite has an elongated shape. This indicates that pearlitic ferrite formed in the sample before M_S was reached. This is typical for eutectoid steels [8]. The pearlite microstructure is very fine and does not show the typical strictly hierarchical lamellar arrangement of ferrite and cementite [442]–[445]. Due to the small size of the cementite it was not possible to obtain EBSP of the cementite lamellae of the pearlitic microstructure. It also was not possible to image the pearlitic lamellar structure using FIB. This suggests that probably instead of perlite, dispersed cementite particles formed in the ferrite through a Divorced Eutectoid Transformation (DET) [8], [446]–[448]. This transformation results in fine carbide particles due to the presence of fine carbide nuclei during austenitization. This processing route is a convenient method to achieve spherodized carbides [449], [450] which enhance the mechanical properties of the alloy. The occurrence of the DET is therefore dependent on the carbon content of the alloy and the austenitization temperature. Additionally, it is possible that the DET and the pearlitic reaction occur during cooling resulting in a mixed transformation product.

A section of the pearlite microstructure was extracted from the EBSD scan in the vicinity of PAG G2 for an analysis of the OR of the pearlitic ferrite. The misorientation angle of the ferrite orientations toward the closest KS variant was then calculated for the austenite orientations of both neighboring austenite grains. The two corresponding maps can be seen in Figure 9.11. The difference in OR for martensite and pearlitic ferrite can be seen in Figure 9.6. Figure 9.11 further shows that the ferrite often does not exhibit a KS OR to the orientation of the austenite grain into which it grew but in many cases to the neighboring austenite grain. This is a consequence of the nucleation at an austenite grain boundary: The orientations of both grains can influence the orientation of the transformation product. Figure 9.11a illustrates that large fractions of the ferrite exhibt small misorientation angles similar to the martensite in the neighboring grain and vice versa. In fact in Figure 9.11a the majority of the ferrite is oriented this way. The same is shown in Figure 9.11b for the other PAG: The majority of the ferrite inside the grain does not exhibit a KS OR towards the parent austenite orientation but a KS OR towards the orientation of the neighbouring austenite grain.
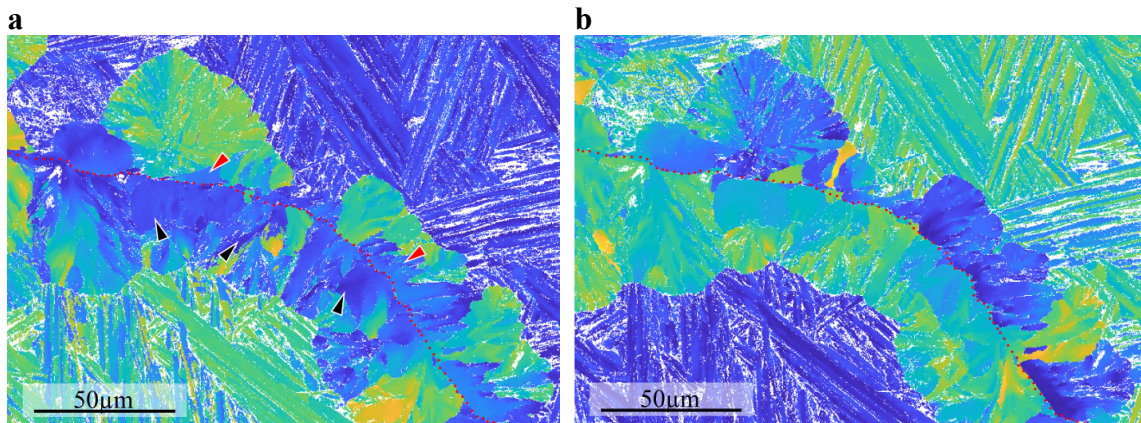
Figure 9.11: Map of the misorientation angle in the same region of the pearlitic ferrite orientations towards the theoretical product orientations calculated from the austenite orientations of the two neighboring austenite grains. **a)** shows the corresponding map relative to the OR based on the austenite orientation of the upper right austenite grain and **b)** shows the misorientation angle relative to the OR based on the orientation of the lower left austenite grain. The prior austenite grain boundary is marked by a dotted red line.

An OM and a corresponding pole figure of the ferrite orientations and the orientations of the KS variants resulting from the orientations of the neighboring austenite grains were calculated in order to investigate the deviation of the OR from the KS OR. The OM of the pearlitic ferrite only is shown below in Figure 9.12a. The corresponding (100) pole figure which can be seen in Figure 9.12b shows the orientations color coded according to the map and the orientations of the KS related products of the two neighboring austenite grains. It illustrates that the orientations of the pearlitic ferrite are spread around these KS variants of both austenite grains. Moreover, the deviating orientations are often located in between these KS product orientations.
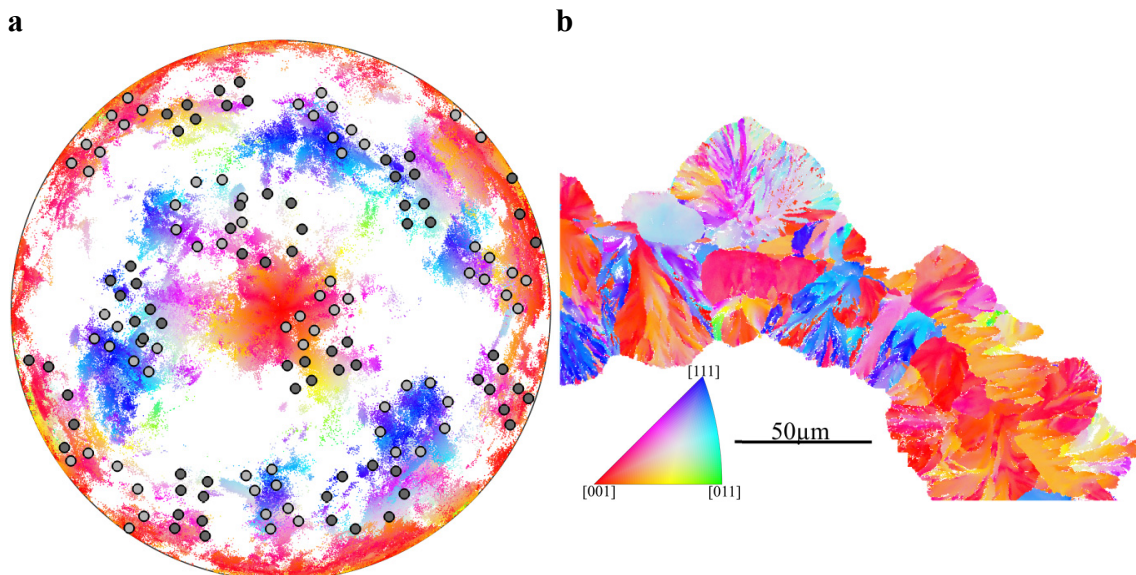
Figure 9.12: a) The orientations of the KS variants of the two neighboring austenite grains are marked with light grey and dark grey circles. The dark grey circles correspond to the orientations associated to the austenite grain below the pearlite and the light grey to the austenite grain above the pearlite. **b)** Orientation map of the pearlite region corresponding to the maps shown in Figure 9.11.

9.4 Summary

The transformation products of a high purity binary FeC alloy were characterized by the combination of parent and product phase orientation mapping. The product microstructure consisted of a mixture of large martensite islands surrounded by pearlite. A very large prior austenite grain size (PAGS) allowed to analyze a very large amount of martensite laths.

The OR calculated from the austenite-martensite orientation pairs were found to be close to the GT OR. Variant pairing showed a prevalence of twin related variant pairings over minimum misorientation angle pairs. This is not in accordance with the tendencies which were observed for the EUROFER alloy suggesting that alloy composition, especially carbon content, may have a strong influence on variant pairing.

The two constituents which can be clearly distinguished by their morphologies were used to test the application of OR mapping to distinguish between the two microstructural constituents based on their type of transformation (displacive or diffusive).

10 Summary and Discussion

Steel has been used for more than 150 years and is still the most important structural material. Research and development on improved and more efficient processing and production of steels in the past have drastically improved the properties of this class of material. It is also a great example of the success of material science: The interplay of alloying chemistry and physical metallurgy enables to tune the properties of steels to meet rising operational requirements. The steady development of new and improved alloying strategies and processing routes until today shows that this path of progress has by no means reached its end.

This development and its importance are reflected by the vast amount of literature on the topic of steel. This ranges from improvements on the level of large scale processing in a steel mill to the observation of microstructural evolution during processing in a lab. It includes phenomenological approaches to the optimization of alloying and heat treatments which are predominantly based on trial and error. But it also covers fundamental observations on crystallography, phase transformations and thermodynamics. This resulted in combination with the advancement of tools for the characterization of materials in a more and more comprehensive base of knowledge regarding every aspect of steelmaking and its processing.

The present study aims towards overcoming the traditional trial and error based approach for the optimization of heat treatments. Therefore, an *in situ* setup for combined HT SEM/EBSD measurements was developed. This setup enables the characterization of materials at different steps of a processing chain. It enables a very comprehensive characterization of phases, their orientations, interfaces and the properties of these interfaces. All this can be accomplished during a wide variety of heat treatment processes: The setup enables to mimic heat treatments including temperatures reaching 1200 °C, heating rates of ca. 50 K/s and quenching rates of up to ca. 300 K/s. These high quenching rates are achieved by a custom made gas injection system. Besides these developments in terms of the experiment, complementary computational methods were developed to handle and structure the recorded data which enable a quantitative description and analysis of microstructural evolution. This set of methods enables spatial correlation of EBSD data allowing for example to directly compare parent and product phase without loss of spatial or angular resolution. The novel approach consists in combining and aligning locally resolved data on crystal orientation. Data can be recorded before and after or during phase transformations. Since the same location of a sample is observed throughout a process or process chain, a data set is generated that can be used to identify important mechanisms or parameters which control the microstructure of a material.

The focus of this thesis was put on the martensitic transformation motivated by the rather small amount of studies available which connect EBSD maps of the austenite microstructure to the martensitic product microstructure. Therefore, the aforementioned computational tools were extended to the particular properties of this phase transformation: Algorithms for the calculation of orientation relationships based on large numbers of pairs of the orientation of parent and product phase were developed. Further algorithms for the calculation of martensite variants enabling further abstraction of the orientation data to variant maps were developed and a quantitative measure of the degree of variant selection was proposed and applied. For the first time, the calculation of variant maps enabled a comprehensive statistical analysis of variant selection and pairing that were based on EBSD measurements of parent and product microstructures. A further algorithm for the automatic estimation of the martensite habit plane based on variant maps allows for the analysis of large numbers of martensite laths.

These computational tools and the use of EBSD scans at the start and end point of the applied temperature changes combined with SEM image sequences of the surface taken in between allowed for the observation of martensite formation in different alloys and from different microstructures of the same alloy. A common observation to all these alloys and microstructures was the influence of austenite twin boundaries on lath martensite morphology and nucleation: The first martensite lath that appeared inside an austenite grain formed always at an austenite twin boundary. This first martensite lath was found to be always a KS variant of both twin and matrix reducing the number of possible martensite orientations from 42 (for the KS OR) to only six variants. An additional nucleation site for martensite was found to be the austenite-ferrite phase boundary for transformation from the intercritical regime (coexistence of austenite and ferrite). The competition between the formation of epitaxial ferrite and martensite during this transformation is determined by the character of the austenite-ferrite phase boundary: Phase boundary segments exhibiting a misorientation not close to the KS OR show high mobilities i.e. more epitaxial ferrite is formed at such bounderies whereas martensite nucleation occurs preferably at phase boundaries with misorientations close to the KS OR. The orientation of the martensite variant that formed at these locations was often observed to coincide with neighboring ferrite orientations.

The austenite-ferrite phase boundary was also identified to be the origin of austenite twin boundaries. It was observed that all austenite twin boundaries formed at the moving austenite-ferrite phase boundary. This process and movements of austenite twin boundaries behind the transformation front were highly dynamic. These observations suggest structural similarities between austenite twin boundaries, austenite-ferrite phase boundaries and the martensite nuclei. This may be attributed to types of dislocations which are common to all of these interfaces. Another common feature is the OR: Austenite-ferrite phase boundaries tend to exhibit an OR close to KS if they are close to their energetic minimum. The OR between austenite and martensite is usually close to KS and an austenite twin boundary can also be accepted to fulfill the KS OR through the twin related KS variants.

The analysis of variant selection and variant pairing showed a common trend for all alloys: Both effects are connected to the accommodation of transformation strains. Depending on the boundary conditions during transformation, different means for the accommodation of transformation strains are available. This includes the formation of a surface relief, the elastic or plastic deformation of a neighboring matrix phase, variant selection and variant pairing and elastic or plastic deformation of the martensite. Variant selection is weaker if other means for the accommodation of transformation strains are available such as deformation of the ferrite matrix in the case of a dual-phase microstructure. Large scale statistical analysis of the martensite habit plane of different steels showed that the scatter of the habit plane was surprisingly large. The estimated habit planes were found to lie in between the ones reported in the literature.

The results of two different PAR algorithms for a martensite microstructure were put to a quantitative test using the austenite EBSD scan measured before quenching. The results showed relative good agreement concerning austenite grain sizes and orientations but failed to reconstruct austenite twinning boundaries which were found to heavily influence martensite nucleation, formation and morphology. This emphasizes not only the importance of accurate microstructural information as the foundation of computational methods for the optimization of steel processing but also is of importance for the understanding and interpretation of microstructural relationships between parent and product phase.

The ORs calculated for different alloys and microstructures from large numbers of austenite and martensite orientations were found to be different for each alloy but were all close to the KS OR. They were found to be sharp and were located in between the well-established ORs. This shows that the well-known ORs (KS, NW, Pitsch, GT, GT') can be used as approximations for the calculation of product orientations but are not characteristic features of the transformation. The measurements instead suggest that there may be a continuum of possible ORs which are located in between the established ORs depending on alloying

chemistry and the accommodated transformation stresses. Similarly, the OR between austenite and ferrite was found to lie in between the established ORs but was found to be less sharp than for the austenite-martensite OR.

With these results, the through-process microstructural characterization developed and used in this thesis sheds new light onto phase formation and microstructural transformation of steels. For example, in this work the importance of annealing twins for the formation of martensite was unveiled. The comparison of austenite EBSD maps calculated by PARs to measured maps showed that PARs fail to reconstruct the location of austenite twin boundaries. This shows that experimental *in situ* EBSD data is needed in order to obtain meaningful results for the simulation of martensite phase transformation and to draw sensible conclusions for nucleation and transformation mechanisms. This is further emphasized by the observed high mobilities of these interfaces. In future, datasets from such experiments may be extended to different processing conditions and combined with emerging techniques such as ML and AI that help in handling and interpreting large amounts of data. This data may be further combined with data from mechanical testing such as nanoindentation and micro tensile tests. Eventually this may lead to new combined experimental and computational approaches that will allow for the identification of processing routes for tailored microstructures of steels with improved properties.

11 Appendix

11.1 Definition of ORs and their Variants

KS Variant	Parallel planes γ	Parallel planes α	Parallel directions γ	Parallel directions α	BG	CPP
1	{111}	{$\bar{1}$01}	⟨$\bar{1}$01⟩	⟨$\bar{1}\bar{1}\bar{1}$⟩	1	1
2	{111}	{10$\bar{1}$}	⟨10$\bar{1}$⟩	⟨$\bar{1}\bar{1}\bar{1}$⟩	2	1
3	{111}	{01$\bar{1}$}	⟨01$\bar{1}$⟩	⟨$\bar{1}\bar{1}\bar{1}$⟩	3	1
4	{111}	{0$\bar{1}$1}	⟨0$\bar{1}$1⟩	⟨$\bar{1}\bar{1}\bar{1}$⟩	1	1
5	{111}	{1$\bar{1}$0}	⟨1$\bar{1}$0⟩	⟨$\bar{1}\bar{1}\bar{1}$⟩	2	1
6	{111}	{$\bar{1}$10}	⟨$\bar{1}$10⟩	⟨$\bar{1}\bar{1}\bar{1}$⟩	3	1
7	{1$\bar{1}$1}	{10$\bar{1}$}	⟨10$\bar{1}$⟩	⟨$\bar{1}$1$\bar{1}$⟩	2	2
8	{1$\bar{1}$1}	{$\bar{1}$01}	⟨$\bar{1}$01⟩	⟨$\bar{1}$1$\bar{1}$⟩	1	2
9	{1$\bar{1}$1}	{$\bar{1}\bar{1}$0}	⟨$\bar{1}\bar{1}$0⟩	⟨$\bar{1}$1$\bar{1}$⟩	3	2
10	{1$\bar{1}$1}	{110}	⟨110⟩	⟨$\bar{1}$1$\bar{1}$⟩	2	2
11	{1$\bar{1}$1}	{011}	⟨011⟩	⟨$\bar{1}$1$\bar{1}$⟩	1	2
12	{1$\bar{1}$1}	{0$\bar{1}\bar{1}$}	⟨0$\bar{1}\bar{1}$⟩	⟨$\bar{1}$1$\bar{1}$⟩	3	2
13	{$\bar{1}$11}	{0$\bar{1}$1}	⟨0$\bar{1}$1⟩	⟨1$\bar{1}\bar{1}$⟩	1	3
14	{$\bar{1}$11}	{01$\bar{1}$}	⟨01$\bar{1}$⟩	⟨1$\bar{1}\bar{1}$⟩	3	3
15	{$\bar{1}$11}	{$\bar{1}$0$\bar{1}$}	⟨$\bar{1}$0$\bar{1}$⟩	⟨1$\bar{1}\bar{1}$⟩	2	3
16	{$\bar{1}$11}	{101}	⟨101⟩	⟨1$\bar{1}\bar{1}$⟩	1	3
17	{$\bar{1}$11}	{110}	⟨110⟩	⟨1$\bar{1}\bar{1}$⟩	3	3
18	{$\bar{1}$11}	{$\bar{1}\bar{1}$0}	⟨$\bar{1}\bar{1}$0⟩	⟨1$\bar{1}\bar{1}$⟩	2	3
19	{$\bar{1}\bar{1}$1}	{1$\bar{1}$0}	⟨1$\bar{1}$0⟩	⟨11$\bar{1}$⟩	3	4
20	{$\bar{1}\bar{1}$1}	{$\bar{1}$10}	⟨$\bar{1}$10⟩	⟨11$\bar{1}$⟩	2	4
21	{$\bar{1}\bar{1}$1}	{011}	⟨011⟩	⟨11$\bar{1}$⟩	1	4
22	{$\bar{1}\bar{1}$1}	{0$\bar{1}\bar{1}$}	⟨0$\bar{1}\bar{1}$⟩	⟨11$\bar{1}$⟩	3	4
23	{$\bar{1}\bar{1}$1}	{$\bar{1}$0$\bar{1}$}	⟨$\bar{1}$0$\bar{1}$⟩	⟨11$\bar{1}$⟩	2	4
24	{$\bar{1}\bar{1}$1}	{101}	⟨101⟩	⟨11$\bar{1}$⟩	1	4

Table 11.1: Definition of the Kurdjumov-Sachs orientation relationship (KS OR). The parallel plains and directions as well as Bain group (BG) and close packed plane (CPP) groups are listed for all 24 variants formed by the OR.

Figure 11.1: Orientations of the variants formed by the KS OR in green and the NW OR in red on a (100) pole figure.

NW	Parallel planes		Parallel directions		BG	CPP
Variant	γ	α	γ	α		
1	{111}	{011}	⟨2̄1̄1̄⟩	⟨01̄1⟩	2	1
2	{111}	{011}	⟨1̄21̄⟩	⟨01̄1⟩	3	1
3	{111}	{011}	⟨1̄1̄2⟩	⟨01̄1⟩	1	1
4	{1̄11}	{011}	⟨2̄1̄1̄⟩	⟨01̄1⟩	2	2
5	{1̄11}	{011}	⟨121̄⟩	⟨01̄1⟩	3	2
6	{1̄11}	{011}	⟨11̄2⟩	⟨01̄1⟩	1	2
7	{11̄1}	{011}	⟨211̄⟩	⟨01̄1⟩	2	3
8	{11̄1}	{011}	⟨1̄2̄1̄⟩	⟨01̄1⟩	3	3
9	{11̄1}	{011}	⟨1̄12⟩	⟨01̄1⟩	1	3
10	{1̄1̄1}	{011}	⟨1̄12⟩	⟨01̄1⟩	2	4
11	{1̄1̄1}	{011}	⟨1̄21⟩	⟨01̄1⟩	3	4
12	{1̄1̄1}	{011}	⟨1̄1̄2̄⟩	⟨01̄1⟩	1	4

Table 11.2: Definition of the Nishiyama-Wassermann orientation relationship (NW OR). The parallel plains and directions as well as Bain group (BG) and close packed plane (CPP) groups are listed for all 12 variants formed by the OR.

a b
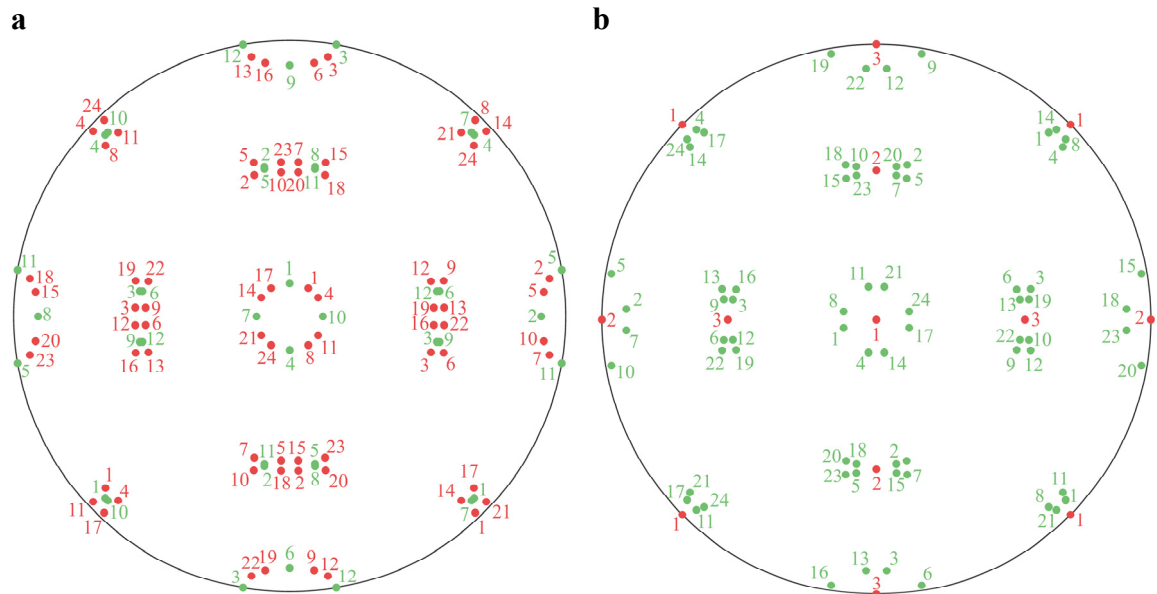
Figure 11.2: a) Shows the orientations of the variants formed by the Pitsch OR in green and the inverse GT OR (i.e. GT') in red on a (100) pole figure. b) shows the orientations of the variants formed by the GT OR in green and the Bain OR in red on a (100) pole figure.

Pitsch	**Parallel planes**		**Parallel directions**		**BG**	**CPP**
Variant	γ	α	γ	α		
1	{100}	{0$\bar{1}\bar{1}$}	⟨01$\bar{1}$⟩	⟨$\bar{1}$1$\bar{1}$⟩	1	1
2	{010}	{$\bar{1}$0$\bar{1}$}	⟨$\bar{1}$01⟩	⟨$\bar{1}\bar{1}$1⟩	2	1
3	{001}	{$\bar{1}\bar{1}$0}	⟨1$\bar{1}$0⟩	⟨1$\bar{1}\bar{1}$⟩	3	1
4	{100}	{0$\bar{1}$1}	⟨011⟩	⟨$\bar{1}$11⟩	1	2
5	{001}	{$\bar{1}\bar{1}$0}	⟨$\bar{1}$10⟩	⟨$\bar{1}$11⟩	2	2
6	{100}	{01$\bar{1}$}	⟨011⟩	⟨$\bar{1}$11⟩	3	2
7	{010}	{$\bar{1}$01}	⟨101⟩	⟨1$\bar{1}$1⟩	1	3
8	{010}	{10$\bar{1}$}	⟨101⟩	⟨1$\bar{1}$1⟩	2	3
9	{100}	{0$\bar{1}\bar{1}$}	⟨0$\bar{1}$1⟩	⟨$\bar{1}\bar{1}$1⟩	3	3
10	{010}	{$\bar{1}$0$\bar{1}$}	⟨10$\bar{1}$⟩	⟨1$\bar{1}\bar{1}$⟩	1	4
11	{001}	{1$\bar{1}$0}	⟨110⟩	⟨11$\bar{1}$⟩	2	4
12	{001}	{$\bar{1}$10}	⟨110⟩	⟨11$\bar{1}$⟩	3	4

Table 11.3: Definition of the Pitsch orientation relationship (Pitsch OR). The parallel plains and directions as well as Bain group (BG) and close packed plane (CPP) groups are listed for all 12 variants formed by the OR.
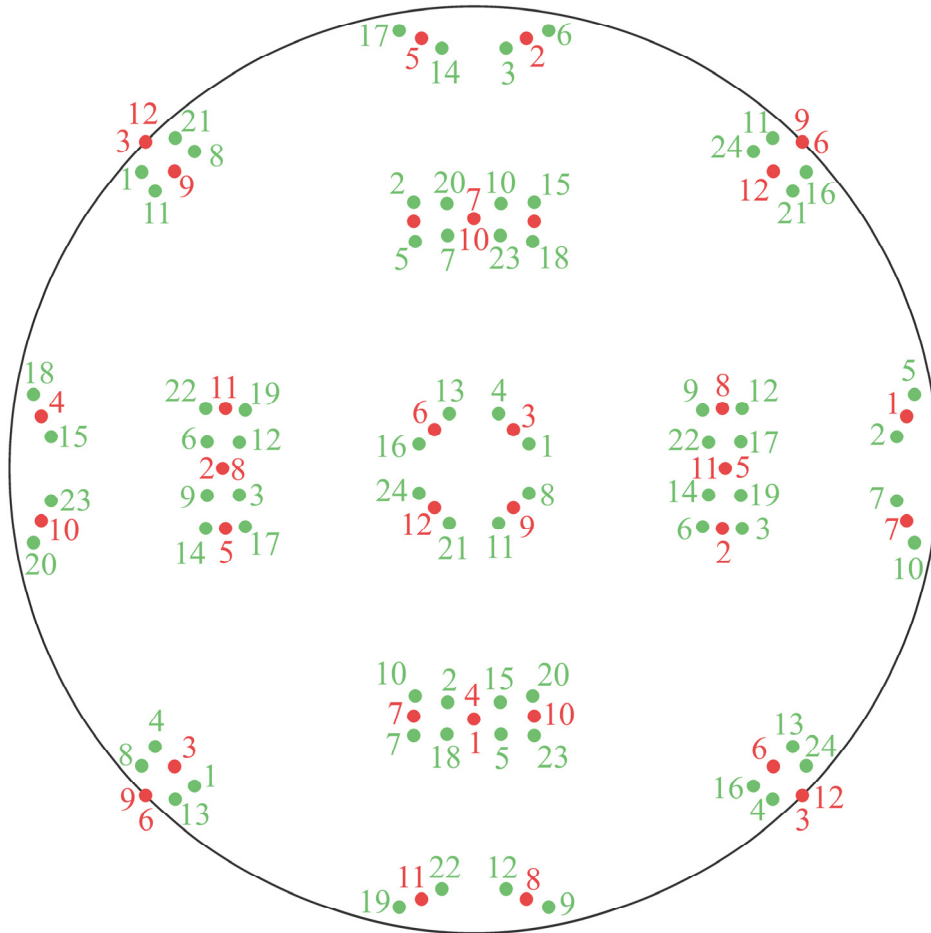
GT	Parallel planes		Parallel directions		BG	CPP
Variant	γ	α	γ	α		
1	{111}	{101}	⟨5̄ 1̄2̄ 17⟩	⟨1̄7̄ 7̄ 17⟩	1	1
2	{111}	{101}	⟨17 1̄2̄ 5̄⟩	⟨17 7̄ 1̄7̄⟩	2	1
3	{111}	{011}	⟨1̄2̄ 17 5̄⟩	⟨7̄ 17 1̄7̄⟩	3	1
4	{111}	{011}	⟨1̄2̄ 5̄ 17⟩	⟨7̄ 1̄7̄ 17⟩	1	1
5	{111}	{110}	⟨17 5̄ 1̄2̄⟩	⟨17 1̄7̄ 7̄⟩	2	1
6	{111}	{110}	⟨5̄ 17 1̄2̄⟩	⟨1̄7̄ 17 7̄⟩	3	1
7	{11̄1}	{101}	⟨1̄7̄ 1̄2̄ 5⟩	⟨1̄7̄ 7̄ 17⟩	2	2
8	{11̄1}	{101}	⟨5 1̄2̄ 1̄7̄⟩	⟨17 7̄ 1̄7̄⟩	1	2
9	{11̄1}	{11̄0}	⟨5 17 12⟩	⟨17 17 7⟩	3	2
10	{11̄1}	{11̄0}	⟨1̄7̄ 5̄ 12⟩	⟨1̄7̄ 1̄7̄ 7⟩	2	2
11	{11̄1}	{01̄1}	⟨12 5̄ 1̄7̄⟩	⟨7 1̄7̄ 1̄7̄⟩	1	2
12	{11̄1}	{01̄1}	⟨12 17 5⟩	⟨7 17 17⟩	3	2
13	{1̄11}	{011}	⟨1̄2̄ 1̄7̄ 5⟩	⟨7̄ 1̄7̄ 17⟩	3	3
14	{1̄11}	{011}	⟨1̄2̄ 5 1̄7̄⟩	⟨7̄ 17 1̄7̄⟩	1	3
15	{1̄11}	{1̄10}	⟨17 5 12⟩	⟨17 17 7⟩	2	3
16	{1̄11}	{1̄10}	⟨5̄ 1̄7̄ 12⟩	⟨1̄7̄ 1̄7̄ 7⟩	3	3
17	{1̄11}	{1̄01}	⟨5̄ 12 1̄7̄⟩	⟨1̄7̄ 7 1̄7̄⟩	1	3
18	{1̄11}	{1̄01}	⟨17 12 5⟩	⟨17 7 17⟩	2	3
19	{1̄1̄1}	{1̄1̄0}	⟨5 1̄7̄ 1̄2̄⟩	⟨17 1̄7̄ 7̄⟩	3	4
20	{1̄1̄1}	{1̄1̄0}	⟨1̄7̄ 5 1̄2̄⟩	⟨1̄7̄ 17 7̄⟩	2	4
21	{1̄1̄1}	{01̄1}	⟨12 5 17⟩	⟨7 17 17⟩	1	4
22	{1̄1̄1}	{01̄1}	⟨12 1̄7̄ 5̄⟩	⟨7 1̄7̄ 1̄7̄⟩	3	4
23	{1̄1̄1}	{1̄01}	⟨1̄7̄ 12 5̄⟩	⟨1̄7̄ 7 1̄7̄⟩	2	4
24	{1̄1̄1}	{1̄01}	⟨5̄ 12 17⟩	⟨17 7 17⟩	1	4

Table 11.4: Definition of the Greninger-Troiano orientation relationship (GT OR). The parallel plains and directions as well as Bain group (BG) and close packed plane (CPP) groups are listed for all 24 variants formed by the OR.

GT' Variant	Parallel planes γ	Parallel planes α	Parallel directions γ	Parallel directions α	BG	CPP
1	$\{\bar{17}\ \bar{7}\ 17\}$	$\{\bar{5}\ \bar{12}\ 17\}$	$\{101\}$	$\{111\}$	1	1
2	$\{17\ \bar{7}\ \bar{17}\}$	$\{17\ \bar{12}\ \bar{5}\}$	$\{101\}$	$\{111\}$	2	1
3	$\{\bar{7}\ 17\ \bar{17}\}$	$\{\bar{12}\ 17\ \bar{5}\}$	$\{011\}$	$\{111\}$	3	1
4	$\{\bar{7}\ \bar{17}\ 17\}$	$\{\bar{12}\ \bar{5}\ 17\}$	$\{011\}$	$\{111\}$	1	1
5	$\{17\ \bar{17}\ \bar{7}\}$	$\{17\ \bar{5}\ \bar{12}\}$	$\{110\}$	$\{111\}$	2	1
6	$\{\bar{17}\ 17\ \bar{7}\}$	$\{\bar{5}\ 17\ \bar{12}\}$	$\{110\}$	$\{111\}$	3	1
7	$\{\bar{17}\ \bar{7}\ 17\}$	$\{\bar{17}\ \bar{12}\ 5\}$	$\{101\}$	$\{1\bar{1}1\}$	2	2
8	$\{17\ \bar{7}\ \bar{17}\}$	$\{5\ \bar{12}\ \bar{17}\}$	$\{101\}$	$\{1\bar{1}1\}$	1	2
9	$\{17\ 17\ 7\}$	$\{5\ 17\ 12\}$	$\{1\bar{1}0\}$	$\{1\bar{1}1\}$	3	2
10	$\{\bar{17}\ \bar{17}\ 7\}$	$\{\bar{17}\ \bar{5}\ 12\}$	$\{1\bar{1}0\}$	$\{1\bar{1}1\}$	2	2
11	$\{7\ \bar{17}\ \bar{17}\}$	$\{12\ \bar{5}\ \bar{17}\}$	$\{0\bar{1}1\}$	$\{1\bar{1}1\}$	1	2
12	$\{7\ 17\ 17\}$	$\{12\ 17\ 5\}$	$\{0\bar{1}1\}$	$\{1\bar{1}1\}$	3	2
13	$\{\bar{7}\ \bar{17}\ 17\}$	$\{\bar{12}\ \bar{17}\ 5\}$	$\{011\}$	$\{\bar{1}11\}$	3	3
14	$\{\bar{7}\ 17\ \bar{17}\}$	$\{\bar{12}\ 5\ \bar{17}\}$	$\{011\}$	$\{\bar{1}11\}$	1	3
15	$\{17\ 17\ 7\}$	$\{17\ 5\ 12\}$	$\{\bar{1}10\}$	$\{\bar{1}11\}$	2	3
16	$\{\bar{17}\ \bar{17}\ 7\}$	$\{\bar{5}\ 17\ 12\}$	$\{\bar{1}10\}$	$\{\bar{1}11\}$	3	3
17	$\{\bar{17}\ 7\ \bar{17}\}$	$\{\bar{5}\ 12\ \bar{17}\}$	$\{\bar{1}01\}$	$\{\bar{1}11\}$	1	3
18	$\{17\ 7\ 17\}$	$\{17\ 12\ 5\}$	$\{\bar{1}01\}$	$\{\bar{1}11\}$	2	3
19	$\{17\ \bar{17}\ \bar{7}\}$	$\{5\ \bar{17}\ \bar{12}\}$	$\{\bar{1}\bar{1}0\}$	$\{\bar{1}\bar{1}1\}$	3	4
20	$\{\bar{17}\ 17\ \bar{7}\}$	$\{\bar{17}\ 5\ \bar{12}\}$	$\{\bar{1}\bar{1}0\}$	$\{\bar{1}\bar{1}1\}$	2	4
21	$\{7\ 17\ 17\}$	$\{12\ 5\ 17\}$	$\{0\bar{1}1\}$	$\{\bar{1}\bar{1}1\}$	1	4
22	$\{7\ \bar{17}\ \bar{17}\}$	$\{12\ \bar{17}\ \bar{5}\}$	$\{0\bar{1}1\}$	$\{\bar{1}\bar{1}1\}$	3	4
23	$\{\bar{17}\ 7\ \bar{17}\}$	$\{\bar{17}\ 12\ \bar{5}\}$	$\{\bar{1}01\}$	$\{\bar{1}\bar{1}1\}$	2	4
24	$\{17\ 7\ 17\}$	$\{5\ 12\ 17\}$	$\{\bar{1}01\}$	$\{\bar{1}\bar{1}1\}$	1	4

Table 11.5: Definition of the inverse Greninger-Troiano orientation relationship (GT' OR). The parallel plains and directions as well as Bain group (BG) and close packed plane (CPP) groups are listed for all 24 variants formed by the OR.

11.2 Standard Probabilities of Orientation Relationships

f (%) $\diagdown$ ω (°)	Kurdjumov-Sachs	Nishiyama-Wassermann & Pitsch	Greninger-Troiano & Inv. Greninger-Troiano	Bain
1		0.01		
2	0.13	0.07	0.13	0.02
3	0.44	0.22	0.44	0.05
4	1.04	0.52	0.98	0.13
5	2.03	1.01	1.79	0.25
6	3.43	1.75	2.90	0.44
7	5.10	2.78	4.25	0.70
8	6.99	4.04	5.80	1.04
9	9.04	5.46	7.50	1.48
10	11.24	7.05	9.38	2.03
11	13.61	8.82	11.46	2.70
12	16.17	10.78	13.60	3.50
13	19.00	12.98	16.23	4.45
14	22.08	15.43	18.99	5.55
15	25.43	18.09	22.01	6.83
16	29.02	21.03	25.30	8.29
17	32.97	24.47	28.86	9.93
18	37.19	27.48	32.71	11.79
19	41.77	31.49	36.88	13.79
20	46.58	35.52	41.35	16.16
21	51.84	39.94	46.19	18.71
22	57.35	44.68	51.33	21.44
23	63.33	49.74	56.85	24.49
24	69.45	55.14	62.71	27.82
25	74.99	60.94	68.93	31.39
26	79.80	66.77	74.66	35.35
27	83.93	72.29	79.56	39.49
28	87.36	77.47	83.78	44.03
29	90.25	82.02	87.34	48.86
30	92.73	86.00	90.33	54.08
31	94.75	89.32	92.80	59.64
32	96.46	92.07	94.88	65.38
33	97.76	94.31	96.54	70.74
34	98.71	96.10	97.81	75.59
35	99.34	97.51	98.74	79.99
36	99.65	98.46	99.28	83.78
37	99.81	99.06	99.59	87.05
38	99.90	99.43	99.76	89.79
39	99.95	99.65	99.86	92.17
40	99.98	99.79	99.93	94.16
41	99.99	99.88	99.97	95.85
42	100.00	99.94	99.99	97.24
43	100.00	99.97	100.00	98.31
44	100.00	99.99	100.00	99.09
45	100.00	100.00	100.00	99.59
46	100.00	100.00	100.00	99.85
47	100.00	100.00	100.00	99.96
48	100.00	100.00	100.00	100.00

Table 11.6: Fraction of the unit sphere covered by the variants of various ORs as a function of the tolerance angle ω.

Bibliography

[1]   Y. J. Li, P. Choi, S. Goto, C. Borchers, D. Raabe, and R. Kirchheim, "Evolution of strength and microstructure during annealing of heavily cold-drawn 6.3 GPa hypereutectoid pearlitic steel wire," *Acta Mater.*, vol. 60, no. 9, pp. 4005–4016, 2012.

[2]   D. Kuhn, H. Medlin, *ASM Handbook – Mechanical Testing and Evaluation*. ASM International, Materials Park, OH, 2000.

[3]   M. Cohen, "Unknowables in the Essence of Materials Science and Engineering," *Mater. Sci. Eng.*, vol. 25, pp. 3–4, 1976.

[4]   G. B. Olson, "Computational Design of Hierarchically Structured Materials," *Science (80-.).*, vol. 277, no. 5330, pp. 1237–1242, 1997.

[5]   J. Yin, M. Hillert, and A. Borgenstam, "Morphology of Proeutectoid Ferrite," *Metall. Mater. Trans. A Phys. Metall. Mater. Sci.*, vol. 48, no. 3, pp. 1425–1443, 2017.

[6]   G. Krauss and S. W. Thompson, "Ferritic Microstructures in Continuously Cooled Low- and Ultralow-carbon Steels.," *ISIJ Int.*, vol. 35, no. 8, pp. 937–945, 1995.

[7]   J. Freudenberger *et al.*, "Materials Science and Engineering," in *Springer Handbook of Mechanical Engineering*, Springer Verlag, Berlin Heidelberg;. 2009, p. 159.

[8]   G. Krauss, *Steels - Processing Structure and Performance*. ASM International, Materials Park, OH, 2005.

[9]   G. Krauss, *Principles of Heat Treatment of Steel*. American Society for Metals, Materials Park, OH, 1980.

[10]   H. I. Aaronson, "The Decomposition of Austenite by Diffusional Processes" 1962, Interscience, New York, pp. 387–546.

[11]   J. W. Christian, *The Theory of Transformations in Metals and Alloys (Part I + II)*, 3rd Edition. Elsevier Science Ltd, Oxford, 2002.

[12]   H. K. D. H. Bhadeshia, *Bainite in steels: Transformations, microstructure and properties*, IOM International, London, 2001.

[13]   C. A. Dube, H. I. Aaronson, and R. F. Mehl, "La formation de la ferrite proeutectoïde dans les aciers au carbone," *Rev. Met. Paris*, vol. 55, no. 3, pp. 201–210, 1958.

[14]   D. Zhang, H. Terasaki, and Y. Komizo, "In situ observation of phase transformation in Fe-0.15C binary alloy," *J. Alloys Compd.*, vol. 484, no. 1–2, pp. 929–933, 2009.

[15]   E. Schmidt, Y. Wang, and S. Sridhar, "A study of nonisothermal austenite formation and decomposition in Fe-C-Mn alloys," *Metall. Mater. Trans. A Phys. Metall. Mater. Sci.*, vol. 37, no. 6, pp. 1799–1810, 2006.

[16]   E. D. Schmidt, E. B. Damm, and S. Sridhar, "A study of diffusion- and interface-controlled migration of the Austenite/Ferrite front during Austenitization of a case-hardenable alloy steel," *Metall. Mater. Trans. A Phys. Metall. Mater. Sci.*, vol. 38, no. 4, pp. 698–715, 2007.

[17]   E. Schmidt, D. Soltesz, S. Roberts, A. Bednar, and S. Sridhar, "The Austenite/Ferrite Front Migration Rate during Heating of IF Steel," *ISIJ Int.*, vol. 46, no. 10, pp. 1500–1509, 2006.

[18]   A. Ray, S. Kr. Ray, and S. R. Mediratta, "Effect of carbides on the austenite grain growth characteristics in 1Cr-1C and 6Cr-1Mo-1C steels," *J. Mater. Sci.*, vol. 25, no. 12, pp. 5070–5076, 1990.

[19]   D. Phelan, "In-situ studies of phase transformations in iron alloys," University of Wollongong, 2002.

[20]   T. Fukino and S. Tsurekawa, "In-Situ SEM/EBSD Observation of α/γ Phase Transformation in Fe-Ni Alloy," *Mater. Trans.*, vol. 49, no. 12, pp. 2770–2775, 2008.

[21]   T. Fukino, S. Tsurekawa, and Y. Morizono, "In-Situ Scanning Electron Microscopy/Electron Backscattered Diffraction Observation of Microstructural Evolution during α → γ Phase Transformation in Deformed Fe-Ni Alloy," in *Metallurgical and Materials Transactions A: Physical Metallurgy and Materials Science*, 2011, vol. 42, no. 3, pp. 587–593.

[22]   I. Lischewski, D. M. Kirch, A. Ziemons, and G. Gottstein, "Investigation of Microstructure Development During α-γ-α Phase Transformation in Steel by Using High Temperature in situ EBSD," pp. 409–413.

[23]   I. Lischewski, D. M. Kirch, A. Ziemons, and G. Gottstein, "Investigation of the α-γ-α phase transformation in steel: High-temperature in situ EBSD measurements," *Texture, Stress. Microstruct.*, vol. 2008, 2008.

[24]   I. Lischewski and G. Gottstein, "Nucleation and variant selection during the α-γ-α phase transformation in microalloyed steel," *Acta Mater.*, vol. 59, no. 4, pp. 1530–1541, 2011.

[25]   I. Lischewski, "Die Variantenselektion während der α-γ-α Phasenumwandlung in Stahl," Rheinisch-Westfälische Hochschule Aachen, 2010.

[26]   G. Brückner and G. Gottstein, "Transformation Textures during Diffusional α→γ→α Phase Transformations in Ferritic Steels.," *ISIJ Int.*, vol. 41, no. 5, pp. 468–477, 2001.

[27]   G. Brückner, J. Pospiech, I. Seidl, and G. Gottstein, "Orientation correlation during diffusional α → γ phase transformation in a ferritic low carbon steel," *Scr. Mater.*, vol. 44, no. 11, pp. 2635–2640, 2001.

[28]   H. K. D. H. Bhadeshia and R. W. K. Honeycombe, *Steels*, 3rd ed. 2006.

[29]   P. J. Jacques, Q. Furnémont, F. Lani, T. Pardoen, and F. Delannay, "Multiscale mechanics of TRIP-assisted multiphase steels: I. Characterization and mechanical testing," *Acta Mater.*, vol. 55, no. 11, pp. 3681–3693, 2007.

[30]   I. B. Timokhina, P. D. Hodgson, and E. V. Pereloma, "Effect of Microstructure on the Stability of Retained Austenite in Transformation-Induced-Plasticity Steels," *Metall. Mater. Trans. A*, vol. 35A, pp. 2331–2341, 2004.

[31]   K. Sugimoto, N. Usui, M. Kobayashi, and S. Hashimoto, "Effects of Volume Fraction and Stability of Retained Austenite on Ductility of TRIP-aided Dual-phase Steels," *ISIJ Int.*, vol. 32, no. 12, pp. 1311–1318, 1992.

[32]   N. H. Van Dijk *et al.*, "Thermal stability of retained austenite in TRIP steels studied by synchrotron X-ray diffraction during cooling," *Acta Mater.*, vol. 53, no. 20, pp. 5439–5447, 2005.

[33]   O. Matsumura, Y. Sakuma, and H. Takechi, "Enhancement of Elongation by Retained Austenite in Intercritical Annealed 0.4C-1.5Si-0.8Mn Steel," *Trans. Iron Steel Inst. Japan*, vol. 27, no. 7, pp. 570–579, 1987.

[34]   K. Sugimoto, T. Iida, J. Sakaguchi, and T. Kashima, "Retained Austenite Characteristics and Tensile Properties in a TRIP Type Bainitic Sheet Steel.," *ISIJ Int.*, vol. 40, no. 9, pp. 902–908, 2000.

[35] F. D. Fischer, Q.-P. Sun, and K. Tanaka, "Transformation-induced plasticity (TRIP)," *Appl. Mech. Rev.*, vol. 49, no. 6, pp. 317–364, 1996.

[36] G. W. Greenwood and R. H. Johnson, "The Deformation of Metals Under Small Stresses During Phase Transformations," *Proc. R. Soc. A Math. Phys. Eng. Sci.*, vol. 283, no. 1394, pp. 403–422, 1965.

[37] H. K. D. H. Bhadeshia, L. E. Svensson, and B. Gretoft, "The influence of alloying elements on the formation of allotriomorphic ferrite in low-alloy steel weld deposits," *J. Mater. Sci. Lett.*, vol. 4, no. 3, pp. 305–308, 1985.

[38] C. Capdevila, F. G. Caballero, and C. G. De Andrés, "Modeling of kinetics of austenite-to-allotriomorphic ferrite transformation in 0.37C-1.45Mn-0.11V microalloyed steel," *Metall. Mater. Trans. A Phys. Metall. Mater. Sci.*, vol. 32, no. 13, pp. 661–669, 2001.

[39] C. R. Hutchinson, H. S. Zurob, and Y. Bréchet, "The growth of ferrite in Fe-C-X alloys: The role of thermodynamics, diffusion, and interfacial conditions," *Metall. Mater. Trans. A Phys. Metall. Mater. Sci.*, vol. 37, no. 6, pp. 1711–1720, 2006.

[40] C. Capdevila, F. G. Caballero, and C. García De Andrés, "Relevant aspects of allotriomorphic and idiomorphic ferrite transformation kinetics," *Mater. Sci. Technol.*, vol. 19, no. 2, pp. 195–201, 2003.

[41] D. W. Kim, D. W. Suh, R. S. Qin, and H. K. D. H. Bhadeshia, "Dual orientation and variant selection during diffusional transformation of austenite to allotriomorphic ferrite," *J. Mater. Sci.*, vol. 45, no. 15, pp. 4126–4132, 2010.

[42] D. W. Kim, R. S. Qin, and H. K. D. H. Bhadeshia, "Transformation texture of allotriomorphic ferrite in steel," *Mater. Sci. Technol.*, vol. 25, no. 000, pp. 892–895, 2009.

[43] F. Ishikawa, T. Takahashi, and T. Ochi, "Intragranular ferrite nucleation in medium-carbon vanadium steels," *Metall. Mater. Trans. A*, vol. 25, no. 5, pp. 929–936, 1994.

[44] T. Yokomizo, M. Enomoto, O. Umezawa, G. Spanos, and R. O. Rosenberg, "Three-dimensional distribution, morphology, and nucleation site of intragranular ferrite formed in association with inclusions," *Mater. Sci. Eng. A*, vol. 344, no. 1–2, pp. 261–267, 2003.

[45] C. Capdevila, F. G. Caballero, and C. García De Andrés, "Modeling of kinetics of isothermal idiomorphic ferrite formation in a medium-carbon vanadium-titanium microalloyed steel," *Metall. Mater. Trans. A Phys. Metall. Mater. Sci.*, vol. 32, no. 7, pp. 1591–1598, 2001.

[46] L. Cheng and K. M. Wu, "New insights into intragranular ferrite in a low-carbon low-alloy steel," *Acta Mater.*, vol. 57, no. 13, pp. 3754–3762, 2009.

[47] J. M. Gregg and H. K. D. H. Bhadeshia, "Solid-state nucleation of acicular ferrite on minerals added to molten steel," *Acta Mater.*, vol. 45, no. 2, pp. 739–748, 1997.

[48] I. Madariaga, I. Gutierrez, and H. K. D. H. Bhadeshia, "Acicular ferrite morphologies in a medium-carbon microalloyed steel," *Metall. Mater. Trans. A Phys. Metall. Mater. Sci.*, vol. 32, no. 9, pp. 2187–2197, 2001.

[49] F. R. Xiao *et al.*, "Challenge of mechanical properties of an acicular ferrite pipeline steel," *Mater. Sci. Eng. A*, vol. 431, no. 1–2, pp. 41–52, 2006.

[50] A. Guo, R. D. K. Misra, J. Liu, L. Chen, X. He, and S. J. Jansto, "An analysis of the microstructure of the heat-affected zone of an ultra-low carbon and niobium-bearing acicular ferrite steel using EBSD and its relationship to mechanical properties," *Mater. Sci. Eng. A*, vol. 527, no. 23, pp. 6440–6448, 2010.

[51] H. K. Sung, S. Y. Shin, W. Cha, K. Oh, S. Lee, and N. J. Kim, "Effects of acicular ferrite on charpy impact properties in heat affected zones of oxide-containing API X80 linepipe steels," *Mater. Sci. Eng. A*, vol. 528, no. 9, pp. 3350–3357, 2011.

[52] J. R. Yang and H. K. D. H. Bhadeshia, "Orientation relationships between adjacent plates of acicular ferrite in steel weld deposits," *Mater. Sci. Technol.*, vol. 5, no. 1, pp. 93–97, 1989.

[53] R. A. Ricks, "The nature of acicular ferrite in HSLA steel weld metals," *J. Mater. Sci.*, vol. 17, pp. 732–740, 1982.

[54] W. L. Costin, O. Lavigne, and A. Kotousov, "A study on the relationship between microstructure and mechanical properties of acicular ferrite and upper bainite," *Mater. Sci. Eng. A*, vol. 663, pp. 193–203, 2016.

[55] J. R. Yang, C. Y. Huang, C. F. Huang, and J. N. Aoh, "Influence of acicular ferrite and bainite microstrcure on thoughness for an ultra-low-carbon alloy steel weld metal," *J. Mater. Sci. Lett.*, vol. 12, pp. 1290–1293, 1993.

[56] A. A. B. Sugden and H. K. D. H. Bhadeshia, "Lower acicular ferrite," *Metall. Trans. A*, vol. 20, no. 9, pp. 1811–1818, 1989.

[57] X. Wang, C. Shang, S. Yang, X. He, and X. Liu, "The refinement technology for bainite and its application," *Mater. Sci. Eng. A*, vol. 438–440, no. SPEC. ISS., pp. 162–165, 2006.

[58] B. L. Bramfitt and J. G. Speer, "A perspective on the morphology of bainite," *Metall. Trans. A*, vol. 21, no. 3, pp. 817–829, 1990.

[59] Y. Ohmori, H. Ohtsubo, Y. C. Jung, S. Okaguchi, and H. Ohtani, "Morphology of bainite and widmanstätten ferrite," *Metall. Mater. Trans. A*, vol. 25, no. 9, pp. 1981–1989, 1994.

[60] J. J. Jonas, Y. He, and G. Langelaan, "The rotation axes and angles involved in the formation of self-accommodating plates of Widmanstätten ferrite," *Acta Mater.*, vol. 72, pp. 13–21, 2014.

[61] Y. Ohmori, H. Ohtsubo, K. Georgima, and N. Maruyama, "Growth of Bainite and Widmanstätten Ferrite," *Mater. Trans.*, vol. 34, no. 3, pp. 216–223, 1993.

[62] D. Phelan, N. Stanford, and R. Dippenaar, "In situ observations of Widmanstätten ferrite formation in a low-carbon steel," *Mater. Sci. Eng. A*, vol. 407, no. 1–2, pp. 127–134, 2005.

[63] J. . Watson and P. . McDougall, "The crystallography of widmanstätten ferrite," *Acta Metall.*, vol. 21, no. 7, pp. 961–973, 1973.

[64] G. Spanos, A. W. Wilson, and M. V. Kral, "New insights into the widmanstätten proeutectoid ferrite transformation: Integration of crystallographic and three-dimensional morphological observations," *Metall. Mater. Trans. A Phys. Metall. Mater. Sci.*, vol. 36, no. 5, pp. 1209–1218, 2005.

[65] M. Hillert, A. Borgenstam, and J. Ågren, "Do bainitic and Widmanstätten ferrite grow with different mechanisms?," *Scr. Mater.*, vol. 62, no. 2, pp. 75–77, 2010.

[66] F. G. Caballero, C. Garcia-Mateo, M. J. Santofimia, M. K. Miller, and C. García de Andrés, "New experimental evidence on the incomplete transformation phenomenon in steel," *Acta Mater.*, vol. 57, no. 1, pp. 8–17, 2009.

[67]   H. K. D. H. Bhadeshia, "A rationalisation of shear transformations in steels," *Acta Metall.*, vol. 29, no. 6, pp. 1117–1130, 1981.

[68]   P. H. Shipway and H. K. D. H. Bhadeshia, "The mechanical stabilisation of Widmanstätten ferrite," *Mater. Sci. Eng. A*, vol. 223, no. 1–2, pp. 179–185, 1997.

[69]   V. V. Basabe, J. J. Jonas, and C. Ghosh, "Formation of Widmanstätten ferrite in a 0.036% Nb low carbon steel at temperatures above the Ae3," *Steel Res. Int.*, vol. 85, no. 1, pp. 8–15, 2014.

[70]   M. D. Geib, D. K. Matlock, and G. Krauss, "The effect of intercritical annealing temperature on the structure of niobium microalloyed dualphase steel," *Metall. Trans. A*, vol. 11, no. 10, pp. 1683–1689, 1980.

[71]   M. J. Santofimia, C. Kwakernaak, W. G. Sloof, L. Zhao, and J. Sietsma, "Experimental study of the distribution of alloying elements after the formation of epitaxial ferrite upon cooling in a low-carbon steel," *Mater. Charact.*, vol. 61, no. 10, pp. 937–942, 2010.

[72]   M. Sarwar, E. Ahmad, K. A. Qureshi, and T. Manzoor, "Influence of epitaxial ferrite on tensile properties of dual phase steel," *Mater. Des.*, vol. 28, no. 1, pp. 335–340, 2007.

[73]   M. Sarwar and R. Priestner, "Influence of ferrite-martensite microstructural morphology on tensile properties of dual-phase steel," *J. Mater. Sci.*, vol. 31, pp. 2091–2095, 1996.

[74]   M. Erdogan and R. Priestner, "Effect of epitaxial ferrite on yielding and plastic flow in dual phase steel in tension and compression," *Mater. Sci. Technol.*, vol. 15, pp. 1273–1284, 1999.

[75]   E. Ahmad, M. Sarwar, T. Manzoor, and N. Hussain, "Effect of rolling and epitaxial ferrite on the tensile properties of low alloy steel," *J. Mater. Sci.*, vol. 41, no. 17, pp. 5417–5423, 2006.

[76]   M. J. Santofimia, L. Zhao, R. Petrov, and J. Sietsma, "Characterization of the microstructure obtained by the quenching and partitioning process in a low-carbon steel," *Mater. Charact.*, vol. 59, no. 12, pp. 1758–1764, 2008.

[77]   M. J. Santofimia, L. Zhao, and J. Sietsma, "Microstructural evolution of a low-carbon steel during application of quenching and partitioning heat treatments after partial austenitization," *Metall. Mater. Trans. A Phys. Metall. Mater. Sci.*, vol. 40, no. 1, pp. 46–57, 2009.

[78]   M. J. Peet, L. C. D. Fielding, A. A. Hamedany, M. Rawson, P. Hill, and H. K. D. H. Bhadeshia, "Strength and toughness of clean nanostructured bainite," *Mater. Sci. Technol. (United Kingdom)*, vol. 33, no. 10, pp. 1171–1179, 2017.

[79]   F. G. Caballero, H. K. D. H. Bhadeshia, K. J. A. Mawella, D. G. Jones, and P. Brown, "Design of novel high strength bainitic steels: Part 1," *Mater. Sci. Technol.*, vol. 17, no. 5, pp. 512–516, 2001.

[80]   F. G. Caballero, H. K. D. H. Bhadeshia, K. J. A. Mawella, D. G. Jones, and P. Brown, "Design of novel high strength bainitic steels: Part 2," *Mater. Sci. Technol.*, vol. 17, no. 5, pp. 517–522, 2001.

[81]   C. Garcia-Mateo and F. G. Caballero, "Ultra-high-strength Bainitic Steels," *ISIJ Int.*, vol. 45, no. 11, pp. 1736–1740, 2005.

[82]   A. Kumar, S. B. Singh, and K. K. Ray, "Influence of bainite/martensite-content on the tensile of low carbon dual-phase steels," *Mater. Sci. Eng. A*, vol. 474, no. 1–2, pp. 270–282, 2008.

[83]   P. C. M. Rodrigues, E. V. Pereloma, and D. B. Santos, "Mechanical properities of an HSLA bainitic steel subjected to controlled rolling with accelerated cooling," *Mater. Sci. Eng. A*, vol. 283, no. 1–2, pp. 136–143, 2000.

[84]   I. A. Yakubtsov, P. Poruks, and J. D. Boyd, "Microstructure and mechanical properties of bainitic low carbon high strength plate steels," *Mater. Sci. Eng. A*, vol. 480, no. 1–2, pp. 109–116, 2008.

[85]   J. G. Speer, D. V. Edmonds, F. C. Rizzo, and D. K. Matlock, "Partitioning of carbon from supersaturated plates of ferrite, with application to steel processing and fundamentals of the bainite transformation," *Curr. Opin. Solid State Mater. Sci.*, vol. 8, no. 3–4, pp. 219–237, 2004.

[86]   C. Garcia-Mateo *et al.*, "Tensile behaviour of a nanocrystalline bainitic steel containing 3wt% silicon," *Mater. Sci. Eng. A*, vol. 549, pp. 185–192, 2012.

[87]   G. Gao, H. Zhang, X. Gui, P. Luo, Z. Tan, and B. Bai, "Enhanced ductility and toughness in an ultrahigh-strength Mn-Si-Cr-C steel: The great potential of ultrafine filmy retained austenite," *Acta Mater.*, vol. 76, pp. 425–433, 2014.

[88]   N. Saeidi and A. Ekrami, "Comparison of mechanical properties of martensite/ferrite and bainite/ferrite dual phase 4340 steels," *Mater. Sci. Eng. A*, vol. 523, no. 1–2, pp. 125–129, 2009.

[89]   C. García-Mateo and F. G. Caballero, "The Role of Retained Austenite on Tensile Properties of Steels with Bainitic Microstructures," *Mater. Trans.*, vol. 46, no. 8, pp. 1839–1846, 2005.

[90]   H. A. Aglan, Z. Y. Liu, M. F. Hassan, and M. Fateh, "Mechanical and fracture behavior of bainitic rail steel," *J. Mater. Process. Technol.*, vol. 151, no. 1-3 SPEC. ISS., pp. 268–274, 2004.

[91]   J. P. Naylor, "The influence of the lath morphology on the yield stress and transition temperature of martensitic- bainitic steels," *Metall. Trans. A*, vol. 10, no. 7, pp. 861–873, 1979.

[92]   Y. Tomita and K. Okabayashi, "Effect of microstructure on strength and toughness of heat-treated low alloy structural steels," *Metall. Trans. A*, vol. 17, no. 7, pp. 1203–1209, 1986.

[93]   H. Terasaki and Y. I. Komizo, "Morphology and crystallography of bainite transformation in a single prior-austenite grain of low-carbon steel," *Metall. Mater. Trans. A Phys. Metall. Mater. Sci.*, vol. 44, no. 6, pp. 2683–2689, 2013.

[94]   L. C. D. Fielding, "The Bainite Controversy," *Mater. Sci. Technol.*, vol. 29, no. 4, pp. 383–399, 2013.

[95]   R. F. Hehemann, K. R. Kinsman, and H. I. Aaronson, "A debate on the bainite reaction," *Metall. Trans.*, vol. 3, no. 5, pp. 1077–1094, 1972.

[96]   M. Hillert, "Diffusion in growth of bainite," *Metall. Mater. Trans. A*, vol. 25, no. 9, pp. 1957–1966, 1994.

[97]   R. W. K. Honeycombe and F. B. Pickering, "Ferrite and bainite in alloy steels," *Metall. Trans.*, vol. 3, no. 5, pp. 1099–1112, 1972.

[98]   H. I. Aaronson, T. Furuhara, J. M. Rigsbee, W. T. Reynolds, and J. M. Howe, "Crystallographic and mechanistic aspects of growth by shear and by diffusional processes," *Metall. Trans. A*, vol. 21, no. 9, pp. 2369–2409, 1990.

[99]   Y. Ohmori and T. Maki, "Bainitic Transformation in View of Displacive Mechanism," *Mater. Trans.*, vol. 32, no. 8, pp. 631–641, 1991.

[100] M. Hillert, "Paradigm shift for bainite," *Scr. Mater.*, vol. 47, no. 3, pp. 175–180, 2002.

[101] R. Le Houillier, G. Bégin, and A. Dubé, "A study of the peculiarities of austenite during the formation of bainite," *Metall. Trans.*, vol. 2, no. 9, pp. 2645–2653, 1971.

[102] H. I. Aaronson, G. Spanos, and W. T. Reynolds, "A progress report on the definitions of bainite," *Scr. Mater.*, vol. 47, no. 3, pp. 139–144, 2002.

[103] H. I. Aaronson and W. T. Reynolds Jr., "Reply to a discussion by J.W. Christian and D.V. Edmonds of papers by Aaronson and co-workers on the proeutectoid ferrite and bainite reactions," *Scr. Metall.*, vol. 22, no. 4, pp. 567–572, 1988.

[104] H. K. D. . Bhadeshia, "The bainite transformation: unresolved issues," *Mater. Sci. Eng. A*, vol. 273–275, pp. 58–66, 1999.

[105] F. G. Caballero, M. K. Miller, C. Garcia-Mateo, and J. Cornide, "New experimental evidence of the diffusionless transformation nature of bainite," *J. Alloys Compd.*, vol. 577, no. SUPPL. 1, pp. S626–S630, 2013.

[106] M. Kang, M. X. Zhang, and M. Zhu, "In situ observation of bainite growth during isothermal holding," *Acta Mater.*, vol. 54, no. 8, pp. 2121–2129, 2006.

[107] J. Hu, L.-X. Du, and J.-J. Wang, "Effect of cooling procedure on microstructures and mechanical properties of hot rolled Nb–Ti bainitic high strength steel," *Mater. Sci. Eng. A*, vol. 554, pp. 79–85, 2012.

[108] W. Zhao, W. Wang, S. Chen, and J. Qu, "Effect of simulated welding thermal cycle on microstructure and mechanical properties of X90 pipeline steel," *Mater. Sci. Eng. A*, vol. 528, no. 24, pp. 7417–7422, 2011.

[109] H. I. Aaronson, W. T. Reynolds, G. J. Shiflet, and G. Spanos, "Bainite viewed three different ways," *Metall. Trans. A*, vol. 21, no. 6, pp. 1343–1380, 1990.

[110] G. Spanos, H. S. Fang, D. S. Sarma, and H. I. Aaronson, "Influence of carbon concentration and reaction temperature upon bainite morphology in Fe-C-2 Pct Mn alloys," *Metall. Trans. A*, vol. 21, no. 6, pp. 1391–1411, 1990.

[111] Z. Ławrynowicz, "Transition from upper to lower bainite in Fe–C–Cr steel," *Mater. Sci. Technol.*, vol. 20, no. 11, pp. 1447–1454, 2004.

[112] T. Ko and A. Cottrell, "The Formation of Bainite," *J. Iron Steel Inst.*, vol. 172, pp. 307–315, 1952.

[113] A. G. Khachaturyan, *Theory of Structural Transformations in Solids*. Dover Publications, Mineola, NY,, 2008.

[114] Z. Nishiyama, *Martensitic Transformation*. Academic Press, Cambridge, 1978.

[115] A. L. Roitburd and G. V. Kurdjumov, "The nature of martensitic transformations," *Mater. Sci. Eng.*, vol. 39, no. 2, pp. 141–167, 1979.

[116] G. Krauss and A. R. Marder, "The morphology of martensite in iron alloys," *Metall. Trans.*, vol. 2, no. 9, pp. 2343–2357, 1971.

[117] J. R. Patel and M. Cohen, "Criterion for the action of applied stress in the martensitic transformation," *Acta Metall.*, vol. 1, no. 5, pp. 531–538, 1953.

[118] A. Stormvinter, P. Hedström, and A. Borgenstam, "Investigation of Lath and Plate Martensite in a Carbon Steel," *Solid State Phenom.*, vol. 172–174, pp. 61–66, 2011.

[119] G. Krauss, "Martensite in steel: strength and structure," *Mater. Sci. Eng. A*, vol. 273–275, pp. 40–57, 1999.

[120] C. M. Wayman, "Shear transformations and microstructure," *Metallography*, vol. 8, no. 2, pp. 105–130, 1975.

[121] T. Maki, "Microstructure and Mechanical Behaviour of Ferrous Martensite," *Mater. Sci. Forum*, vol. 56–58, pp. 157–168, 1990.

[122] H. Kitahara, R. Ueji, M. Ueda, N. Tsuji, and Y. Minamino, "Crystallographic analysis of plate martensite in Fe-28.5 at.% Ni by FE-SEM/EBSD," *Mater. Charact.*, vol. 54, no. 4–5, pp. 378–386, 2005.

[123] R. P. Reed, "The plate-like martensite transformation in Fe-Ni alloys," *Acta Metall.*, vol. 15, no. 8, pp. 1287–1296, 1967.

[124] M. Umemoto, E. Yoshitake, and I. Tamura, "The morphology of martensite in Fe-C, Fe-Ni-C and Fe-Cr-C alloys," *J. Mater. Sci.*, vol. 18, no. 10, pp. 2893–2904, 1983.

[125] S. Morito, H. Tanaka, R. Konishi, T. Furuhara, and T. Maki, "The morphology and crystallography of lath martensite in Fe-C alloys," *Acta Mater.*, vol. 51, pp. 1789–1799, 2003.

[126] B. P. J. Sandvik and C. M. Wayman, "Characteristics of lath martensite: Part I. crystallographic and substructural features," *Metall. Trans. A*, vol. 14, no. 4, pp. 809–822, 1983.

[127] B. P. J. Sandvik and C. M. Wayman, "Characteristics of lath martensite: Part II. The martensite-austenite interface," *Metall. Trans. A*, vol. 14, no. 4, pp. 823–834, 1983.

[128] B. P. J. Sandvik and C. M. Wayman, "Characteristics of lath martensite: Part III. Some theoretical considerations," *Metall. Trans. A*, vol. 14, no. 4, pp. 835–844, 1983.

[129] H. Kitahara, R. Ueji, N. Tsuji, and Y. Minamino, "Crystallographic features of lath martensite in low-carbon steel," *Acta Mater.*, vol. 54, no. 5, pp. 1279–1288, 2006.

[130] S. Nambu, N. Shibuta, M. Ojima, J. Inoue, T. Koseki, and H. K. D. H. Bhadeshia, "In situ observations and crystallographic analysis of martensitic transformation in steel," *Acta Mater.*, vol. 61, no. 13, pp. 4831–4839, 2013.

[131] S. Morito, J. Nishikawa, and T. Maki, "Dislocation density within lath martensite in Fe-C and Fe-Ni alloys," *ISIJ Int.*, vol. 43, no. 9, pp. 1475–1477, 2003.

[132] B. P. J. Sandvik and C. M. Wayman, "Some crystallographic characteristics of the (252)f martensite transformation in Fe-alloys," *Metall. Trans. A*, vol. 14, no. 12, pp. 2469–2477, 1983.

[133] H. Sato and S. Zaefferer, "A study on the formation mechanisms of butterfly-type martensite in Fe-30% Ni alloy using EBSD-based orientation microscopy," *Acta Mater.*, vol. 57, no. 6, pp. 1931–1937, 2009.

[134] M. Umemoto and I. Tamura, "The Morphology and Substructure of Butterfly Martensite in Ferrous Alloys," *J. Phys. Colloq.*, vol. 43, no. 4, pp. 523–528, 1982.

[135] A. Shibata, T. Murakami, S. Morito, T. Furuhara, and T. Maki, "The origin of midrib in lenticular martensite," *Nippon Kinzoku Gakkaishi/Journal Japan Inst. Met.*, vol. 73, no. 4, pp. 290–298, 2009.

[136] T. Chiba, G. Miyamoto, and T. Furuhara, "Variant selection of lenticular martensite by ausforming," *Scr. Mater.*, vol. 67, no. 4, pp. 324–327, 2012.

[137] T. Maki, S. Shimooka, S. Fujiwara, and I. Tamura, "Formation Temperature Thin Plate Martensite and Growth Behavior of in Fe-Ni-C Alloys," *Trans. Japan Instuitute Met.*, vol. 16, no. 1, pp. 35–41, 1975.

[138] M. P. Kashchenko and V. G. Chashchina, "Key role of transformation twins in comparison of results of crystal geometric and dynamic analysis for thin-plate martensite," *Phys. Met. Metallogr.*, vol. 114, no. 10, pp. 821–825, 2013.

[139] H. Okamoto, M. Oka, and I. Tamura, "Couplings of Thin-plate Martensites in in Fe-Ni-C Alloy," *Trans. Japan Inst. Met.*, vol. 19, no. 12, pp. 674–684, 1978.

[140] J. W. Christian, "Accomodation strains in martensite formation and the use of a dilatation parameter," *Acta Metall.*, vol. 6, pp. 377–379, 1958.

[141] J. D. Eshelby, "The determination of the elastic field of an ellipsoidal inclusion and related problems," *Proc. R. Soc. London A*, vol. 241, pp. 376–396, 1957.

[142]   J. D. Eshelby, "The elastic field outside an ellipsoidal inclusion," *Proc. R. Soc. London A*, vol. 252, pp. 561–569, 1959.

[143]   H. S. Yang and H. K. D. H. Bhadeshia, "Austenite Grain Size and the Martensite-Start Temperature," *Scr. Mater.*, vol. 60, pp. 493–495, 2009.

[144]   P. J. Brofman and G. S. Ansell, "On the effect of fine grain size on the Ms temperature in Fe-27Ni-0.025C alloys," *Metall. Trans. A*, vol. 14, no. 9, pp. 1929–1931, 1983.

[145]   T. Hanamura, S. Torizuka, S. Tamura, S. Enokida, and H. Takechi, "Effect of Austenite Grain Size on Transformation Behavior , Microstructure and Mechanical Properties of 0 . 1C – 5Mn Martensitic Steel," *ISIJ Int.*, vol. 53, no. 12, pp. 2218–2225, 2013.

[146]   A. García-Junceda, C. Capdevila, F. G. Caballero, and C. G. de Andrés, "Dependence of martensite start temperature on fine austenite grain size," *Scr. Mater.*, vol. 58, no. 2, pp. 134–137, 2008.

[147]   R. A. Farrar, Z. Zhang, S. R. Bannister, and G. S. Barritte, "The effect of prior austenite grain size on the transformation behaviour of C-Mn-Ni weld metal," *J. Mater. Sci.*, vol. 28, no. 5, pp. 1385–1390, 1993.

[148]   S. J. Donachie and G. S. Ansell, "The effect of quench rate on the properties and morphology of ferrous martensite," *Metall. Trans. A*, vol. 6, no. 11, pp. 1863–1875, 1975.

[149]   D. G. Hennessy, V. Sharma, and G. S. Ansell, "Tempering kinetics of alloy steels as a function of quench rate and Ms temperature," *Metall. Trans. A*, vol. 14, no. 6, pp. 1013–1019, 1983.

[150]   G. S. Ansell, S. J. Donachie, and R. W. Messler, "The effect of quench rate on the martensitic transformation in Fe-C alloys," *Metall. Trans.*, vol. 2, no. 9, pp. 2443–2449, 1971.

[151]   D. E. Laughlin and K. Hono, *Physical Metallurgy*. Elsevier B.V., Amsterdam, 2014.

[152]   C. L. Magee, "The kinetics of martensite formation in small particles," *Metall. Trans.*, vol. 2, no. 9, pp. 2419–2430, 1971.

[153]   R. E. Cech, D. Turnbull, and R. E. Turnbull, "Heterogeneous nucleation of the martensite transformation.," *Trans. AIME*, vol. 8, no. 2, pp. 124–132, 1956.

[154]   M. A. Jaswon, *The Mechanism of Phase Transformations*, 18th ed., no. 33. London: Institute of Metals, 1956.

[155]   L. Kaufman and M. Cohen, "Thermodynamics and kinetics of martensitic transformations," *Prog. Met. Phys.*, vol. 7, pp. 165–246, 1958.

[156]   G. B. Olson and M. Cohen, "A general mechanism of martensitic nucleation: Part II. FCC → BCC and other martensitic transformations," *Metall. Trans. A*, vol. 7, no. 12, pp. 1905–1914, 1976.

[157]   G. B. Olson and M. Cohen, "A mechanism for the strain-induced nucleation of martensitic transformations," *J. Less-Common Met.*, vol. 28, no. 1, pp. 107–118, 1972.

[158]   A. L. Greer and K. F. Kelton, *Nucleation in condensed matter: applications in materials and biology*. Amsterdam; Boston: Elsevier, 2010.

[159]   A. J. Bogers and W. G. Burgers, "Partial dislocations on the {110} planes in the B.C.C. lattice and the transition of the F.C.C. into the B.C.C. lattice," *Acta Metall.*, vol. 12, no. 2, pp. 255–261, 1964.

[160]   G. B. Olson and M. Cohen, "A Perspective on Martensite Nucleation," *Annu. Rev. Mater. Sci.*, vol. 2, no. 1, pp. 1–19, 1981.

[161]   S. Dash and N. Brown, "Nucleation and growth of martensite in fe-32.3% Ni alloy," *Acta Metall.*, vol. 14, no. 5, pp. 595–603, 1966.

[162]   K. E. Easterling and A. R. Thölen, "The Nucleation of Martensite in Steel," *Acta Metall.*, vol. 24, pp. 333–341, 1976.

[163]   S. Kajiwara, "Roles of diclocations and grain boundaries in martensite nucleation," *Metall. Trans. A*, vol. 17A, pp. 1693–1702, 1986.

[164]   T. Song and B. C. De Cooman, "Martensite Nucleation at Grain Boundaries Containing Intrinsic Grain Boundary Dislocations," *ISIJ Int.*, vol. 54, no. 10, pp. 2394–2403, 2014.

[165]   P. L. Ferraglio and K. Mukherjee, "The Dynamics of Nucleation and Growth of a Thermoelastic Martensite an a Splat Quenched Au-47.5 at. % Cd Alloy," *Acta Metall.*, vol. 22, pp. 835–845, 1974.

[166]   K. E. Easterling and G. C. Weatherly, "On the nucleation of martensite in iron precipitates," *Acta Metall.*, vol. 17, no. 7, pp. 845–852, 1969.

[167]   J. Gaggero and D. Hull, "On the nucleation of martensite," *Acta Metall.*, vol. 10, pp. 995–998, 1962.

[168]   M. Suezawa and H. E. Cook, "On the Nucleation of Martensite," *Acta Metall.*, vol. 28, no. 4, pp. 423–432, 1980.

[169]   W. Krauss, S. K. Pabi, and H. Gleiter, "On the Mechanism of Martensite Nucleation," *Acta Metall.*, vol. 37, no. 1, pp. 25–30, 1989.

[170]   E. S. Machlin and M. Cohen, "Isothermal Mode of the Martensitic Transformation," *Trans. AIME*, vol. 4, no. 5, pp. 489–500, 1952.

[171]   G. Guénin and P. F. Gobin, "A localized soft mode model for the nucleation of thermoelastic martensitic transformation: Application to the β → 9r transformation," *Metall. Trans. A*, vol. 13, no. 7, pp. 1127–1134, 1982.

[172]   P.-A. Lindgard and O. G. Mouritsen, "Theory and Model for Martensitic Transformations," *Phys. Rev. Lett.*, vol. 57, no. 19, pp. 2458–2461, 1986.

[173]   V. I. Levitas and D. L. Preston, "Three-dimensional Landau theory for multivariant stress-induced martensitic phase transformations. I. Austenite↔martensite," *Phys. Rev. B*, vol. 66, p. 134206, 2002.

[174]   P. Entel, R. Meyer, K. Kadau, H. C. Herper, and E. Hoffmann, "Martensitic transformations : first-principles calculations combined with molecular-dynamics simulations," *Eur. Phys. J. B*, vol. 5, no. 3, pp. 379–388, 1998.

[175]   P. C. Clapp, "A Localized Soft Mode Theory for Martensitic Transformations," *Phys. Status Solidi*, vol. 57, no. 2, pp. 561–569, 1973.

[176]   G. A. Maugin and S. Cadet, "Existence of solitary waves in martensitic alloys," *Int. J. Eng. Sci.*, vol. 29, no. 2, pp. 243–258, 1991.

[177]   V. I. Levitas, D. L. Preston, and D. Lee, "Three-dimensional Landau theory for multivariant stress-induced martensitic phase transformations. III. Alternative potentials, critical nuclei, kink solutions, and dislocation theory," *Phys. Rev. B*, vol. 68, p. 134201, 2003.

[178]   J. A. Krumhansl and J. R. Schrieffer, "Dynamics and statistical mechanics of a one-dimensional model Hamiltonian for structural phase transitions," *Phys. Rev. B*, vol. 11, p. 3535, 1975.

[179]   S. Aubry, "A unified approach to the interpretation of displacive and order – disorder systems . I . Thermodynamical aspect," *J. Chem. Phys.*, vol. 62, p. 3217, 1975.

[180] S. Aubry, "A unified approach to the interpretation of displacive and order–disorder systems. II. Displacive systems," *J. Chem. Phys.*, vol. 64, p. 3392, 1976.

[181] G. B. Olson and M. Cohen, "Interphase-boundary dislocations and the concept of coherency," *Acta Metall.*, vol. 27, no. 12, pp. 1907–1918, 1979.

[182] M. Grujicic and G. B. Olson, "Dynamics of martensitic interfaces," *Interface Sci.*, vol. 6, no. 1–2, pp. 155–164, 1998.

[183] J. Wu, J. M. Howe, and W.-Z. Zhang, "An in situ transmission electron microscopy study of interface growth during martensitic transformation in an Fe–Ni–Mn alloy," *Acta Mater.*, vol. 59, pp. 3297–3303, 2011.

[184] F. Maresca and W. A. Curtin, "The austenite/lath martensite interface in steels: Structure, athermal motion, and in-situ transformation strain revealed by simulation and theory," *Acta Mater.*, vol. 134, pp. 302–323, 2017.

[185] E. J. Mittemeijer, *Fundamentals of Materials Science*. Springer, Berlin, Heidelberg, 2010.

[186] C. M. Wayman, *Introduction to the crystallography of martensitic transformations*. New York: Collier-Macmillan, 1964.

[187] A. Shibata, S. Morito, T. Furuhara, and T. Maki, "Local orientation change inside lenticular martensite plate in Fe-33Ni alloy," *Scr. Mater.*, vol. 53, no. 5, pp. 597–602, 2005.

[188] T. Maki and C. M. Wayman, "Transmission electron microscopy studies of thin foil martensite in Fe-Ni and Fe-Ni-C alloys," *Acta Metall.*, vol. 25, no. 6, pp. 681–693, 1977.

[189] F. J. Schoen, J. L. Nilles, and W. S. Owen, "Crystallographic aspects of Fe-Ni and Fe-Ni-C dilute alloy martensites," *Metall. Trans.*, vol. 2, no. 9, pp. 2489–2494, 1971.

[190] M. A. Jaswon and J. A. Wheeler, "Atomic displacements in the austenite–martensite transformation," *Acta Crystallogr.*, vol. 1, no. 4, pp. 216–224, 1948.

[191] G. Ghosh and V. Raghavan, "Autocatalysis and the extent of plate association in isothermally formed martensite in an Fe-Ni-Mn alloy," *Scr. Metall.*, vol. 20, no. 6, pp. 849–854, 1986.

[192] P. R. Rios and J. R. C. Guimarães, "Formal analysis of isothermal martensite spread," *Mater. Res.*, vol. 11, no. 1, pp. 103–108, 2008.

[193] T. Furuhara, N. Takayama, and G. Miyamoto, "Key Factors in Grain Refinement of Martensite and Bainite," *Mater. Sci. Forum*, vol. 638–642, pp. 3044–3049, 2010.

[194] L. Morsdorf, C. C. Tasan, D. Ponge, and D. Raabe, "3D structural and atomic-scale analysis of lath martensite: Effect of the transformation sequence," *Acta Mater.*, vol. 95, pp. 366–377, 2015.

[195] H. J. Bunge, *Texture Analysis in Materials Science*. Butterworth-Heinemann, Oxford, 1982.

[196] A. P. Sutton and R. W. Balluffi, *Interfaces in Crystalline Materials*. Oxford University Press, 2007.

[197] F. C. Frank, "Orientation mapping," *Metall. Trans. A*, vol. 19, no. 3, pp. 403–408, 1988.

[198] A. Morawiec and D. P. Field, "Rodrigues parameterization for orientation and misorientation distributions," *Philos. Mag. A*, vol. 73, no. 4, pp. 1113–1130, 1996.

[199] A. Heinz and P. Neumann, "Representation of orientation and disorientation data for cubic, hexagonal, tetragonal and orthorhombic crystals," *Acta Crystallogr. Sect. A*, vol. 47, no. 6, pp. 780–789, 1991.

[200] P. G. Callahan, M. Echlin, T. M. Pollock, S. Singh, and M. De Graef, "Three-dimensional texture visualization approaches : theoretical analysis and examples research papers," *J. Appl. Cryst.*, vol. 50, pp. 430–440, 2017.

[201] S. Patala, J. K. Mason, and C. A. Schuh, "Improved representations of misorientation information for grain boundary science and engineering," *Prog. Mater. Sci.*, vol. 57, no. 8, pp. 1383–1425, 2012.

[202] R. K. Ray and J. J. Jonas, "Transformation Textures in Steels," *Int. Mater. Rev.*, vol. 35, no. 1, pp. 1–36, 1990.

[203] G. Nolze, "Characterization of the fcc/bcc orientation relationship by EBSD using pole figures and variants," *Zeitschrift für Met.*, vol. 95, no. 9, pp. 744–755, 2004.

[204] V. G. Kurdjumow and G. Sachs, "Über den Mechanismus der Stahlhärtung," *Zeitschrift für Phys.*, vol. 64, no. 5–6, pp. 325–343, 1930.

[205] G. Wassermann, "Ueber den Mechanismus der α–γ-Umwandlung des Eisens," *Mitt K-Wilh-Inst Eisenforsch*, vol. 17, pp. 149–155, 1935.

[206] A. B. Greninger and A. R. Troiano, "The mechanism of martensite formation," *Trans. Am. Inst. Min. Metall. Eng.*, vol. 185, no. 9, pp. 509–598, 1949.

[207] W. Pitsch, "Der Orientierungszusammenhang zwischen Zementit und Ferrit im Perlit," *Acta Metall.*, vol. 10, no. 1, pp. 79–80, Jan. 1962.

[208] E. C. Bain, "The Nature of Martensite," *Trans. Am. Inst. Min. Metall. Eng.*, vol. 70, pp. 25–46, 1924.

[209] A. Stormvinter, G. Miyamoto, T. Furuhara, P. Hedström, and A. Borgenstam, "Effect of carbon content on variant pairing of martensite in Fe-C alloys," *Acta Mater.*, vol. 60, no. 20, pp. 7265–7274, 2012.

[210] A. F. Gourgues, H. M. Flower, and T. C. Lindley, "Electron backscattering diffraction study of acicular ferrite, bainite, and martensite steel microstructures," *Mater. Sci. Technol.*, vol. 16, no. 1, pp. 26–40, 2000.

[211] P. P. Suikkanen, C. Cayron, A. . Deardo, and L. P. Karjalainen, "Crystallographic analysis of martensite in 0.2C-2.0Mn-1.5Si-0.6Cr steel by EBSD," *J. Mater. Sci. Technol.*, vol. 27, no. 10, pp. 920–930, 2011.

[212] S. Kang, J. G. Speer, R. W. Regier, H. Nako, S. C. Kennett, and K. O. Findley, "The analysis of bainitic ferrite microstructure in microalloyed plate steels through quantitative characterization of intervariant boundaries," *Mater. Sci. Eng. A*, vol. 669, pp. 459–468, 2016.

[213] T. Nyyssönen, M. Isakov, P. Peura, and V. T. Kuokkala, "Iterative Determination of the Orientation Relationship Between Austenite and Martensite from a Large Amount of Grain Pair Misorientations," *Metall. Mater. Trans. A Phys. Metall. Mater. Sci.*, vol. 47, no. 6, pp. 2587–2590, 2016.

[214] C. Cayron, F. Barcelo, and Y. De Carlan, "Reply to 'comments on "The mechanisms of the fcc-bcc martensitic transformation revealed by pole figures," *Scr. Mater.*, vol. 64, no. 1, pp. 103–106, 2011.

[215] G. Nolze, "Improved determination of fcc/bcc orientation relationships by use of high-indexed pole figures," *Cryst. Res. Technol.*, vol. 41, no. 1, pp. 72–77, Jan. 2006.

[216] C. Cayron, "One-step theory of fcc-bcc martensitic transformation," *Acta Cryst.*, vol. A69, no. arXiv:1211.0495 [cond-mat.mtrl-sci], pp. 498–450, 2013.

[217] C. Cayron, "Continuous atomic displacements and lattice distortion during fcc-bcc martensitic transformation," *Acta Mater.*, vol. 96, pp. 189–202, 2015.

[218] S. Morito, X. Huang, T. Furuhara, T. Maki, and N. Hansen, "The morphology and crystallography of lath martensite in alloy steels," *Acta Mater.*, vol. 54, no. 19, pp. 5323–5331, 2006.

[219] J. C. Bokros and E. R. Parker, "The mechanism of the martensite burst transformation in Fe-Ni single crystals," *Acta Metall.*, vol. 11, no. 12, pp. 1291–1301, 1963.

[220] J. F. W. Bishop and R. Hill, "XLVI. A theory of the plastic distortion of a polycrystalline aggregate under combined stresses.," *London, Edinburgh, Dublin Philos. Mag. J. Sci.*, vol. 42, no. 327, pp. 414–427, 1951.

[221] J. F. W. Bishop and R. Hill, "CXXVIII. A theoretical derivation of the plastic properties of a polycrystalline face-centred metal," *London, Edinburgh, Dublin Philos. Mag. J. Sci.*, vol. 42, no. 334, pp. 1298–1307, 1951.

[222] M. Sum and J. J. Jonas, "A dislocation reaction model for variant selection during the austenite-to-martensite transformation," *Textures Microstruct.*, vol. 31, no. 4, pp. 187–215, 1999.

[223] N. J. Wittridge and J. J. Jonas, "The Austenite-to-Martensite Transformation in Fe - 30 % Ni After Deformation by Simple Shear," vol. 48, 2000.

[224] N. J. Wittridge, J. J. Jonas, and J. H. Root, "A dislocation-based model for variant selection during the γ-to-α′ transformation," *Metall. Mater. Trans. A Phys. Metall. Mater. Sci.*, vol. 32, no. 4, pp. 889–901, 2001.

[225] S. Kundu and H. K. D. H. Bhadeshia, "Transformation texture in deformed stainless steel," *Scr. Mater.*, vol. 55, no. 9, pp. 779–781, 2006.

[226] S. Kundu, K. Hase, and H. K. D. H. Bhadeshia, "Crystallographic texture of stress-affected bainite," *Proc. R. Soc. A Math. Phys. Eng. Sci.*, vol. 463, no. 2085, pp. 2309–2328, 2007.

[227] H. Abe, K. Ito, and R. Fukumoto, "Fe-30.2 wt%Ni合金の集合組織," *J Jpn Inst Met.*, vol. 31, pp. 1300–1305, 1967.

[228] H. Abe and K. Ito, "Effect of Ni content on the texture of martensite in Ni-Fe alloy rolled above Ms transformation temperature," *J. Japan Inst. Met.*, vol. 31, p. 1300, 1967.

[229] M. P. Butron-Guillen, C. S. Da Costa Viana, and J. J. Jonas, "A variant selection model for predicting the transformation texture of deformed austenite," *Metall. Mater. Trans. A Phys. Metall. Mater. Sci.*, vol. 28, no. 9, pp. 1755–1768, 1997.

[230] J. J. Jonas, S. Mu, T. Al-Samman, G. Gottstein, L. Jiang, and E. Martin, "The role of strain accommodation during the variant selection of primary twins in magnesium," *Acta Mater.*, vol. 59, no. 5, pp. 2046–2056, 2011.

[231] J. J. Jonas and N. J. Wittridge, "The γ-to-α Transformation Transformation of of Hot Hot Rolled Rolled Austenite Austenite The," *Met. Mater.*, vol. 6, no. 3, pp. 211–220, 2000.

[232] J. R. Patel and M. Cohen, "Criterion for the action of applied stress in the martensitic transformation," *Acta Metall.*, vol. 1, no. 5, pp. 531–538, 1953.

[233] E. Furubayashi, "Transformation Texture Analysis with Bain Relation - Monte Carlo Simulations," *Tetsu-to-Hagane*, vol. 71, no. 10, pp. 1359–1366, 1985.

[234] Y. Higo, F. Lecroisey, and T. Mori, "Relation between applied stress and orientation relationship of α′ martensite in stainless steel single crystals," *Acta Metall.*, vol. 22, no. 3, pp. 313–323, 1974.

[235] G. Miyamoto, N. Iwata, N. Takayama, and T. Furuhara, "Quantitative analysis of variant selection in ausformed lath martensite," *Acta Mater.*, vol. 60, no. 3, pp. 1139–1148, 2012.

[236] K. Ameyama, T. Maki, and T. I, "Morphology and Crystallography of the Precipitation of Austenite at Ferrite Grain Boundaries in Two-Phase Stainless Steel," *J Jpn Inst Met.*, vol. 50, no. 7, pp. 602–611, 1986.

[237] J. J. Jonas, M. P. Butrón-Guillén, and C. S. da Costa Viana, "Effect of grain aspect ratio and cooling rate on variant selection during the γ-to-α transformation," *11th Int. Conf. Textures Mater.*, vol. 1, pp. 575–591, 1996.

[238] M. Humbert, B. Gardiola, C. Esling, G. Flemming, and K. E. Hensger, "Modelling of the variant selection mechanism in the phase transformation of HSLA steel produced by compact strip production," *Acta Mater.*, vol. 50, no. 7, pp. 1741–1747, 2002.

[239] F. J. Humphreys and P. S. Bate, "Measuring the alignment of low-angle boundaries formed during deformation," *Acta Mater.*, vol. 54, no. 3, pp. 817–829, 2006.

[240] P. Bate and B. Hutchinson, "The Effect of elastic interactions between displacive transformations on textures in steels," *Acta Mater.*, vol. 48, no. 12, pp. 3183–3192, 2000.

[241] T. Tomida, M. Wakita, M. Yasuyama, S. Sugaya, Y. Tomota, and S. C. Vogel, "Memory effects of transformation textures in steel and its prediction by the double Kurdjumov-Sachs relation," *Acta Mater.*, vol. 61, no. 8, pp. 2828–2839, 2013.

[242] T. Tomida and M. Wakita, "Transformation Texture in Hot-rolled Steel Sheets and Its Quantitative Prediction," *ISIJ Int*, vol. 52, no. 4, pp. 601–609, 2012.

[243] T. Tomida, M. Wakita, M. Yoshida, and N. Imai, "A Variant Selection Rule in Transformation in Steel and Prediction of Transformation Texture," *Mater. Sci. Forum*, vol. 638–642, pp. 2846–2851, 2010.

[244] T. Tomida, "Variant selection mechanism by elastic anisotropy and double K-S relation for transformation texture in steel; difference between martensite and ferrite," *Acta Mater.*, vol. 146, pp. 25–41, 2018.

[245] B. Verlinden, P. Bocher, E. Girault, and E. Aernoudt, "Austenite texture and bainite/austenite orientation relationships in TRIP steel," *Scr. Mater.*, vol. 45, no. 8, pp. 909–916, 2001.

[246] S. Godet, J. C. Glez, Y. He, J. J. Jonas, and P. J. Jacques, "Grain-scale characterization of transformation textures," *J. Appl. Crystallogr.*, vol. 37, no. 3, pp. 417–425, 2004.

[247] L. Malet, M. R. Barnett, P. J. Jacques, and S. Godet, "Variant selection during the γ-to-αb phase transformation in hot-rolled bainitic TRIP-aided steels," *Scr. Mater.*, vol. 61, no. 5, pp. 520–523, 2009.

[248] W. Gong, Y. Tomota, M. S. Koo, and Y. Adachi, "Effect of ausforming on nanobainite steel," *Scr. Mater.*, vol. 63, no. 8, pp. 819–822, 2010.

[249] C. A. Apple, R. N. Caron, and G. Krauss, "Packet microstructure in Fe-0.2 pct C martensite," *Metall. Trans.*, vol. 5, no. 3, pp. 593–599, 1974.

[250] K. Wakasa and C. M. Wayman, "Crystallography and morphology of ferrous lath martensite," *Metallography*, vol. 14, no. 1, pp. 49–60, 1981.

[251] T. Swarr and G. Krauss, "The effect of structure on the deformation of as-quenched and tempered martensite in an Fe-0.2 pct C alloy," *Metall. Trans. A*, vol. 7, no. 1, pp. 41–48, 1976.

[252] T. Inoue, S. Matsuda, Y. Okamura, and K. Aoki, "The Fracture of a Low Carbon Tempered Martensite," *Trans. JIM*, vol. 11, no. 2, pp. 36–43, 1970.

[253]   S. Morito, H. Yoshida, T. Maki, and X. Huang, "Effect of block size on the strength of lath martensite in low carbon steels," *Mater. Sci. Eng. A*, vol. 438–440, pp. 237–240, 2006.

[254]   C. M. Wayman, "The phenomenological theory of martensite crystallography: Interrelationships," *Metall. Mater. Trans. A*, vol. 25, no. 9, pp. 1787–1795, 1994.

[255]   H. K. D. H. Bhadeshia, *Worked Examples in the Geometry of Crystals*, 2nd Edition. The Institute of Metals, 1987, London.

[256]   M. S. Wechsler, D. S. Liebermann, and T. A. Read, "On the theory of the formation of martensite," *Trans. Am. Inst. Min. Metall. Eng.*, vol. 197, pp. 1503–1515, 1953.

[257]   J. K. Mackenzie and J. S. Bowles, "The crystallography of martensite transformations II," *Acta Metall.*, vol. 2, no. 1, pp. 138–147, 1954.

[258]   J. K. Mackenzie and J. S. Bowles, "The crystallography of martensite transformations I," *Acta Metall.*, vol. 2, no. 1, pp. 129–137, 1954.

[259]   J. S. Bowles and C. M. Wayman, "The bain strain, lattice correspondences, and deformations related to martensitic transformations," *Metall. Trans.*, vol. 3, no. 5, pp. 1113–1121, 1972.

[260]   J. S. Bowles and J. K. Mackenzie, "The crystallography of martensite transformations III. Face-centred cubic to body-centred tetragonal transformations," *Acta Metall.*, vol. 2, no. 2, pp. 224–234, 1954.

[261]   A. P. Baur, C. Cayron, and R. E. Logé, "{225} γ habit planes in martensitic steels: From the PTMC to a continuous model," *Sci. Rep.*, vol. 7, no. December 2016, pp. 1–10, 2017.

[262]   C. Cayron, B. Artaud, and L. Briottet, "Reconstruction of parent grains from EBSD data," *Mater. Charact.*, vol. 57, no. 4–5, pp. 386–401, 2006.

[263]   C. Cayron, "ARPGE: A computer program to automatically reconstruct the parent grains from electron backscatter diffraction data," *J. Appl. Crystallogr.*, vol. 40, no. 6, pp. 1183–1188, 2007.

[264]   A. Chabok, E. van der Aa, J. T. M. De Hosson, and Y. T. Pei, "Mechanical behavior and failure mechanism of resistance spot welded DP1000 dual phase steel," *Mater. Des.*, vol. 124, pp. 171–182, 2017.

[265]   A. Al Shahrani, N. Yazdipour, A. Dehghan-Manshadi, A. A. Gazder, C. Cayron, and E. V. Pereloma, "The effect of processing parameters on the dynamic recrystallisation behaviour of API-X70 pipeline steel," *Mater. Sci. Eng. A*, vol. 570, pp. 70–81, 2013.

[266]   C. Ranger, V. Tari, S. Farjami, M. J. Merwin, L. Germain, and A. Rollett, "Austenite Reconstruction Elucidates Prior Grain Size Dependence of Toughness in a Low Alloy Steel," *Metall. Mater. Trans. A*, vol. 49, no. 10, pp. 4521–4535, 2018.

[267]   F. Archie, X. Li, and S. Zaefferer, "Micro-damage initiation in ferrite-martensite DP microstructures: A statistical characterization of crystallographic and chemical parameters," *Mater. Sci. Eng. A*, vol. 701, no. June, pp. 302–313, 2017.

[268]   L. Briottet *et al.*, "Fatigue crack initiation and growth in a CrMo steel under hydrogen pressure," *Int. J. Hydrogen Energy*, vol. 40, no. 47, pp. 17021–17030, 2015.

[269]   Y. J. Li, D. Ponge, P. Choi, and D. Raabe, "Segregation of boron at prior austenite grain boundaries in a quenched martensitic steel studied by atom probe tomography," *Scr. Mater.*, vol. 96, no. C, pp. 13–16, 2015.

[270]   L. Wei and T. W. Nelson, "Influence of heat input on post weld microstructure and mechanical properties of friction stir welded HSLA-65 steel," *Mater. Sci. Eng. A*, vol. 556, pp. 51–59, 2012.

[271]   N. Bernier, L. Bracke, L. Malet, and S. Godet, "An alternative to the crystallographic reconstruction of austenite in steels," *Mater. Charact.*, vol. 89, pp. 23–32, 2014.

[272]   M. Kubota, K. Ushioda, G. Miyamoto, and T. Furuhara, "Analysis of Recrystallization Behavior of Hot-Deformed Austenite Reconstructed from EBSD Orientation Maps of Lath Martensite," *Mater. Sci. Forum*, vol. 879, pp. 2389–2394, 2016.

[273]   T. Krämer, L. Eisenhut, L. Germain, D. Rupp, E. Detemple, and C. Motz, "Assessment of EBSD Analysis and Reconstruction Methods as a Tool for the Determination of Recrystallized Fractions in Hot-Deformed Austenitic Microstructures," *Metall. Mater. Trans. A Phys. Metall. Mater. Sci.*, vol. 49, no. 7, pp. 2795–2802, 2018.

[274]   C. Du *et al.*, "Martensite crystallography and chemistry in dual phase and fully martensitic steels," *Mater. Charact.*, vol. 139, pp. 411–420, 2018.

[275]   L. Morsdorf, O. Jeannin, D. Barbier, M. Mitsuhara, D. Raabe, and C. C. Tasan, "Multiple mechanisms of lath martensite plasticity," *Acta Mater.*, vol. 121, pp. 202–214, 2016.

[276]   M. Abbasi, D. I. Kim, T. W. Nelson, and M. Abbasi, "EBSD and reconstruction of pre-transformation microstructures, examples and complexities in steels," *Mater. Charact.*, vol. 95, pp. 219–231, 2014.

[277]   T. Chiba, G. Miyamoto, and T. Furuhara, "Comparison of Variant Selection between Lenticular and Lath Martensite Transformed from Deformed Austenite," *ISIJ Int.*, vol. 53, no. 5, pp. 915–919, 2013.

[278]   E. J. Payton, A. Aghajani, F. Otto, G. Eggeler, and V. A. Yardley, "On the nature of internal interfaces in a tempered martensite ferritic steel and their evolution during long-term creep," *Scr. Mater.*, vol. 66, no. 12, pp. 1045–1048, 2012.

[279]   L. Germain, N. Gey, R. Mercier, P. Blaineau, and M. Humbert, "An advanced approach to reconstructing parent orientation maps in the case of approximate orientation relations: Application to steels," *Acta Mater.*, vol. 60, no. 11, pp. 4551–4562, 2012.

[280]   G. Miyamoto, N. Iwata, N. Takayama, and T. Furuhara, "Reconstruction of Parent Austenite Grain Structure Based on Crystal Orientation Map of Bainite with and without Ausforming," *ISIJ Int.*, vol. 51, no. 7, pp. 1174–1178, 2011.

[281]   G. Miyamoto, N. Takayama, and T. Furuhara, "Accurate measurement of the orientation relationship of lath martensite and bainite by electron backscatter diffraction analysis," *Scr. Mater.*, vol. 60, no. 12, pp. 1113–1116, 2009.

[282]   L. Germain, "Apports des reconstructions des microtextures parentes dans l'etude des aciers et des aciers et des alliages de titane," Université de Lorraine, 2014.

[283]   P. Blaineau, "Restitution de la microtexture parente à partir de la microtexture héritée mesurée par EBSD, application aux aciers faiblement alliés," Université Paul Verlaine de Metz, France, 2011.

[284]   N. Gey, P. Blaineau, L. Germain, M. Humbert, D. Barbier, and A. Perlade, "Restitution of the Shapes and Orientations of the Prior Austenitic Grains from Inherited Alpha' Orientation Maps in Steels," *Solid State Phenom.*, vol. 172–174, pp. 911–915, 2011.

[285]   M. Humbert, P. Blaineau, L. Germain, and N. Gey, "Refinement of orientation relations occurring in phase transformation based on considering only the orientations of the variants," *Scr. Mater.*, vol. 64, no. 2, pp. 114–117, 2011.

[286] M. Abbasi, T. W. Nelson, C. D. Sorensen, and L. Wei, "An approach to prior austenite reconstruction," *Mater. Charact.*, vol. 66, pp. 1–8, 2012.

[287] L. Wei, "Investigating Correlations of Microstructures, Mechanical Properties and FSW Process Variables in Friction Stir Welded HSLA-65 Steel," Brigham Young University, 2009.

[288] V. Tari, A. D. Rollett, and H. Beladi, "Back calculation of parent austenite orientation using a clustering approach," *J. Appl. Crystallogr.*, vol. 46, no. 1, pp. 210–215, 2013.

[289] E. Gomes and L. A. I. Kestens, "Fully automated orientation relationship calculation and prior austenite reconstruction by random walk clustering," *IOP Conf. Ser. Mater. Sci. Eng.*, vol. 82, no. 1, 2015.

[290] S. Weyand, D. Britz, D. Rupp, and F. Mücklich, "Investigation of Austenite Evolution in Low-Carbon Steel by Combining Thermo-Mechanical Simulation and EBSD Data," *Mater. Perform. Charact.*, vol. 4, no. 3, pp. 322–340, 2015.

[291] L. Sanz, B. Pereda, and B. López, "Validation and Analysis of the Parameters for Reconstructing the Austenite Phase from Martensite Electron Backscatter Diffraction Data," *Metall. Mater. Trans. A Phys. Metall. Mater. Sci.*, vol. 48, no. 11, pp. 5258–5272, 2017.

[292] J. Zhang, L. Morsdorf, and C. C. Tasan, "Multi-probe microstructure tracking during heat treatment without an in-situ setup: Case studies on martensitic steel, dual phase steel and β-Ti alloy," *Mater. Charact.*, vol. 111, pp. 137–146, 2016.

[293] E. J. Mittemeijer and U. Welzel, *Modern Diffraction Methods*. Weinheim: Wiley-VCH Verlag GmbH & Co. KGaA, 2012.

[294] E. J. Mittemeijer and P. Scardi, *Diffraction Analysis of the Microstructure of Materials*. Springer-Verlag Berlin Heidelberg, 2004.

[295] L. Meier, M. Hofmann, P. Saal, W. Volk, and H. Hoffmann, "In-situ measurement of phase transformation kinetics in austempered ductile iron," *Mater. Charact.*, vol. 85, pp. 124–133, 2013.

[296] S. E. Offerman *et al.*, "Grain Nucleation and Growth During Phase Transformations," *Science*, vol. 298, no. November, pp. 1003–1006, 2002.

[297] P. Weisbecker, G. Geandier, and B. Appolaire, "Austenitization and precipitate dissolution in high nitrogen steels : an in situ high temperature X-ray synchrotron diffraction analysis using the Rietveld method," *Mater. Sci. Eng. A*, vol. 393, pp. 63–70, 2005.

[298] S. S. Babu *et al.*, "In-Situ Observations of Lattice Parameter Fluctuations in Austenite and Transformation to Bainite," *Metall Mater Trans A*, vol. 36, no. December, pp. 3281–3289, 2005.

[299] J. W. Elmer, T. A. Palmer, W. Zhang, and T. Debroy, "Time resolved X-ray diffraction observations of phase transformations in transient arc welds," Science and Technology of Welding & Joining, vol. 13, no. 3, pp. 265–277, 2008.

[300] M. Yonemura, T. Osuki, H. Terasaki, Y. Komizo, M. Sato, and A. Kitano, "In-Situ Observation for Weld Solidification in Stainless Steels Using Time-Resolved X-ray Diffraction," *Materials transactions*, vol. 47, no. 2, pp. 310–316, 2006.

[301] T. Kannengiesser, S. S. Babu, Y. Komizo, and A. Ramirez, *In-situ Studies with Photons, Neutrons and Electrons Scattering*. Springer-Verlag Berlin Heidelberg, 2010.

[302] T. Kannengiesser, S. S. Babu, Y. Komizo, and A. Ramirez, *In-situ Studies with Photons, Neutrons and Electrons Scattering II*. Springer International Publishing, 2014.

[303] G. Dehm, J. M. Howe, and J. Zweck, *In-Situ Electron Microscopy: Applications in Physics, Chemistry and Materials Science*. WILEY-VCH Verlag, Weinheim, 2012.

[304] F. Banhart, *In-Situ Electron Microscopy at High Resolution*. World Scientific Publishing Singapore, 2008.

[305] E. P. Butler, "In situ experiments in the transmission electron microscope," *Reports Prog. Phys.*, vol. 42, no. 5, pp. 833–889, 1979.

[306] G. R. Purdy, "The dynamics of transformation interfaces in steels—II. Transformations in FE-C-MO alloys at intermediate temperatures," *Acta Metall.*, vol. 26, no. 3, pp. 487–498, 1978.

[307] G. R. Purdy, "The dynamics of transformation interfaces in steels—I. The ferrite-austenite interface in Fe-C-Mo alloys," *Acta Metall.*, vol. 26, no. 3, pp. 477–486, 1978.

[308] M. Nemoto, "The Formation of Austenite from Mixtures of Ferrite and Cementite as Observed by HVEM," *Metall. Trans. A*, vol. 8, no. 3, pp. 431–437, 1977.

[309] M. Nemoto, "In situ observation of dissolution of cementite in steel," *J. Microsc.*, vol. 97, pp. 239–247, 1973.

[310] M. Onink, F. D. Tichelaar, C. M. Brakman, E. J. Mittemeijer, and S. van der Zwaag, "An in situ hot stage transmission electron microscopy study of the decomposition of Fe-C austenites," *J. Mater. Sci.*, vol. 30, no. 24, pp. 6223–6234, 1995.

[311] F. A. Khalid and D. V Edmonds, "Observations concerning transformation interfaces in steels," *Acta Metall. Mater.*, vol. 41, no. 12, pp. 3421–3434, 1993.

[312] M. K. Kang, J. L. Sun, and Q. M. Yang, "High-Temperature Transmission Electron Microscopy In Situ Study of Lower Bainite Carbide Precipitation," *Metall. Trans. A*, vol. 21, pp. 853–858, 1990.

[313] W. B. Hutchinson and R. K. Ray, "On the feasibility of in situ observations of recrystallization in the high voltage microscope," *Philos. Mag. A*, vol. 28, no. 4, pp. 953–960, 1973.

[314] H. Chikama, H. Shibata, T. Emi, and M. Suzuki, "'In-situ' Real Time Observation of Planar to Cellular and Cellular to Dendritic Transition of Crystals Growing in Fe–C Alloy Melts," *Mater. Trans. JIM*, vol. 37, no. 4, pp. 620–626, 1996.

[315] H. Shibata, Y. Arai, M. Suzuki, and T. Emi, "Kinetics of Peritectic Reaction and Transformation in Fe-C Alloys," *Metall. Mater. Trans. B*, vol. 31, no. 5, pp. 981–991, 2000.

[316] H. Yin, H. Shibata, T. Emi, and M. Suzuki, "Agglomeration of Various Inclusion Pa rticles on Molten Steel Surf ace mm," *ISIJ Int.*, vol. 37, no. 10, pp. 946–955, 1997.

[317] H. Shibata, H. Yin, S. Yoshinaga, T. Emi, and M. Suzuki, "In-situ Observation of Engulfment and Pushing of Nonmetallic Inclusions in Steel Melt by Advancing Melt/Solid Interface," *ISIJ Int.*, vol. 38, no. 2, pp. 149–156, 1998.

[318] S. Zhang, S. Morito, and Y. Komizo, "Variant Selection of Low Carbon High Alloy Steel within an Austenite Grain during Martensite Transformation," *Tetsu-to-Hagane*, vol. 97, no. 7, pp. 399–405, 2011.

[319] A. F. Gourgues-Lorenzon, "Application of electron backscatter diffraction to the study of phase transformations," *Int. Mater. Rev.*, vol. 52, no. 2, pp. 65–128, 2007.

[320] A. F. Gourgues-Lorenzon, "Application of electron backscatter diffraction to the study of phase transformations : present and possible future," *J. Microsc.*, vol. 233, no. 3, pp. 460–473, 2009.

[321] S. Kahl, R. L. Peng, M. Calmunger, B. Olsson, and S. Johansson, "In situ EBSD during tensile test of aluminum AA3003 sheet," *Micron*, vol. 58, pp. 15–24, 2014.

[322] H. Borkar, S. Seifeddine, and A. E. W. Jarfors, "In-situ EBSD study of deformation behavior of Al – Si – Cu alloys during tensile testing," *Mater. Des.*, vol. 84, pp. 36–47, 2015.

[323] C. Niederberger, W. M. Mook, X. Maeder, and J. Michler, "In situ electron backscatter diffraction (EBSD) during the compression of micropillars," *Mater. Sci. Eng. A*, vol. 527, no. 16–17, pp. 4306–4311, 2010.

[324] H. Nakamichi, F. J. Humphreys, and I. Brough, "Recrystallization phenomena in an IF steel observed by in situ EBSD experiments," *J. Microsc.*, vol. 230, pp. 464–471, 2008.

[325] S. I. Wright, D. P. Field, and M. M. Nowell, "Impact of Local Texture on Recrystallization and Grain Growth via In-Situ EBSD," *Mater. Sci. Forum*, vol. 495–497, pp. 1121–1130, 2005.

[326] N. Bozzolo, S. Jacomet, and R. E. Logé, "Fast in-situ annealing stage coupled with EBSD: A suitable tool to observe quick recrystallization mechanisms," *Mater. Charact.*, vol. 70, pp. 28–32, 2012.

[327] C. Kerisit, R. E. Logé, S. Jacomet, V. Llorca, and N. Bozzolo, "EBSD coupled to SEM in situ annealing for assessing recrystallization and grain growth mechanisms in pure tantalum," *J. Microsc.*, vol. 250, no. 3, pp. 189–199, 2004.

[328] Q. He, T. Huang, L. Shuai, Y. Zhang, and G. Wu, "Scripta Materialia In-situ investigation of the evolution of annealing twins in high purity aluminium," *Scr. Mater.*, vol. 153, pp. 68–72, 2018.

[329] G. G. E. Seward, S. Celotto, D. J. Prior, J. Wheeler, and R. C. Pond, "In situ SEM-EBSD observations of the hcp to bcc phase transformation in commercially pure titanium," *Acta Mater.*, vol. 52, no. 4, pp. 821–832, 2004.

[330] T. Watanabe, K. Obara, and S. Tsurekawa, "In-situ Observations on Interphase Boundary Migration and Grain Growth during α / γ Phase Transformation in Iron Alloys," *Mater. Sci. Forum*, vol. 467–470, pp. 819–824, 2004.

[331] G. Zijlstra, M. S. B. van Daalen, D. I. Vainchtein, V. Ocelík, and J. T. M. De Hosson, "Interphase boundary motion elucidated through in-situ high temperature electron back-scatter diffraction," *Mater. Des.*, vol. 132, pp. 138–147, 2017.

[332] H. S. Ubhi, J. Parsons, N. Othen, S. Campbell, R. Poole, and a Gholinia, "In-situ EBSD Phase Transformation and Recrystallisation," *J. Phys. Conf. Ser.*, vol. 522, p. 012011, 2014.

[333] J. Donoghue, A. Gholinia, J. Quinta, and P. Prangnell, "In-situ high temperature EBSD analysis of the effect of a deformation step on the alpha to beta transition in additive manufactured Ti-6Al-4V," in *Proceedings of the 13th World Conference on Titanium*, 2016, pp. 1283–1288.

[334] G. Zijlstra, "Material structure and functionality in product manufacturing," Rijksuniversiteit Groningen, 2018.

[335] E. A. Torres and A. J. Ramírez, "In situ scanning electron microscopy," *Sci. Technol. Weld. Join.*, vol. 16, no. 1, pp. 68–798, 2011.

[336] G. G. E. Seward *et al.*, "High-Temperature Electron Backscatter Diffraction and Scanning Electron Microscopy Imaging Techniques : In-situ Investigations of Dynamic Processes," *Scanning*, vol. 24, no. 5, pp. 232–240, 2006.

[337] D. M. Kirch *et al.*, "Laser powered heating stage in a scanning electron microscope for microstructural investigations at elevated temperatures Laser powered heating stage in a scanning electron microscope for microstructural investigations at elevated temperatures," *Rev. Sci. Instrum.*, vol. 79, no. 4, 2008.

[338] T. Fukino, S. Tsurekawa, and Y. Morizono, "In-Situ Scanning Electron Microscopy/Electron Backscattered Diffraction Observation of Microstructural Evolution during α → γ Phase Transformation in Deformed Fe-Ni Alloy," *Metall. Mater. Trans. A*, vol. 42, no. 3, pp. 587–593, 2010.

[339] K. W. Hansen, "Phase Transformation Study of X70 Steel by EBSD during In Situ Heating and Quenching," NTNU Trondheim, 2012.

[340] K. W. Hansen, T. G. Sætran, M. Karlsen, T. A. Nilsen, W. Dall, and J. Hjelen, "Phase transformation study of arctic steels by EBSD during in situ heating and gas quenching," in *Proceedings of the International Offshore and Polar Engineering Conference*, 2012, pp. 297–304.

[341] A.-J. Enstad, "EBSD-karakterisering av et HSLA-stål under in situ varmebehandling," Norges teknisk-naturvitenskapelige Universitet, 2011.

[342] M. Wenk, "Gefüge und Mikromechanik von Dualphasenstahl," Karlsruher Institut für Technologie (KIT), 2016.

[343] S. Schreijäg, "Microstructure and Mechanical Behavior of Deep Drawing DC04 Steel at Different Length Scales," Karlsruher Institut für Technologie (KIT), 2013.

[344] LabJack Corporation, "LabJack." .

[345] National Instruments Inc., "LabVIEW." .

[346] SensorTherm GmbH, "Metis M311 / M322 Datenblatt," No. 485, 2016.

[347] G. W. Hess, "Thermocouple conduction error with radiation heat loss," Aerospace and Mech. Eng., The University of Arizona, 1965.

[348] T. Fu, P. Tan, and M. Zhong, "Experimental research on the influence of surface conditions on the total hemispherical emissivity of iron-based alloys," *Exp. Therm. Fluid Sci.*, vol. 40, pp. 159–167, 2012.

[349] B. P. Keller, S. E. Nelson, K. L. Walton, T. K. Ghosh, R. V. Tompson, and S. K. Loyalka, "Total hemispherical emissivity of Inconel 718," *Nucl. Eng. Des.*, vol. 287, pp. 11–18, 2015.

[350] C. Da Wen, "Investigation of steel emissivity behaviors: Examination of Multispectral Radiation Thermometry (MRT) emissivity models," *Int. J. Heat Mass Transf.*, vol. 53, no. 9–10, pp. 2035–2043, 2010.

[351] M. Vollmer and K.-P. Mollman, *Infrared Thermal Imaging: Fundamentals, Research and Applications*. WILEY-VCH Verlag, Weinheim, 2010.

[352] M. A. Davies, T. Ueda, R. M'Saoubi, B. Mullany, and A. L. Cooke, "On The Measurement of Temperature in Material Removal Processes," *CIRP Ann. - Manuf. Technol.*, vol. 56, no. 2, pp. 581–604, 2007.

[353] Henkel, "Bonderite L-GP 386 Acheson," 2015.

[354] W. Sabuga and R. Todtenhaupt, "Effect of roughness on the emissivity of the precious metals silver, gold, palladium, platinum, rhodium, and iridium," *High Temp. - High Press.*, vol. 33, no. 3, pp. 261–269, 2001.

[355] F. Kreith, R. M. Manglik, and M. S. Bohn, *Principles of heat transfer*, 7th ed. Stamford: Cengage Learning, 2011.

[356] R. Holoboff, B. L. Hote, R. Speri, and O. Delcourt, "Gas quenching with helium," *Adv. Mater. Process.*, vol. 143, no. 2, pp. 23–26, 1993.

[357] F. Faura, A. Campo, and B. Zamora, "A Mixture of Pure Gases that Produce Maximum Heat Transfer Characteristics for Quenching," *J. Mater. Eng. Perform.*, vol. 7, pp. 420–424, 1998.

[358] G. H. Aylward and T. J. V. Findlay, *SI chemical data*, 5. ed. Chichester: Wiley, 2002.

[359] R. Hielscher, "MTEX toolbox." [Online]. Available: http://mtex-toolbox.github.io.

[360]   S. Kullback and R. A. Leibler, "On Information and Sufficiency," *Ann. Math. Stat.*, vol. 22, no. 1, pp. 79–86, 1951.

[361]   R. L. Dobrushin, "Prescribing a system of random variables by conditional distributions," *Theor. Prob. Appl.*, vol. 15, pp. 458–486, 1970.

[362]   F. Bachmann, R. Hielscher, and H. Schaeben, "Grain detection from 2d and 3d EBSD data-Specification of the MTEX algorithm," *Ultramicroscopy*, vol. 111, no. 12, pp. 1720–1733, 2011.

[363]   H. Schaeben, "The de la Vallée Poussin Standars Orientation Density Function," *Textures Microstruct.*, vol. 33, no. 1, pp. 365–373, 1999.

[364]   R. Hielscher, "Kernel density estimation on the rotation group and its application to crystallographic texture analysis," *J. Multivar. Anal.*, vol. 119, pp. 119–143, 2013.

[365]   A. Morawiec, *Orientations and Rotations: Computations in Crystallographic Textures*, 1st ed. Springer-Verlag Berlin Heidelberg, 2004.

[366]   F. Barcelo, Y. De Carlan, J.-L. Behade, and B. Fournier, "Orientation relationship in Eurofer martensitic steels," *Phase Transitions*, vol. 82, no. 11, pp. 808–820, 2009.

[367]   K. Verbeken, L. Barbé, and D. Raabe, "Evaluation of the Crystallographic Orientation Relationships between FCC and BCC Phases in TRIP Steels," *ISIJ Int.*, vol. 49, no. 10, pp. 1601–1609, 2009.

[368]   P. L. Ryder, W. Pitsch, and R. F. Mehl, "Crystallography of the precipitation of ferrite on austenite grain boundaries in a Co + 20% Fe alloy," *Acta Metall.*, vol. 15, no. 9, pp. 1431–1440, 1967.

[369]   C. Cayron, "Groupoid of orientational variants," *Acta Cryst.*, vol. A62, pp. 21–40, 2006.

[370]   F. Wagner and C. Esling, "Numbering the crystallographic variants in phase transformation," *J. Appl. Cryst.*, vol. 25, pp. 724–730, 1992.

[371]   A. Danon, C. Servant, A. Alamo, and J. C. Brachet, "Heterogeneous austenite grain growth in 9Cr martensitic steels: Influence of the heating rate and the austenitization temperature," *Mater. Sci. Eng. A*, vol. 348, no. 1–2, pp. 122–132, 2003.

[372]   M. Klimenkov, R. Lindau, E. Materna-Morris, and A. Möslang, "TEM characterization of precipitates in EUROFER 97," *Prog. Nucl. Energy*, vol. 57, pp. 8–13, 2012.

[373]   C. Dethloff, E. Gaganidze, and J. Aktaa, "Quantitative TEM analysis of precipitation and grain boundary segregation in neutron irradiated EUROFER 97," *J. Nucl. Mater.*, vol. 454, no. 1–3, pp. 323–331, 2014.

[374]   M. Tamura, K. Shinozuka, K. Masamura, K. Ishizawa, and S. Sugimoto, "Solubility product and precipitation of TaC in Fe–8Cr–2W steel," *J. Nucl. Mater.*, vol. 258–263, pp. 1158–1162, 1998.

[375]   Z. Nishiyama, "X-ray investigation of the mechanism of the transformation from face-centred cubic lattice to body-centred cubic," *Sci. Reports Tohoku Imp. Univ. Ser. 1 Math. Physics, Chem.*, vol. 23, pp. 637–664, 1934.

[376]   W. Liu, P. Song, C. Zhang, D. Yun, C. fa Yao, and Z. gang Yang, "Crystallographic analysis of lath martensite in a 13Cr-5Ni steel by electron backscattering diffraction," *J. Iron Steel Res. Int.*, vol. 25, no. 2, pp. 213–220, 2018.

[377]   S. Raju, B. Jeya Ganesh, A. K. Rai, R. Mythili, S. Saroja, and B. Raj, "A study on martensitic phase transformation in 9Cr-1W-0.23V-0.063Ta-0.56Mn- 0.09C-0.02N (wt.%) reduced activation steel using differential scanning calorimetry," *J. Nucl. Mater.*, vol. 405, no. 1, pp. 59–69, 2010.

[378]   J. A. Klostermann and W. G. Burgers, "Surface martensite in iron nickel," *Acta Metall.*, vol. 12, no. 4, pp. 355–360, 1964.

[379]   H. K. D. H. Bhadeshia, *Bainite in steels: transformations, microstructure and properties*. IOM Communications, London, 2001.

[380]   C. P. Luo and G. C. Weatherly, "The crystallography of heterogeneous nucleation in a Ni-45 wt% Cr alloy," *Acta Metall.*, vol. 37, no. 3, pp. 791–801, 1989.

[381]   K. Ameyama and T. Maki, "Precipitation of austenite at deformation twin boundaries of ferrite in two phase stainless steel," *Scr. Metall. Mater.*, vol. 24, no. 1, pp. 173–178, 1990.

[382]   T. Furuhara and T. Maki, "Variant selection in heterogeneous nucleation on defects in diffusional phase transformation and precipitation," *Mater. Sci. Eng. A*, vol. 312, no. 1–2, pp. 145–154, 2001.

[383]   D. S. Sarma, J. A. Whiteman, and J. H. Woodhead, "Habit plane and morphology of lath martensites," *Met. Sci.*, vol. 10, no. 11, pp. 391–395, 1976.

[384]   H. M. Otte and T. A. Read, "Habit planes of martensite in chrome-carbon steel," *J. Met.*, vol. 9, no. February, pp. 412–416, 1957.

[385]   V. Randle, H. Davies, and I. Cross, "Grain boundary misorientation distributions," *Curr. Opin. Solid State Mater. Sci.*, vol. 5, no. 1, pp. 3–8, 2001.

[386]   A. Morawiec, "Distributions of Misorientation Angles and Misorientation Axes for Crystallites with Different Symmetries," *Acta Crystallogr. Sect. A Found. Crystallogr.*, vol. 53, no. 3, pp. 273–285, 1997.

[387]   J. S. Kallend, P. P. Morris, and G. J. Davies, "Texture transformations - the misorientation distribution function," *Acta Metall.*, vol. 24Kallend, no. 4, pp. 361–370, 1976.

[388]   J. Pospiech, K. Sztwiertnia, and F. Haessner, "The Misorientation Distribution Function," *Textures Microstruct.*, vol. 6, no. 3, pp. 201–215, 1986.

[389]   W. Freeden and M. Z. Nashed, *Handbook of Geomathematics*. Springer, Berlin Heidelberg, 2014.

[390]   F. Barcelo, J.-L. Bechade, and B. Fournier, "Orientation relationship in various 9%Cr ferritic/martensitic steels–EBSD comparison between Nishiyama–Wassermann, Kurdjumov–Sachs and Greninger–Troiano," *Phase Transitions*, vol. 83, no. 8, pp. 601–614, 2010.

[391]   C. Cayron, "EBSD imaging of orientation relationships and variant groupings in different martensitic alloys and Widmanstätten iron meteorites," *Mater. Charact.*, vol. 94, pp. 93–110, 2014.

[392]   Y. Toji, G. Miyamoto, and D. Raabe, "Carbon partitioning during quenching and partitioning heat treatment accompanied by carbide precipitation," *Acta Mater.*, vol. 86, pp. 137–147, Mar. 2015.

[393]   R. Krakow *et al.*, "On three-dimensional misorientation spaces," 2017.

[394]   L. Germain, N. Gey, M. Humbert, A. Hazotte, P. Bocher, and M. Jahazi, "An automated method to analyze separately the microtextures of primary αp grains and the secondary αs inherited colonies in bimodal titanium alloys," *Mater. Charact.*, vol. 54, no. 3, pp. 216–222, 2005.

[395] G. Miyamoto, N. Iwata, N. Takayama, and T. Furuhara, "Mapping the parent austenite orientation reconstructed from the orientation of martensite by EBSD and its application to ausformed martensite," *Acta Mater.*, vol. 58, no. 19, pp. 6393–6403, 2010.

[396] K. D. Zilnyk, D. R. Almeida Junior, H. R. Z. Sandim, P. R. Rios, and D. Raabe, "Misorientation distribution between martensite and austenite in Fe-31 wt%Ni-0.01 wt%C," *Acta Mater.*, vol. 143, pp. 227–236, 2018.

[397] F. Archie, M. Z. Mughal, M. Sebastiani, E. Bemporad, and S. Zaefferer, "Anisotropic distribution of the micro residual stresses in lath martensite revealed by FIB ring-core milling technique," *Acta Mater.*, vol. 150, pp. 327–338, 2018.

[398] R. Esterl, M. Sonnleitner, M. Stadler, G. Wölger, and R. Schnitzer, "Microstructural Characterization of Ultra-High Strength Martensitic Steels," *Prakt. Metallogr.*, vol. 55, pp. 203–222, 2018.

[399] S. K. Pradhan, T. S. Prithiv, and S. Mandal, "Through-thickness microstructural evolution during grain boundary engineering type thermomechanical processing and its implication on sensitization behavior in austenitic stainless steel," *Mater. Charact.*, vol. 134, no. July, pp. 134–142, 2017.

[400] G. R. Speich, V. A. Demarest, and R. L. Miller, "Formation of Austenite During Intercritical Annealing of Dual-Phase Steels," *Metall. Mater. Trans. A*, vol. 12, no. 8, pp. 1419–1428, 1981.

[401] P. R. Howell, "The Crystallography of the Austenite-Ferrite / Carbide Transformation in Fe-Cr-C Alloys," *Metall. Trans. A*, vol. 10A, no. September, pp. 1213–1222, 1979.

[402] E. Cotrina, a. Iza-Mendia, B. López, and I. Gutiérrez, "Study of the ferrite grain coarsening behind the transformation front by electron backscattered diffraction techniques," *Metall. Mater. Trans. A*, vol. 35, no. 1, pp. 93–102, 2004.

[403] E. Novillo, D. Hernández, I. Gutiérrez, and B. López, "Analysis of ferrite grain growth mechanisms during γ−α transformation in a niobium alloyed steel using EBSD," *Mater. Sci. Eng. A*, vol. 385, no. 1–2, pp. 83–90, 2004.

[404] R. Bengochea, B. López, and I. Gutierrez, "Microstructural evolution during the austenite-to-ferrite transformation from deformed austenite," *Metall. Mater. Trans. A Phys. Metall. Mater. Sci.*, vol. 29, no. 2, pp. 417–426, 1998.

[405] M. J. Santofimia, L. Zhao, R. Petrov, C. Kwakernaak, W. G. Sloof, and J. Sietsma, "Microstructural development during the quenching and partitioning process in a newly designed low-carbon steel," *Acta Mater.*, vol. 59, no. 15, pp. 6059–6068, 2011.

[406] M. J. Santofimia, T. Nguyen-Minh, L. Zhao, R. Petrov, I. Sabirov, and J. Sietsma, "New low carbon Q&P steels containing film-like intercritical ferrite," *Mater. Sci. Eng. A*, vol. 527, no. 23, pp. 6429–6439, 2010.

[407] S. L. Shrestha, A. J. Breen, P. Trimby, G. Proust, S. P. Ringer, and J. M. Cairney, "An automated method of quantifying ferrite microstructures using electron backscatter diffraction (EBSD) data," *Ultramicroscopy*, vol. 137, no. September, pp. 40–47, 2014.

[408] J.-Y. Kang, S.-J. Park, and M.-B. Moon, "Phase Analysis on Dual-Phase Steel Using Band Slope of Electron Backscatter Diffraction Pattern," *Microsc. Microanal.*, vol. 19, no. Supplement S5, pp. 13–16, 2013.

[409] E. P. Kwon, S. Fujieda, K. Shinoda, and S. Suzuki, "Characterization of transformed and deformed microstructures in transformation induced plasticity steels using electron backscattering diffraction," *Mater. Sci. Eng. A*, vol. 528, no. 15, pp. 5007–5017, 2011.

[410] S. Zaefferer, J. Ohlert, and W. Bleck, "A study of microstructure, transformation mechanisms and correlation between microstructure and mechanical properties of a low alloyed TRIP steel," *Acta Mater.*, vol. 52, no. 9, pp. 2765–2778, 2004.

[411] M. de Meyer, L. Kestens, and B. C. de Cooman, "Texture development in cold rolled and annealed C-Mn-Si and C-Mn-Al-Si TRIP steels," *Mater. Sci. Technol.*, vol. 17, no. 11, pp. 1353–1359, 2001.

[412] C. Mesplont and B. C. De Cooman, "Effect of austenite deformation on crystallographic texture during transformations in microalloyed bainitic steel," *Mater. Sci. Technol.*, vol. 19, no. 7, pp. 875–886, 2003.

[413] B. Hutchinson, L. Ryde, E. Lindh, and K. Tagashira, "Texture in hot rolled austenite and resulting transformation products," *Mater. Sci. Eng. A*, vol. 257, no. 1, pp. 9–17, Nov. 1998.

[414] S. I. Wright and M. M. Nowell, "EBSD image quality mapping," *Microsc. Microanal.*, vol. 12, no. 1, pp. 72–84, 2006.

[415] H. M. Flower and T. C. Lindley, "Electron backscattering diffraction study of acicular ferrite, bainite, and martensite steel microstructures," *Mater. Sci. Technol.*, vol. 16, no. 1, pp. 26–40, 2000.

[416] J. Wu, P. . Wray, C. . Garcia, M. Hua, and A. . Deardo, "Image quality analysis: A new method of characterizing microstructures," *ISIJ Int.*, vol. 45, no. 2, pp. 254–262, 2005.

[417] H. Yoshida, S. Takagi, S. Sakai, S. Morito, and T. Ohba, "Crystallographic Analysis of Lath Martensite in Ferrite-Martensite Dual Phase Steel Sheet Annealed after Cold-Rolling," *ISIJ Int.*, vol. 55, no. 10, pp. 2198–2205, Oct. 2015.

[418] T. Nagano and M. Enomoto, "Calculation of the interfacial energies between α and γ iron and equilibrium particle shape," *Metall. Mater. Trans. A*, vol. 37, no. March, pp. 929–937, 2006.

[419] V. Randle, "Twinning-related grain boundary engineering," *Acta Mater.*, vol. 52, no. 14, pp. 4067–4081, 2004.

[420] J. Nakano and P. J. Jacques, "Effects of the thermodynamic parameters of the hcp phase on the stacking fault energy calculations in the Fe-Mn and Fe-Mn-C systems," *Calphad Comput. Coupling Phase Diagrams Thermochem.*, vol. 34, no. 2, pp. 167–175, 2010.

[421] P. Y. Volosevich, V. N. Gridnev, and Y. N. Petrov, "Influence of manganese and the stacking fault energy of iron–manganese alloys," *Fiz. Met. Met.*, vol. 41, no. 1, pp. 372–376, 1976.

[422] R. E. Schramm and R. P. Reed, "Stacking fault energies of seven commercial austenitic stainless steels," *Metall. Trans. A*, vol. 6, no. 7, pp. 1345–1351, 1975.

[423] L. Vitos, J. O. Nilsson, and B. Johansson, "Alloying effects on the stacking fault energy in austenitic stainless steels from first-principles theory," *Acta Mater.*, vol. 54, no. 14, pp. 3821–3826, 2006.

[424] H. Gholizadeh, "The Influence of Alloying and Temperature on the Stacking-fault Energy of Iron-based Alloys," Montanuniversität Leoben, 2013.

[425] D. J. H. Cockayne, M. L. Jenkins, and I. L. F. Ray, "The measurement of stacking-fault energies of pure face-centred cubic metals," *Philos. Mag.*, vol. 24, no. 192, pp. 1383–1392, 1971.

[426] S. Mahajan, C. S. Pande, M. A. Imam, and B. B. Rath, "Formation of annealing twins in f.c.c. crystals," *Acta Mater.*, vol. 45, no. 6, pp. 2633–2638, 1997.

[427] H. Gleiter, "The formation of annealing twins," *Acta Metall.*, vol. 17, no. 12, pp. 1421–1428, 1969.

[428] R. L. Fullman and J. C. Fisher, "Formation of annealing twins during grain growth," *J. Appl. Phys.*, vol. 22, no. 11, pp. 1350–1355, 1951.

[429]   S. Dash and N. Brown, "An investigation of the origin and growth of annealing twins," *Acta Metall.*, vol. 11, no. 9, pp. 1067–1075, 1963.

[430]   M. A. Meyers and L. E. Murr, "A model for the formation of annealing twins in F.C.C. metals and alloys," *Acta Metall.*, vol. 26, no. 6, pp. 951–962, 1978.

[431]   C. S. Pande, M. A. Imam, and B. Rath, "Study of Annealing Twins in FCC Metals and Alloys." *Metall. Mater. Trans. A*, 1990, 21, 2891–2896.

[432]   M. Enomoto, "Structure, energy and migration of phase boundaries in steels," in *Phase Transformations in Steels 1*, E. Pereloma and D. V. Edmonds, Eds. Elsevier, 2012, pp. 157–183.

[433]   J. M. Rigsbee and H. I. Aaronson, "The interfacial structure of the broad faces of ferrite plates," *Acta Metall.*, vol. 27, no. 3, pp. 365–376, 1979.

[434]   H. I. Aaronson, M. Enomoto, and J. K. Lee, *Mechanisms of diffusional phase transformations in metals and alloys*. CRC Press, 2016.

[435]   G. J. Shiflet and J. H. van der Merwe, "The role of structural ledges at phase boundaries—II. F.C.C.-B.C.C. interfaces in Nishiyama-Wasserman orientation," *Acta Metall. Mater.*, vol. 42, no. 4, pp. 1189–1198, 1994.

[436]   G. J. Shiflet and J. H. Merwe, "The role of structural ledges as misfit- compensating defects: fcc-bcc interphase boundaries," *Metall. Mater. Trans. A*, vol. 25, no. 9, pp. 1895–1903, 1994.

[437]   H. Song and J. J. Hoyt, "A molecular dynamics simulation study of the velocities, mobility and activation energy of an austenite-ferrite interface in pure Fe," *Acta Mater.*, vol. 60, no. 10, pp. 4328–4335, 2012.

[438]   S. Tateyama, Y. Shibuta, and T. Suzuki, "Orientation Relationship in Fcc–Bcc Phase Transformation Kinetics of Iron: a Molecular Dynamics Study," *ISIJ Int.*, vol. 50, no. 8, pp. 1211–1216, 2010.

[439]   C. Brandl, T. C. Germann, A. G. Perez-Bergquist, and E. K. Cerreta, "Grain boundary motion under dynamic loading: Mechanism and large-scale molecular dynamics simulations," *Mater. Res. Lett.*, vol. 1, no. 4, pp. 220–227, 2013.

[440]   T. Tsuru, Y. Kaji, T. Tsukada, and Y. Shibutani, "Atomistic Simulations of Stress Concentration and Dislocation Nucleation," *Progess Nucl. Sci. Technol.*, vol. 2, pp. 20–23, 2011.

[441]   J. Kacher, B. P. Eftink, B. Cui, and I. M. Robertson, "Dislocation interactions with grain boundaries," *Curr. Opin. Solid State Mater. Sci.*, vol. 18, no. 4, pp. 227–243, 2014.

[442]   C. Zheng, L. Li, W. Yang, and Z. Sun, "Microstructure evolution and mechanical properties of eutectoid steel with ultrafine or fine (ferrite + cementite) structure," *Mater. Sci. Eng. A*, vol. 599, pp. 16–24, 2014.

[443]   A. Durgaprasad *et al.*, "Defining a relationship between pearlite morphology and ferrite crystallographic orientation," *Acta Mater.*, vol. 129, pp. 278–289, 2017.

[444]   T. Takahashi, D. Ponge, and D. Raabe, "Investigation of Orientation Gradients in Pearlite in Hypoeutectoid Steel by use of Orientation Imaging Microscopy," *Steel Res. Int.*, vol. 78, no. 1, pp. 38–44, 2007.

[445]   Y. Adachi, S. Morooka, K. Nakajima, and Y. Sugimoto, "Computer-aided three-dimensional visualization of twisted cementite lamellae in eutectoid steel," *Acta Mater.*, vol. 56, no. 20, pp. 5995–6002, 2008.

[446]   T. Oyama, O. D. Sherby, J. Wadsworth, and B. Walser, "Application of the divorced eutectoid transformation to the development of fine-grained, spheroidized structures in ultrahigh carbon steels," *Scr. Metall.*, vol. 18, pp. 799–804, 1984.

[447]   J. D. Verhoeven, "The Role of the Divorced Eutectoid Transformation in the Spheroidization of 52100 Steel," *Metall. Mater. Trans. A*, vol. 31A, no. October, pp. 2431–2438, 2000.

[448]   J. D. Verhoeven and E. D. Gibson, "The Divorced Eutectoid Transformation in Steel," *Metall. Mater. Trans. A*, vol. 29A, pp. 1181–1189, 1998.

[449]   O. D. Sherby, T. Oyama, D. W. Kum, B. Walser, and J. Wadsworth, "Ultrahigh Carbon Steels," *J. Metall.*, pp. 50–56, 1985.

[450]   N. V Luzginova, L. Zhao, and J. Sietsma, "The Cementite Spheroidization Process in High-Carbon Steels with Different Chromium Contents," *Metall. Mater. Trans. A*, vol. 39A, pp. 513–521, 2008.